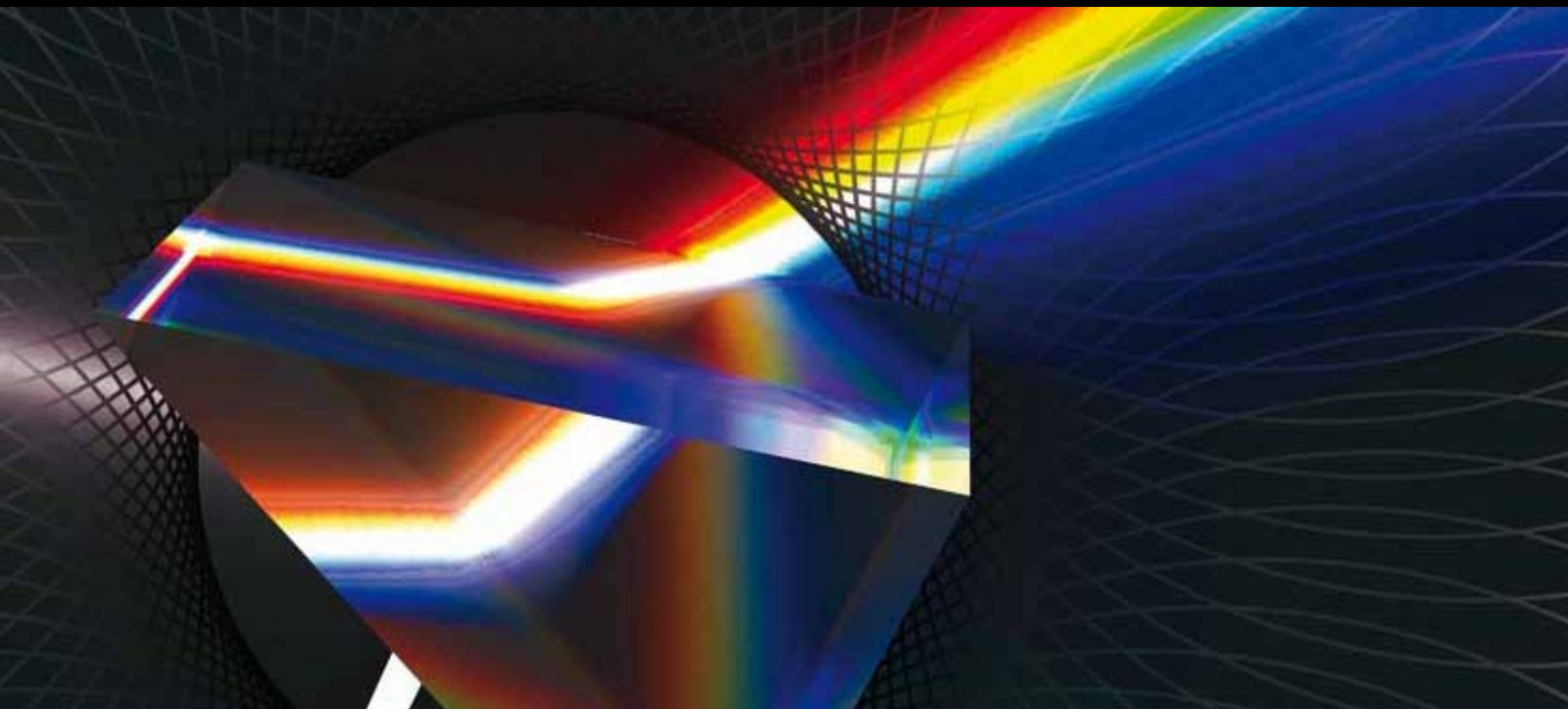


NONLINEAR FIBRE-BASED PHOTONIC TECHNOLOGIES

GUEST EDITORS: SONIA BOSCOLO, JUAN DIEGO ANIA CASTAÑÓN,
CHRISTOPHE FINOT, AND MIGUEL GONZÁLEZ HERRÁEZ





Nonlinear Fibre-Based Photonic Technologies

International Journal of Optics

Nonlinear Fibre-Based Photonic Technologies

Guest Editors: Sonia Boscolo, Juan Diego Ania Castañón,
Christophe Finot, and Miguel González Herráez



Copyright © 2012 Hindawi Publishing Corporation. All rights reserved.

This is a special issue published in “International Journal of Optics.” All articles are open access articles distributed under the Creative Commons Attribution License, which permits unrestricted use, distribution, and reproduction in any medium, provided the original work is properly cited.

Editorial Board

Alejandro Aceves, USA
Fortunato Tito Arcchi, Italy
Victor Arrizon, Mexico
Gaetano Assanto, Italy
Jose Azana, Canada
Ole Bang, Denmark
Randy A. Bartels, USA
Augusto Belendez, Spain
E. Bernabeu, Spain
Le Nguyen Binh, Germany
Keith J. Blow, UK
A. D. Boardman, UK
Wojtek J. Bock, Canada
Neil Broderick, UK
Hrvoje Buljan, Croatia
A. Cartaxo, Portugal
Giulio Cerullo, Italy
K. S. Chiang, Hong Kong
W. C. H. Choy, Hong Kong
David Coutts, Australia
Ilaria Cristiani, Italy
Michael J. Damzen, UK
Vittorio Degiorgio, Italy
Cornelia Denz, Germany
Ivan Djordjevic, USA
Niloy K. Dutta, USA
Robert G. Elliman, Australia

Charles M. Falco, USA
Mahmoud Fallahi, USA
Pietro Ferraro, Italy
Mário F. Ferreira, Portugal
Rashid A. Ganeev, Uzbekistan
Hooshang Ghafouri-Shiraz, UK
Ivan Glesk, UK
Qihuang Gong, China
N. A. Halliwell, UK
Sang-Kook Han, Republic of Korea
Sulaiman Wadi Harun, Malaysia
W. F. Hsieh, Taiwan
Mark Humphrey, Australia
Nicusor Iftimia, USA
Mohammed N. Islam, USA
Chennupati Jagadish, Australia
Wonho Jhe, Korea
Mirosław A. Karpierz, Poland
Yu S. Kivshar, Australia
Wieslaw Krolikowski, Australia
Nayot Kurukitkoson, Thailand
R. Leitgeb, Switzerland
Gong Ru Lin, Taiwan
Michael E. Marhic, UK
Lorenzo Marrucci, Italy
John McInerney, Ireland
Andrea Melloni, Italy

Adam Miranowicz, Poland
Roberto Morandotti, Canada
Uwe Morgner, Germany
Dragomir Neshev, Australia
Jean-Michel Nunzi, Canada
Takashige Omatsu, Japan
Wolfgang Osten, Germany
Ben Ovryn, USA
Nicolae C. Panoiu, UK
Vittorio M. N. Passaro, Italy
Gang-Ding Peng, Australia
Reji Philip, India
Armando Nolasco Pinto, Portugal
Adrian Podoleanu, UK
Jianan Qu, Hong Kong
Chenggen Quan, Singapore
Marek Samoc, Poland
John T. Sheridan, Ireland
Ping Shum, Singapore
Mohammad Taghizadeh, UK
R. P. Tatam, UK
Markus E. Testorf, USA
Mustapha Tlidi, Belgium
Stefano Trillo, Italy
Stefan Wabnitz, Italy
Boris Y. Zeldovich, USA

Contents

Nonlinear Fibre-Based Photonic Technologies, Sonia Boscolo, Juan Diego Ania Castañón, Christophe Finot, and Miguel González Herráez
Volume 2012, Article ID 530648, 2 pages

Nonlinear Pulse Shaping in Fibres for Pulse Generation and Optical Processing, Sonia Boscolo and Christophe Finot
Volume 2012, Article ID 159057, 14 pages

In-Fiber Subpicosecond Pulse Shaping for Nonlinear Optical Telecommunication Data Processing at 640 Gbit/s, J. Azaña, L. K. Oxenløwe, E. Palushani, R. Slavík, M. Galili, H. C. H. Mulvad, H. Hu, Y. Park, A. T. Clausen, and P. Jeppesen
Volume 2012, Article ID 895281, 16 pages

Bragg-Scattering Four-Wave Mixing in Nonlinear Fibers with Intracavity Frequency-Shifted Laser Pumps, Katarzyna Krupa, Michela Bettinzana, Alessandro Tonello, Vincent Couderc, Philippe Di Bin, Stefan Wabnitz, and Alain Barthélémy
Volume 2012, Article ID 263828, 7 pages

Multiple-Pulse Operation and Bound States of Solitons in Passive Mode-Locked Fiber Lasers, A. Komarov, F. Amrani, A. Dmitriev, K. Komarov, D. Meshcheriakov, and F. Sanchez
Volume 2012, Article ID 418469, 13 pages

The Proper Orthogonal Decomposition for Dimensionality Reduction in Mode-Locked Lasers and Optical Systems, Eli Shlizerman, Edwin Ding, Matthew O. Williams, and J. Nathan Kutz
Volume 2012, Article ID 831604, 18 pages

Nonlinear Optical Signal Processing for Tbit/s Ethernet Applications, L. K. Oxenløwe, M. Galili, H. C. Hansen Mulvad, H. Hu, J. L. Areal, E. Palushani, H. Ji, A. T. Clausen, and P. Jeppesen
Volume 2012, Article ID 573843, 14 pages

Amplification of Frequency-Modulated Similariton Pulses in Length-Inhomogeneous Active Fibers, I. O. Zolotovskii, D. I. Sementsov, A. A. Sysolyatin, A. S. Belanov, and M. S. Yavtushenko
Volume 2012, Article ID 979632, 6 pages

Manipulating the Propagation of Solitons with Solid-Core Photonic Bandgap Fibers, O. Vanvincq, A. Kudlinski, A. Bétourné, A. Mussot, Y. Quiquempois, and G. Bouwmans
Volume 2012, Article ID 157319, 12 pages

Editorial

Nonlinear Fibre-Based Photonic Technologies

**Sonia Boscolo,¹ Juan Diego Ania Castañón,²
Christophe Finot,³ and Miguel González Herráez⁴**

¹*Institute of Photonic Technologies, School of Engineering and Applied Science, Aston University, Birmingham B4 7ET, UK*

²*Instituto de Óptica, CSIC, Serrano 121, 28006 Madrid, Spain*

³*Laboratoire Interdisciplinaire Carnot de Bourgogne, Unité Mixte de Recherche CNRS 5209, 9 avenue Alain Savary, 21078 Dijon, France*

⁴*Departamento de Electrónica, Universidad de Alcalá de Henares, Alcalá de Henares, 28871 Madrid, Spain*

Correspondence should be addressed to Sonia Boscolo, s.a.boscolo@aston.ac.uk

Received 6 March 2012; Accepted 6 March 2012

Copyright © 2012 Sonia Boscolo et al. This is an open access article distributed under the Creative Commons Attribution License, which permits unrestricted use, distribution, and reproduction in any medium, provided the original work is properly cited.

The field of photonics is one of the fastest growing research areas in modern science, having a direct and almost immediate impact on the development of new technologies in fields ranging from telecommunications to the biosciences. Photonics, effectively an interdisciplinary field at the interface of physics, material science, and engineering, is very strongly linked to the field of nonlinear science. Though nonlinear physics has a rather long history, beginning with the works of Newton and Huygens, science and technologies of the 19th and most of the 20th century have been dominated by linear mathematical models and linear physical phenomena. Over the last decades, there has been growing recognition of physical systems in which nonlinearity introduces a rich variety of fundamentally new properties that can never be observed in linear models or implemented in linear devices.

From a practical standpoint, nonlinearity adds to the difficulty of understanding and predicting the system properties. However, with suitable design and control, it is possible to master and exploit nonlinear physical interactions and processes to yield tremendous benefits. The understanding and mastering of nonlinear optical systems has the potential to enable a new generation of engineering concepts.

Although silica exhibits much lower optical nonlinearity than crystals of such materials as lithium niobate or beta barium borate, silica fibres can provide a comparatively enormous interaction length (more than 1 km) and tight confinement (less than $2 \mu\text{m}^2$ mode area), which offers the long-recognized possibility of using optical fibres for nonlinear interactions. In high-speed optical communications such nonlinear effects generally degrade the integrity of

the transmitted signal, but the same effects can be used to realize a variety of optical functions that have practical applications in the field of light-wave technology. Nonlinear processes that have been exploited in demonstrations and applications include stimulated Brillouin and Raman scattering, as well as aspects of the Kerr effect variously called self-phase modulation, cross-phase modulation, four-photon (four-wave) mixing, cross-polarization modulation, and parametric gain. Important examples of established and new emerging nonlinear fibre-based photonic technologies essentially relying on nonlinear phenomena include all-optical signal processing and regeneration in ultrafast telecommunications, optical gating, switching and frequency conversion, optical waveform generation and pulse shaping, optical parametric amplification, Raman amplifiers and lasers, high-power pulsed and continuous-wave lasers, broadband and supercontinuum (SC) light sources, and other applications. This is the area which is addressed in this special issue: the development of novel photonic approaches, techniques, systems, and devices exploiting nonlinear effects in optical fibres.

The use of nonlinear photonic technologies for managing signals in the all-optical domain has enabled applications in such diverse areas as optical telecommunications, metrology, optical sensing, microwave engineering, image processing, and optical computing, to name a few. Advantages of processing the information in the all-optical domain include the large available bandwidth and the parallelism intrinsic to the optical approach, which translate into high processing speeds. Although photonic technologies already play

an important role in the context of high-speed communications networks, their scope is, at present, largely restricted to the transport layer rather than being used for complex routing, processing and switching tasks which are performed in the electronic domain after an optical to electrical conversion which is costly and reduces system speed and latency. Today, electronic techniques of signal manipulation are advanced compared to all-optical processing devices which are still at the research stage rather than under commercial development. Hence, considerable knowledge still has to be accumulated, and new methodologies need to be explored before a true breakthrough can be achieved in this field, allowing the range of functions and operations currently accomplished electronically to be performed in the optical domain. Furthermore, by using optical rather than electronic processing, additional functionality may be possible.

Several textbooks exist that cover various aspects of nonlinear fibre-based optical technology. There are also several tutorial and invited papers devoted to the topic. The purpose of this special issue is to provide a flavor of the state-of-the-art, recent developments and trends in the field from both theoretical and experimental perspectives. The issue comprises eight papers submitted by distinguished researchers and their colleagues in their respective fields, who were invited to contribute with an overview of the latest advances in their own research area.

J. Azaña et al. review recent work on the design and fabrication of all-fibre (long-period grating-based) devices for optical pulse shaping, particularly picosecond and subpicosecond flat-top pulse generation, and their application in nonlinear optical telecommunication data processing, particularly switching (demultiplexing) of optical time-division multiplexed data signals in fibre-optic telecommunication links operating at bit rates up to 640 Gbit/s. S. Boscolo et al. review recent theoretical and experimental progress on the use of fibre nonlinearities for the generation and shaping of optical pulses and the applications of advanced pulse shapes in all-optical signal processing, with a focus on ultrahigh repetition rate pulse sources, parabolic and triangular pulse generation, coherent SC sources, and applications such as optical regeneration, linear distortion compensation, signal postprocessing in optical communication systems, optical signal doubling, and frequency conversion. I. O. Zolotovskii et al. report theoretical predictions of the generation of stable self-similar frequency-modulated optical pulses in a length-inhomogeneous fibre gain medium, which enables subpicosecond pulse amplification up to the nanojoule energies. O. Vanvincq et al. review recent theoretical and experimental work on manipulating the Raman gain-induced soliton self-frequency shift dynamics in special solid-core photonic band-gap fibres and its impact on SC generation, with the results showing efficient tailoring of the SC spectral extension as well as strong noise reduction at the SC long-wavelength edge. K. Krupa et al. discuss nonlinear frequency conversion based on Bragg-scattering four-wave mixing in highly nonlinear fibre using a novel cost-effective and partially coherent pumping scheme, with the experimental results demonstrating efficient and tunable conversion

despite the large bandwidth and statistical independence of the pumps. E. Shlizerman et al. use the method of proper orthogonal decomposition (POD) to demonstrate that low-dimensional models generated by a POD analysis provide a good framework for characterizing the underlying dynamics and bifurcation behavior in mode-locked laser systems, and determining the optimal working regime for the laser (maximal suppression of the multipulsing instability). A. Komarov et al. present results of their research on multipulse operation of passive mode-locked fibre lasers, addressing in particular the formation of bound steady states of interacting solitons in the presence of different nonlinear loss shaping mechanisms, the possibility of information coding in soliton trains with various bounds between neighboring pulses, and the formation of bound-enhancing powerful soliton wings as a result of dispersive wave emission due to lumped nonlinear losses. Finally, L. K. Oxenløwe et al. review recent experimental advances in nonlinear optical signal processing for Ethernet applications, with a focus on 1.28 Tb/s data generation and demultiplexing.

Acknowledgments

We would like to thank all the authors for their invaluable contributions and original ideas, the reviewers for providing thorough evaluations of the submitted papers, and the Editorial Staff of the International Journal of Optics for suggesting that we organize this special issue and for their work in coordinating the editorial process. It has been our pleasure putting this special issue together, and we hope that you enjoy reading it.

*Sonia Boscolo
Juan Diego Ania Castañón
Christophe Finot
Miguel González Herráez*

Review Article

Nonlinear Pulse Shaping in Fibres for Pulse Generation and Optical Processing

Sonia Boscolo¹ and Christophe Finot²

¹ Photonics Research Group, School of Engineering and Applied Science, Aston University, Birmingham B4 7ET, UK

² Laboratoire Interdisciplinaire Carnot de Bourgogne, UMR 6303 CNRS, Université de Bourgogne, 21078 Dijon, France

Correspondence should be addressed to Sonia Boscolo, s.a.boscolo@aston.ac.uk

Received 16 November 2011; Accepted 9 January 2012

Academic Editor: Juan Diego Ania Castañón

Copyright © 2012 S. Boscolo and C. Finot. This is an open access article distributed under the Creative Commons Attribution License, which permits unrestricted use, distribution, and reproduction in any medium, provided the original work is properly cited.

The development of new all-optical technologies for data processing and signal manipulation is a field of growing importance with a strong potential for numerous applications in diverse areas of modern science. Nonlinear phenomena occurring in optical fibres have many attractive features and great, but not yet fully explored, potential in signal processing. Here, we review recent progress on the use of fibre nonlinearities for the generation and shaping of optical pulses and on the applications of advanced pulse shapes in all-optical signal processing. Amongst other topics, we will discuss ultrahigh repetition rate pulse sources, the generation of parabolic shaped pulses in active and passive fibres, the generation of pulses with triangular temporal profiles, and coherent supercontinuum sources. The signal processing applications will span optical regeneration, linear distortion compensation, optical decision at the receiver in optical communication systems, spectral and temporal signal doubling, and frequency conversion.

1. Introduction

The use of photonic technologies for data processing in the all-optical domain has a strong potential for a variety of interesting applications in such diverse areas as optical telecommunications, metrology, optical sensing, microwave engineering, advanced microscopy image processing, optical computing, and many others. Advantages of processing the information in the all-optical domain include the large available bandwidth and the (potential) parallelism intrinsic to the optical approach, which translate into high-processing speeds. However, today electronic techniques of signal manipulation are advanced compared to all-optical processing devices, which are still at the research stage rather than under commercial development. A key feature of electronics, enabling many different applications, is the capability of generating electrical waveforms with arbitrary temporal profiles by use of simple integrated circuits. This capability is so far unmatched in the optical frequency range, where bulky and complex devices are required to shape the light fields. Hence, considerable knowledge still has to be accumulated and new methodologies need to be explored

before a true breakthrough can be achieved in this field, allowing the range of functions and operations currently accomplished electronically, to be performed in the optical domain. Furthermore, by using optical rather than electronic processing additional functionality may be possible.

In order to realize such all-optical processing, nonlinear photonics is seen as a key technology. Optical fibre materials exhibit a nonlinear response to strong electric fields, such those of optical signals confined within the small fibre core. In high-speed optical communications such nonlinear effects generally degrade the integrity of the transmitted signal but the same effects can be used to realize a variety of optical functions that have practical applications in the field of lightwave technology. In this paper, we provide a snapshot of recent results and advances in the use of nonlinear effects in optical fibres for optical waveform generation and pulse shaping and in the applications of advanced pulse profiles in all-optical signal processing. We would like to note that the main attention in this paper will be focused on results obtained in our groups, and that it is not our intention here to comprehensively cover all the possible examples of fibre-based pulse shaping and signal processing.

2. Fibre Nonlinearities

The third-order $\chi^{(3)}$ optical nonlinearity in silica-based single-mode (SM) fibres is one of the most important effects that can be used for all-optical signal processing. This happens not only because the third-order nonlinearity provides ultra-fast response times in the femtosecond range, but also because it is responsible for a wide range of phenomena such as third-harmonic generation, nonlinear refraction (Kerr nonlinearity), and stimulated Raman and Brillouin scattering [1]. The rapid recent developments of microstructured fibres with extremely small effective core areas and exhibiting enhanced nonlinear characteristics [2] and of fibres using materials with refractive indexes higher than that of the silica glass [3] have enabled dramatic reduction of the required fibre lengths for nonlinear processing compared to conventional fibres. Such progress has paved the way for the integration of fibre-based nonlinear processing functions on photonic chips.

The intensity dependence of the refractive index of a fibre gives rise to different effects depending on the shape of the input signal; the most widely studied effects are self-phase modulation (SPM) and cross-phase modulation (XPM). Considering the localized optical pulse evolution in a fibre medium and neglecting higher order effects in the fibre, pulse propagation can be described by the nonlinear Schrödinger (NLS) equation [4]:

$$\psi_z = -i\frac{\beta_2}{2}\psi_{tt} + i\gamma|\psi|^2\psi, \quad (1)$$

where $\psi(z, t)$ is the slowly varying pulse envelope in the comoving system of coordinates, β_2 and $\gamma = 2\pi n_2/(\lambda A_{\text{eff}})$ are the respective group-velocity (second-order) dispersion (GVD) and Kerr nonlinearity coefficients of the fibre, n_2 is the nonlinear-index coefficient, λ the central wavelength of the pulse, and A_{eff} the effective core area. As a result of the nonlinear term in (1), upon propagation in the fibre the pulse acquires an intensity-dependent nonlinear phase shift as $\phi(z, t) = \gamma|\psi(0, t)|^2z$, namely, the frequency chirp $-\phi_t$. When the length scale associated with the pulse where the GVD effects take place: $L_D = T_0^2/|\beta_2|$ (with T_0 being some temporal characteristic value of the initial pulse) is much larger compared with both the fibre length and the nonlinear length $L_{\text{NL}} = 1/(\gamma P_0)$ (with P_0 being the peak power of the initial pulse), the dispersive term in (1) can be neglected. In this case, the presence of a chirp causes a nonlinear broadening of the pulse spectrum. When two (or more) pulses copropagate inside a fibre, one still obtains an NLS equation for each pulse but these equations are coupled through XPM [4]. In this case, the nonlinear phase evolution for each pulse depends also on the power of the other pulses according to the expression $\phi_i(z, t) = \gamma_i(|\psi_i(0, t)|^2 + 2\sum_{j \neq i} |\psi_j(0, t)|^2)z$. XPM occurs only when the pulses overlap. Similar to the SPM case, XPM leads to additional nonlinear chirping and spectral shaping.

When the effects of chromatic dispersion are considered in combination with the Kerr nonlinearity, rich pulse dynamics arise from the interplay between dispersive and nonlinear effects depending on the sign of the dispersion

and the relative magnitudes of the associated length scales. A well-known and fascinating example is the formation of optical solitons [5, 6] in the anomalous dispersion regime of a fibre ($\beta_2 < 0$) as a result of a cooperation between GVD and SPM. On the contrary, in the regime of normal dispersion pulse dynamics are highly affected by the phenomenon of optical wave breaking [7–9].

In the next Section we will discuss some newly emerged qualitative features of the optical pulse evolution in a fibre under the combined action of dispersion and nonlinearity.

3. Optical Pulse Generation and Shaping Using Fibre Nonlinearities

Techniques for generating, controlling, manipulating, and measuring ultrashort optical pulses and specialized waveforms have become increasingly important in many scientific areas including, amongst others, ultrahigh-speed optical communications [10], optical signal processing, and biophotonics. To date, conventional picosecond and femtosecond pulse shaping in the optical domain have been implemented using devices, such as liquid crystal spatial light modulators [11, 12], wavelength-to-time mapping [13, 14], acoustooptic modulators, and electrooptical phase arrays, that impart user-specified spectral amplitude and phase to the pulse. Though powerful and flexible, this approach has the drawback of requiring a rather bulky and expensive apparatus, entailing a level of cost and complexity that is not often commensurate to the used laser system and target application. In order to fulfill telecommunication requirements, more compact techniques for pulse shaping have been developed, which include the use of super-structured fibre Bragg gratings [15], long-period fibre grating filters [16], and arrayed waveguide gratings that are well suited for line by line processing of high-repetition periodic pulse shapes [17, 18]. However, in all these pulse shapers using linear techniques, the bandwidth of the input pulse determines the maximum bandwidth of the output. Indeed, a linear manipulation cannot increase the pulse bandwidth, and so to create shorter pulses nonlinear effects must be used. This limitation of the linear approaches becomes very stringent when synthesizing advanced pulse shapes such as rectangular pulses, for which a large optical bandwidth is required to reproduce accurately the spectral side lobes linked to the temporal compactness of the pulse. Moreover, in those applications that require spectral narrowing, linear filtering introduces a power penalty that is at least proportional to the ratio of the target spectrum to the input one.

The combination of third-order nonlinear processes and chromatic dispersion in optical fibres can provide efficient new solutions to overcome the aforementioned limitations. The pulse-shaping examples discussed below highlight some of the advantages offered by a passive, all-optical nonlinear fibre-based approach to pulse shaping.

3.1. Ultrahigh Repetition Rate Pulse Train Generation. As a first illustration of the possible nonlinear pulse shaping mechanisms in optical fibres, we review here the generation of ultrashort pulse trains with very high repetition rates

resulting from the passive evolution of optical pulses in an anomalously dispersive fibre in the presence of Kerr nonlinearity. As mentioned in the previous Section, in the anomalous GVD regime of a fibre, the NLS equation (1) admits families of soliton solutions. While fundamental solitons are characterized by an exact balance between the GVD and SPM effects ($N = \sqrt{L_D/L_{NL}} = 1$), in the case of higher order solitons ($N > 1$) SPM dominates initially but GVD soon catches up and leads to pulse contraction. This stage of temporal compression can be used for generating pulses with ultrashort durations [19–21]. However, the compressed pulses exhibit a low-amplitude structure outside the central lobe. An alternative technique that prevents sidelobe formation relies on the progressive evolution of the peak power and temporal duration of a fundamental soliton in a distributed amplifier or a dispersion decreasing (DD) fibre [22, 23]. Step-like or comb-like [24] dispersion profiled structures based on carefully chosen sets of fibres have been successfully used to emulate continuous DD fibre profiles.

The generation of high repetition rate pulse sources has largely benefited from the nonlinear compression effect taking place in the anomalous dispersion region, and several works have demonstrated the nonlinear reshaping of a sinusoidal beat-signal into well-separated pulses, the pulse repetition rate being simply determined by the frequency separation between the two continuous-wave (CW) laser sources. This technique has been successfully demonstrated with various experimental setups including DD fibres, adiabatic Raman compression in standard fibres, and step-like and comb-like dispersion profiled fibres. More recently, this nonlinear compression effect has been observed through a multiple four-wave mixing (FWM) process in a single anomalously dispersive fibre, and repetition rates ranging from a few tens gigahertz to 1 terahertz have been achieved [25]. In the frequency domain, such nonlinear compression can be viewed as the result of a modulation instability [26] experienced by the initial beat signal during propagation in the fibre, with the generation of new sidebands via FWM: two pump photons at ω_1 and ω_2 interact to generate two first-order sideband photons at $\omega_1 - \Omega$ and $\omega_2 + \Omega$, $\Omega = \omega_2 - \omega_1$ being the pump frequency detuning. High-order sidebands are then generated due to multiple FWM interactions. We note that a powerful alternative technique for realizing high-repetition-rate short-pulse sources relies on harmonic passive mode locking of fibre lasers [27–30]. The advantage of laser cavities as such compared to nonlinear pulse shaping in one-stage fibre systems is the possibility of achieving lower pulse train duty cycles. However, laser cavities have the drawbacks that they require mode locking, they cannot be referenced to an external clock directly and are not very suitable for the generation of pulses with ultrahigh repetition rates above a hundred gigahertz.

A typical experimental setup for the generation of high repetition rate pulse trains at telecommunication wavelengths is sketched in Figure 1(a). The initial beat signal is easily obtained via temporal superposition of two CWs with slightly different wavelengths delivered by external cavity lasers or a single CW directly modulated by an intensity modulator. A phase modulator driven at a frequency of a

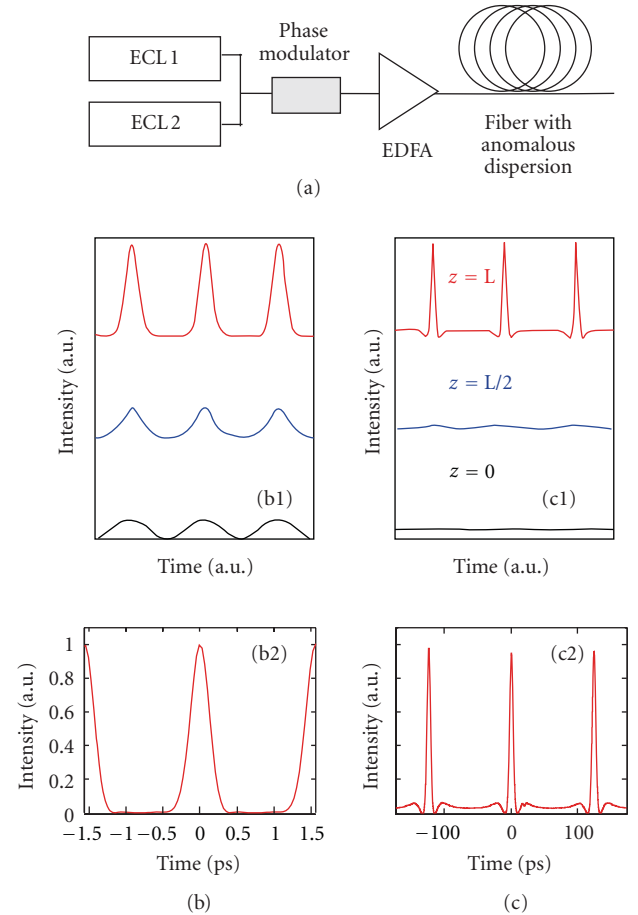


FIGURE 1: (a) Experimental setup for high repetition rate pulse train generation. (b, c) Results obtained for the optimum output shape and for the best compression, respectively. The temporal intensity profiles at different stages as predicted by numerical simulations (subplots 1) are compared to the experimental results (subplots 2) obtained by the FROG technique (b2—results adapted from [25]) or by an optical sampling oscilloscope (c2—results adapted from [31]).

few hundreds of megahertz is used to avoid the deleterious effects of Brillouin back scattering. The beat signal is then amplified up to the Watt level by an erbium-doped fibre amplifier (EDFA) and propagated through a suitable optical fibre with anomalous dispersion to realize the nonlinear reshaping. According to the pulse source parameters that are chosen (pulse repetition rate, initial peak power, nonlinearity and dispersion coefficients of the compression fibre, and fibre length), various output pulse shapes can be obtained. Intensity and phase measurements based on the frequency resolved optical gating (FROG) technique [32] show that high-quality compressed pulses with a Gaussian intensity profile and nearly constant phase can be achieved at a typical duty cycle of 1/5 [25, 33] (Figure 1(b)). Lower duty cycles can still be obtained with a single fibre, but at the expenses of increased sidelobes in the wings of the pulses [34]. Such sidelobes can be partly avoided by using specially designed

arrangements of segments of fibres [35–37] or other comb-like structures.

We would like to note that the reshaping of a sinusoidal beat signal into ultrashort structures can be understood in terms of the nonlinear dynamics of “Akhmediev breathers” [38, 39]. In this context, the extreme spatiotemporal localization that can be observed (see, e.g., Figure 1(c)) is explained as a result of the formation of Peregrine solitons [31, 40], mathematical solutions of the standard NLS equation that have been first derived in 1983 in the hydrodynamics context [41] but have never been demonstrated experimentally before 2010, and using experiments in optical fibres. These observations offer a promising way to better understand the problem of the occurrence of rogue waves in optics and hydrodynamics [42, 43].

3.2. Generation of Parabolic Pulses in Active and Passive Fibres. Strong pulse reshaping can also occur in the normal regime of dispersion of a fibre. An important example that has generated a great deal of attention in the last decade is the occurrence of self-similar dynamical effects in the nonlinear propagation of ultrashort pulses in normally dispersive (ND) optical fibre amplifying media [44]. Results have demonstrated a fundamentally new operating regime where the interaction of Kerr nonlinearity, dispersion, and optical gain is exploited to generate a particular class of pulses with a parabolic intensity profile and a strictly linear frequency chirp. These pulses then propagate in a self-similar manner, holding certain relations (scaling) between pulse power, duration, and chirp parameter. The results for the self-similar parabolic pulses are obtained by assuming that a fibre amplifier can be described by the NLS equation with gain

$$\psi_z = -i\frac{\beta_2}{2}\psi_{tt} + i\gamma|\psi|^2\psi + \frac{g}{2}\psi, \quad (2)$$

where g is the distributed gain coefficient. Using a self-similar ansatz and standard amplitude/phase decomposition, one can find self-similar parabolic pulse solutions in the quasiclassical limit of (2) ($\beta_2(|\psi|_{tt})/(2\gamma|\psi|^3) \ll 1$), whose dynamic evolution is summarized as [45, 46]

$$\begin{aligned} |\psi(z, t)| &= a(z)\sqrt{1 - t^2/\tau(z)^2}\theta(\tau(z) - |t|), \\ \arg \psi(z, t) &= b(z)t^2 + \phi_0(z), \quad a(z) = a_0 e^{gz/3}, \\ \tau(z) &= \tau_0 e^{gz/3}, \quad b(z) = -\frac{g}{6\beta_2}, \end{aligned} \quad (3)$$

in the case of constant gain. Here, $\theta(x)$ is the Heaviside function. The amplitude term indeed reveals a parabolic intensity profile, and the phase term a parabolic phase modulation or linear chirp with chirp rate $b/2$. The peak amplitude and width of the pulse scale from their initial values, and the initial values depend only on the initial energy and amplifier parameters. These solutions possess the remarkable property of being a global attractor to the system for arbitrary initial conditions [47, 48]. By analogy with the well-known stable dynamics of solitary waves or

solitons, these self-similar parabolic pulses have come to be known as “similaritons”. In contrast to solitons, similaritons can tolerate strong nonlinearity without wave breaking. The normal GVD effectively linearizes the accumulated phase of the pulse allowing for the spectral bandwidth to increase without destabilizing the pulse [49]. The unique properties of similariton pulses have motivated many theoretical and experimental studies (see, e.g., [46, 48, 50–53]).

Experimental demonstrations of similariton generation relying on amplification from either rare-earth doping (with ytterbium [45, 56–59] or erbium [51] dopants) or Raman scattering [50, 54, 60] have been achieved, confirming the potential of this method especially when dealing with the generation of high-power ultrashort pulses. Thanks to the high level of linearity of the chirp developed during parabolic amplification and as long as the impact of third-order fibre dispersion is moderate [52, 61, 62], it is possible to efficiently compensate for the chirp slope, so that compressed pulses with very low substructures and temporal durations much shorter than the initial seed pulse can be obtained [45, 51, 56–59]. As an illustration, Figures 2(a) and 2(b) show the setup and results of an experiment where similaritons are generated through Raman amplification at telecommunication wavelengths [54]. Moreover, recent fibre lasers that use self-similar pulse shaping in the normal dispersion regime have been demonstrated to achieve high-energy pulses [63–66].

In addition to fibre amplifiers and lasers, stable similariton pulses can be generated in passive fibres provided a suitable longitudinal variation of the dispersion is introduced [55, 67–69] (Figure 2(c)). This approach is based on the observation that a longitudinal decrease of the normal dispersion is formally equivalent to linear gain. Recently, a simple approach to the generation of parabolic pulses that uses progressive nonlinear pulse reshaping in a ND fibre with fixed dispersion has been demonstrated [70]. However, in contrast with the asymptotic similariton solutions obtained in fibre amplifiers, the generated parabolic waveforms represent transient states of the nonlinear pulse evolution in the passive fibre medium [71]. As such, they have a finite life distance that depends sensibly on the initial conditions (pulse shape, energy, and chirp profile). Nevertheless, stabilization of the parabolic features is possible by use of a second propagation stage in a fibre with specially adjusted nonlinear and dispersive characteristics relative to the first fibre [70, 71].

3.3. Generation of Triangular Pulses. Parabolic shapes are not the only pulse waveforms that can be generated in a passive ND fibre. Recently, the combination of pulse prechirping and nonlinear propagation in a section of ND fibre has been introduced as a method for passive nonlinear pulse shaping, which provides a simple way of generating various advanced field distributions, including flat-top- and triangular-profiled pulses with a linear chirp [71]. In this scheme, Kerr nonlinearity and GVD lead to various reshaping processes of an initial conventional pulse (e.g., a Gaussian pulse) according to the chirping value and power level at the entrance of the fibre. In particular,

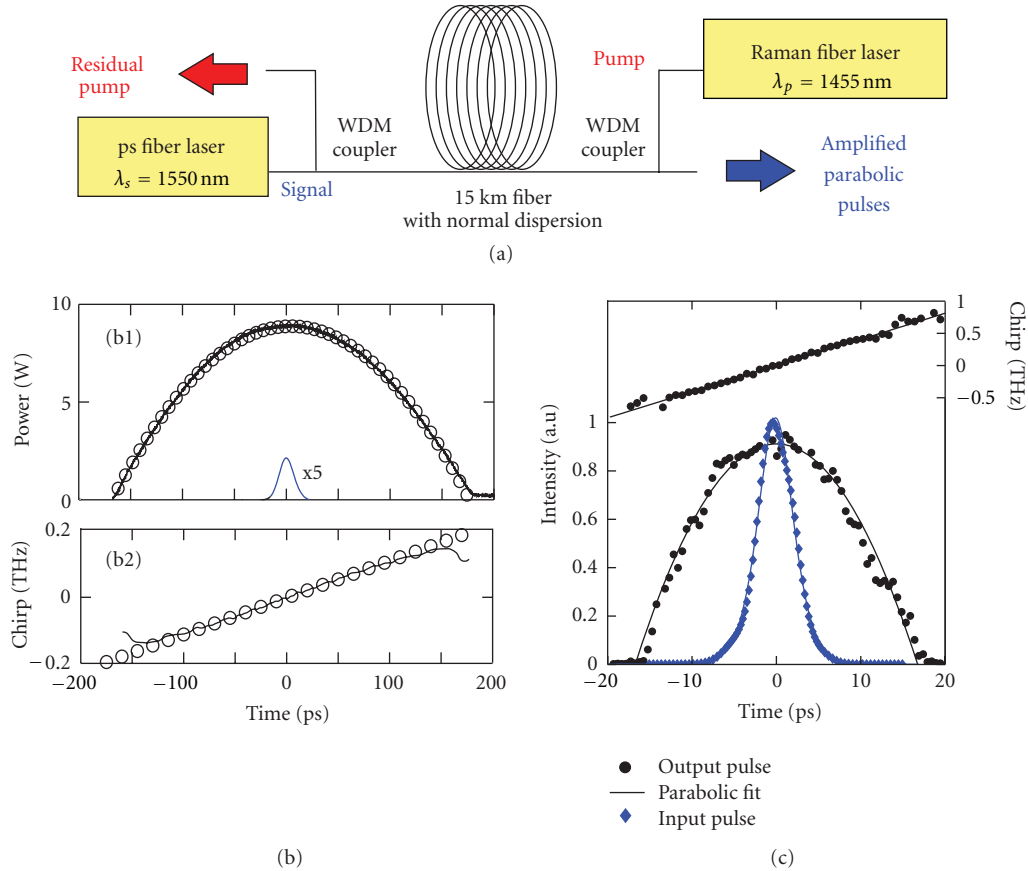


FIGURE 2: (a) Experimental setup for parabolic pulse generation through Raman amplification at telecommunication wavelengths. (b) Results obtained in the Raman amplifier (adapted from [54]): temporal intensity profile (subplot b1) and chirp profile (subplot b2) of the output pulse from the amplifier. The experimental results (solid black lines) are compared to a parabolic and a linear fit (open black circles), respectively. The intensity profile of the initial pulse is also shown (solid blue line). (c) Results obtained in a ND decreasing fibre (adapted from [55]): experimental temporal intensity and chirp profiles at the fibre output (black circles) compared to a parabolic and a linear fit (solid black lines), respectively. The initial intensity profile is also shown (blue diamonds).

triangular pulses can be generated for a positive initial chirp parameter (using the definition ibt^2 for the phase profile) and sufficiently high energies.

These theoretical results have been confirmed experimentally by intensity and phase measurements of the generated pulses [72] (Figure 3(b)). In the experimental setup used (Figure 3(a)), the control of the pulse prechirping value was realized by propagation through different lengths of standard SM fibre with anomalous GVD, which imposed a positive chirp parameter on the pulse. The prechirped pulses were amplified to different power levels using an EDFA and then propagated through a ND fibre to realize the pulse reshaping.

Different nonlinear dynamics may lead to the generation of triangular pulses in a passive ND fibre. Indeed, it has been recently shown qualitatively and numerically that temporal triangular intensity profiles can result from the progressive reshaping of initially parabolic pulses driven by the fourth-order dispersion (FOD) of the fibre [53]. The overall temporal effect of FOD on parabolic pulse propagation is to stretch and enhance the power reduction in the pulse wings,

leading to a triangular profile. Furthermore, the possibility of triangular pulse shaping in mode-locked ring-cavity fibre lasers has been first reported in [73]. It has been numerically demonstrated that for normal net dispersion, formation of two distinct steady-state solutions of stable single pulses can be obtained in a laser cavity in different regions of the system parameter space: the previously known similariton [63] and a triangular-profiled pulse with a linear frequency chirp.

3.4. Coherent Continuums for Optical Telecommunications.

One of the most well-known examples of pulse reshaping in the spectral domain is in supercontinuum (SC) generation. SC generation in optical fibres, and more specifically, in photonic crystal fibres with enhanced nonlinearity, is an established technique for producing broadband light sources in a wide range of research fields including metrology, biophotonics, and optical telecommunications [74, 75]. In telecommunications, the broadened spectrum can be spectrally sliced to generate wavelength multiplexed pulse trains [76–78]. The principle of operation of a multiwavelength source is illustrated in Figure 4(a). An initial high-power

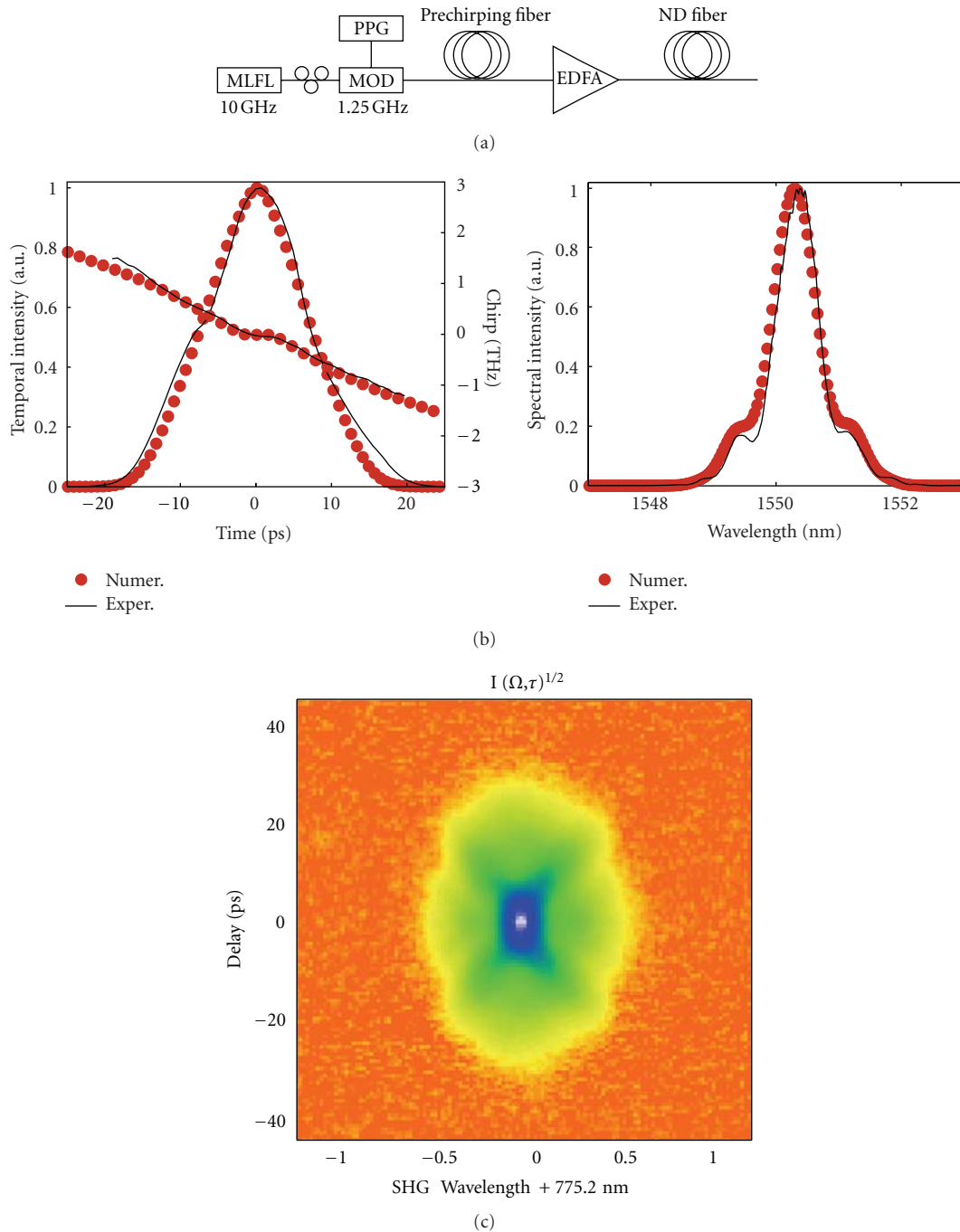


FIGURE 3: (a) Experimental setup for triangular pulse generation. (b) Experimental and numerical temporal intensity and chirp (ϕ_t) profiles retrieved from second-harmonic generation (SHG) FROG (left) and optical spectra (right) of the generated pulses for an example length of prechirping fibre. (c) SHG-FROG spectrogram of the pulse in (b). Results adapted from [72].

mode-locked picosecond or femtosecond pulse train with a repetition rate of several gigahertz is spectrally broadened through SPM in a kilometer-long highly nonlinear (HNL) fibre. At the fibre output, the spectrum is sliced by adequate bandpass filters (BPFs) to obtain pulse trains that have the same repetition rate as the initial train but new central frequencies.

Typically the broadest spectra are generated in anomalously dispersive fibres, where the broadening mechanism is strongly influenced by soliton dynamics [80]. However, solitonic effects and modulation instability lead to decreased temporal coherence and spectral flatness of the continuum generated in the anomalous dispersion regime [81]. By contrast, the nonlinear pulse evolution in ND fibres leads

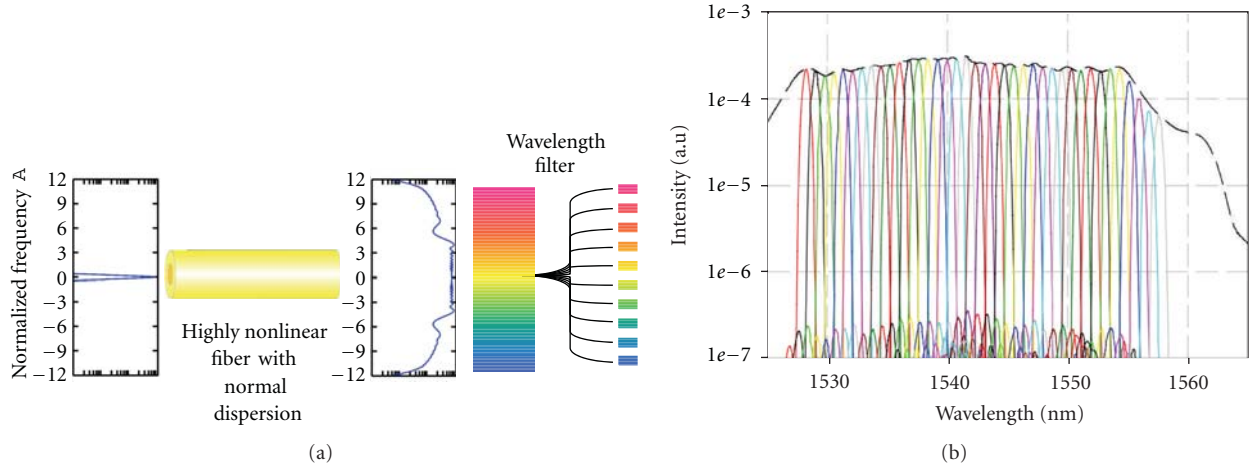


FIGURE 4: (a) Principle of operation of a multiwavelength picosecond source. (b) Experimental spectrum of a parabolic-shaped pulse after propagation in a ND-HNL fibre (black dashed line) and superposition of the measured spectra of 38 sliced channels. Results adapted from [79].

to flatter spectra and improved temporal coherence, but at the expenses of relatively narrower spectra [82, 83]. Hence frequency broadening using a ND fibre is an attractive choice whenever a moderate amount of broadening alongside good spectral and temporal stability of the output pulses are targeted. However, the main limits to spectral pulse quality in the normal dispersion regime are the spectral ripple arising from SPM of conventional laser pulses, and the effects of optical wave breaking which may lead to significant change in the temporal pulse shape and severe energy transfer into the wings of the spectrum. These effects can in principle be avoided by using preshaped input pulses with a parabolic temporal intensity profile, which would preserve their shape whilst propagating within the fibre and, thus, result in spectrally flat, highly coherent pulses. Continuum with low-spectral ripple and high-energy density in the central part is indeed achievable through parabolic pulse propagation in ND-HNL fibre [79], and low-noise multiwavelength picosecond sources covering the whole C-band of optical telecommunications have been demonstrated based on this technique [12, 16, 79] (Figure 4(b)).

4. Applications of Parabolic and Triangular Pulses in Signal Processing

Applications of parabolic pulses have not been limited to ultrashort high-power pulse generation and highly coherent continuum sources, but several optical processing techniques have taken advantage of their specific features. These include optical regeneration [84, 85] including pulse retiming [86], prereceiver nonlinear processing in the optical domain [87, 88], and mitigation of linear waveform distortions [89, 90]. The simple intensity profile of triangular pulses is also highly desired for a range of processing applications, including time domain add-drop multiplexing [91, 92], wavelength conversion [93–95], optical signal doubling [96], time-to-frequency mapping of multiplexed signals [97], and

enhanced spectral compression [98, 99]. In this Section, we will review some of these applications.

4.1. 2R Regeneration. As a first example, here we discuss the usage of parabolic pulses in 2R (reamplification, retiming) signal regeneration in an extension of the technique proposed by Mamyshev [100]. The method relies on SPM in a nonlinear medium (fibre) and subsequent offset spectral filtering to suppress the noise in the zero-bit slots and the amplitude fluctuations in the one-bit pulses of return-to-zero (RZ) optical data streams. In the schematic of the Mamyshev regenerator depicted in Figure 5(a), the signal to be regenerated is first amplified to the optimum power level, and an optical BPF is also used to reduce the amplified spontaneous emission noise power. Then spectral broadening is achieved in a HNL fibre, and the broadened spectrum is partially sliced by a second BPF, which is shifted with respect to the input signal frequency in order to transmit SPM-generated frequencies and reject the original spectrum. The central frequency and output pulse shape of the regenerated signal are determined by the central frequency and spectral profile of the offset filter, respectively. The SPM phase shift experienced in the HNL fibre depends on the instantaneous power (cf. Section 2). Hence, a high-intensity pulse induces more SPM phase shift and spectrally broadens more than the low-intensity noise [100]. Filtering the new SPM-generated frequencies with the offset filter leads to a power transfer function for the pulses and the noise which is close to a binary one [101].

Spectral filtering of similariton pulses can improve the ability of the Mamyshev regenerator to eliminate spurious noise pulses as well as to simultaneously reduce any fluctuations in the signal one-bit level [84]. This ability relies on the specific features of self-similar amplification. Indeed, a spectrum broadened through self-similar amplification has a smooth profile (cf. Section 3.4), whereas a SPM-broadened spectrum is generally accompanied by oscillatory structures

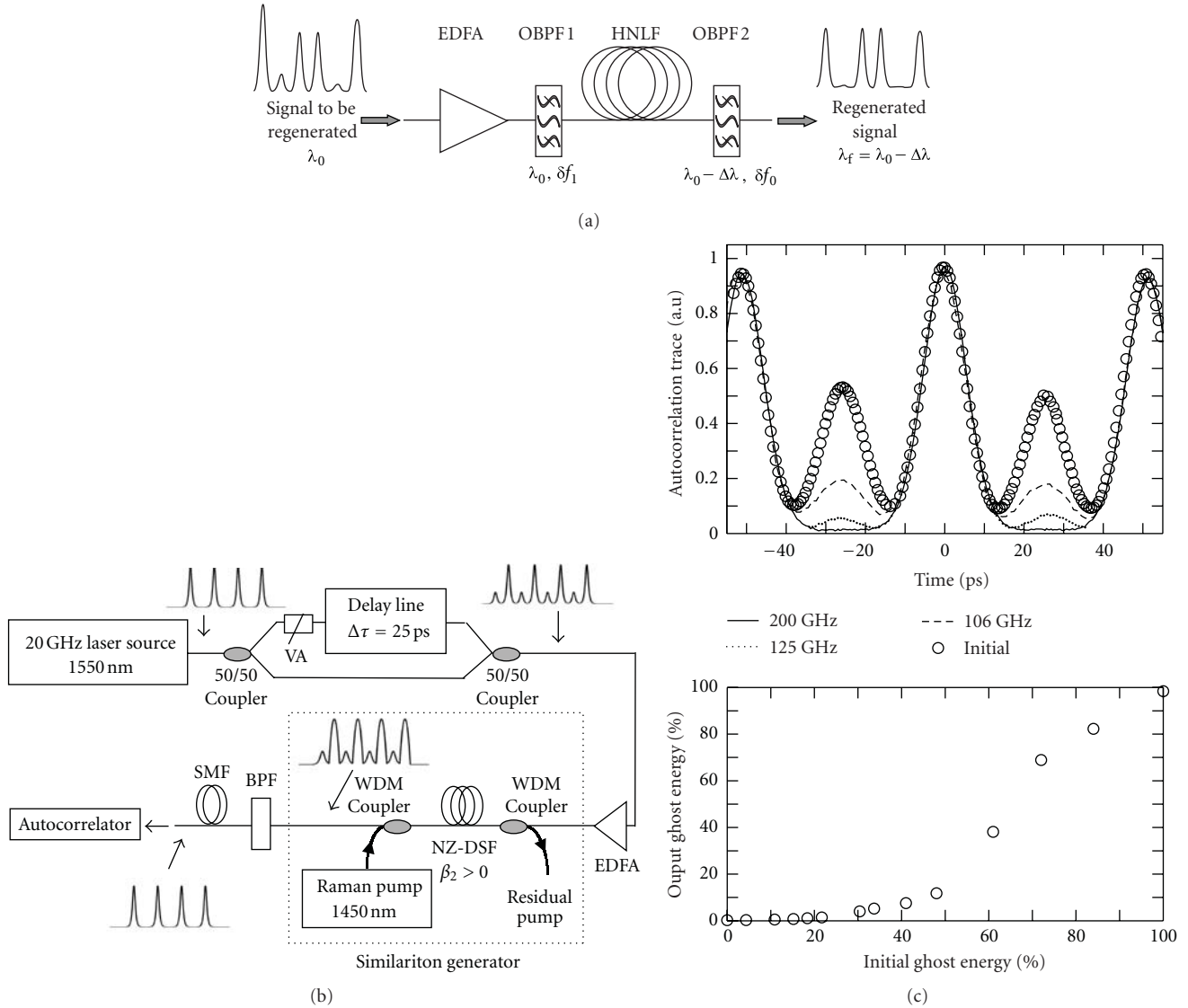


FIGURE 5: (a) Schematic of an optical regenerator based on SPM and filtering (after [100]). (b) Experimental setup for 40 Gbit/s similariton-based regeneration. (c) Top, autocorrelation traces of the pulse train at the Raman amplifier input (circles) and output for different values of the filter offset (dashed, dotted, and solid curves). Bottom, output versus input proportion of the spurious noise pulse energy with respect to the ones energy for a fixed filter offset. Results adapted from [84].

covering the entire frequency range. Moreover, the spectrum and chirp obtained by SPM both depend on the details of the initial pulse (shape, chirp, and energy), leading to some amplitude and time fluctuations of the regenerated pulses. In contrast, the similariton-based spectral broadening and similariton-induced chirp depend only on the initial pulse energy and/or amplifier parameters, respectively (cf. Section 3.2), so that both amplitude and timing jitter are reduced. In particular, the energy-dependent spectral broadening is responsible for efficient discrimination of high-energy pulses (ones) from low-energy pulses (zeros) with the offset BPF. An implementation of the similariton-based regeneration technique at 40 Gbit/s data rate where similariton pulses are generated through distributed Raman amplification in a ND fibre is illustrated in Figures 5(b) and 5(c). It is

worth noting here that a distributed amplification is helpful in increasing the energy yield of the regenerator which is a highly dissipative element [102].

4.2. Linear-Distortion Compensation. As a second example of the application of parabolic pulses in signal processing, we review here the realization of a time-domain all-optical Fourier transformation (OFT) technique. Time-domain OFT in which the spectral profile is converted into a waveform in the time domain makes it possible to eliminate the waveform distortion caused by linear perturbations in optical fibres, such as higher order dispersion, jitter and polarization-mode dispersion [103–106]. Time-domain OFT is realized ideally by applying a quadratic temporal phase modulation (time lens) to a distorted pulse:

$\psi_{\text{chirp}}(t) = \psi(t) \exp(ib t^2)$ and passing the linearly chirped pulse through a dispersive medium such as a short piece of fibre. When the accumulated dispersion of the medium $D = \beta_2 L$ equates the inverse of the chirp coefficient b (i.e., when the chirp is fully compensated), the output waveform is proportional to the spectral amplitude before OFT: $\chi(t) = \sqrt{i/(2\pi D)} \exp(-ibt^2) \tilde{\psi}(t/D)$, where $\tilde{\psi}(\omega)$ is the Fourier transform of $\psi(t)$, and the frequency ω is converted into time t through the relationship $\omega = t/D$. Since generally the spectral envelope profile has no distortion even if its time-domain waveform is distorted by linear perturbations, this frequency-to-time mapping indicates that a distortion-free pulse waveform can be obtained in the time domain after OFT. In [103–106], this compensation technique was investigated by using electrooptic phase modulators. But this way the quadratic modulation region was restricted to around the center of the sinusoidal modulation imparted by the phase modulator. Thus, any parts of the pulse extending beyond the quadratic region could not be properly transformed, and only the section of the target pulse sitting within the quadratic region could be compensated (Figure 6).

The use of XPM with parabolic pulses as a time lens has been recently proposed as a promising way to overcome the aforementioned limitation [89, 90]. Indeed, the chirp induced by XPM on the target pulse is proportional to the gradient of the intensity profile of the parabolic control pulse: $-\phi_t = -2bt$, $b = \mp 2\gamma a^2 L/\tau^2$, so it is exactly linear and thus ideal OFT can be achieved by complete chirp compensation. Here, a and τ are the respective peak amplitude and characteristic width of the parabolic pulse (cf. Section 3.2), and the sign \mp is for either a standard “bright” or a dark parabolic pulse [17]. The parabolic XPM-based OFT technique has been successfully experimentally demonstrated to achieve cancellation of the third-order dispersion-induced distortion of short-optical pulses [89, 90].

4.3. Optical Decision at the Receiver. In this section, we review a possible application of parabolic/flat-top pulses to the improvement of the signal bit-error rate (BER) in an optical communication system by using optical decision before the receiver. An attractive approach to the design of the optical receiver for high-speed fibre communication systems using RZ data formats is based on employing an additional all-optical decision element (ODE) just before the conventional receiver [87, 107–109]. In this way, the first decision is carried out in the optical domain, thus improving the quality of the received signal. The attractive possibility of improving the BER by using optical devices has been studied in some recent works [88, 110, 111]. The conceptual basis of the BER improvement by optical devices comes from the information theory: an intrinsic BER improvement is possible whenever the decision performed by the device in the optical domain is based on information that is different from the information used by the decision circuit of the (suboptimal) receiver in the electrical domain. In [88] an application of this general concept was demonstrated, based on using an advanced optical receiver enhanced by a nonlinear ODE. The example of an ODE scheme used in [88] exploits the nonlinear mechanism that leads to the

formation of parabolic pulses and the resultant flattening of the signal waveform (cf. Section 3.2). The method is based on the nonlinear reshaping of a pulse towards a broad and flat temporal waveform that can occur upon propagation in a ND fibre [9] and subsequent slicing of the pulse temporal profile by an optical temporal gate (e.g., an amplitude modulator with a sharp nonlinear transfer function or a nonlinear optical loop mirror provided with a clock) [85] or XPM-based techniques.

The basic mechanism that is responsible for BER improvement in this scheme can be understood in the following way. The pulse temporal broadening and flattening in the ND fibre permits to recover the center of the bit slot for those pulses that are significantly shifted from the bit slot center in the input pulse train because of timing jitter (Figure 7(a)). Such strongly time-shifted pulses, once they are converted into electrical pulses and arrive at the decision point, might be missed by the threshold detector in those conventional receivers that use a relatively small fraction of the bit period. In contrast, the bit slot recovery in the ND fibre enables such pulses to be recognized as marks in the ODE-enhanced receiver. The slicing of the central portion of the broadened pulse temporal profile by the temporal gate enables efficient suppression of the timing jitter of the pulses which, in turn, improves the receiver sensitivity [87]. This approach is illustrated in Figure 7(b), which shows that BER improvement over the conventional scheme, indeed, can be achieved using nonlinear signal processing in the optical domain before the conventional receiver. It is worth noting that the same processing technique based on temporal slicing of nonlinearly flattened pulse waveforms can also be used in all-optical 3R (2R + re-timing) signal regeneration [85].

4.4. Optical Signal Doubling and Frequency Conversion. Here we discuss the use of triangular pulses in the context of optical signal doubling and frequency conversion. A technique of copying optical pulses in both the frequency and time domains based on a combination of either XPM with a triangular pump pulse or SPM of a triangular pulse in a nonlinear Kerr medium and subsequent propagation in a dispersive medium was introduced in [96] and experimentally demonstrated in [95]. In this scheme, spectral doubling of an optical signal is made possible by the XPM or SPM phase shift generated by a temporal intensity profile with a linear gradient: $\phi(t) = \phi_0(1 - |t/\tau|)$, $\phi_0 \propto a^2\gamma L$ (a and τ being the peak amplitude and characteristic width of a triangular pulse, resp.), which translates into a constant and distinct (opposite sign) frequency chirp induced onto the leading (downshifted) and trailing (upshifted) edges of the signal pulse. As a result of this constant and distinct chirp, under certain conditions the pulse spectrum develops a structure consisting of two equal peaks. The separation between the two spectral peaks increases with the maximum nonlinear phase shift ϕ_0 , while their form is almost preserved. Under subsequent propagation of the modulated signal pulse in a linear dispersive medium, the produced spectral separation of the pulse components leads to their subsequent separation in time, thus allowing temporal replication of the pulse. In the case of normal dispersion, the pulse develops into a

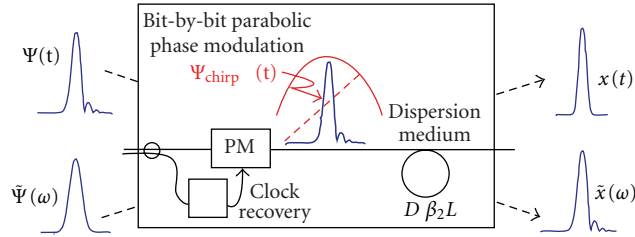


FIGURE 6: Schematic diagram of time-domain OFT (after [90]).

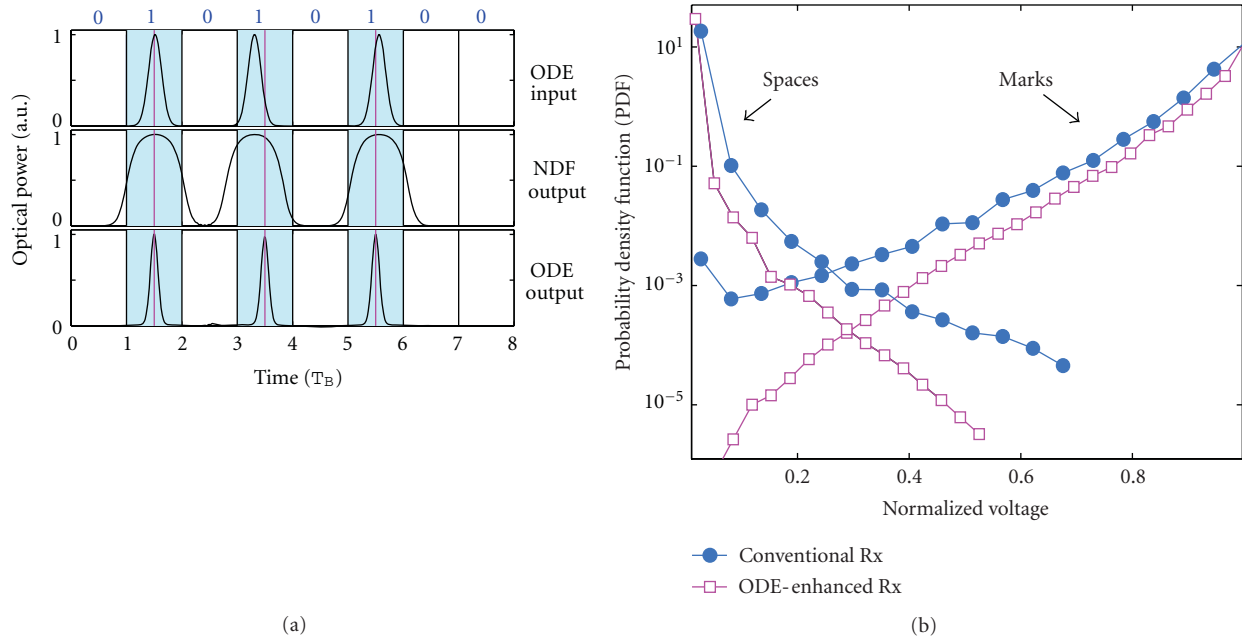


FIGURE 7: (a) Schematic illustration of the optical decision at an ODE-enhanced receiver. (b) Numerically calculated probability density functions for the voltage of the marks and spaces in the conventional and ODE-enhanced receivers for a 40 Gbit/s RZ input signal with a random jitter of the pulse temporal position. Results adapted from [88].

structure consisting of two identical pulses where the original pulse splits down the middle. The two pulse parts separate in time while experiencing dispersive broadening. The relative velocity of separation is proportional to the separation between the two peaks of the nonlinearly modulated pulse spectrum. Pulse splitting and separation occur also in the case of anomalous dispersion after an initial stage of pulse compression. Exact analytic expressions for the nonlinearly modulated pulse spectrum and the pulse temporal intensity distribution clearly show the features described above [96]. Applying spectral filtering to the XPM/SPM modulated signal is also possible to realize efficient and clean frequency conversion [93–95].

Figure 8 shows results of the experiment reported in [95]. Similarly to [72], triangular pulses were generated by passive nonlinear reshaping in a ND fibre. Spectral pulse doubling was realized through the SPM experienced by the triangular pulses over their life distance in a HNL fibre. The output SPM-shaped spectrum from the HNL fibre was sent into either a linear standard SM fibre segment to realize

temporal pulse doubling or a wavelength demultiplexer filter for frequency conversion processing.

5. Conclusion

We have provided an overview of several recent examples of the use of nonlinear phenomena in optical fibres for the generation and shaping of optical pulses. We have discussed the generation of ultrashort pulse trains with very high-repetition rates in the anomalous dispersion regime of a fibre, the generation of parabolic-shaped pulses in active and passive ND fibres, the generation of pulses with triangular intensity profiles in passive ND fibres, and the generation of coherent continuums for optical telecommunications in ND fibres. Examples of new techniques or improvements in existing techniques of all-optical nonlinear fibre-based signal processing enabled by specialized pulse waveforms have been reviewed. Specifically, we have presented applications of parabolic pulses in optical signal regeneration, compensation of linear waveform distortions, and signal postprocessing in

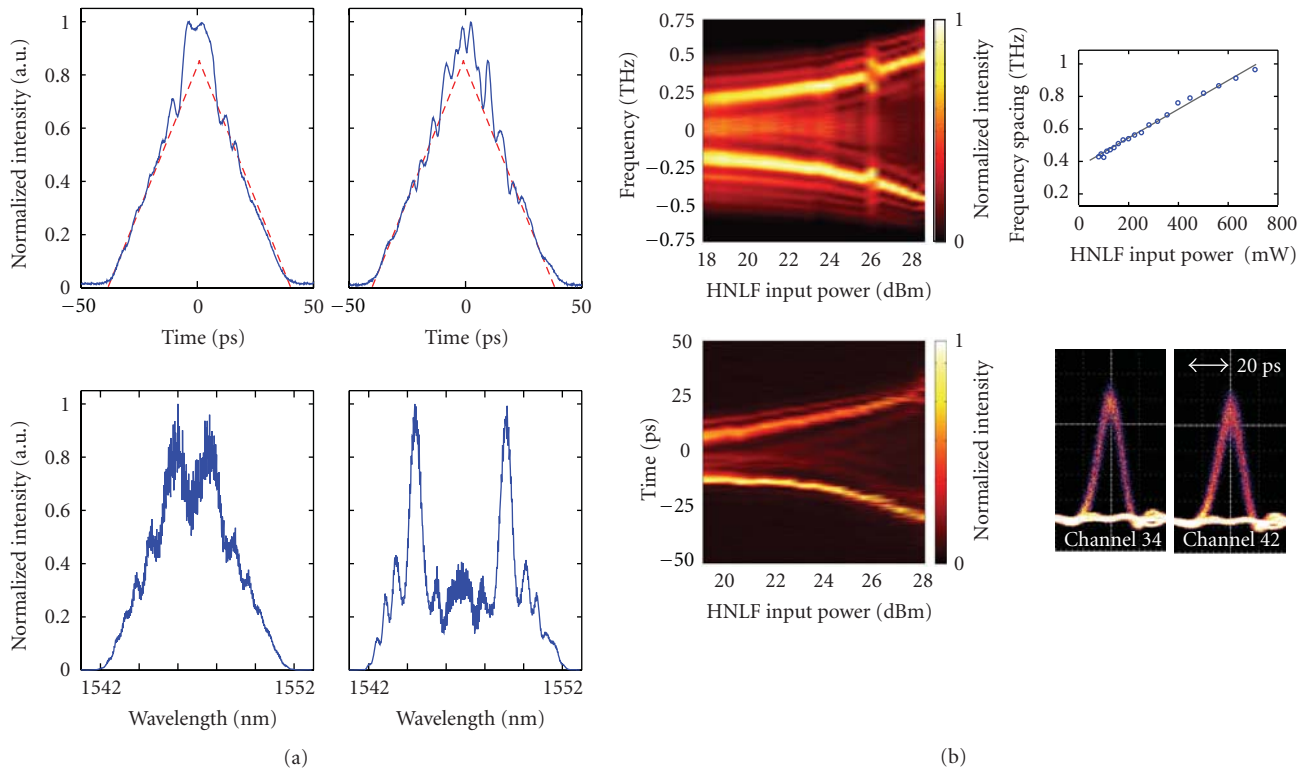


FIGURE 8: (a) Temporal (top) and spectral (bottom) intensity profiles after the ND reshaping fibre (left) and after the HNL fibre (right). (b) Top, evolution of the output spectrum from the HNL fibre with the input power (left) and dependence of the frequency spacing between the two spectral peaks on the input power (right). Bottom, evolution of the temporal intensity profile at the output of the linear SM fibre with the input power to the HNL fibre (left) and eye diagrams of a 10 Gbit/s pulse train obtained after spectral filtering for the ITU channels 34 and 42. Results adapted from [95].

optical communication systems. Applications of triangular pulses in optical signal doubling and frequency conversion have also been discussed.

Acknowledgments

The authors would like to acknowledge and thank our colleagues, namely, Prof. Sergei K. Turitsyn, Dr. Paul Harper, Dr. Anton I. Latkin, Prof. Keith J. Blow, Dr. Julien Fatome, Dr. Kamal Hammani, Dr. Bertrand Kibler, Prof. Guy Millot, and Prof. John M. Dudley and the Optoelectronics Research Center (Southampton, UK). The authors also acknowledge support from the British Council (Alliance Grant 10.002), the Ministère des Affaires Étrangères et Européennes (Alliance Grant 22836ZJ), the Agence Nationale de la Recherche, and the Conseil Regional de Bourgogne (PARI Photcom).

References

- [1] Y. R. Shen, *Principles of Nonlinear Optics*, John Wiley & Sons, New York, NY, USA, 1984.
- [2] J. C. Knight, "Photonic crystal fibres," *Nature*, vol. 424, no. 6950, pp. 847–851, 2003.
- [3] B. J. Eggleton, B. Luther-Davies, and K. Richardson, "Chalcogenide photonics," *Nature Photonics*, vol. 5, no. 3, pp. 141–148, 2011.
- [4] G. P. Agrawal, *Nonlinear Fiber Optics*, Academic Press, San Diego, Calif, USA, 4th edition, 2006.
- [5] A. Hasegawa and F. Tappert, "Transmission of stationary nonlinear optical pulses in dispersive dielectric fibers I. Anomalous dispersion," *Applied Physics Letters*, vol. 23, no. 3, pp. 142–144, 1973.
- [6] L. F. Mollenauer and J. P. Gordon, *Solitons in Optical Fibers: Fundamentals and Applications*, Academic Press, San Diego, Calif, USA, 2006.
- [7] W. J. Tomlinson, R. H. Stolen, and A. M. Johnson, "Optical wave breaking of pulses in nonlinear optical fibers," *Optics Letters*, vol. 10, no. 9, pp. 457–459, 1985.
- [8] D. Anderson, M. Desaix, M. Lisak, and M. L. Quiroga-Teixeiro, "Wave breaking in nonlinear-optical fibers," *Journal of the Optical Society of America B*, vol. 9, no. 8, pp. 1358–1361, 1992.
- [9] C. Finot, B. Kibler, L. Provost, and S. Wabnitz, "Beneficial impact of wave-breaking for coherent continuum formation in normally dispersive nonlinear fibers," *Journal of the Optical Society of America B*, vol. 25, no. 11, pp. 1938–1948, 2008.
- [10] J. Azaña, L. K. Oxenløwe, E. Palushani et al., "In-fiber sub-picosecond pulse shaping for nonlinear optical telecommunication data processing at 640 Gbit/s," *International Journal of Optics*, vol. 2012, Article ID 895281, 16 pages, 2012.
- [11] A. M. Weiner, "Femtosecond pulse shaping using spatial light modulators," *Review of Scientific Instruments*, vol. 71, no. 5, pp. 1929–1960, 2000.

- [12] A. M. Clarke, D. G. Williams, M. A. F. Roelens, and B. J. Eggleton, "Reconfigurable optical pulse generator employing a Fourier-domain programmable optical processor," *Journal of Lightwave Technology*, vol. 28, no. 1, pp. 97–103, 2010.
- [13] D. Nguyen, M. U. Piracha, D. Mandridis, and P. J. Delfyett, "Dynamic parabolic pulse generation using temporal shaping of wavelength to time mapped pulses," *Optics Express*, vol. 19, no. 13, pp. 12305–12311, 2011.
- [14] J. Ye, L. S. Yan, W. Pan et al., "Photonic generation of triangular-shaped pulses based on frequency-to-time conversion," *Optics Letters*, vol. 36, no. 8, pp. 1458–1460, 2011.
- [15] P. Petropoulos, M. Ibsen, A. D. Ellis, and D. J. Richardson, "Rectangular pulse generation based on pulse reshaping using a superstructured fiber Bragg grating," *Journal of Lightwave Technology*, vol. 19, no. 5, pp. 746–752, 2001.
- [16] D. Krčmařík, R. Slavík, Y. G. Park, and J. Azaña, "Nonlinear pulse compression of picosecond parabolic-like pulses synthesized with a long period fiber grating filter," *Optics Express*, vol. 17, no. 9, pp. 7074–7087, 2009.
- [17] T. Hirooka, M. Nakazawa, and K. Okamoto, "Bright and dark 40 GHz parabolic pulse generation using a picosecond optical pulse train and an arrayed waveguide grating," *Optics Letters*, vol. 33, no. 10, pp. 1102–1104, 2008.
- [18] K. Kashiwagi, H. Ishizu, and T. Kurokawa, "Fiber transmission characteristics of parabolic pulses generated by optical pulse synthesizer," *Japanese Journal of Applied Physics*, vol. 50, no. 9, Article ID 092501, 2011.
- [19] B. Kibler, R. Fischer, P. A. Lacourt et al., "Optimised one-step compression of femtosecond fibre laser soliton pulses around 1550 nm to below 30 fs in highly nonlinear fibre," *Electronics Letters*, vol. 43, no. 17, pp. 915–916, 2007.
- [20] A. A. Amorim, M. V. Tognetti, P. Oliveira et al., "Sub-two-cycle pulses by soliton self-compression in highly nonlinear photonic crystal fibers," *Optics Letters*, vol. 34, no. 24, pp. 3851–3853, 2009.
- [21] L. F. Mollenauer, R. H. Stolen, and J. P. Gordon, "Experimental observation of picosecond pulse narrowing and solitons in optical fibers," *Physical Review Letters*, vol. 45, no. 13, pp. 1095–1098, 1980.
- [22] S. V. Chernikov and P. V. Mamyshev, "Femtosecond soliton propagation in fibers with slowly decreasing dispersion," *Journal of the Optical Society of America B*, vol. 8, no. 8, pp. 1633–1641, 1991.
- [23] S. V. Chernikov, D. J. Richardson, E. M. Dianov, and D. N. Payne, "Picosecond soliton pulse compressor based on dispersion decreasing fibre," *Electronics Letters*, vol. 28, no. 19, pp. 1842–1844, 1992.
- [24] S. V. Chernikov, J. R. Taylor, and R. Kashyap, "Comblike dispersion-profiled fiber for soliton pulse train generation," *Optics Letters*, vol. 19, no. 8, pp. 539–541, 1994.
- [25] J. Fatome, S. Pitois, and G. Millot, "20-GHz-to-1-THz repetition rate pulse sources based on multiple four-wave mixing in optical fibers," *IEEE Journal of Quantum Electronics*, vol. 42, no. 10, Article ID 01703695, pp. 1038–1046, 2006.
- [26] K. Tai, A. Hasegawa, and A. Tomita, "Observation of modulational instability in optical fibers," *Physical Review Letters*, vol. 56, no. 2, pp. 135–138, 1986.
- [27] B. Ortaç, A. Hideur, G. Martel, and M. Brunel, "2-GHz passive harmonically mode-locked Yb-doped double-clad fiber laser," *Applied Physics B*, vol. 81, no. 4, pp. 507–509, 2005.
- [28] A. Komarov, H. Leblond, and F. Sanchez, "Passive harmonic mode-locking in a fiber laser with nonlinear polarization rotation," *Optics Communications*, vol. 267, no. 1, pp. 162–169, 2006.
- [29] A. Komarov, A. Haboucha, and F. Sanchez, "Ultrahigh-repetition-rate bound-soliton harmonic passive mode-locked fiber lasers," *Optics Letters*, vol. 33, no. 19, pp. 2254–2256, 2008.
- [30] J. Schröder, S. Coen, F. Vanholsbeeck, and T. Sylvestre, "Passively mode-locked Raman fiber laser with 100 GHz repetition rate," *Optics Letters*, vol. 31, no. 23, pp. 3489–3491, 2006.
- [31] K. Hammani, B. Kibler, C. Finot et al., "Peregrine soliton generation and breakup in standard telecommunications fiber," *Optics Letters*, vol. 36, no. 2, pp. 112–114, 2011.
- [32] R. Trebino, *Frequency-Resolved Optical Gating: The Measurement of Ultrashort Laser Pulses*, Kluwer Academic, Norwell, Mass, USA, 2000.
- [33] J. Fatome, S. Pitois, C. Fortier et al., "Multiple four-wave mixing in optical fibers: 1.5-3.4-THz femtosecond pulse sources and real-time monitoring of a 20-GHz picosecond source," *Optics Communications*, vol. 283, no. 11, pp. 2425–2429, 2010.
- [34] S. Pitois, C. Finot, J. Fatome, B. Sinardet, and G. Millot, "Generation of 20-GHz picosecond pulse trains in the normal and anomalous dispersion regimes of optical fibers," *Optics Communications*, vol. 260, no. 1, pp. 301–306, 2006.
- [35] C. Finot, J. Fatome, S. Pitois, and G. Millot, "All-fibered high-quality low duty-cycle 20-GHz and 40-GHz picosecond pulse sources," *IEEE Photonics Technology Letters*, vol. 19, no. 21, pp. 1711–1713, 2007.
- [36] C. Fortier, B. Kibler, J. Fatome, C. Finot, S. Pitois, and G. Millot, "All-fibered high-quality low duty-cycle 160-GHz femtosecond pulse source," *Laser Physics Letters*, vol. 5, no. 11, pp. 817–820, 2008.
- [37] I. E. Mansouri, J. Fatome, C. Finot, S. Pitois, and M. Lintz, "All-fibered high-quality stable 20- and 40-GHz picosecond pulse generators for 160-Gb/s OTDM applications," *IEEE Photonics Technology Letters*, vol. 23, no. 20, pp. 1487–1489, 2011.
- [38] N. Akhmediev and V. I. Korneev, "Modulation instability and periodic solutions of the nonlinear Schrödinger equation," *Theoretical and Mathematical Physics*, vol. 69, no. 2, pp. 1089–1093, 1986.
- [39] K. Hammani, B. Wetzal, B. Kibler et al., "Spectral dynamics of modulation instability described using Akhmediev breather theory," *Optics Letters*, vol. 36, no. 11, pp. 2140–2142, 2011.
- [40] B. Kibler, J. Fatome, C. Finot et al., "The Peregrine soliton in nonlinear fibre optics," *Nature Physics*, vol. 6, no. 10, pp. 790–795, 2010.
- [41] D. H. Peregrine, "Water waves, nonlinear Schrödinger equations and their solutions," *The Journal of the Australian Mathematical Society B*, vol. 25, no. 1, pp. 16–43, 1983.
- [42] J. M. Dudley, C. Finot, G. Millot et al., "Extreme events in optics: challenges of the MANUREVA project," *European Physical Journal*, vol. 185, no. 1, pp. 125–133, 2010.
- [43] D. R. Solli, C. Ropers, P. Koonath, and B. Jalali, "Optical rogue waves," *Nature*, vol. 450, no. 7172, pp. 1054–1057, 2007.
- [44] J. M. Dudley, C. Finot, G. Millot, and D. J. Richardson, "Self-similarity in ultrafast nonlinear optics," *Nature Physics*, vol. 3, no. 9, pp. 597–603, 2007.
- [45] M. E. Fermann, V. I. Kruglov, B. C. Thomsen, J. M. Dudley, and J. D. Harvey, "Self-similar propagation and amplification of parabolic pulses in optical fibers," *Physical Review Letters*, vol. 84, no. 26, pp. 6010–6013, 2000.
- [46] S. Boscolo, S. K. Turitsyn, V. Y. Novokshenov, and J. H. B. Nijhof, "Self-similar parabolic optical solitary waves,"

- Theoretical and Mathematical Physics*, vol. 133, no. 3, pp. 1647–1656, 2002.
- [47] V. L. Kruglov and J. D. Harvey, “Asymptotically exact parabolic solutions of the generalized nonlinear Schrödinger equation with varying parameters,” *Journal of the Optical Society of America B*, vol. 23, no. 12, pp. 2541–2550, 2006.
- [48] C. Finot and L. Wu, “Influence of the initial phase profile on the asymptotic self-similar parabolic dynamics,” *Journal of Nonlinear Optical Physics and Materials*, vol. 18, no. 4, pp. 709–721, 2009.
- [49] D. Anderson, M. Desaix, M. Karlsson, M. Lisak, and M. L. Quiroka-Teixeiro, “Wave-breaking-free pulses in nonlinear-optical fibers,” *Journal of the Optical Society of America B*, vol. 10, no. 7, pp. 1185–1190, 1993.
- [50] C. Finot, G. Millot, and J. M. Dudley, “Asymptotic characteristics of parabolic similariton pulses in optical fiber amplifiers,” *Optics Letters*, vol. 29, no. 21, pp. 2533–2535, 2004.
- [51] C. Billet, J. M. Dudley, N. Joly, and J. C. Knight, “Intermediate asymptotic evolution and photonic bandgap fiber compression of optical similaritons around 1550 nm,” *Optics Express*, vol. 13, no. 9, pp. 3236–3241, 2005.
- [52] B. G. Bale and S. Boscolo, “Impact of third-order fibre dispersion on the evolution of parabolic optical pulses,” *Journal of Optics A*, vol. 12, no. 1, Article ID 015202, 2010.
- [53] B. G. Bale, S. Boscolo, K. Hammani, and C. Finot, “Effects of fourth-order fiber dispersion on ultrashort parabolic optical pulses in the normal dispersion regime,” *Journal of the Optical Society of America B*, vol. 28, no. 9, pp. 2059–2065, 2011.
- [54] K. Hammani, C. Finot, S. Pitois, J. Fatome, and G. Millot, “Real-time measurement of long parabolic optical similaritons,” *Electronics Letters*, vol. 44, no. 21, pp. 1239–1240, 2008.
- [55] C. Finot, B. Barviau, G. Millot, A. Guryanov, A. Sysoliatin, and S. Wabnitz, “Parabolic pulse generation with active or passive dispersion decreasing optical fibers,” *Optics Express*, vol. 15, no. 24, pp. 15824–15835, 2007.
- [56] J. P. Limpert, T. Schreiber, T. Clausnitzer et al., “High-power femtosecond Yb-doped fiber amplifier,” *Optics Express*, vol. 10, no. 14, pp. 628–638, 2002.
- [57] A. Malinowski, A. Piper, J. H. V. Price et al., “Ultrashort-pulse Yb³⁺-fiber-based laser and amplifier system producing > 25-W average power,” *Optics Letters*, vol. 29, no. 17, pp. 2073–2075, 2004.
- [58] P. Dupriez, C. Finot, A. Malinowski et al., “High-power, high repetition rate picosecond and femtosecond sources based on Yb-doped fiber amplification of VECSELS,” *Optics Express*, vol. 14, no. 21, pp. 9611–9616, 2006.
- [59] D. N. Papadopoulos, Y. Zaouter, M. Hanna et al., “Generation of 63 fs 4.1 MW peak power pulses from a parabolic fiber amplifier operated beyond the gain bandwidth limit,” *Optics Letters*, vol. 32, no. 17, pp. 2520–2522, 2007.
- [60] C. Finot, G. Millot, S. Pitois, C. Billet, and J. M. Dudley, “Numerical and experimental study of parabolic pulses generated via Raman amplification in standard optical fibers,” *IEEE Journal on Selected Topics in Quantum Electronics*, vol. 10, no. 5, pp. 1211–1218, 2004.
- [61] S. Zhang, C. Jin, Y. Meng, X. Wang, and H. Li, “Propagation of high-power parabolic pulses in cubicon fiber amplifiers,” *Journal of the Optical Society of America B*, vol. 27, no. 6, pp. 1272–1278, 2010.
- [62] Vladimir I. Kruglov, Claude Agueraray, and John D. Harvey, “Propagation and breakup of pulses in fiber amplifiers and dispersion-decreasing fibers with third-order dispersion,” *Physical Review A*, vol. 84, no. 2, Article ID 023823, 14 pages, 2011.
- [63] F. Ö. Ilday, J. R. Buckley, W. G. Clark, and F. W. Wise, “Self-similar evolution of parabolic pulses in a laser,” *Physical Review Letters*, vol. 92, no. 21, Article ID 213902, 4 pages, 2004.
- [64] F. W. Wise, A. Chong, and W. H. Renninger, “High-energy femtosecond fiber lasers based on pulse propagation at normal dispersion,” *Laser and Photonics Reviews*, vol. 2, no. 1–2, pp. 58–73, 2008.
- [65] C. Agueraray, D. Méchin, V. I. Kruglov, and J. D. Harvey, “Experimental realization of a mode-locked parabolic Raman fiber oscillator,” *Optics Express*, vol. 18, no. 8, pp. 8680–8687, 2010.
- [66] B. Oktem, C. Ülgüdür, and F. O. Ilday, “Soliton-similariton fibre laser,” *Nature Photonics*, vol. 4, no. 5, pp. 307–311, 2010.
- [67] T. Hirooka and M. Nakazawa, “Parabolic pulse generation by use of a dispersion-decreasing fiber with normal group-velocity dispersion,” *Optics Letters*, vol. 29, no. 5, pp. 498–500, 2004.
- [68] B. Kibler, C. Billet, P. A. Lacourt, R. Ferriere, L. Larger, and J. M. Dudley, “Parabolic pulse generation in comb-like profiled dispersion decreasing fibre,” *Electronics Letters*, vol. 42, no. 17, pp. 965–966, 2006.
- [69] A. Plocky, A. A. Sysoliatin, A. I. Latkin et al., “Experiments on the generation of parabolic pulses in waveguides with length-varying normal chromatic dispersion,” *JETP Letters*, vol. 85, pp. 319–322, 2007.
- [70] C. Finot, L. Provost, P. Petropoulos, and D. J. Richardson, “Parabolic pulse generation through passive nonlinear pulse reshaping in a normally dispersive two segment fiber device,” *Optics Express*, vol. 15, no. 3, pp. 852–864, 2007.
- [71] S. Boscolo, A. I. Latkin, and S. K. Turitsyn, “Passive nonlinear pulse shaping in normally dispersive fiber systems,” *IEEE Journal of Quantum Electronics*, vol. 44, no. 12, pp. 1196–1203, 2008.
- [72] H. Wang, A. I. Latkin, S. Boscolo, P. Harper, and S. K. Turitsyn, “Generation of triangular-shaped optical pulses in normally dispersive fibre,” *Journal of Optics*, vol. 12, no. 3, Article ID 035205, 2010.
- [73] S. Boscolo and S. K. Turitsyn, “Pulse shaping in mode-locked ring-cavity fibre lasers,” in *Proceedings of Lasers and Electro-Optics Europe and 12th European Quantum Electronics Conference (CLEO EUROPE/EQEC '11)*, Munich, German, May 2011, paper EH4.6.
- [74] R. R. Alfano, *The Supercontinuum Laser Source*, Springer, New York, NY, USA, 2006.
- [75] J. M. Dudley and J. R. Taylor, *Supercontinuum Generation in Optical Fibers*, Cambridge University Press, New York, NY, USA, 2010.
- [76] L. Boivin and B. C. Collings, “Spectrum slicing of coherent sources in optical communications,” *Optical Fiber Technology*, vol. 7, no. 1, pp. 1–20, 2001.
- [77] Y. Takushima and K. Kikuchi, “10-GHz, over 20-channel multiwavelength pulse source by slicing super-continuum spectrum generated in normal-dispersion fiber,” *IEEE Photonics Technology Letters*, vol. 11, no. 3, pp. 322–324, 1999.
- [78] Z. Yusoff, P. Petropoulos, K. Furusawa, T. M. Monro, and D. J. Richardson, “A 36-Channel x 10-GHz spectrally sliced pulse source based on supercontinuum generation in normally dispersive highly nonlinear holey fiber,” *IEEE Photonics Technology Letters*, vol. 15, no. 12, pp. 1689–1691, 2003.
- [79] F. Parmigiani, C. Finot, K. Mukasa et al., “Ultra-flat SPM-broadened spectra in a highly nonlinear fiber using parabolic pulses formed in a fiber Bragg grating,” *Optics Express*, vol. 14, no. 17, pp. 7617–7622, 2006.

- [80] J. M. Dudley, G. Genty, and S. Coen, "Supercontinuum generation in photonic crystal fiber," *Reviews of Modern Physics*, vol. 78, no. 4, pp. 1135–1184, 2006.
- [81] M. Nakazawa, K. Tamura, H. Kubota, and E. Yoshida, "Coherence degradation in the process of supercontinuum generation in an optical fiber," *Optical Fiber Technology*, vol. 4, no. 2, pp. 215–223, 1998.
- [82] A. M. Heidt, "Pulse preserving flat-top supercontinuum generation in all-normal dispersion photonic crystal fibers," *Journal of the Optical Society of America B*, vol. 27, no. 3, pp. 550–559, 2010.
- [83] L. E. Hooper, P. J. Mosley, A. C. Muir, W. J. Wadsworth, and J. C. Knight, "Coherent supercontinuum generation in photonic crystal fiber with all-normal group velocity dispersion," *Optics Express*, vol. 19, no. 6, pp. 4902–4907, 2011.
- [84] C. Finot, S. Pitois, and G. Millot, "Regenerative 40 Gbit/s wavelength converter based on similariton generation," *Optics Letters*, vol. 30, no. 14, pp. 1776–1778, 2005.
- [85] S. Boscolo and S. K. Turitsyn, "All-optical signal regeneration by temporal slicing of nonlinearly flattened optical waveform," *IEEE Photonics Technology Letters*, vol. 17, no. 6, pp. 1235–1237, 2005.
- [86] F. Parmigiani, P. Petropoulos, M. Ibsen, and D. J. Richardson, "Pulse retiming based on XPM using parabolic pulses formed in a fiber Bragg grating," *IEEE Photonics Technology Letters*, vol. 18, no. 7, pp. 829–831, 2006.
- [87] S. Boscolo, S. K. Turitsyn, and K. J. Blow, "Time domain all-optical signal processing at a RZ optical receiver," *Optics Express*, vol. 13, no. 16, pp. 6217–6227, 2005.
- [88] I. O. Nasieva, S. Boscolo, and S. K. Turitsyn, "Bit error rate improvement by nonlinear optical decision element," *Optics Letters*, vol. 31, no. 9, pp. 1205–1207, 2006.
- [89] T. T. Ng, F. Parmigiani, M. Ibsen, Z. Zhang, P. Petropoulos, and D. J. Richardson, "Compensation of linear distortions by using XPM with parabolic pulses as a time lens," *IEEE Photonics Technology Letters*, vol. 20, no. 13, pp. 1097–1099, 2008.
- [90] T. Hirooka and M. Nakazawa, "All-optical 40-GHz time-domain Fourier transformation using XPM with a dark parabolic pulse," *IEEE Photonics Technology Letters*, vol. 20, no. 22, pp. 1869–1871, 2008.
- [91] J. Li, B. E. Olsson, M. Karlsson, and P. A. Andrekson, "OTDM add-drop multiplexer based on XPM-induced wavelength shifting in highly nonlinear fiber," *Journal of Lightwave Technology*, vol. 23, no. 9, pp. 2654–2661, 2005.
- [92] F. Parmigiani, P. Petropoulos, M. Ibsen, P. J. Almeida, T. T. Ng, and D. J. Richardson, "Time domain add-drop multiplexing scheme enhanced using a saw-tooth pulse shaper," *Optics Express*, vol. 17, no. 10, pp. 8362–8369, 2009.
- [93] F. Parmigiani, M. Ibsen, T. T. Ng, L. Provost, P. Petropoulos, and D. J. Richardson, "An efficient wavelength converter exploiting a grating-based saw-tooth pulse shaper," *IEEE Photonics Technology Letters*, vol. 20, no. 17, pp. 1461–1463, 2008.
- [94] F. Parmigiani, M. Ibsen, P. Petropoulos, and D. J. Richardson, "Efficient all-optical wavelength-conversion scheme based on a saw-tooth pulse shaper," *IEEE Photonics Technology Letters*, vol. 21, no. 24, Article ID 5291729, pp. 1837–1839, 2009.
- [95] N. Verschueren and C. Finot, "Pulse doubling and wavelength conversion through triangular nonlinear pulse reshaping," *Electronics Letters*, vol. 47, no. 21, pp. 1194–1196, 2011.
- [96] A. I. Latkin, S. Boscolo, R. S. Bhamber, and S. K. Turitsyn, "Doubling of optical signals using triangular pulses," *Journal of the Optical Society of America B*, vol. 26, no. 8, pp. 1492–1496, 2009.
- [97] R. S. Bhamber, S. Boscolo, A. I. Latkin, and S. K. Turitsyn, "All-optical TDM to WDM signal conversion and partial regeneration using XPM with triangular pulses," in *Proceedings of the 34th European Conference on Optical Communication (ECOC '08)*, pp. 1–2, Brussels, Belgium, 2008, paper Th.1.B.2.
- [98] E. R. Andresen, J. M. Dudley, D. Oron, C. Finot, and H. Rigneault, "Transform-limited spectral compression by self-phase modulation of amplitude-shaped pulses with negative chirp," *Optics Letters*, vol. 36, no. 5, pp. 707–709, 2011.
- [99] C. Finot, F. Parmigiani, P. Petropoulos, and D. J. Richardson, "Parabolic pulse evolution in normally dispersive fiber amplifiers preceding the similariton formation regime," *Optics Express*, vol. 14, no. 8, pp. 3161–3170, 2006.
- [100] P. V. Mamyshev, "All-optical data regeneration based on self-phase modulation effect," in *Proceedings of the 24th European Conference on Optical Communication (ECOC '98)*, pp. 475–476, Madrid, Spain, September 1998.
- [101] L. Provost, C. Finot, P. Petropoulos, K. Mukasa, and D. J. Richardson, "Design scaling rules for 2R-optical self-phase modulation-based regenerators," *Optics Express*, vol. 15, no. 8, pp. 5100–5113, 2007.
- [102] C. Finot, J. Fatome, S. Pitois, G. Millot, and E. Pincemin, "Active Mamyshev regenerator," *Optical Review*, vol. 18, no. 3, pp. 257–263, 2011.
- [103] M. Romagnoli, P. Franco, R. Corsini, A. Schiffrini, and M. Midrio, "Time-domain Fourier optics for polarization-mode dispersion compensation," *Optics Letters*, vol. 24, no. 17, pp. 1197–1199, 1999.
- [104] L. A. Jiang, M. E. Grein, H. A. Haus, E. P. Ippen, and H. Yokoyama, "Timing jitter eater for optical pulse trains," *Optics Letters*, vol. 28, no. 2, pp. 78–80, 2003.
- [105] M. Nakazawa and T. Hirooka, "Distortion-free optical transmission using time-domain optical Fourier transformation and transform-limited optical pulses," *Journal of the Optical Society of America B*, vol. 22, no. 9, pp. 1842–1855, 2005.
- [106] T. Hirooka and M. Nakazawa, "Optical adaptive equalization of high-speed signals using time-domain optical Fourier transformation," *Journal of Lightwave Technology*, vol. 24, no. 7, pp. 2530–2540, 2006.
- [107] N. Yoshikane, I. Morita, T. Tsuritani, A. Agata, N. Edagawa, and S. Akiba, "Benefit of SPM-based all-optical reshaper for long-haul DWDM transmission systems," *Journal of Selected Topics in Quantum Electronics*, vol. 10, pp. 412–420, 2004.
- [108] M. Matsuura, N. Kishi, and T. Miki, "Performance improvement of optical RZ-receiver by utilizing an all-optical waveform converter," *Optics Express*, vol. 13, no. 13, pp. 5074–5079, 2005.
- [109] P. Ghelfi, M. Secondini, M. Scaffardi, F. Fresi, A. Bogoni, and L. Poti, "Impact of an additional all-optical decision element in band-limited receivers for RZ systems," *Journal of Lightwave Technology*, vol. 25, no. 7, pp. 1728–1734, 2007.
- [110] M. Rochette, J. N. Kutz, J. L. Blows, D. Moss, J. T. Mok, and B. J. Eggleton, "Bit-error-ratio improvement with 2R optical regenerators," *IEEE Photonics Technology Letters*, vol. 17, no. 4, pp. 908–910, 2005.
- [111] M. Rochette, J. L. Blows, and B. J. Eggleton, "3R optical regeneration: an all-optical solution with BER improvement," *Optics Express*, vol. 14, no. 14, pp. 6414–6427, 2006.

Review Article

In-Fiber Subpicosecond Pulse Shaping for Nonlinear Optical Telecommunication Data Processing at 640 Gbit/s

J. Azaña,¹ L. K. Oxenløwe,² E. Palushani,² R. Slavík,^{3,4} M. Galili,² H. C. H. Mulvad,² H. Hu,² Y. Park,^{1,5} A. T. Clausen,² and P. Jeppesen²

¹Centre Energie, Matériaux et Télécommunications, Institut National de la Recherche Scientifique (INRS), Montreal, QC, Canada H5A 1K6

²DTU Fotonik, Technical University of Denmark, Ørsteds Square 343, 2800 Lyngby, Denmark

³ORC, University of Southampton, Southampton SO17 1BJ, UK

⁴Institute of Photonic Engineering, Academy of Sciences of the Czech Republic, 18251 Prague, Czech Republic

⁵Automated Precision Inc., 15000 Johns Hopkins Drive, Rockville, MD 20850, USA

Correspondence should be addressed to L. K. Oxenløwe, lkox@fotonik.dtu.dk

Received 16 June 2011; Accepted 26 September 2011

Academic Editor: Miguel Gonzalez Herraiez

Copyright © 2012 J. Azaña et al. This is an open access article distributed under the Creative Commons Attribution License, which permits unrestricted use, distribution, and reproduction in any medium, provided the original work is properly cited.

We review recent work on all-fiber (long-period fiber grating) devices for optical pulse shaping, particularly flat-top pulse generation, down to the subpicosecond range and their application for nonlinear switching (demultiplexing) of optical time-division multiplexed (OTDM) data signals in fiber-optic telecommunication links operating up to 640 Gbit/s. Experiments are presented demonstrating error-free 640-to-10 Gbit/s demultiplexing of the 64 tributary channels using the generated flat-top pulses for temporal gating in a Kerr-effect-based nonlinear optical loop mirror. The use of flat-top pulses has critical benefits in the demultiplexing process, including a significantly increased timing-jitter tolerance (up to ~ 500 fs, i.e., 30% of the bit period) and the associated improvement in the bit-error-rate performance (e.g., with a sensitivity increase of up to ~ 13 dB as compared with the use of Gaussian-like gating pulses). Long-period fiber grating pulse shapers with reduced polarization dependence are fabricated and successfully used for polarization-independent 640-to-10 Gbit/s demultiplexing experiments.

1. Introduction

Techniques for the precise synthesis and control of the temporal shape of optical pulses with durations in the picosecond and subpicosecond regimes [1] are of fundamental importance for a wide range of applications in ultrahigh-bit-rate optical communications, particularly to enhance the performance of a range of nonlinear optics-based data-processing operations [1–10]. As a very relevant example, (sub)picosecond flat-top (rectangular-like) optical pulses are highly desired in applications requiring the use of a well-defined temporal gating window, for example, for nonlinear time-domain switching of optical telecommunication data. The use of flat-top optical pulses as control/gating pulses in nonlinear time-domain optical switches translates into important advantages as compared with the (more conventional) use of Gaussian-like optical control pulses. Figure 1

illustrates the concept of nonlinear optical switching for temporal demultiplexing of serial optical time-division multiplexed (OTDM) data. For optimum performance, the gating pulse has to be shorter than the one-bit time window and at the same time it should have constant intensity over a time interval as long as possible. Both of these requirements can be fulfilled when using flat-top pulses. Indeed, as illustrated in Figure 1, flat-top optical control pulses increase the tolerance to timing jitter in the system, thus improving the overall performance of the nonlinear switching scheme, for example, leading to a significantly improved receiver sensitivity (needed input signal power to achieve a bit error rate, BER $< 10^{-9}$) [2–6].

Flat-top optical pulse waveforms can be generated from Gaussian-like optical pulses (easily generated from mode-locked laser systems) using many different pulse-shaping techniques [1–7, 11–15]. From a practical viewpoint, the

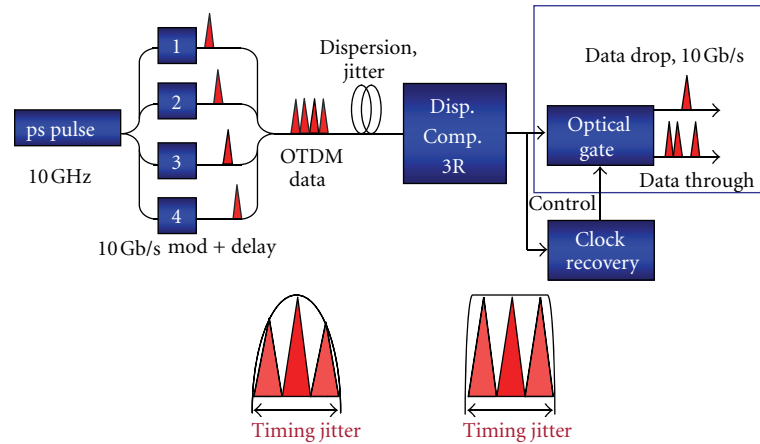


FIGURE 1: General schematic of demultiplexing in OTDM by nonlinear switching and illustration of the timing-jitter tolerance improvement achieved by use of flat-top pulse gating.

two following features are highly desired: (i) linear pulse reshaping techniques are attractive because they generally require a simpler implementation and are independent of the input optical pulse power; (ii) an all-fiber implementation allows for low insertion loss, robust, and low-cost realization with full compatibility with fiber-based systems. Notice that in a linear re-shaping method, the steepness of the rise/decay edges in the synthesized flat-top waveform is limited by the input optical bandwidth. Concerning linear *all-fiber* flat-top temporal pulse shapers, a very interesting method is based on the use of customized in-fiber Bragg (short-period) gratings (FBGs) operating in reflection [2–4, 12]. A FBG device is essentially a (quasi)periodic perturbation of the fiber refractive index that is permanently photo-induced along the length of a relatively short section of the optical fiber [16]. FBGs are designed to induce coupling between two counter-propagating modes, namely, the same fundamental mode in the fiber as it propagates in two opposite directions, around a target resonance wavelength. Roughly speaking, FBGs behave as wavelength-selective mirrors. For flat-top pulse re-shaping, an FBG is used as a linear filter operating over an input Gaussian-like (or soliton-like) optical pulse and the grating coupling-strength and period profiles are designed to achieve the desired sinc-like spectral transfer function. This pulse-shaping strategy is thus based on the proper manipulation of the spectral-domain features of the input optical pulse in order to obtain the spectral profile that corresponds to the desired temporal profile. This so-called Fourier-domain approach has been extensively used in conventional optical pulse shapers based on nonfiber solutions, namely, bulk diffraction gratings [1] and integrated arrayed-waveguide gratings [11]. The main limitations of FBG-based optical pulse shapers are that (i) a complex amplitude and phase grating profile is usually required and (ii) due to the FBG limited bandwidth, temporal waveforms shorter than a few tens of picoseconds cannot be easily synthesized. This latter limitation is related to the spatial resolution of the grating-strength variation that can be practically photo-inscribed along the fiber.

It has been previously anticipated [17] that the two mentioned limitations could be overcome using long-period fiber gratings, LPGs, instead of FBGs. LPGs are based on coupling between two copropagating modes, typically the fiber fundamental (core) mode and any of the fiber's cladding modes [16]. In particular, two different LPG-based concepts have been proposed for optical flat-top pulse shaping. The first one [17] is a general method, eventually enabling the synthesis of almost any desired pulse shape by properly tailoring the grating coupling-strength and period variations. However, this method is difficult to implement in practice since the pulse re-shaping operation typically needs to be realized via a “core mode to cladding mode” coupling or vice versa [18] (i.e., the input and output signals must be in different fiber propagation modes). The second method is based on the use of an ultrafast optical differentiator, that is, a linear optical filter designed to calculate the first time derivative of an incoming arbitrary optical waveform. In particular, it has been shown that flat-top pulse waveforms can be synthesized by propagation of a Gaussian-like optical pulse through an optical differentiator by properly detuning the input pulse central wavelength with respect to the resonance (zero-transmission) wavelength of the differentiator [14]. Ultrafast optical differentiators capable of operation over THz bandwidths (corresponding to input time features well in the subpicosecond range) can be created using either a single uniform LPG operating in full coupling condition [19, 20] or a Mach-Zehnder-(MZ-) type all-fiber interferometer created by concatenation of two ultrabroadband uniform LPGs [21].

LPG-based optical pulse shapers [14, 15, 22] have enabled the synthesis of flat-top optical pulses well in the subpicosecond range, that is, with full-width-at-half-maximum, FWHM, time widths as short as ~ 700 fs [23], about 10–20-times shorter than with any other reported all-fiber method, for example, FBG-based pulse shapers. This improvement has in turn enabled the development of a range of nonlinear optical telecommunication data processing schemes enhanced by flat-top pulse shapers at unprecedented bit rates, namely, up to 640 Gbit/s [24–27]. Error-free

demultiplexing of OTDM signals with significantly improved timing-jitter tolerances has been demonstrated using LPG-based pulse shapers. This represents a critical advance in the field because for high-speed serial data transmission that operates at rates of 160 Gbit/s and above, management of the timing jitter becomes extremely important while being increasingly challenging [28–33]. In addition, the LPG pulse shapers can be fabricated to exhibit very low polarization sensitivity [23, 26, 27]; this latter feature can be exploited to create polarization-independent OTDM demultiplexing systems [27].

This work reviews recent progress on the design and fabrication of all-fiber (LPG-based) picosecond and subpicosecond flat-top optical pulse shapers [14, 15, 17–22] and their application to nonlinear optical telecommunication data processing [23–27], particularly demultiplexing of OTDM serial data using nonlinear optical loop mirror switches with flat-top gating pulses, at bit rates up to 640 Gbit/s. The reviewed set of experiments demonstrate error-free 640-to-10 Gbit/s data signal demultiplexing over the 64 OTDM channels with a significantly improved performance over the use of Gaussian-like control/gating pulses, for example, in terms of receiver sensitivity (up to ~ 13 dB, with a penalty over the 10 Gbit/s back-to-back measurements as low as ~ 0.5 dB), time jitter tolerance (up to ~ 500 fs, corresponding to $\sim 30\%$ of the OTDM signal bit period), and optimized polarization insensitivity. The paper is structured as follows: Section 2 reviews the principle of the flat-top pulse shaping based on ultrafast optical differentiation Section 2.1 together with two different LPG-based implementations, namely, a single-LPG filter Section 2.2 and a double-LPG MZ-type interferometer Section 2.3. The application of these two pulse-shaping technologies for demultiplexing of 640-Gbit/s OTDM data signals is revisited in Section 3, including the most relevant experiments based on the use of single-LPG pulse shapers Section 3.1 and those based on the use of double-LPG pulse shapers Section 3.2, such as polarization-independent demultiplexing. Finally, Section 4 outlines the main conclusions and future prospects of the work reviewed here.

2. Flat-Top Pulse-Shaping Principle and Long-Period Fiber Grating (LPG) Implementations

2.1. Flat-Top Pulse Shaping Based on Optical Differentiation. The flat-top pulse reshaping technique used in the reviewed work is based on a filtering scheme that employs an optical temporal differentiator [14]. It has been anticipated that *any* desired ultrafast temporal waveform could be synthesized as a linear superposition of a Gaussian-like pulse and its successive time derivatives [34]. The used flat-top pulse reshaping method is based on this general property and in particular, it exploits the fact that a flat-top intensity waveform can be well approximated by only two terms of the general series, that is, by a proper combination of the input Gaussian-like pulse and its first time derivative. In what follows we describe an extremely simple mechanism to implement this idea; this

mechanism is based on the use of an optical differentiator where the relative weight between the two required temporal terms is easily adjusted through frequency detuning between the input pulse and the differentiator resonance [14].

Optical temporal differentiation [19, 20] (that operates over the complex time-domain envelope of an optical signal) can be realized using a linear filter that has a spectral transfer function proportional to $i(\omega - \omega_0)$, where ω_0 is the central frequency of the optical differentiator (frequency of zero transmission), ω is the angular optical frequency variable, and i is the imaginary unit. When considering an input optical pulse of temporal envelope $u(t)$ (spectrally centred at ω_{car}), with a resulting output optical pulse of temporal envelope $v(t)$, the differentiator was shown to provide the following filtering function [14]

$$v(t) \propto \frac{\partial u(t)}{\partial t} + i\Delta\omega u(t), \quad (1)$$

where $\Delta\omega = \omega_{\text{car}} - \omega_0$. Assuming that the input optical pulse is transform limited with a real temporal envelope $u(t)$, the temporal intensity profile of the signal at the optical differentiator output can be written as follow:

$$|v(t)|^2 \propto \left| \frac{\partial u(t)}{\partial t} \right|^2 + \Delta\omega^2 |u(t)|^2. \quad (2)$$

The whole principle, described in what follows, is schematically shown in Figure 2. For $\omega_{\text{car}} = \omega_0$ ($\Delta\omega = 0$) the device operates as an optical differentiator. However, for $\omega_{\text{car}} \neq \omega_0$, the output $|v(t)|^2$ consists of a sum of the differentiated waveform and the original waveform, with a relative weight given by the detuning factor $\Delta\omega^2$. When $u(t)$ is a temporally symmetric pulse (e.g., Gaussian-like waveform), the differentiated pulse is a symmetric double-pulse [15]. Hence, the resulting output intensity waveform is a superposition of the differentiated waveform (double-pulse intensity profile, first term in (2)) and the original Gaussian pulse intensity profile (second term in (2)), where the Gaussian pulse intensity peak coincides with the energy valley in the double-pulse waveform. The amount of energy of the original Gaussian pulse that is present in the generated pulse is proportional to the frequency detuning factor $\Delta\omega$. As the frequency detuning $\Delta\omega$ increases, the differentiated pulse is gradually reshaped in such a way that the central valley of the temporal double-pulse intensity is filled by the residual original Gaussian profile, leading to the formation of a single flat-top pulse for an optimal frequency detuning. Generally, the generated flat-top optical pulse is not transform-limited, that is, the pulse temporal profile exhibits a certain nonlinear phase variation. This poses no problem with applications in which only the intensity profile is of interest, for example, nonlinear optical switching experiments based on the Kerr-effect (e.g., cross-phase modulation, XPM) in which the flat-top pulse waveform is used as the pump pulse.

Unlike other fiber pulse-shaping techniques, for example, based on Fourier filtering [1, 11–13], the optical differentiation-based scheme does not require precise control of the relation between the input pulse and the filter characteristics in terms of bandwidth, provided the differentiator bandwidth is larger than that of the input pulse. This gives an

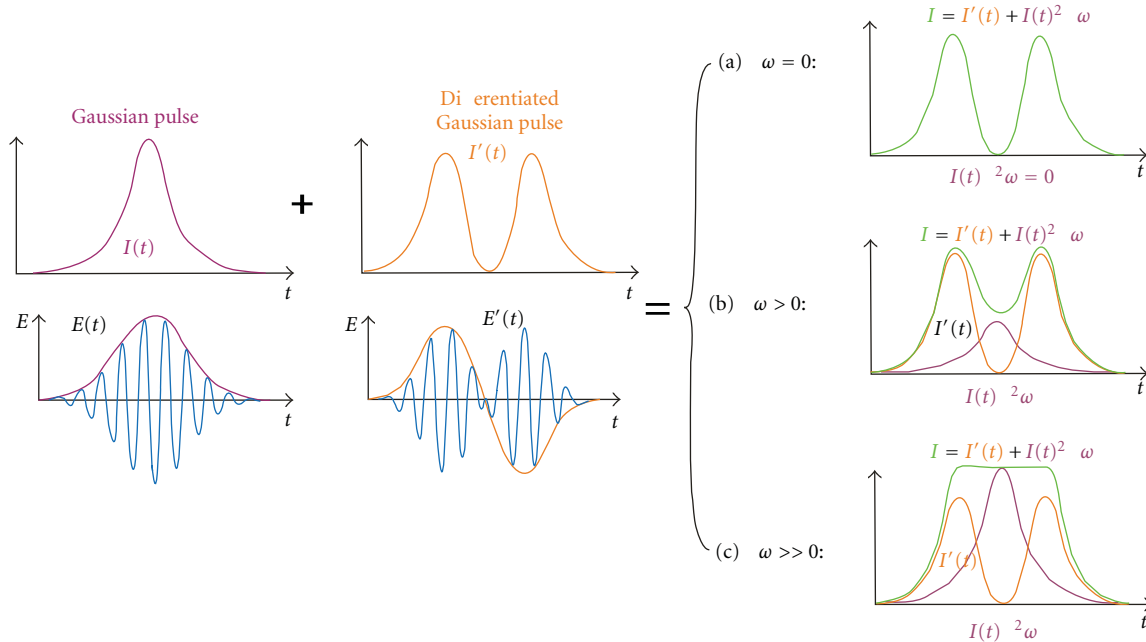


FIGURE 2: Principle of flat-top pulse generation using a frequency-detuned optical differentiator, $\Delta\omega = \omega_{\text{car}} - \omega_0$.

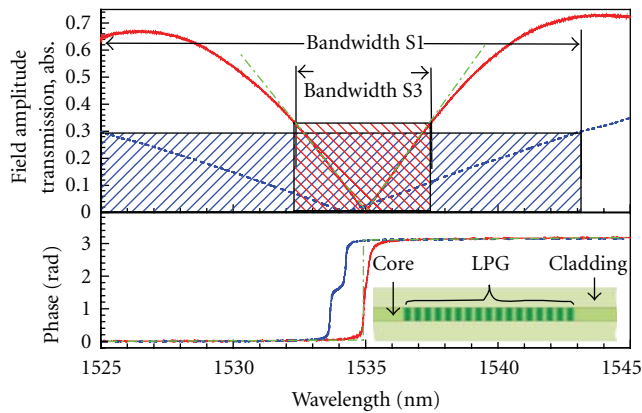


FIGURE 3: Amplitude and phase characteristics of the fiber LPG filters. Measured field amplitude and phase characteristics of the realized long, S3 (red) and short S1 (blue) LPGs together with the theoretical characteristics of an ideal differentiator similar to S3 (green, dash-dotted lines). The S3 and S1 LPG operational bandwidths (highlighted in the figure) are 5.5 nm and 19 nm, respectively. The inset shows a fiber uniform LPG, where the level of green corresponds to the refractive index.

additional flexibility as a single differentiation device can be used with different short-pulse sources emitting pulses of various durations and shapes. The rise/fall edges of the flat-top pulse are determined by the rise/fall edges of the input pulse (more specifically, by its differential), while the duration of the flat-top pulse is scaled with the duration of the input pulse. As a result, flat-top pulses of different durations can be generated from the same differentiation device by simply tuning the time width of the input optical pulse (this also requires a proper adjustment of the pulse-LPG frequency detuning) [14].

2.2. Implementation Based on a Single-LPG Optical Differentiator. In a first implementation, we created the optical differentiator using a single uniform LPG [19, 20]. As discussed above, an optical temporal differentiator is essentially a linear filtering device providing a spectral transfer function proportional to $i(\omega - \omega_0)$. Consequently, the two key features of the filter's transmission are (i) it depends linearly on the base-band ω frequency, and (ii) it is zero at the signal central frequency ω_0 . These two key features imply an exact π phase shift across the central frequency ω_0 . The ideal complex transmission of an optical differentiator is schematically shown in Figure 3.

The required energy depletion at the signal central frequency can be produced by resonance-induced complete energy transfer elsewhere. Specifically, in fiber optics, this can be achieved by resonant transfer of light between two modes of the optical fiber waveguide. Resonant light coupling is induced when the light propagates through the two interacting modes with identical speeds, which is practically attainable, for example, by an increase or decrease of the light speed in one of the modes using a suitable phase diffraction grating [16]. The specific diffraction grating used in our experiments, which is realized as a periodic change of the refractive index along the direction of light propagation within a single optical fiber, induces resonant coupling between two co-propagating modes and is commonly called long-period fiber grating (LPG) [35]. The term "long" refers to its period, which typically varies from tens to hundreds of micrometers, as opposed to short-period gratings (fiber Bragg gratings, FBGs), where the light is backscattered, resulting in coupling between modes traveling in opposite directions (in a Bragg geometry, the corrugation period is approximately half the optical wavelength, micrometers, or less).

The phase matching condition in order to achieve mode coupling between the core mode and the forward propagating cladding modes is given by

$$\beta_{01} - \beta_{cl}^{(n)} = \frac{2\pi}{\Lambda}, \quad (3)$$

where β_{01} and $\beta_{cl}^{(n)}$ are, respectively, the propagation constants of the core and the n th-cladding mode, and Λ is the periodicity of the grating. The ratio of power coupled into the n th-cladding mode to the initial power contained in the core mode is given by

$$\frac{P_{cl}^{(n)}(L)}{P_{01}(0)} = \frac{\sin^2 \left[\kappa L \sqrt{1 + (\delta/\kappa)^2} \right]}{1 + (\delta/\kappa)^2}, \quad (4)$$

where δ is the detuning parameter

$$\delta = \frac{1}{2} \left[\beta_{01} - \beta_{cl}^{(n)} - \frac{2\pi}{\Lambda} \right], \quad (5)$$

L is the grating length, and κ is the rate of the induced coupling per unit length between the core guided mode and cladding mode(s) [35]. To obtain efficient coupling between these modes, the period of the LPG must be properly adjusted to cause light diffraction from the core mode into the chosen cladding mode. Due to the different dispersion slopes of these two modes, the resonant coupling occurs only at a specific frequency ω_0 , referred to as the LPG resonance frequency. It is known that if the device is designed to exactly satisfy the condition $\kappa L = \pi/2$ then the grating induces a total (100%) energy coupling from the input guided core mode into the cladding mode (at ω_0). An optical fiber-based LPG specifically designed to provide 100% coupling between the fiber core mode and one of its cladding modes at the resonance frequency provides both the required π phase shift and the transmission linear dependence that is necessary for time differentiation (assuming that the input optical signals are centered at the LPG resonance frequency) [19]. Such an LPG, coincidentally, has the required spectral linear response over a bandwidth as broad as several terahertz [20].

To implement an LPG-based optical differentiator, stringent control of the fiber LPG coupling strength (which must be fixed exactly at $\kappa L = \pi/2$) is required. The transmission spectral responses of two LPG samples fabricated for optical differentiation are reported in Figure 3. These samples were made in a standard fiber sample (SMF-28, Corning Inc.), using the established point-by-point technique with a CO₂ laser [36], and they have physical lengths of 2.6 cm (sample S1) and 8.9 cm (sample S3), respectively, and a grating period of 415 μm . To perform a very fine tuning of the grating strength (coupling coefficient), we used a technique which takes advantage of the coupling coefficient dependence on the fiber longitudinal strain [37].

The amplitude and phase characteristics of the fiber LPG samples were measured by an Optical Vector Analyzer (Luna Technologies), and are shown in Figure 3. The linear and quadratic terms in the phase curve—caused by the delay and linear chromatic dispersion, respectively—have been

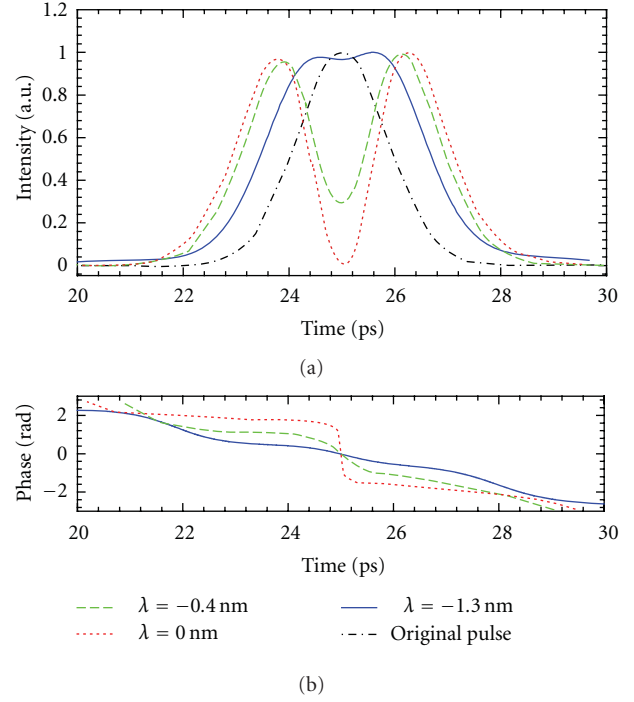


FIGURE 4: Experimentally generated intensity (a) and phase (b) temporal profiles of the synthesized waveforms at the uniform LPG output when a 1.8 ps input pulse is launched at the input for different input pulse-LPG wavelength detuning ($\Delta\lambda$) conditions.

subtracted. We measured an exact π phase shift at the filter resonance wavelength (1535 nm for S1, 1534 nm for S3), which is an essential feature to obtain the desired filtering operation. The LPGs exhibited an extremely deep attenuation, breaking the 60 dB limit, confirming operation at almost exact full-coupling condition, as required by our application. The usable (“operational”) bandwidths of the fabricated LPGs were approximately 19 nm (S1) and 5.5 nm (S3). Notice that the “operational” bandwidth is the LPG resonance bandwidth over which the fiber filter provides the desired filtering function (i.e., a linear function of frequency). This corresponds approximately to the bandwidth over which the LPG transmission (in intensity) is lower than 10%.

As discussed in Section 2.1, for flat-top pulse generation, the LPG resonance frequency must be properly detuned from the carrier frequency of the input Gaussian-like pulse [14]. Figure 4 shows experimental results on the formation of a flat-top optical pulse via propagation of a nearly-transform-limited Gaussian-like pulse through the LPG sample S3 reported above with a proper frequency (wavelength) detuning [14]. The input pulses in the experiment shown in Figure 4 were Gaussian-like optical pulses generated from a passively mode-locked wavelength-tunable fiber laser (Pritel Inc.) with full-width-half-maximum (FWHM) pulse width of 1.8 ps. The pulses from the laser were first launched into a polarization controller, as the fiber LPG was slightly birefringent [38], and were subsequently propagated through the LPG-based pulse shaper. The output spectrum was monitored using

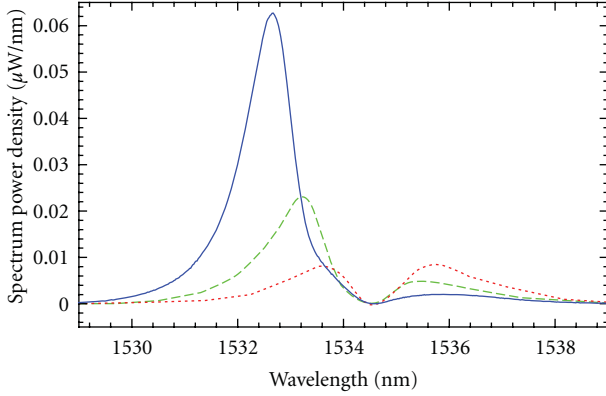


FIGURE 5: Measured spectra corresponding to the synthesized waveforms in Figure 4.

an optical spectrum analyzer (OSA). We used a fiber-based Fourier-transform spectral interferometry (FTSI) setup to retrieve the complex temporal waveform of the output pulse (in this setup, the input pulse was used as the reference pulse) [39, 40]. FTSI allowed us to monitor the obtained temporal waveform and optimize the experiment conditions, namely, wavelength detuning (in our experiment, this was achieved via fiber laser tuning) and slight adjustment of the LPG coupling coefficient (via LPG straining), so that to achieve the desired flat-top temporal waveform. Figures 4(a) and 4(b) show the amplitude and phase temporal profiles recorded at the LPG output for different values of the pulse-LPG wavelength detuning, $\Delta\lambda = 0$ (dotted, red curves), -0.4 nm (dashed, green curves), and -1.3 nm (solid, blue curves), as well as the initial Gaussian pulse (dash-dotted, black curve). The measured spectra corresponding to the three shown temporal waveforms are shown in Figure 5. The estimated FWHM time width of the experimentally generated flat-top waveform (for $\Delta\lambda = -1.3$ nm) is ≈ 3.2 ps. The energetic efficiency of the performed filtering process (ratio of the output power to the input power) was measured to be 5.5%. Energetic efficiency can be increased by use of an LPG with a narrower resonance bandwidth, that is, approaching the input pulse bandwidth [19].

Due to the large bandwidth inherently provided by LPGs, this technique is well suited for pulse re-shaping operations down to the subpicosecond regime and as a result, it is easily scalable to ultrahigh bit rates (e.g., 640 Gbit/s). In addition, as mentioned above, flat-top pulses of different durations can be achieved from the same LPG pulse shaper by simply modifying the input pulse time-width and the corresponding pulse-LPG frequency detuning. For instance, 1-ps (FWHM) flat-top pulses were generated using this same LPG sample, S3, from ~ 600 fs Gaussian-like input pulses [14]. Using numerical simulations, we have estimated that flat-top waveforms with time widths down to ≈ 550 fs (from ≈ 290 -fs input Gaussian-like pulses) could be efficiently synthesized using this LPG sample, S3. Shorter flat-top pulses could be generated using an LPG with a broader resonance bandwidth, for example, sample S1.

As another interesting advantage of the single LPG flat-top pulse re-shaping method, we have shown that a consid-

erable group-velocity dispersion-induced distortion on the flat-top pulse profile, for example, as caused by propagation through a few meters of standard SMF, can be compensated through a simple axial strain applied along the LPG [15].

Notice that the above reported LPG was photo-inscribed from one of the sides of the optical fiber. This procedure yields nonuniform refractive index change across the fiber cross-section, which typically introduces a slight photo-induced birefringence [38]. This causes the resonance frequency to vary depending on the polarization of the input light. Fiber illumination simultaneously from three sides of the fiber can be achieved using two-mirrors-assisted CO₂ laser radiation [41]. This configuration yields azimuthally symmetric illumination of the fiber, greatly reducing the photo-induced birefringence in the LPG. More discussions on this important practical issue, including detailed evaluation of the LPG resonance birefringence, can be found in Section 3.1 below.

2.3. Implementation Based on a Double-LPG Optical Differentiator. Optical differentiation can be achieved using a two-arm (e.g., Mach-Zehnder, MZ-type) interferometer operated around any of its destructive interference frequencies [42]. Such an interferometer device can be created in an all-fiber format using two concatenated uniform LPGs [21]. This configuration offers an increased stability against environmental fluctuations and the potential for ultra-broadband operation bandwidths, well in the THz range. In what follows, we review the principle of operation of a two-arm interferometer as an optical differentiator and its implementation using concatenated LPGs.

A symmetric (splitting/coupling ratio of 50%), unbalanced (the two interfering paths are of different lengths) interferometer has the following spectral transfer function:

$$H_t(\omega - \omega_0) \approx 1 + \exp(i\omega\tau) = 1 + \exp[i(\omega - \omega_0)\tau] \exp(i\omega_0\tau), \quad (6)$$

where τ is the relative time delay between the two interferometer arms. Setting the interferometer to operate at a minimum transmission ($H_t(\omega - \omega_0) = 0$) at the carrier frequency ($\omega = \omega_0$), it follows from (6) that

$$\tau = \frac{\pi(2m + 1)}{\omega_0}, \quad (7)$$

where m is an arbitrary integer. Introducing this value into (6) we obtain:

$$H_t(\omega - \omega_0) \approx 1 - \exp\left[\frac{i\pi(2m + 1)(\omega - \omega_0)}{\omega_0}\right]. \quad (8)$$

The function in (8) can be approximated over a sufficiently narrow bandwidth centered at ω_0 by the first terms of the Taylor series expansion:

$$\begin{aligned} \cos\left(\frac{\pi(2m + 1)(\omega - \omega_0)}{\omega_0}\right) &\cong 1, \\ \sin\left(\frac{\pi(2m + 1)(\omega - \omega_0)}{\omega_0}\right) &\cong \frac{\pi(2m + 1)(\omega - \omega_0)}{\omega_0}, \end{aligned} \quad (9)$$

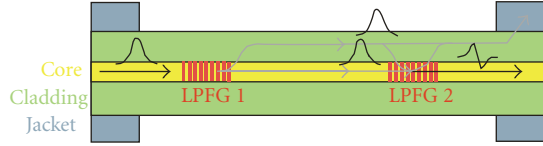


FIGURE 6: Schematics of the LPG-based common path interferometer for flat-top pulse shaping. The light is split by the first LPG, then propagates in the core and cladding modes with different speeds and is superimposed coherently using the second LPG.

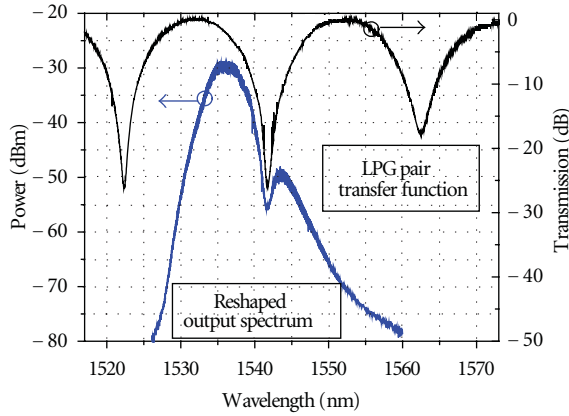


FIGURE 7: Transfer function of the LPG filters pair and reshaped spectrum of a 700 fs Gaussian-like pulse detuned <4 nm away from the destructive interference wavelength of the LPG pair.

resulting in

$$H_t(\omega - \omega_0) \approx \frac{-i(\omega - \omega_0)\pi(2m + 1)}{\omega_0} = -i(\omega - \omega_0)\tau, \quad (10)$$

which is the transmission function required for optical temporal differentiation. As follows from the above discussion, the expression in (10) strictly holds over a narrow bandwidth of frequencies (around ω_0) that satisfy the condition $(\omega - \omega_0) \ll \pi/\tau$. Said another way, a broader differentiation bandwidth can be achieved by decreasing the relative time delay in the interferometer. However, as implied by (10), a reduced relative delay translates into a larger attenuation (higher insertion loss) in the interferometer spectral transfer function, leading to a decreased energetic efficiency in the device operation.

This symmetric unbalanced MZ interferometer device can be created using an all-fiber device consisting of a cascade of two LPGs, Figure 6 [21]. The light is split by the first LPG, then propagates in the core and cladding modes with different speeds and is superimposed coherently using the second LPG. The key in obtaining optical differentiation is a precise symmetry of the MZ interferometer in terms of the splitting ratios in order to obtain full destructive interference. The first LPG couples 50% of light into a cladding mode. Subsequently, 50% of energy propagates in the cladding mode while the other 50% propagates in the core mode. The light propagating in the core mode accumulates (with

respect to the cladding-propagating portion of the signal) a delay τ due to the difference in the group velocities between the core and cladding modes. As both modes propagate within the same fiber and as the interferometer length is typically of the order of a few to tens of centimeters, any environmental change influences both modes in nearly the same manner, which results in a very robust device operation. Moreover, as mentioned above, the LPGs can be fabricated so that their performance is almost independent on the input polarization [41]. In this way, the filter can be made very weakly polarization dependent.

As discussed, for flat-top pulse generation, a nearly transform-limited Gaussian-like optical pulse with a central frequency properly detuned with respect to the differentiator resonance (destructive interference) frequency must be launched at the device input. Figure 7 reports the spectral transfer function of a pair of cascaded LPGs, inscribed in a conventional telecommunication standard SMF, which have a period of $387 \mu\text{m}$ and are spaced 28 mm apart [27]. This leads to a time delay of 390 fs between the recombined cladding and core pulses. This pair of LPGs was inscribed using two-mirrors-assisted CO_2 laser side radiation, considerably reducing the photoinduced birefringence. After inscription of the first LPG with resonant attenuation slightly over 3 dB (typically 3.2 dB) we moved the translation stage by a distance L and inscribed the second LPG. During inscription of the second LPG, the transmission was monitored along both axes of birefringence after each period inscribed (using a superluminescent light-emitting diode, fiber polarizer, polarization controller, and optical spectrum analyzer) and the inscription process was stopped when the resonant attenuation of two consecutive MZ interference destructive interference wavelengths (that appeared around the LPG resonance wavelength) attained its maximum value—typically more than 30 dB. As the coupling strength of LPGs was slightly strain dependent, the strain applied to the fiber with the two LPGs inscribed was used subsequently to maintain the point of operation.

Figure 8 shows the simulated output pulse intensity profiles for different input pulse—LPG detuning factors, when the input pulse is a 700 fs Gaussian (almost double the inter-modal relative time delay) [27]. Figure 8 displays the fully destructive interference case (trace 1), with a central dip in the pulse shape and spectrum (the device is working as an optical differentiator [5]), and the partially destructive interference case (traces 2-3), where the dip gets filled up to achieve a flat-top pulse. Tuning the input pulse wavelength to an offset <4 nm from the destructive interference wavelength of the LPG interferometer leads to formation of a flat-top pulse shape, as seen in trace 3. The corresponding measured output spectrum is represented in Figure 7. This corresponds to a generated ~ 1.2 ps flat-top pulse centered at 1536 nm.

Notice that a similar LPG configuration (cascaded LPG device illustrated in Figure 6) can be used for *transform-limited* flat-top pulse generation [22]. To achieve a transform-limited pulse at the system output, the input pulse time width must be precisely fixed according to the interferometer relative delay; in addition, the input pulse must be spectrally centered at a constructive-interference frequency of the

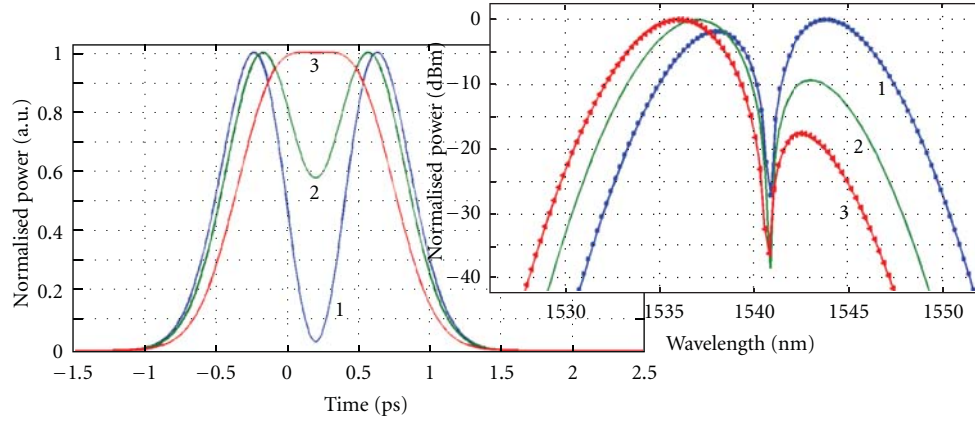


FIGURE 8: Traces in ascending order of pulse intensity profiles (left) and respective spectra (right) for detuning of the signal input wavelength away from the interference fringe of the cascaded LPG filter pair.

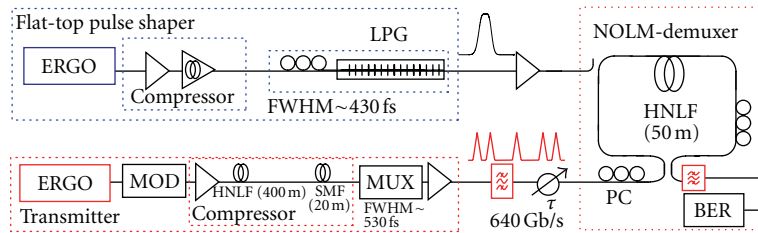


FIGURE 9: Setup for 640 Gbit/s. ERGO—erbium glass oscillator, PC—polarization controller, MOD—modulator, BER—bit error rate.

device. Different pulse waveforms could be generated using this same pulse coherent superposition concept by simply changing the interpulse relative delay [13]. In another recent experiment, a similar double-LPG device was used to generate parabolic-like optical pulses aimed at ultra-broadband flat spectral broadening (supercontinuum generation) by nonlinear propagation through a normally dispersive optical fiber [43].

3. Nonlinear Optical Time Division Demultiplexing at 640 Gbit/s Using Flat-Top Pulse Gating

3.1. Flat-Top Pulse Gating Schemes Based on a Single-LPG Shaper. The single-LPG scheme for flat-top optical pulse shaping described in Section 2.1 above has been successfully employed to generate optimized gating (control) pulses for error-free and jitter-tolerant nonlinear switching in optical time division multiplexing (OTDM) systems operating up to 640 Gbit/s [24–26]. The use of flat-top control pulses for demultiplexing in OTDM schemes has proved greatly advantageous as compared with the use of Gaussian-like pulses: flat-top pulse gating offers significant improvements in receiver sensitivity and timing-jitter tolerance. We reiterate that increasing tolerance to timing jitter in the system is of critical importance for serial data transmission in telecommunication links operating at rates of 160 Gbit/s and above.

In a first experimental demonstration [25], picosecond flat-top pulses generated from a single-LPG detuned differ-

entiator were employed as gating pulses in a 640-to-10 Gbit/s demultiplexing configuration and they were demonstrated to provide an ~ 13 dB improvement in receiver sensitivity as compared to the use of Gaussian-like control pulses and a jitter tolerance of ~ 500 fs, nearly 30% of the one-bit time window.

Figure 9 shows a schematic of the experimental setup. It consists of three principal parts that will be described subsequently: the flat-top pulse generator, the transmitter, and the demultiplexer, a nonlinear optical loop mirror (NOLM).

The NOLM consists of a *Sagnac* interferometer [28] containing a 50 m long section of a highly nonlinear fiber (HNLf, dispersion slope ~ 0.018 ps/nm² km, zero dispersion at 1554 nm, and nonlinear coefficient of $\gamma \sim 10.5$ W⁻¹ km⁻¹). The signal propagates inside the loop in both (opposite) directions and interferes at the NOLM's input/output coupler. Without the presence of the gating signal, the phase difference experienced by light propagating in both directions is zero, which results in constructive interference at the input port of the NOLM, that is, the signal is reflected back. In the presence of the gating pulse that propagates unidirectionally in the NOLM only, the copropagating signal light experiences a Kerr-effect-induced nonlinear phase shift, which introduces a phase difference between signals propagating in both directions. Adjusting the parameters (e.g., the gating signal intensity) to produce a phase difference equal to π , the signal, which is overlapped with the gating pulse, is directed to the NOLM output port. For optimum operation, the gating signal has to be propagated simultaneously with the target data pulse. To minimize dispersion-induced delays,

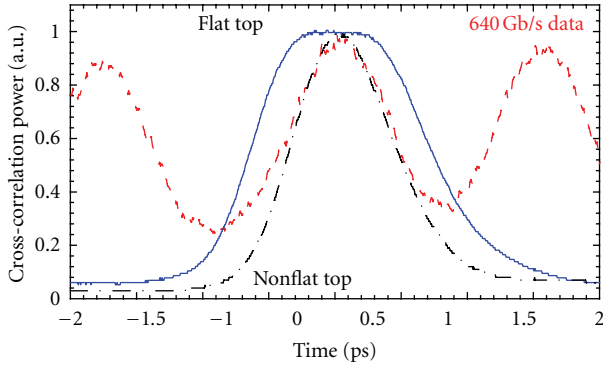


FIGURE 10: Cross-correlation of the data (dashed), flat-top (solid), and nonflat-top (dash-dot) gating pulses.

the signal and gating pulses should be respectively located at each different side of the zero-dispersion wavelength of the NOLM (1554 nm). Nonetheless, any delay between these two pulses (caused, e.g., by the timing jitter) severely degrades the performance. As the tolerance to the timing jitter scales with the one-bit time slot duration, higher repetition rate systems are generally more timing-jitter sensitive.

The flat-top pulse generator consists of an ERGO (erbium glass oscillator) pulse source emitting 1.2 ps full-width-half-maximum (FWHM) pulses at 10 GHz at 1543 nm with rms timing jitter of 90 fs (measured by the von der Linde method [44], integrating the phase noise spectrum from 1 kHz to 1 GHz). These pulses are further soliton compressed using an optical amplifier in saturation to obtain 450 fs pulses (measured with an autocorrelator). Subsequently, the pulses are propagated through the LPG filter. The used LPG is 110 mm long with a period of 530 μm and is made in a standard SMF-28 fiber using CO₂ laser irradiation and the point-by-point technique [36]. Its coupling strength that is close to the full coupling condition (zero transmission at the resonance wavelength) is slightly tunable using axial strain [37]. The FWHM of the LPG notch is 6 nm in power transmission. Following optimization of the frequency detuning between the input pulse and LPG resonance, flat-top pulses that give a cross-correlation FWHM of ~ 1.4 ps are obtained at the LPG output. The sampling pulse used for the cross-correlation is a 500 fs FWHM Gaussian-shaped pulse (measured using an autocorrelator). The temporal characteristics of the flat-top pulses at the LPG shaper output are shown in Figure 10. The flat-top width of the pulses measured at 98% of the pulse cross-correlation peak power is measured to be 550 fs. Considering the relatively long duration of the sampling pulse used for the cross-correlation, the actual pulse flat-top part is expected to be slightly larger and the FWHM slightly smaller compared to the cross-correlation values. Due to an unwanted photoinduced birefringence of our in-house made LPG-based filter, a polarization controller is employed to operate the LPG-based filter within one principal axis of birefringence. The energetic efficiency of the filtering process (ratio of the signal powers at the LPG output and input) was measured to be 24%.

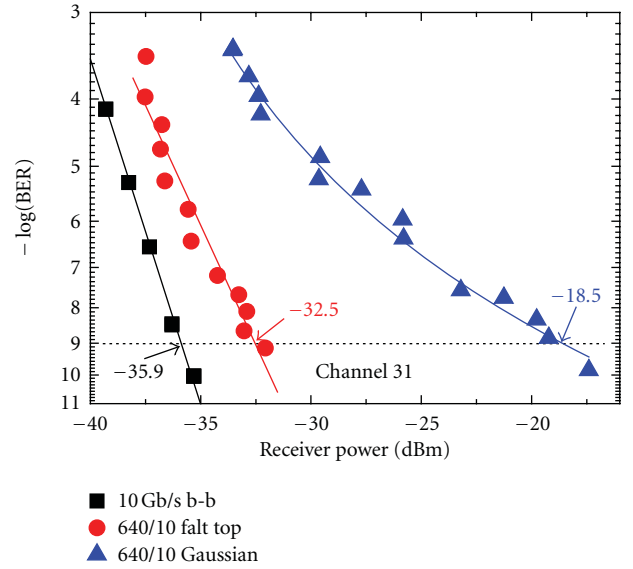


FIGURE 11: BER characteristics: back-to-back (squares), using flat-top pulses (circles), and using nonflat-top pulses (triangles). The demultiplexing results are from the same data channel.

The transmitter consists of another 10 GHz ERGO source emitting at 1557 nm, a pulse compressor based on HNLF followed by SMF-28 standard fiber giving pulses of 530 fs FWHM duration (estimated from autocorrelation measurements) with measured rms timing jitter of 70 fs. The pulse train is data modulated at 10 Gbit/s (2^7-1 PRBS) and optical time division multiplexed (OTDM) up to 640 Gbit/s, see cross-correlation trace of the data signal in Figure 10. Thus, the 640 Gbit/s serial data signal is composed by 64 channels, each at 10 Gbit/s. Please note that in practice, the data modulated pulses are multiplexed to 40 Gbit/s before compression, in order to avoid unwanted dispersive broadening in the first multiplexer-stages. The multiplexer (MUX) is polarization and PRBS maintaining (for 2^7-1 PRBS word length) with a $(2^7-1)/2$ bits fiber delay in each MUX stage. The cross-correlation measurement of the multiplexed 640 Gbit/s data signal evidences that the individual data channels have been temporally aligned with the correct distance to neighboring channels, that is, about 1.57 ps, and the pulses are adequately narrow to obtain a reasonable resolution of the individual channels using the 500 fs reference pulses.

The amplified flat-top gating signal and properly delayed transmitter signal are launched into the NOLM demultiplexer. The 10 Gbit/s demultiplexed signal at the NOLM output is filtered by a band-pass filter (1.4 nm) to filter out noise and residual gating signal at 1543 nm before being analyzed using a bit error ratio (BER) analyzer. We used a free-running ERGO as a master clock and then o/e converted its pulses to lock all other subsystems to it. This reduced the timing jitter to 70 fs rms for the data and 90 fs for the clock pulses. For the system evaluation (results shown in Figure 11), we measure the back-to-back sensitivity at 10 Gbit/s first. Subsequently, we characterize the 640-Gbit/s setup: we measure power penalty using the optical gate based

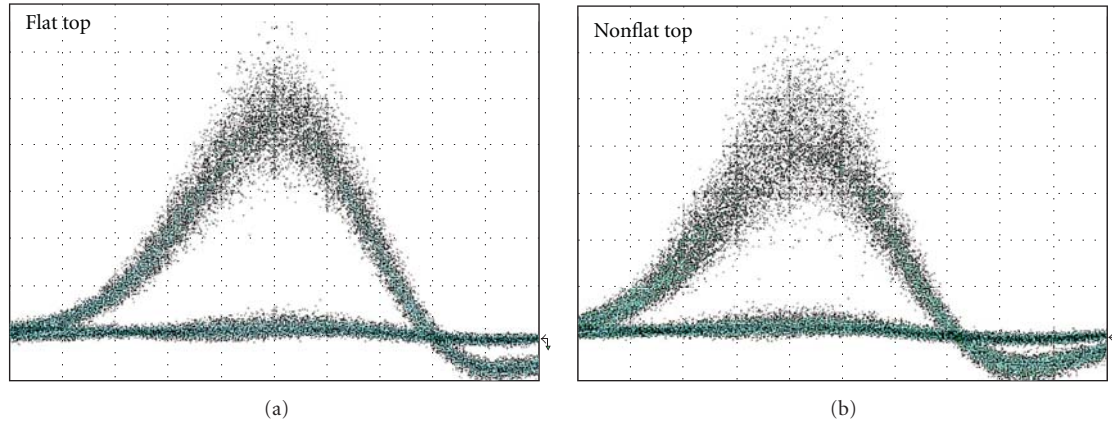


FIGURE 12: Eye diagrams obtained for flat-top and non-flat-top gating pulses.

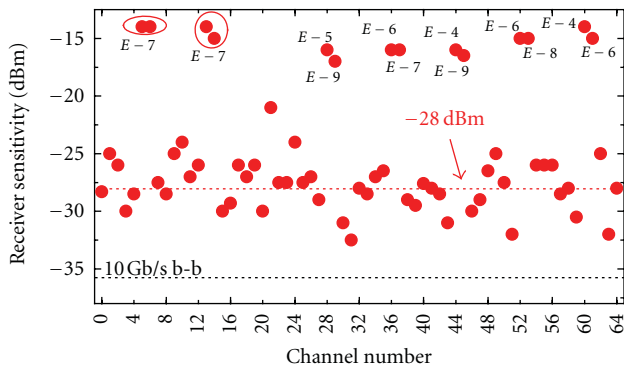


FIGURE 13: Demultiplexing of all 64 tributary channels using flat-top gating pulses.

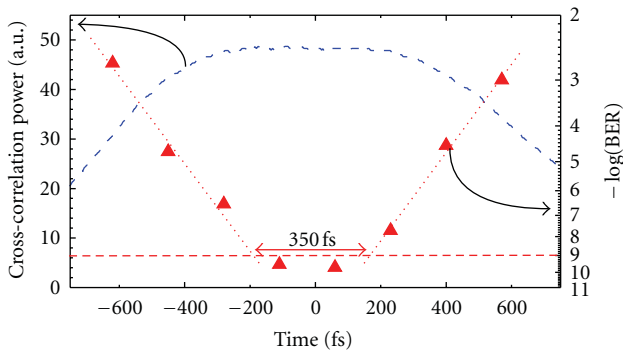


FIGURE 14: BER timing-jitter tolerance (triangles) and intensity profile of the used flat-top pulse (dashed).

on the flat-top pulses and for comparison with a non-flat-top pulse. The non-flat-top reference pulse is prepared by simply detuning the LPG, which enables us to remain on the same data channel, yielding a fair comparison of the two pulse types. The non-flat-top reference pulse is a Gaussian-like shaped 900 fs FWHM pulse, see plot in Figure 10.

From Figure 11 we see that the use of non-flat-top gating pulses results in an additional power penalty of 13 dB for the error-free level of $\text{BER} = 10^{-9}$ compared to the flat-top case,

where the penalty is only 3.5 dB with respect to the 10 Gbit/s back to back. Moreover, there is an error floor using non-flat-top pulses indicating that the system is limited by relative timing jitter, which is over 110 fs rms in our system (considering independent transmitter and gating signals timing jitter of 70 fs and 90 fs, resp.). This is confirmed by the fact that the use of the flat-top gating pulses with a flat-top width five-times wider than the system rms timing jitter does not lead to the appearance of an error floor. That is, the non-flat-top error floor does not stem from interference from neighboring channels but only from timing mismatch with the data pulse caused by their relative jitter. For this reason flat-top pulses perform better, because their shape combined with the non-linear mechanism of performing the demultiplexing process leads to a quasisquare switching window. This is further confirmed by the eye diagrams that are shown in Figure 12. We clearly see that using the non-flat-top gating pulses leads to amplitude noise, which is typical for timing jitter-limited systems. Again, influence of this phenomenon is considerably reduced when flat-top gating pulses are used. All these measurements were carried out on the same data channel.

Furthermore, we measure the system performance for all 64 tributary channels. Figure 13 shows the sensitivities for all 64 channels when using the flat-top pulses to gate with. We see that it is possible to resolve all channels and demultiplex them. But since some of the channels partially overlap, we see that some pairs of channels are not as good as the rest, and 12 of the 64 channels are not error-free due to the suboptimum MUX alignment. This is purely a feature of the multiplexer and is consequently not associated with the gating pulses. In fact the flat-top-pulses clearly reveal the quality of the multiplexed signal in a much better way than the non-flat-top pulse would have been able to with its large penalty. Furthermore, with 52 channels error free, it can be concluded that the flat-top pulses are unambiguously appropriate for 640 Gbit/s operation.

The previous data clearly shows that the used flat-top gating pulses are capable of mitigating the system timing jitter being over 110 fs rms. To find a maximum value of the timing jitter that can be tolerated by the demultiplexer with the available flat-top pulses, we increase the power at

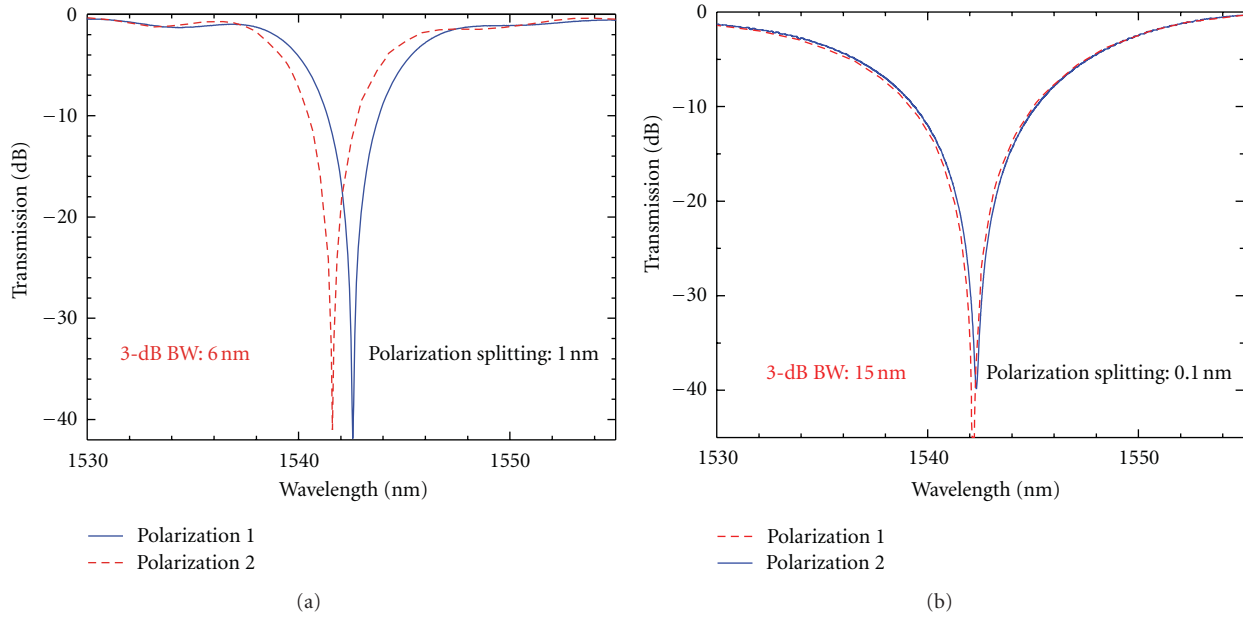


FIGURE 15: Measured spectral transmission responses of the LPG differentiators used (a) on the [25] (results shown in Figures 10–14) and (b) on the [26] (results shown in Figure 16) for the two orthogonal input light polarization states.

the receiver by 5 dB over the error-free level and vary the delay between the data and gating pulses. Subsequently, we measure the BER for different levels of this delay, Figure 14. The flat-top waveform is also shown in order to visualize the relation between the gating pulse flat-top duration and the amount of delay that can be tolerated for error-free operation (with BER < 10^{-9}). We see that an additional time displacement of 350 fs can be tolerated. Together with the system jitter of 110 fs, this gives almost 500 fs tolerance or 30% of the 640 Gbit/s time slot, which is a value very close to the flat part of the flat-top pulse of 550 fs. For non-flat-top gating pulses, the system does not tolerate any additional timing jitter, indicating that the system is already limited by its timing jitter of 110 fs rms.

In addition to the above critical advantages, it has been also demonstrated that the use of flat-top control pulses in a nonlinear time-domain demultiplexing system may help in achieving polarization-independent operation [45]. The latter is a highly desired feature in an optical demultiplexer, enabling it to process incoming optical data signals with arbitrary states of polarization, as it is usually the case in practical systems. For this purpose, the flat-top pulse-shaping element should be polarization independent. As mentioned above, LPG-based pulse shapers with significantly reduced polarization dependence can be created by fabricating the LPG devices through a two-mirror assisted CO₂ laser radiation configuration, which yields azimuthally symmetric illumination of the fiber [41], greatly reducing the photo-induced birefringence in the fabricated LPGs. Figure 15(b) shows the measured transmission spectral response for the two orthogonal light polarization states of a single LPG differentiator fabricated using this improved configuration [26]. As anticipated, a nearly polarization-independent re-

sponse is achieved (polarization splitting ~ 0.1 nm), in sharp contrast to the conventional single-side illuminated LPG differentiator (polarization splitting ~ 1 nm), see Figure 15(a) showing the measured spectral responses for the two orthogonal light polarization states of the LPG used in the nonlinear switching experiments described above [25]. Notice that the newly fabricated LPG differentiator also exhibits a significantly larger operation bandwidth (FWHM bandwidth of the resonance notch ~ 15 nm) than that used in our previous experiments (~ 6 nm). This enables the generation of shorter flat-top pulse waveforms (~ 840 -fs FWHM from a 500 fs input Gaussian-like pulse) with an improved intensity-profile quality, leading to a significantly improved BER performance when employed for 640-to-10 Gbit/s demultiplexing in the nonlinear switch [26]. In particular, the optimized LPG differentiator yields less than 0.5 dB receiver sensitivity penalty relative to the 10 Gbit/s back-to-back measurements, see results in Figure 16, as compared with the >3 dB penalty measured for the previous LPG filters, see results in Figure 11 above. A total timing jitter tolerance of ~ 310 fs has been experimentally estimated when using the newly generated flat-top pulse waveform [26]. The observed decrease in the jitter tolerance (as compared with the results obtained with the previous flat-top pulse, ~ 500 fs) can be attributed to the fact that the new pulse has a shorter flat-top section.

3.2. Flat-Top Pulse Gating Schemes Based on Double LPG for Polarization-Independent Demultiplexing. Polarization-independent (PI) operation is one of the most desired features of an optical demultiplexer, enabling it to process incoming optical data signals with arbitrary states of polarizations. But nonlinear effects such as cross-phase modulation (XPM) or four wave mixing (FWM), which

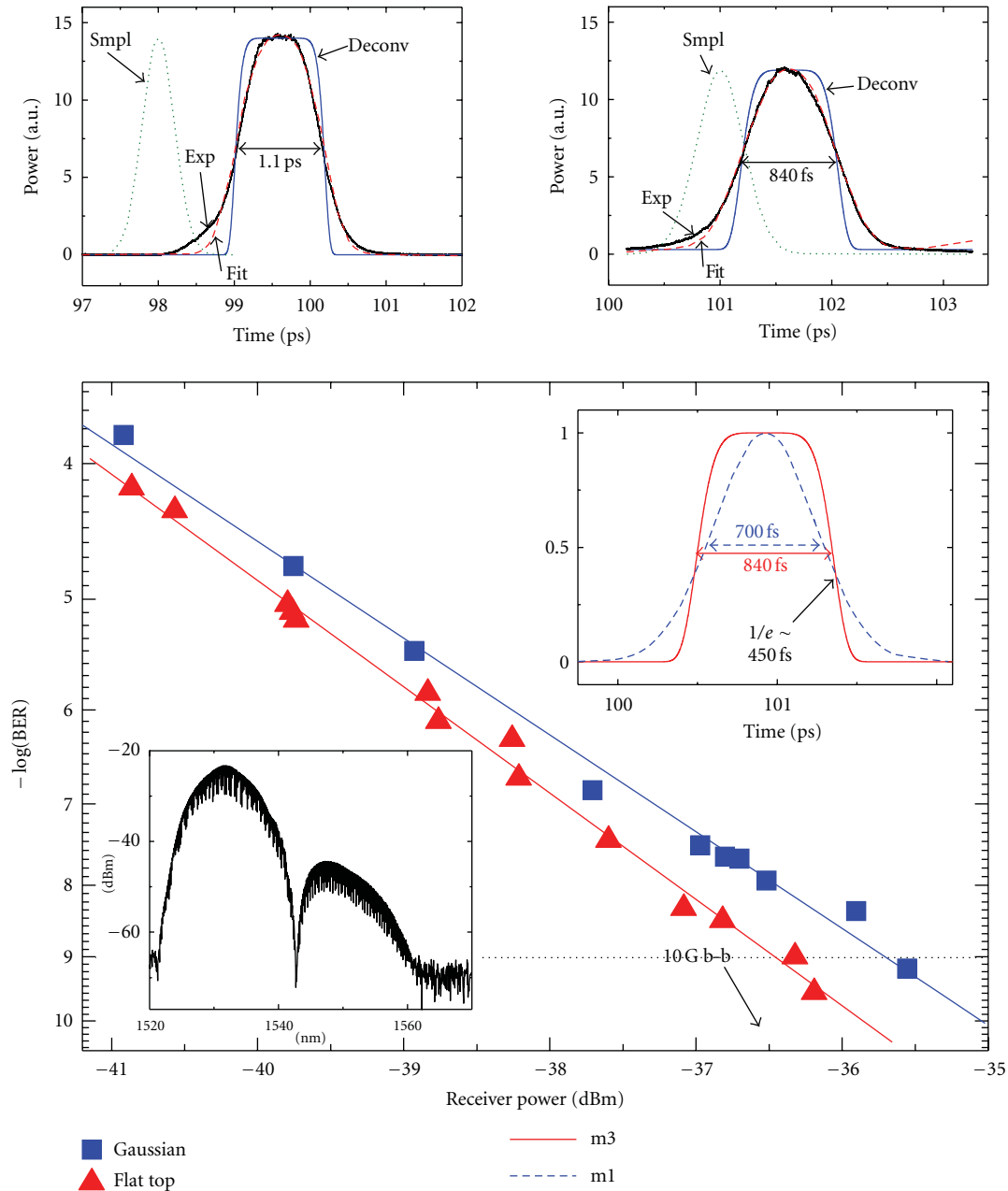


FIGURE 16: Flat-top pulses and 640 Gbit/s demultiplexing with subpicosecond flat-top pulse. Top: measured cross-correlation traces of the generated flat-top pulses of various widths and deconvoluted waveforms. Bottom: BER performance with and without flat-top pulse. Insets show the spectral (lower left) profile of the flat-top pulse and the temporal (upper right) corresponding waveforms of the flat-top super-Gaussian (or order $M = 3$) and Gaussian ($m = 1$) control pulses.

are used in ultrahigh-speed all-optical demultiplexing, are inherently polarization dependent. This is the case also for the standard NOLM, since it is based on an XPM-induced phase shift.

The principle for canceling the data polarization-dependence of the NOLM is based on the careful use of its periodic power transfer function without introduction of any structural modifications [45]. The operation is shown in Figure 17. The polarization states are shown to the left: the control polarization is set to a linear state along the

y -axis, and the data is in a random (elliptical) state with field-components E_x and E_y along the x - and y -axes, respectively. The XPM phase shift $\Delta\varphi_y$ induced by the control pulse on the parallel E_y -component is three-times larger compared to the XPM phase shift $\Delta\varphi_x$ induced on the perpendicular component E_x . The power transfer function of the NOLM as a function of the phase-shift is shown to the right. It is possible to find conditions under which the XPM phase-shifts of the two data-polarization components E_y and E_x , $\Delta\varphi_y$ and $\Delta\varphi_x = 1/3\Delta\varphi_y$, respectively, give rise to equal

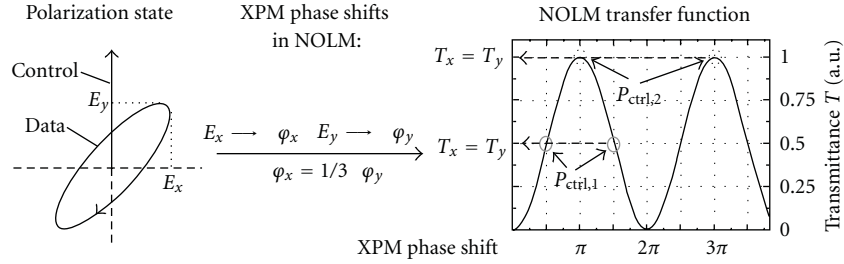


FIGURE 17: Principle behind polarization-independent operation of a standard NOLM.

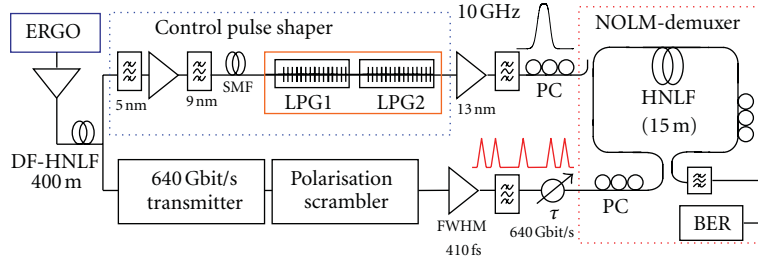


FIGURE 18: Setup for PI-NOLM operation.

transmissions T_y and T_x . This will result in a polarization-independent switching operation and it occurs at $(\Delta\phi_x; \Delta\phi_y) = (\pi/2; 3\pi/2)$ and $(\Delta\phi_x; \Delta\phi_y) = (\pi; 3\pi)$. These conditions can be achieved by carefully adjusting the average control pulse power P_{ctrl} , since the XPM-phase shift is proportional to P_{ctrl} . It is easy to understand that PI operation of the NOLM would benefit from the utilization of flat-top control pulses. This is related to the fact that a constant control pulse power would result in a constant phase shift along the data channel to be demultiplexed.

The double-LPG flat-top pulse shaper described in Section 2.3 above has been successfully employed for polarization-independent nonlinear switching in a 640-to-10 Gbit/s demultiplexing experiment [27]. Figure 18 shows the experimental setup for the PI-NOLM operation using the cascaded LPG pair as a flat-top pulse shaper (see detailed descriptions on this specific pulse shaper in Section 2.3 above). An ERGO pulse source runs at 10 GHz and emits 1.5 ps wide pulses at 1542 nm, which are used to create a supercontinuum in 400 m of dispersion flattened highly nonlinear fiber (DF-HNLF). The output from the DF-HNLF is used to generate the control and data signal by using two optical band-pass filters centered respectively at 1536 and 1555 nm.

The double-LPG filter is used for generation of a 1.2 ps flat-top pulse centered at 1536 nm from an input 700 fs Gaussian-like pulse. The generated flat-top pulse is subsequently used as control in an NOLM with 15 m HNLF (dispersion slope $S \approx 0.015$ ps/(nm² km), zero dispersion at $\lambda_0 = 1545$ nm, and nonlinear coefficient $\gamma \approx 10.5$ W⁻¹ km⁻¹). The data is a 640 Gbit/s OTDM signal (PRBS 2⁷-1, single polarization) centered at 1555 nm, with 410 fs wide pulses. The data is subsequently demultiplexed down to 10 Gbit/s for BER characterization.

The polarization state of the data signal is randomized in a polarization scrambler running at 113 kHz. The standard

NOLM operation (nonpolarization insensitive operation) is reached for $P_{\text{ctrl}} = 26.5$ dBm. When the scrambler is turned on the demultiplexed eye is severely deteriorated (Figure 19(a)), independently on the polarization state of the control. When P_{ctrl} is increased to 27.6 dBm and the control polarization is optimized, then the NOLM works in PI mode. With the scrambler on, the eye remains open as seen in Figure 19(b). By using a slow photodetector it is possible to measure 0.7 dB residual polarization dependence of the PI-NOLM operation when the scrambler is on.

Figure 20 shows the BER measurement for the standard and PI-NOLM operation. As can be seen, when the scrambler is off, the power sensitivity (at BER = 10⁻⁹) is the same for both cases. When the scrambler is turned on, then the standard NOLM exhibits an error floor above BER = 10⁻⁷. In contrast, the PI-NOLM shows just a power penalty of ~1 dB. These measurements confirm both the flat-top pulse enhanced performance of the nonlinear switch and the PI operation of the NOLM.

4. Conclusions

In this paper, we have reviewed some recent work on the design and fabrication of all-fiber (LPG-based) picosecond and subpicosecond flat-top optical pulse shapers and their application for nonlinear optical telecommunication data processing, particularly demultiplexing of OTDM serial data using NOLM-based switches with flat-top gating pulses, at bit rates up to 640 Gbit/s. The reviewed set of experiments demonstrate error-free 640-to-10 Gbit/s data signal demultiplexing over the 64 OTDM channels with a significantly improved performance over the use of Gaussian-like control/gating pulses, for example, in terms of receiver sensitivity (up to ~13 dB), timing-jitter tolerance (up to ~500 fs, corresponding to ~30% of the OTDM signal bit period), and optimized polarization insensitivity.

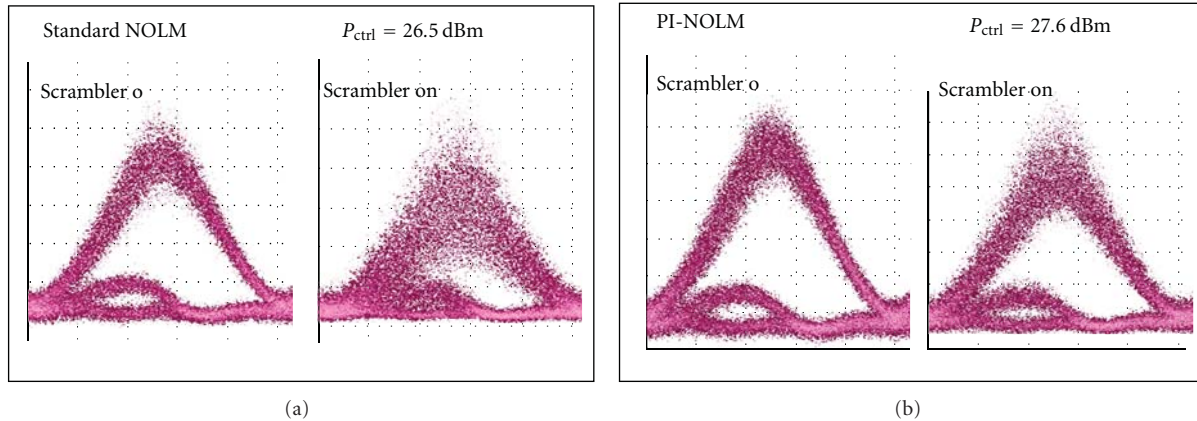


FIGURE 19: Eye diagrams for the demultiplexed 10 Gbit/s signal for the (a) standard, and (b) PI-NOLM operations, with polarization scrambler on and off.

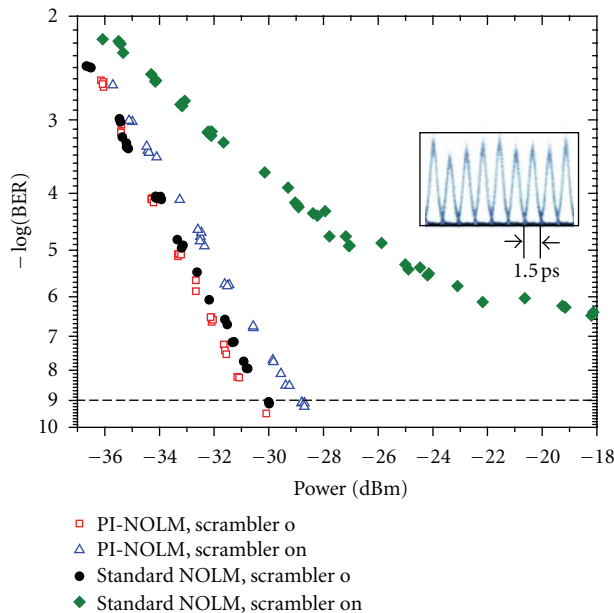


FIGURE 20: BER curves for the standard and PI-NOLM operation. Inside: 640 Gbit/s eye diagram.

The described LPG-based optical pulse-shaping methods can be readily used for generation of even shorter flat-top pulse waveforms, opening the path for the creation of optical time-division demultiplexing platforms with an optimized performance at 1.2 Tbit/s and above. Moreover, other temporal pulse shapes of practical interest (e.g., triangular or parabolic waveforms) could be generated in the subpicosecond regime using similar LPG approaches, potentially enabling the implementation of other pulse shaping-enhanced telecommunication signal processing/generation operations (e.g., optimized wavelength conversion, signal copying, time-to-wavelength mapping, high-repetition rate femtosecond pulse generation, etc.) at unprecedented bit rates, that is, at 640 Gbit/s and above.

Acknowledgments

This paper was supported in part by the Natural Sciences and Engineering Research Council (NSERC) of Canada and by the Les Fonds Québécois de la Recherche sur la Nature et les Technologies (FQRNT). It was also supported by the European Research Council (ERC) starter grant project SOCRATES and the Danish National Research Council funded project NOSFERATU. OFS Fitel Denmark Aps is gratefully acknowledged for providing the nonlinear fibers used in these experiments.

References

- [1] A. M. Weiner, "Femtosecond optical pulse shaping and processing," *Progress in Quantum Electronics*, vol. 19, no. 3, pp. 161–237, 1995.
- [2] F. Parmigiani, P. Petropoulos, M. Ibsen, and D. J. Richardson, "All-optical pulse reshaping and retiming systems incorporating pulse shaping fiber Bragg grating," *Journal of Lightwave Technology*, vol. 19, pp. 746–752, 2001.
- [3] J. H. Lee, P. C. Teh, P. Petropoulos, M. Ibsen, and D. J. Richardson, "All-optical modulation and demultiplexing systems with significant timing jitter tolerance through incorporation of pulse-shaping fiber Bragg gratings," *IEEE Photonics Technology Letters*, vol. 14, no. 2, pp. 203–205, 2002.
- [4] J. H. Lee, L. K. Oxenløwe, M. Ibsen et al., "All-optical TDM data demultiplexing at 80 Gb/s with significant timing jitter tolerance using a fiber bragg grating based rectangular pulse switching technology," *Journal of Lightwave Technology*, vol. 21, no. 11, pp. 2518–2523, 2003.
- [5] S. Watanabe, R. Ludwig, F. Futami et al., "Ultrafast all-optical 3R-regeneration," *IEICE Transactions on Electronics*, vol. E87-C, no. 7, pp. 1114–1118, 2004.
- [6] L. K. Oxenløwe, M. Galili, A. T. Clausen, and P. Jeppesen, "Generating a square switching window for timing jitter tolerant 160 Gb/s demultiplexing by the optical Fourier transform technique," in *Proceedings of the 32nd European Conference on Optical Communications (ECOC '06)*, Cannes, France, 2006, paper We2.3.4.
- [7] T. Otani, T. Miyazaki, and S. Yamamoto, "Optical 3R regenerator using wavelength converters based on electroabsorption

- modulator for all-optical network applications,” *IEEE Photonics Technology Letters*, vol. 12, no. 4, pp. 431–433, 2000.
- [8] A. I. Latkin, S. Boscolo, R. S. Bhamber, and S. K. Turitsyn, “Optical frequency conversion, pulse compression and signal copying using triangular pulses,” in *Proceedings of the European Conference on Optical Communication (ECOC '08)*, Brussels, Belgium, 2008, paper Mo.3.F.4.
- [9] F. Parmigiani, M. Ibsen, T. T. Ng, L. Provost, P. Petropoulos, and D. J. Richardson, “An efficient wavelength converter exploiting a grating-based saw-tooth pulse shaper,” *IEEE Photonics Technology Letters*, vol. 20, no. 17, pp. 1461–1463, 2008.
- [10] F. Parmigiani, C. Finot, K. Mukasa et al., “Ultra-flat SPM-broadened spectra in a highly nonlinear fiber using parabolic pulses formed in a fiber Bragg grating,” *Optics Express*, vol. 14, no. 17, pp. 7617–7622, 2006.
- [11] T. Kurokawa, H. Tsuda, K. Okamoto et al., “Time-space-conversion optical signal processing using arrayed-waveguide grating,” *Electronics Letters*, vol. 33, no. 22, pp. 1890–1891, 1997.
- [12] P. Petropoulos, M. Ibsen, A. D. Ellis, and D. J. Richardson, “Rectangular pulse generation based on pulse reshaping using a superstructured fiber Bragg grating,” *Journal of Lightwave Technology*, vol. 19, no. 5, pp. 746–752, 2001.
- [13] Y. Park, M. H. Asghari, T. J. Ahn, and J. Azaña, “Transform-limited picosecond pulse shaping based on temporal coherence synthesization,” *Optics Express*, vol. 15, no. 15, pp. 9584–9599, 2007.
- [14] Y. Park, M. Kulishov, R. Slavík, and J. Azaña, “Picosecond and sub-picosecond flat-top pulse generation using uniform long-period fiber gratings,” *Optics Express*, vol. 14, no. 26, pp. 12671–12678, 2006.
- [15] R. Slavík, Y. Park, and J. Azaña, “Tunable dispersion-tolerant picosecond flat-top waveform generation using an optical differentiator,” *Optics Express*, vol. 15, no. 11, pp. 6717–6726, 2007.
- [16] R. Kashyap, *Fiber Bragg Gratings*, Academic Press, San Diego, Calif, USA, 2nd edition, 2009.
- [17] M. Kulishov and J. Azaña, “Ultrashort pulse propagation in uniform and nonuniform waveguide long-period gratings,” *Journal of the Optical Society of America A*, vol. 22, no. 7, pp. 1319–1333, 2005.
- [18] R. Slavík, M. Kulishov, Y. Park, and J. Azaña, “Long-period-fiber-grating-based filter configuration enabling arbitrary linear filtering characteristics,” *Optics Letters*, vol. 34, no. 7, pp. 1045–1047, 2009.
- [19] M. Kulishov and J. Azaña, “Long-period fiber gratings as ultrafast optical differentiators,” *Optics Letters*, vol. 30, no. 20, pp. 2700–2702, 2005.
- [20] R. Slavík, Y. Park, M. Kulishov, R. Morandotti, and J. Azaña, “Ultrafast all-optical differentiators,” *Optics Express*, vol. 14, no. 22, pp. 10699–10707, 2006.
- [21] R. Slavík, Y. Park, D. Krčmařík, and J. Azaña, “Stable all-fiber photonic temporal differentiator using a long-period fiber grating interferometer,” *Optics Communications*, vol. 282, no. 12, pp. 2339–2342, 2009.
- [22] R. Slavík, Y. Park, and J. Azaña, “Long-period fiber-grating-based filter for generation of picosecond and subpicosecond transform-limited flat-top pulses,” *IEEE Photonics Technology Letters*, vol. 20, no. 10, pp. 806–808, 2008.
- [23] E. Palushani, H. Hu, L. K. Oxenløwe et al., “640 Gb/s timing tolerant demultiplexing using a cascaded long-period fiber grating pulse shaper,” in *Proceedings of the 35th European Conference on Optical Communication (ECOC '09)*, Vienna, Austria, 2009, paper Tu4.3.3.
- [24] R. Slavík, L. K. Oxenløwe, M. Galili et al., “Demultiplexing of 320-Gb/s OTDM data using ultrashort flat-top pulses,” *IEEE Photonics Technology Letters*, vol. 19, no. 22, pp. 1855–1857, 2007.
- [25] L. K. Oxenløwe, R. Slavík, M. Galili et al., “640 Gb/s timing jitter-tolerant data processing using a long-period fiber-grating-based flat-top pulse shaper,” *IEEE Journal on Selected Topics in Quantum Electronics*, vol. 14, no. 3, Article ID 4538055, pp. 566–572, 2008.
- [26] L. K. Oxenløwe, M. Galili, H. C. M. Mulvad, R. Slavík, A. T. Clausen, and P. Jeppesen, “Polarisation-independent sub-picosecond flat-top pulse generation for ultra-fast 640 Gbit/s gating,” in *Proceedings of the Optical Fiber Conference (OFC '09)*, San Diego, Calif, USA, March 2009, paper OWS5.
- [27] E. Palushani, H. Hu, M. Galili et al., “640 Gbit/s polarisation-independent demultiplexing in a standard nonlinear-optical-loop-mirror using a cascaded long-period grating pulse shaper,” in *Proceedings of the 23rd Annual Photonics Society Meeting*, Denver, Colo, USA, November 2010, paper TuM2.
- [28] T. Yamamoto, E. Yoshida, and M. Nakazawa, “Ultrafast nonlinear optical loop mirror for demultiplexing 640Gbit/s TDM signals,” *Electronics Letters*, vol. 34, no. 10, pp. 1013–1014, 1998.
- [29] A. I. Siahlo, A. T. Clausen, L. K. Oxenløwe, J. Seoane, and P. Jeppesen, “640 Gb/s OTDM transmission and demultiplexing using a NOLM with commercially available highly non-linear fiber,” in *Proceedings of the Conference on Lasers and Electro-Optics (CLEO '05)*, vol. 2, pp. 883–885, 2005, paper CTuO1.
- [30] H. G. Weber, C. Schubert, S. Ferber et al., “Single channel 1.28 Tbit/s and 2.56 Tbit/s DQPSK transmission,” *Electronics Letters*, vol. 42, pp. 178–179, 2006.
- [31] S. Watanabe, “Optical signal processing using nonlinear fibers,” *Journal of Optical and Fiber Communications Reports*, vol. 3, no. 1, pp. 1–24, 2006.
- [32] D. Zibar, L. K. Oxenløwe, H. C. H. Mulvad et al., “The impact of gating timing jitter on a 160 Gb/s demultiplexer,” in *Proceedings of the Optical Fiber Conference (OFC '06)*, vol. 2006, 2006, paper OTuB2.
- [33] E. Tangdiongga, Y. Liu, H. de Waardt et al., “All-optical demultiplexing of 640 to 40 Gbits/s using filtered chirp of a semiconductor optical amplifier,” *Optics Letters*, vol. 32, no. 7, pp. 835–837, 2007.
- [34] M. H. Asghari and J. Azaña, “Proposal and analysis of a reconfigurable pulse shaping technique based on multi-arm optical differentiators,” *Optics Communications*, vol. 281, no. 18, pp. 4581–4588, 2008.
- [35] A. M. Vengsarkar, P. J. Lemaire, J. B. Judkins, V. Bhatia, T. Erdogan, and J. E. Sipe, “Long-period fiber gratings as band-rejection filters,” *Journal of Lightwave Technology*, vol. 14, no. 1, pp. 58–65, 1996.
- [36] D. D. Davis, T. K. Gaylord, E. N. Glytsis, S. G. Kosinski, S. C. Mettler, and A. M. Vengsarkar, “Long-period fibre grating fabrication with focused CO₂ laser pulses,” *Electronics Letters*, vol. 34, no. 3, pp. 302–303, 1998.
- [37] R. Slavík, “Extremely deep long-period fiber grating made with CO₂ laser,” *IEEE Photonics Technology Letters*, vol. 18, no. 16, pp. 1705–1707, 2006.
- [38] T. Erdogan and V. Mizrahi, “Characterization of UV-induced birefringence in photosensitive Ge-doped silica optical fibers,” *Journal of the Optical Society of America B*, vol. 11, no. 10, pp. 2100–2105, 1994.
- [39] L. Lepetit, G. Chériaux, and M. Joffre, “Linear technique of phase measurement by femtosecond spectral interferometry for applications in spectroscopy,” *Journal of the Optical Society of America B*, vol. 12, no. 12, pp. 2467–2474, 1995.

- [40] Y. Park, F. Li, and J. Azaña, "Characterization and optimization of optical pulse differentiation using spectral interferometry," *IEEE Photonics Technology Letters*, vol. 18, no. 17, pp. 1798–1800, 2006.
- [41] V. Grubsky and J. Feinberg, "Fabrication of axially symmetric long-period gratings with a carbon dioxide laser," *IEEE Photonics Technology Letters*, vol. 18, no. 21, pp. 2296–2298, 2006.
- [42] Y. Park, J. Azaña, and R. Slavík, "Ultrafast all-optical first- and higher-order differentiators based on interferometers," *Optics Letters*, vol. 32, no. 6, pp. 710–712, 2007.
- [43] D. Krčmařík, R. Slavík, Y. G. Park, and J. Azaña, "Nonlinear pulse compression of picosecond parabolic-like pulses synthesized with a long period fiber grating filter," *Optics Express*, vol. 17, no. 9, pp. 7074–7087, 2009.
- [44] D. von der Linde, "Characterization of the noise in continuously operating mode-locked lasers," *Applied Physics B*, vol. 39, no. 4, pp. 201–217, 1986.
- [45] H. C. H. Mulvad, M. Galili, L. K. Oxenløwe, A. T. Clausen, L. Grüner-Nielsen, and P. Jeppesen, "Polarization-independent high-speed switching in a standard non-linear optical loop mirror," in *Proceedings of the Optical Fiber Conference (OFC '08)*, San Diego, Calif, USA, 2008, paper OMN3.

Research Article

Bragg-Scattering Four-Wave Mixing in Nonlinear Fibers with Intracavity Frequency-Shifted Laser Pumps

**Katarzyna Krupa,¹ Michela Bettinzana,² Alessandro Tonello,¹ Vincent Couderc,¹
Philippe Di Bin,¹ Stefan Wabnitz,² and Alain Barthélémy¹**

¹*XLIM, UMR CNRS 6172, Université de Limoges, 123 av A. Thomas, 87060 Limoges, France*

²*Dipartimento di Ingegneria dell'Informazione, Università di Brescia, Via Branze 38, 25123 Brescia, Italy*

Correspondence should be addressed to Alessandro Tonello, alessandro.tonello@unilim.fr

Received 8 July 2011; Accepted 5 September 2011

Academic Editor: Christophe Finot

Copyright © 2012 Katarzyna Krupa et al. This is an open access article distributed under the Creative Commons Attribution License, which permits unrestricted use, distribution, and reproduction in any medium, provided the original work is properly cited.

We experimentally study four-wave mixing in highly nonlinear fibers using two independent and partially coherent laser pumps and a third coherent signal. We focus our attention on the Bragg-scattering frequency conversion. The two pumps were obtained by amplifying two intracavity frequency-shifted feedback lasers working in a continuous wave regime.

1. Introduction

Over the last decades, the nonlinear phenomena of parametric four-wave mixing (FWM) have been intensively studied in view of their great potential to provide a large variety of all-optical functionalities for ultrafast signal processing [1–4]. In particular, optical parametric amplification, frequency conversion, phase conjugation, and nonlinear switching have been widely explored. The main interest was developed for FWM with coherent pumps, since this technique may provide high conversion efficiencies with appropriate dispersion curves [5]. Nevertheless, in recent years, FWM in optical fibers with incoherent or partially coherent pumps has attracted great attention, in view of its polarization-independent gain and increased resilience to stimulated Brillouin scattering (SBS) [6, 7]. Let us remember that SBS limits the direct use of intense and narrowband lasers in nonlinear fiber. For the specific case of highly nonlinear fibers (hereafter HNLF) the Brillouin threshold may be in the order of few tens of milliwatt for a fiber length of 500 m. The common way to increase the Brillouin threshold requires the adoption of phase modulation of pumps. For the case of two-pump parametric devices, optimal architectures of phase modulations have been proposed to suppress SBS. These solutions are based on phase modulators, generally

driven by a pseudorandom bitsequence generator [4, 5, 8, 9] at GHz repetition frequency. With pure phase modulation the pumps can be spectrally broadened without affecting the time domain intensity.

The adoption of incoherent pumps may represent a cost-effective solution to study FWM in different scenarios and may open a novel kind of applications, even if this may take place at the expense of low conversion efficiency and spectral broadening of the converted signal. The interplay between four-wave mixing processes with mixed coherent-incoherent pumps may also open entirely new features as reported very recently in [10]. Till now, most of investigations on nonlinear effects with incoherent pumping have been conducted for single pump FWM processes and so far, little attention has been paid to a specific type of FWM generally called Bragg-scattering FWM (BS-FWM) [6, 10]. The low-noise nature of the BS-FWM is a very attractive feature [8, 11], which makes this process an excellent candidate for light-by-light manipulation with possible extension to the case of very weak signals. These optical functionalities may be of interest to manipulate optical quantum states in view of frequency conversion in quantum networks.

In this paper, we study the case of BS-FWM with partially coherent pumps in HNLF. For this purpose we used two broadband intra-cavity frequency-shifted feedback lasers

(IFSFLs) that operated in the continuous wave (CW) regime. Although these pumps are independent and exhibit low coherence time, we experimentally observed a clear signature of frequency conversion. In addition, we discuss the competition between BS-FWM and other types of FWM simultaneously occurring in HNLFs. In particular, we experimentally demonstrate the competition with degenerate (i.e., single pump) FWM.

2. Experimental Setup and Pump Sources

In the case of a parametric frequency conversion, the coherence time of the pump t_C should be compared to the characteristic evolution time t_P to establish such a nonlinear interaction. In HNLF and for powers in the order of 50 mW one could estimate t_P from the effective nonlinear length and group speed [12]. Whereas t_C from our pumps is instead associated to the bandwidth of at least 50 GHz of our pumps, so we may expect that the nonlinear interplay becomes affected by the partial coherence of pumps.

To study the case of BS-FWM frequency conversion in such a different regime we propose the experimental setup presented in Figure 1. Instead of filtering amplified spontaneous emission (ASE) sources (often employed in previous studies of incoherent FWM [6]) in our experiment we used a pair of intra-cavity frequency-shifted feedback lasers (IFSFLs) that we independently amplified to obtain two intense pumps.

The coherence properties of IFSFLs have been widely investigated and exploited in metrology and in astronomical imaging [13–15]. This kind of laser has also been proposed to increase by several orders of magnitude the SBS threshold in [16] allowing supercontinuum generation from an amplified IFSFL with several Watts of input power. However BS-FWM requires two distinct pumps. Thus, we developed two identical tunable fiber IFSFLs that operated at different wavelengths. Each IFSFL has been separately amplified by an erbium-doped fiber amplifier (EDFA) and protected against unwanted back reflections by an isolator. To reduce the ASE noise we put one bandpass filter at the input and two bandpass filters at the output of each EDFA (DiCon thin-film filters with 5 nm bandwidth each). These sets of filters carve the spectrum of each pump to reduce the background spectral level without significantly affecting the 3 dB bandwidth of the sources. Next, the two pumps were combined by a 50/50 fiber coupler and multiplexed with a third signal from a commercially available tunable extended cavity laser (laser power of 4 mW) through a 95/5 “tap” coupler. Pumps and signal were injected into a 480 m long off-the-shelf segment of HNLF with nominal zero dispersion wavelength (ZDW) of 1545 nm.

The spectrum at the output end of the fiber was analyzed by an optical spectrum analyzer (OSA) and by a 1 GHz photodiode connected either to an oscilloscope (OSC) or to a radio frequency (RF) analyzer. In what follows we will refer to a set of measurements in which the average powers of pump 1, 2, and signal at the input end of HNLF were 43 mW, 62 mW, and 0.12 mW, respectively.

The two central elements of our experimental setup are the fiber IFSFLs. We present their synoptic scheme in Figure 2. Each laser cavity consists of a 20 m long polarization maintaining (PM) erbium-doped fiber pumped by a laser diode emitting at 1480 nm and an inline PM acousto-optic frequency shifter (AOFS) controlled by a fixed RF driver at 110 MHz. The cavity mirrors are provided by a fiber FC-PC connector (see Figure 2, on the right) to introduce a natural Fresnel-type back reflection; the laser is connected to an output fiber with a FC-APC connector through a mating sleeve containing an air gap. The second mirror is represented on the left-hand side of Figure 2 by a blazed grating in Littrow configuration working at the first diffraction order. The microlens has a focal length $f' = 8$ mm while the grating has density of 600 grooves per millimeter. The central wavelength of the laser can be freely tuned all over the bandwidth permitted by the erbium gain by a simple rotation of the grating. The two IFSFLs are identical copies, and they are both based on this scheme: they were tuned to the upper and lower spectrum edge allowed by such lasers (1540 nm and 1563 nm for pump 1 and 2, resp.) so as to obtain the largest possible difference between their carrier frequencies. The corresponding frequency difference in this case is of 2.87 THz.

The free-space optics section reported in Figure 2 provides the transfer function of intra-cavity frequency dependent loss. In the case of perfect collimation, it turns out that the filtered bandwidth is inversely proportional to the focal length f' of the microlens. The fiber end close to the lens was cleaved with an angle of 8° to reduce any undesired back reflection. Under these conditions the low numerical aperture of the fiber provides the filtering mechanism. In order to smooth the optical spectrum, we used the AOFS inside the fiber cavity. A dynamical equilibrium can be found between frequency shifting, tight frequency-dependent loss, and broadband gain. However, a more detailed analysis of the RF spectrum at the output of one of the IFSFL unveils its complex behavior, as reported on the left-hand side of Figure 3.

We observe the presence of a comb of frequencies regularly spaced by 3.6 MHz, which compares well with the reciprocal of the round trip time of the fiber cavity. We compare these results with the direct numerical calculation coming from a model described in [17] (see Figure 3(b)). To implement equation (3) of [17] we assumed a fiber length of 27 m (in fact both the doped fiber and the AOFS are spliced to PM standard monomode fiber patchcords on both ends), a group index of 1.45, a frequency shift of 2×110 MHz (the AOFS is seen two times per round trip), and a random phase for each frequency comb component. Note that in our case the AOFS is driven by a radio frequency which is much higher than the inverse of the round trip time of the cavity.

The dynamical evolution of the IFSFLs is also a key point for applications in nonlinear optics. Indeed we observed as many other authors that our IFSFLs may operate in a CW or in a pulsed regime (see, e.g., [18]), depending on the level of feedback in the cavity. However, it would be desirable that the IFSFLs work close to a CW mode to observe BS-FWM as one would expect that a nonsynchronized pulsed regime

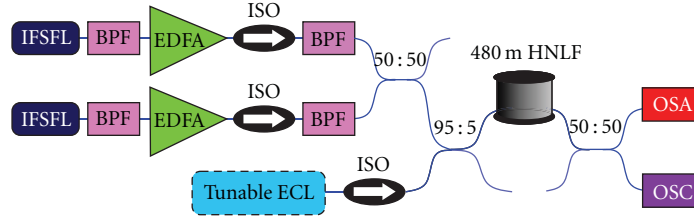


FIGURE 1: Experimental setup; IFSFL: intra-cavity frequency-shifted feedback laser, BPF: bandpass filter, EDFA: erbium-doped fiber amplifier, ISO: isolator, ECL: extended cavity tunable laser, HNLF: highly non-linear fiber, OSA: optical spectrum analyzer, and OSC: oscilloscope.

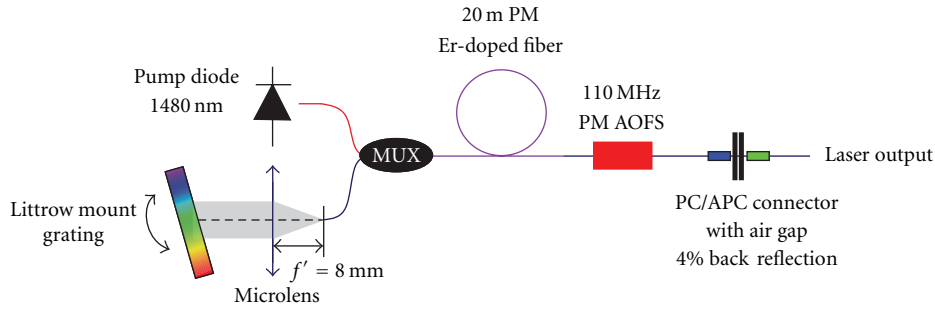


FIGURE 2: Setup of each IFSFL; MUX: multiplexer, PM: polarization maintaining, and AOFS: acousto-optic frequency shifter.

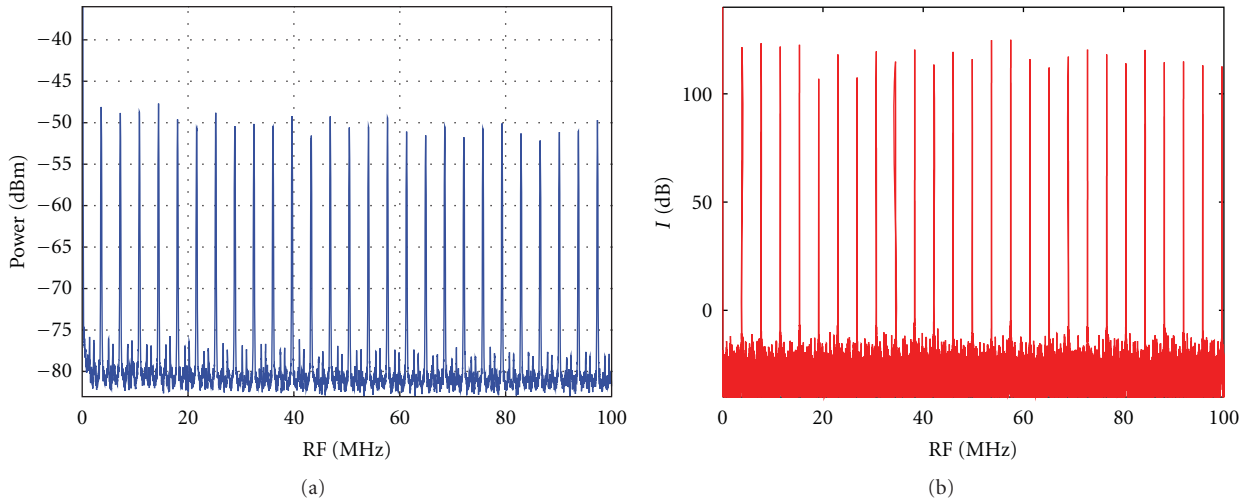


FIGURE 3: (a) Experimental RF spectrum for IFSFL 1 with a preamplified RF analyzer: the frequency comb free spectral range is of 3.6 MHz; (b) numerical simulation of RF photodiode current (spectrum of equation (3) of [17]).

between the pumps may drastically degrade the conversion efficiency in a dual pump process. According to [18], the bifurcation point between CW and pulsed solution can be influenced by the pump diode power. To keep the IFSFLs operating in the CW regime, we have then set their diode currents to a low value (65 mA for both lasers). For higher values of diode current one observes a rapid transition to time-periodic solutions [18] by direct observation of the laser output through a photodiode and an oscilloscope. The working points of our lasers were finely adjusted by verifying

the absence of relaxation oscillations with an oscilloscope and a 1 GHz bandwidth InGaAs photodetector.

3. Background Theory

Four-wave mixing is usually characterized as 3 distinct processes depending on the relative positions of the pumps, signal, and idler frequencies (see Figure 4(a)) [4, 8]: modulation instability (MI), phase conjugation (PC), and Bragg-scattering (BS). All of them may be simultaneously

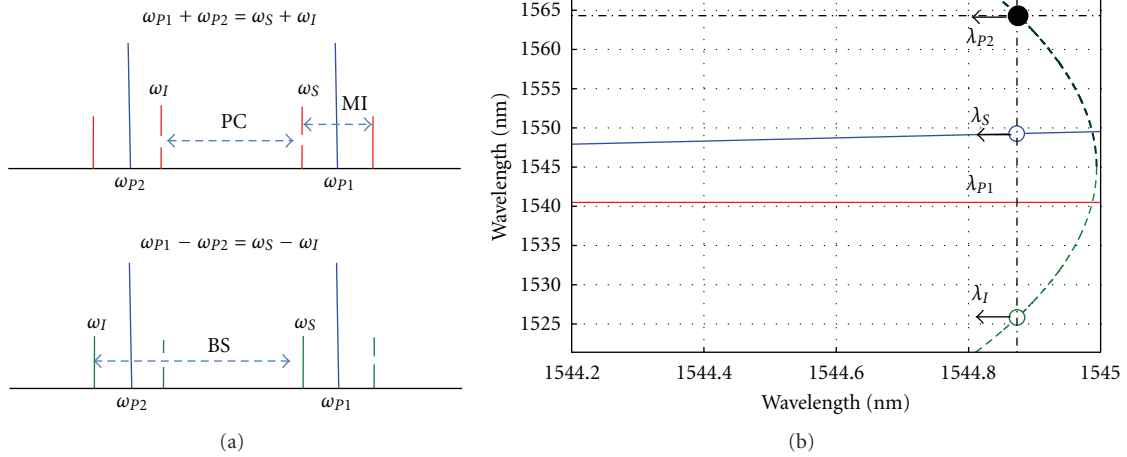


FIGURE 4: (a) Four-wave mixing processes, from [4]; (b) example of BS-FWM phase-matching diagram: thick solid (dashed) line (curve) for pump 1 (pump 2); thin solid (dashed) line (curve) for signal (idler).

observable [5] especially for low dispersion values, as it will be shown at the end of Section 4. MI requires one pump process. PC and BS require instead two distinct pumps. BS-FWM has a low noise nature as the frequency conversion may take place at phase matching in the absence of exponential gain.

For BS-FWM energy and momentum conservation give for angular frequencies ω_j and wave-vector k_j ($j = P1, P2, S$, for the pump 1, pump 2, signal and idler resp.) [4, 5, 11]:

$$\omega_I = \omega_S + (\omega_{P1} - \omega_{P2}), \quad (1)$$

$$k_I = k_S + (k_{P1} - k_{P2}). \quad (2)$$

The dependence of wave vectors on angular frequency leads to the determination of the best conditions for frequency conversion. In close proximity to the ZDW, the dispersion coefficient of an HNLf is generally approximated by a linear function of wavelength. Under this approximation, if one fixes for instance the wavelength of the pump 1, one can build a chart of optimization for the remaining wavelengths combining (1) and (2) [4, 5]. An example for such a diagram is given in Figure 4(b) for a fiber with ZDW of 1545 nm and dispersion slope of 0.018 ps/(km nm²). The horizontal axis represents a common reference wavelength: its corresponding angular frequency is the mean value between the frequency of the idler and that of pump 2. One can start to choose a value for the wavelength for pump 2 by covering the corresponding thick dashed curve: the wavelength for pump 2 will be the vertical coordinate of the selected point. Then from the chart one can automatically predict the best signal wavelength and hence the position of the corresponding idler. One should draw first a vertical line that matches the selected choice of pump 2. The wavelengths for signal and idler will be read at the intersection points with the other curves. More specifically the signal will be read at the intersection with the thin solid line while the idler will come from the intersection with the thin dashed curve. In practice, it is likely that the ZDW may fluctuate by

about 1 nm along the fiber length, according to the analysis presented in [19] for similar types of fibers. This fact may degrade the overall conversion efficiency [5].

4. Experimental Results and Discussion

Let us first focus on the spectral region between 1520 nm and 1535 nm, where the BS-FWM appears whenever the signal is varied between 1547.3 nm and 1554.3 nm. The collection of these experimental results is shown in Figure 5(a). Note that the BS-FWM sideband varies from 1524.5 nm to 1531.5 nm and keeps a fixed distance of 2.87 THz from the signal. BS-FWM is then a follower of the signal frequency, being the frequency distance between signal and idler in BS-FWM decided by the pumps frequencies. We better show this effect in Figure 5(b) where the experimental results of signal and idler carrier wavelength compare well with the energy conservation law of (1). However, in the same spectral range we observe a competition with the degenerated FWM driven by pump 1. Hereafter we will indicate this effect as modulation instability (MI) independently from the presence or absence of parametric gain. Note that we work with very low dispersion values and one of these sidebands is seeded by the input signal itself. Differently from BS-FWM, the sidebands of MI-FWM follow a symmetry law around the pump. Such symmetry in spectrum is very well known and can be understood again from the energy conservation law that reads as $\omega_I = 2\omega_{P1} - \omega_S$. If we assume that the angular frequency of signal is detuned from that of a pump P1 as $\omega_S = \omega_{P1} - \Omega$, then it turns out that $\omega_I = \omega_{P1} + \Omega$.

Therefore if we keep fixed the spectral position of pumps and we gradually reduce the angular frequency ω_S (i.e., we increase the signal wavelength) we can observe two opposite behaviors: the angular frequency ω_I of degenerated FWM will increase whereas that of BS-FWM will decrease. In our experiment this fact leads even to a superposition of the two idlers at 1528.75 nm, when the signal is tuned precisely at $\lambda_S = 1551.42$ nm. This crossing effect upon signal wavelength

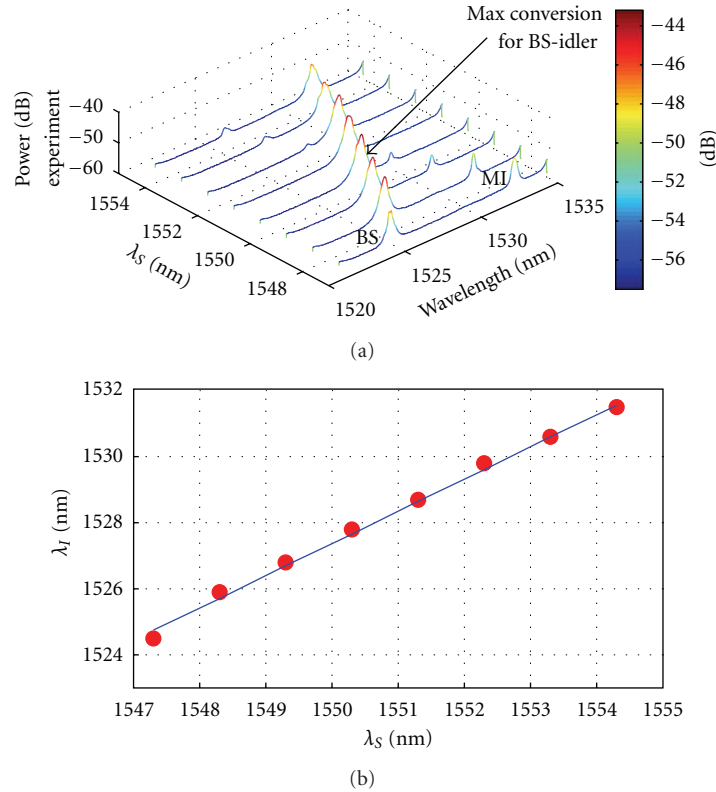


FIGURE 5: (a) Collection of experimental spectra upon different input signal wavelengths; (b) BS-FWM idler wavelength upon signal wavelength; dots: experimental results; solid line: equation (1).

is also shown in Figure 5(a). The coexistence of these two parametric processes and their tiny frequency separation should be then considered carefully in applications. Note that pump 1 is very close to the ZDW and a selection rule of parametric processes, based on phase mismatch may become less effective in practice.

As we show in Figure 6(a), we obtained in our experiment 16 dB from the background noise level at the idler central wavelength for the case of maximally efficient BS-FWM. Note that in our spectral measurements we set to 1 kHz the video bandwidth digital filter of the optical spectrum analyzer. The maximum conversion is found for a signal at 1550.3 nm. The discrepancy from phase matching (1549.8 nm) may be due to uncertainties in the dispersion parameters of the fiber and to the fluctuation in ZDW along the beam propagation in the fiber [5], as we have already mentioned. We obtained a depletion of the signal of about 1 dB and a ratio between the spectral peak of the idler and that of the signal of the signal of -20 dB: this result is much lower than that reported in [5] for the case of coherent pumps with direct phase modulation. This is mainly due to the difference in fiber parameters and choice of wavelengths. Additionally note that the experiments show that the idler is spectrally broadened as it comes from a combination of broadband pumps and a narrowband signal [6]. In the experiments we estimated the 3 dB bandwidths of pumps as 20 GHz and 44 GHz for IFSL 1 and 2, respectively, (our spectrum analyzer has a minimum

resolution of 0.05 nm which correspond to 6.24 GHz at these wavelengths). We experimentally obtained a 57 GHz wide BS-idler at 1527.8 nm and for a signal wavelength $\lambda_s = 1550.3$ nm.

Note that in our experiment we can shift the signal within the relatively wide spectral range and still obtain efficient BS-idler generation (see Figure 5(b)). This effect may be potentially applicable for the simultaneous conversion of a large spectrum. In our case, the conversion efficiency BS-FWM varies by less than 3 dB when the signal is tuned by 9 nm.

Let us now report on the case of the two external sidebands (see a and b in Figure 6(b)). By using the word “spontaneous” in the label, we mean that these sidebands are directly generated by the two pumps and they do not require a third signal to appear. Their spectral position is entirely due to the spectral positions of pumps: with respect to pump 1 (pump 2), sideband a (b) is at the same frequency detuning of pump 2 (pump 1). Because of the low dispersion of the fiber and relatively high intensity of pumps, sidebands a and b have large amplitudes. Note that the amplitude of the left-side spontaneous FWM idler (see a in Figure 6(b)) is larger than that of the right-side one (see b in Figure 6(b)). There are also some additional frequency conversion effects. Since their appearance is strongly connected to the fine adjustment of the working points of IFSLs, we report our best observation in Figure 7. More specifically we observed the signature of MI-FWM around pump 2 and PC-FWM.

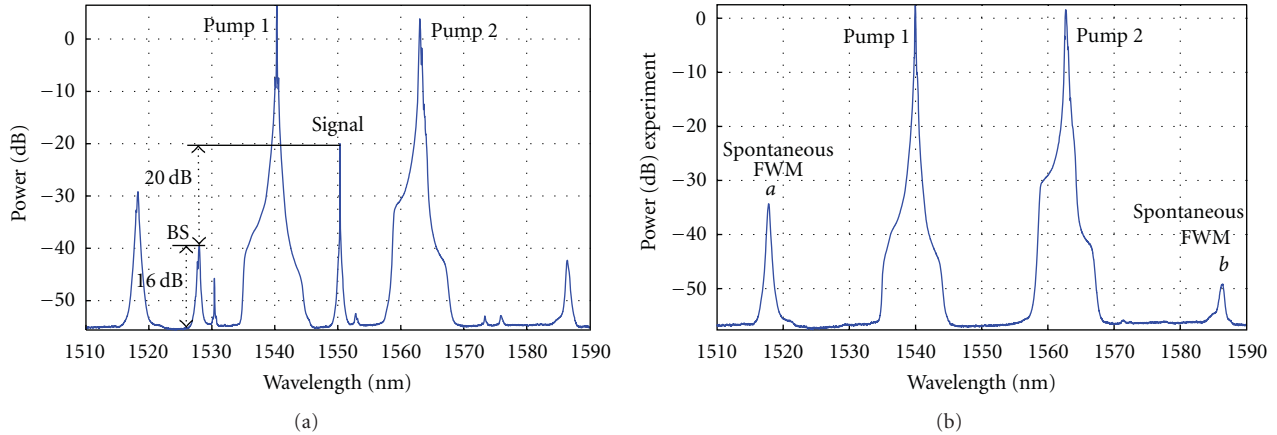


FIGURE 6: (a) experimental output spectrum obtained for the signal wavelength at 1550.3 nm: maximal conversion of BS-FWM; phase-matching conditions for BS-FWM. (b) experimental output with two pumps only.

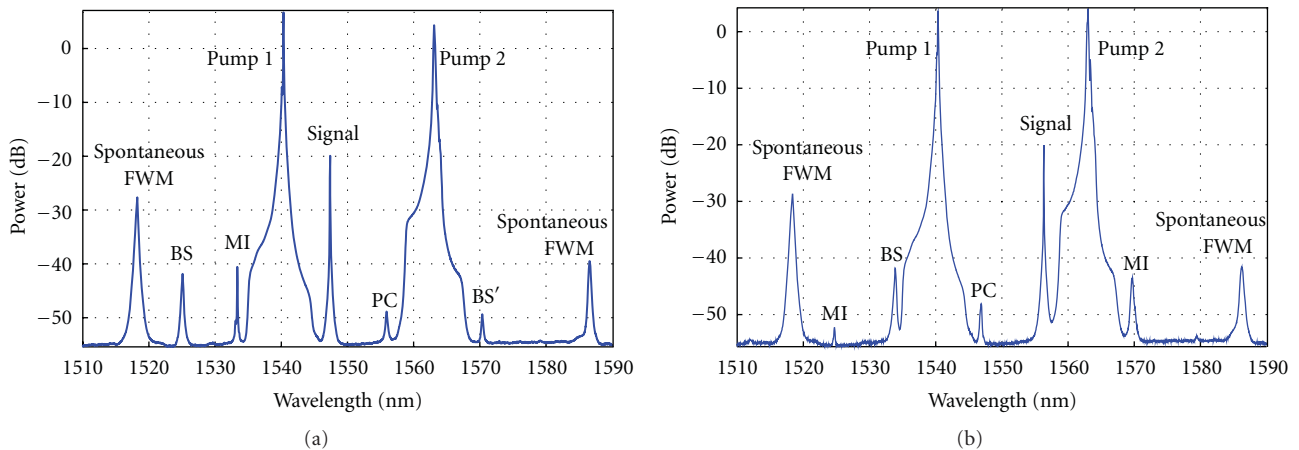


FIGURE 7: Experimental output spectrum obtained for signal wavelength at 1547.3 nm (a) and 1556.3 nm (b); existence of multiple simultaneous FWM processes.

We also observed another kind of BS-FWM that comes from the subtraction instead of the sum of the beating frequency of 2.87 THz (BS'). The conversion efficiencies of these last processes remain low, probably due to the large phase mismatch. We show in Figure 7 two output spectra taken with a signal at 1547.3 nm (a) and 1556.3 nm (b).

5. Conclusion

In this paper, we studied BS-FWM in HNLF with a novel cost-effective and partially coherent pumping scheme. We experimentally demonstrated efficient and tunable BS-FWM despite the large bandwidth of the pumps and their complete statistical independence. The spectral peak of the converted BS-FWM is 20 dB below that of the original signal and 16 dB above the background noise level. We noted coexistence of multiple independent FWM processes. In particular, we observed a relevant competition BS-FWM and MI-FWM. Our measurements agree well with a theoretical analysis based on the phase-matching diagram for the case of monochromatic waves. In conclusion, nonlinear fiber optics

frequency converters based on broadband pumps appear to be promising for their implementation in all-optical signal processing devices.

Acknowledgments

The authors acknowledge the financial support from the Region Limousin and from the French National Research Agency under Grant ANR-08-JCJC-0122 PARADHOQS. They thank Alain Dextet for his assistance in manufacturing some of the mechanical parts used in the experiment.

References

- [1] C. J. McKinstrie, S. Radic, and A. R. Chraplyvy, "Parametric amplifiers driven by two pump waves," *IEEE Journal on Selected Topics in Quantum Electronics*, vol. 8, no. 3, pp. 538–547, 2002.
- [2] R. Slavik, F. Parmigiani, J. Kakande et al., "All-optical phase and amplitude regenerator for next-generation telecommunications systems," *Nature Photonics*, vol. 4, no. 10, pp. 690–695, 2010.

- [3] J. Hansryd, P. A. Andrekson, M. Westlund, J. Li, and P. O. Hedekvist, "Fiber-based optical parametric amplifiers and their applications," *IEEE Journal on Selected Topics in Quantum Electronics*, vol. 8, no. 3, pp. 506–520, 2002.
- [4] D. Méchin, R. Provo, J. D. Harvey, and C. J. McKinstrie, "180-nm wavelength conversion based on Bragg scattering in an optical fiber," *Optics Express*, vol. 14, no. 20, pp. 8995–8999, 2006.
- [5] R. Provo, S. Murdoch, J. D. Harvey, and D. Méchin, "Bragg scattering in a positive β_4 fiber," *Optics Letters*, vol. 35, no. 22, pp. 3730–3732, 2010.
- [6] Y. Yan and C. Yang, "Four-wave mixing between coherent signal and incoherent pump light in nonlinear fiber," *Journal of Lightwave Technology*, vol. 27, no. 22, pp. 4954–4959, 2009.
- [7] D. Nodop, D. Schimpf, J. Limpert, and A. Tünnermann, "SBS suppression in high power fiber pulse amplifiers employing a superluminescence diode as seed source," in *Proceedings of the Conference on Lasers and Electro-Optics (CLEO EUROPE '11)*, Munich, Germany, May 2011, paper CJ7.6 THU.
- [8] A. H. Gnauck, R. M. Jopson, C. J. McKinstrie, J. C. Centanni, and S. Radic, "Demonstration of low-noise frequency conversion by Bragg Scattering in a Fiber," *Optics Express*, vol. 14, no. 20, pp. 8989–8994, 2006.
- [9] S. Radic, R. M. Jopson, A. Gnauck, C. J. McKinstrie, J. C. Centanni, and A. R. Chaplyvy, "Stimulated-brillouin-scattering suppression using a single modulator in two-pump parametric architectures," in *Proceedings of the Optical Fiber Communication Conference (OFC '05)*, Anaheim, Calif, USA, March 2005, paper OWN5.
- [10] J. Schröder, A. Boucon, S. Coen, and T. Sylvestre, "Interplay of four-wave mixing processes with a mixed coherent-incoherent pump," *Optics Express*, vol. 18, no. 25, pp. 25833–25838, 2010.
- [11] H. J. McGuinness, M. G. Raymer, C. J. McKinstrie, and S. Radic, "Quantum frequency translation of single-photon states in a photonic crystal fiber," *Physical Review Letters*, vol. 105, no. 11, Article ID 093604, 2010.
- [12] Y. Yan and Y. Changxi, "Coherent light wave generated from incoherent pump light in nonlinear kerr medium," *Journal of the Optical Society of America B*, vol. 26, no. 11, pp. 2059–2063, 2009.
- [13] H. G. Chatellus and J.-P. Pique, "Coherence properties of modeless lasers," in *Proceedings of the Science, Quantum of Quasars Workshop*, Grenoble, France, December 2009.
- [14] L. P. Yatsenko, B. W. Shore, and K. Bergmann, "Coherence in the output spectrum of frequency shifted feedback lasers," *Optics Communications*, vol. 282, no. 2, pp. 300–309, 2009.
- [15] L. P. Yatsenko, B. W. Shore, and K. Bergmann, "An intuitive picture of the physics underlying optical ranging using frequency shifted feedback lasers seeded by a phase-modulated field," *Optics Communications*, vol. 282, no. 11, pp. 2212–2216, 2009.
- [16] P. A. Champert, V. Couderc, and A. Barthélémy, "1.5–2.0- μm multiwatt continuum generation in dispersion-shifted fiber by use of high-power continuous-wave fiber source," *IEEE Photonics Technology Letters*, vol. 16, no. 11, pp. 2445–2447, 2004.
- [17] K. Nakamura, T. Miyahara, and H. Ito, "Observation of a highly phase-correlated chirped frequency comb output from a frequency-shifted feedback laser," *Applied Physics Letters*, vol. 72, no. 21, pp. 2631–2633, 1998.
- [18] M. Stellpflug, G. Bonnet, B. W. Shore, and K. Bergmann, "Dynamics of frequency shifted feedback lasers: Simulation studies," *Optics Express*, vol. 11, no. 17, pp. 2060–2080, 2003.
- [19] B. Auguié, A. Mussot, A. Boucon, E. Lantz, and T. Sylvestre, "Ultralow chromatic dispersion measurement of optical fibers with a tunable fiber laser," *IEEE Photonics Technology Letters*, vol. 18, no. 17, pp. 1825–1827, 2006.

Research Article

Multiple-Pulse Operation and Bound States of Solitons in Passive Mode-Locked Fiber Lasers

A. Komarov,¹ F. Amrani,² A. Dmitriev,¹ K. Komarov,³ D. Meshcheriakov,^{1,3} and F. Sanchez²

¹ Department of Laser Systems, Novosibirsk State Technical University, 630092 Novosibirsk, Russia

² Laboratoire de Photonique d'Angers EA 4644, Université d'Angers, 49000 Angers, France

³ Institute of Automation and Electrometry, Russian Academy of Sciences, 630090 Novosibirsk, Russia

Correspondence should be addressed to A. Komarov, andnsk@iae.nsk.su

Received 3 May 2011; Accepted 25 July 2011

Academic Editor: Sonia Boscolo

Copyright © 2012 A. Komarov et al. This is an open access article distributed under the Creative Commons Attribution License, which permits unrestricted use, distribution, and reproduction in any medium, provided the original work is properly cited.

We present results of our research on a multiple-pulse operation of passive mode-locked fiber lasers. The research has been performed on basis of numerical simulation. Multihysteresis dependence of both an intracavity energy and peak intensities of intracavity ultrashort pulses on pump power is found. It is shown that the change of a number of ultrashort pulses in a laser cavity can be realized by hard as well as soft regimes of an excitation and an annihilation of new solitons. Bound steady states of interacting solitons are studied for various mechanisms of nonlinear losses shaping ultrashort pulses. Possibility of coding of information on basis of soliton trains with various bonds between neighboring pulses is discussed. The role of dispersive wave emitted by solitons because of lumped intracavity elements in a formation of powerful soliton wings is analyzed. It is found that such powerful wings result in large bounding energies of interacting solitons in steady states. Various problems of a soliton interaction in passive mode-locked fiber lasers are discussed.

1. Introduction

Lasers generating ultrashort optical pulses are widely employed in diversified areas of science, technology, and engineering [1–7]. Applications of such lasers range from testing of ultrahigh speed semiconductor devices to precision processing of materials, from triggering of tracing chemical reactions to sophisticated surgical applications in medicine. These lasers are used for study of ultrahigh speed processes in atomic and molecular physics, in solid-state physics, and in chemistry and biology. They are employed for investigation of light-matter interactions under ultrahigh intensity levels. Lasers of ultrashort optical pulse with a high repetition rate are a key element in high-speed optical communications. Ultrashort pulse lasers are extensively used for micromachining, biomedical diagnostic, in light detection, and ranging (lidar) systems, and so forth.

The great diversity of applications of ultrashort pulse lasers calls for further development and perfection of this type of quantum generators. At the present time, one of main ways for creation of perfect ultrashort pulse sources is related

to passive mode-locked fiber lasers [8–16]. Nonlinear losses forming ultrashort pulses in fiber lasers are usually realized by the nonlinear polarization rotation technique. These lasers have unique potentialities. They are reliable, compact, flexible, and of low cost. Such generators can be conveniently pumped with commercially available semiconductor lasers. The nonlinear losses based on the nonlinear polarization rotation technique are fast, practically inertia-free. For them, the depth of the modulation and the saturating intensity are easily controlled through the orientation angles of intracavity phase plates. The great variety of operating regimes is an important feature of this type of lasers. Indeed, these lasers have demonstrated bistability between continuous wave and mode-locking regimes, spike operation, and Q-switching [17, 18]. They can operate either with a single pulse in the laser cavity or in a multiple-pulse regime. The latter is connected with the effect of a quantization of intracavity lasing radiation into individual identical solitons [17–21]. Lasers operating in multiple-pulse regimes demonstrate multistability: the number of pulses in an established operation depends on initial conditions [17, 20].

The dependence of the number of pulses on pumping and on orientation angles exhibits hysteresis phenomena [22]. Analogical regimes are realized in lasers with another mechanisms of nonlinear losses (semiconductor saturable absorber mirror (SESAM), saturable absorbers based on quantum dots, carbon nanotubes, graphene, and so on [23–25]).

The type of a soliton interaction plays a crucial role in the established multiple-pulse regimes of fiber lasers [26–30]. In the case of pulse attraction, bound solitons structures can be formed. Such structures were theoretically and experimentally investigated by many authors [11, 13, 16, 26, 28, 30–32]. Possibility of a realization of strong bonds between solitons ($\sim 10\%$ of an individual soliton energy) was found in the paper [33]. As this takes place, steady states of pair interacting solitons form a two-soliton molecule with a set of energy levels corresponding to various types of bonds between pulses. With a use of this effect, the high-stable noise-proof information sequences of bound solitons can be realized. In such sequences, a high-density coding of the information is realized through various distributions of different energy bonds along the soliton chains.

A long-distance mechanism of repulsion of ultrasort pulses results in the regime of harmonic passive mode-locking [34–37] (the regime of a multiple-pulse generation in which distances between all neighboring pulses take the same value). The harmonic passive mode-locked fiber lasers are of great interest as ultrashort optical pulse sources with a high repetition rate which are employed in high-speed optical communications. This lasing regime can be also realized on basis of a sequence of bound solitons with a single type of a bond between neighboring pulses which fills completely a total laser resonator. In this case, the expected rate of repetition of ultrashort pulses in the output laser radiation is of the order of inverse ultrashort pulse duration and can lay in the terahertz frequency range for subpicosecond pulses [38, 39].

A quantization of intracavity radiation into individual identical solitons is a useful phenomenon for a creation of ultrashort pulse generators with a high rate of a repetition of ultrashort pulses. The greater number of pulses in laser cavity results in the greater rate of the repetition of pulses in output radiation. However, this phenomenon is a serious obstacle for creation of generators with high energy of individual pulses. Really, in consequence of this phenomenon, an increase of pumping results in an increase in number of pulses in the laser resonator, thus the energy of an individual pulse remains approximately as before.

The effective control of intersoliton interactions opens new opportunities for management of generation regimes of fiber lasers. For realization of such control, it is necessary to know the properties of soliton interaction at a fundamental level. In this paper, we present our results on a formation of multiple-pulse regimes connected with interaction of lasing solitons through a gain medium, inertia-free nonlinear losses, and a nonlinear refractive index. The paper contains the original results on the multihysteresis dependence of the lasing energy characteristics (a total energy of an intracavity radiation, peak intensities of individual solitons, an amplification coefficient, etc.) on pumping, the results

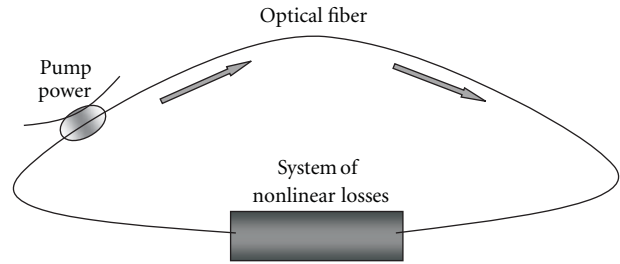


FIGURE 1: Schematic representation of the investigated ring passive mode-locked fiber laser.

on the realization of hard and soft regimes of excitation and annihilation of solitons in a laser cavity under multiple-pulse operation, and the results on an interaction of solitons through dispersive waves (these waves are emitted by solitons because of lumped elements in a laser cavity). For a completeness of a description of these phenomena, we also discuss earlier our results on the given subjects (a soliton quantization, information ultrashort pulse trains in fiber lasers with the nonlinear polarization rotation technique, etc.).

This paper is organized as follows. In Section 2, we present the results on multihysteresis phenomena due to a competition and a coexistence of solitons in a laser cavity. Section 3 is devoted to bound steady states related with the interaction of solitons through an interference of their wings in a intracavity medium with fast nonlinear losses and Kerr nonlinearity of refractive index. In Section 4, we analyze the interaction of solitons in fiber laser with lumped saturable absorber. Section 5 is devoted to mechanisms of a realization of powerful long-distance soliton wings which are connected with dispersive waves emitted by solitons because of lumped intracavity elements. Such powerful wings result in a strong intersoliton interaction with great bound energies. In Section 6, we discuss the presented results. The most important ones from them are presented in Section 7.

2. Multiple-Pulse Operation and Hysteresis Phenomena in Fiber Lasers

The laser under investigation is schematically represented in Figure 1. The system forming nonlinear losses through a nonlinear polarization rotation technique was described in detail in [20]. For isotropic fiber, it involves all necessary elements for the polarization control. In this system, a radiation passes sequentially through the first quarter wave plate, the second half wave plate, the polarizer, and the third quarter wave plate. The space orientation of the three phase plates is determined by the angles α_1 , α_2 , α_3 , respectively (α_i is an angle of one eigenaxis of a corresponding plate with respect to the passing axis of the polarizer). After the polarizing isolator, the electric field has a well-defined linear polarization. Such state of polarization does not experience polarization rotation in the fiber because the rotation angle is proportional to the area of the polarization ellipse. Consequently, it is necessary to place the third

quarter wave plate after the polarizer which transforms the linear polarization into the elliptic one. The rotation of the polarization ellipse resulting from the optical Kerr nonlinearity is proportional to the light intensity, the area of the polarization ellipse, and the fiber length. At the output of the fiber, the direction of the elliptical polarization of the central part of the pulse can be rotated towards the passing axis of the polarizer by the second half wave plate. Then, this elliptical polarization can be transformed into a linear one by the first quarter wave plate. In this situation, the losses for the central part of the pulse are minimized while the wings undergo strong losses. The evolution of the radiation in the investigated laser is described by the following set of equations [20]:

$$\frac{\partial E}{\partial \zeta} = (D_r + iD_i) \frac{\partial^2 E}{\partial \tau^2} + (G + iq|E|^2)E, \quad (1)$$

$$E_{n+1}(\tau) = -\eta[\cos(pI_n + \alpha_0) \cos(\alpha_1 - \alpha_3) + i \sin(pI_n + \alpha_0) \sin(\alpha_1 + \alpha_3)]E_n(\tau), \quad (2)$$

where $E(\zeta, \tau)$ is the electric field amplitude, τ is a time coordinate expressed in units $\delta t = \sqrt{|\beta_2|L}/2$ (here β_2 is the second-order group-velocity dispersion for fiber and L is the fiber length), ζ is the normalized propagation distance $\zeta = z/L$, D_r and D_i are the frequency dispersions for a gain-loss and for a refractive index, respectively, and q is the Kerr nonlinearity. The term G in the second parenthesis in (1) describes the saturable amplification

$$G = \frac{a}{1 + bJ}, \quad (3)$$

where $J = \int |E|^2 d\tau$ is the total energy of the intracavity radiation (the integration is carried out on the whole round-trip period), a is the pumping parameter, and b is the saturation one). The second term in these parentheses is connected with Kerr nonlinearity of the fiber. Equation (2) determines the relation between the time-distributions of the field before and after n -th pass of radiation through the polarizer (η is the transmission coefficient of the intracavity polarizer). Parameters α_0 , I , p are determined by relations $\alpha_0 = 2\alpha_2 - \alpha_1 - \alpha_3$, $I = |E|^2$, $p = \sin(2\alpha_3)/3$. The amplitude $E(\tau)$ is subject to periodic boundary conditions with period equal to one round trip.

The numerical procedure starts from the evaluation of the electric field after passing through the Kerr medium, the phase plates, and the polarizer, using (2). The resulting electric field is then used as the input field to solve (1) over a distance L , using a standard split-step Fourier algorithm. The computed output field is used as the new input for (2). This iterative procedure is repeated until a steady state is achieved. For the numerical simulations, we use typical parameters of ytterbium- and erbium-doped fiber lasers operating in the normal and anomalous dispersion regimes.

Figure 2 shows the distribution of radiation in a laser resonator $I(\tau)$ as the function of a number of passes of the field through the cavity ζ . After a transient process, the

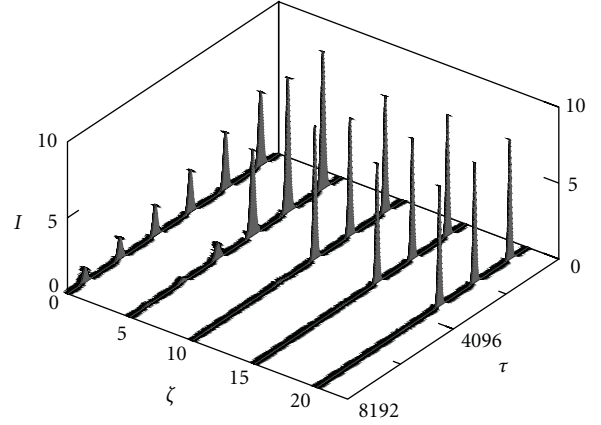


FIGURE 2: Transient evolution of the field in the fiber laser. The temporal distribution of the intracavity intensity $I(\tau)$ versus the round-trip number ζ . $a = 3$, $b = 0.017$, $q = 1$, $D_i = -1$, $D_r = D_{r0}G$, $D_{r0} = 0.34$, $\alpha_0 = -1.1$, $\alpha_3 = -\alpha_1 = 0.2$.

stationary operation with identical pulses is realized. The difference in the peak intensities of initial pulses models a random spread in amplitudes of pulses of an initial noise radiation. Figure 3 demonstrates the number of identical pulses in a laser cavity in the established stationary operation as the function of pumping a . With changing pump a the pulses are created and annihilated one by one. The corresponding changes in the intracavity radiation energy J , in the peak intensity of intracavity identical pulses I_0 , and in the amplification G are shown in Figures 4, 5, and 6, respectively. The vertical arrows in these figures are connected to a change of a number of pulses N in the laser resonator that is due to a change of pumping a (see Figure 3). From the dependences $I_0 = I_0(a)$ and $G = G(a)$ (see Figures 5 and 6), we obtain the dependence $G = G(I_0)$. The total amplification of a steady-state pulse consists of two parts. The first part is due to the gain $G(I_0)$. The second part Λ is due to nonlinear losses and a dispersion of intracavity elements. In stationary regime, the total amplification is equal to zero, that is $\Lambda = -G(I_0)$. The dependence of nonlinear-dispersion part Λ of the total amplification coefficient for an individual soliton as the function of its peak intensity I_0 is presented in Figure 7. This dependence is a key factor determining a competition and a coexistence of solitons in an established stationary regime. In the interval $I_0 < I_{cr2}$, the dependence $\Lambda = \Lambda(I_0)$ is monotonously increasing. Here, the pulse with a greater peak intensity I_0 has a greater amplification Λ . As a result of the soliton competition, no multiple-pulse regimes is realized. After a transient process, the generation with single soliton in a laser cavity is established. In the interval $I_{cr2} < I_0 < I_{cr1}$, a multiple-pulse generation is possible. Here, the pulse with a greater peak intensity I_0 has a less amplification Λ . As a result, after transient process, all pulses in a laser cavity have the same peak intensity I_0 and the same other parameters (a duration, an energy, a chirp, and so on). It is, so-called, the effect of quantization of a laser radiation on identical solitons. When, with decreasing pump a , the peak intensity of identical pulses I_0 reaches the value I_{cr2}

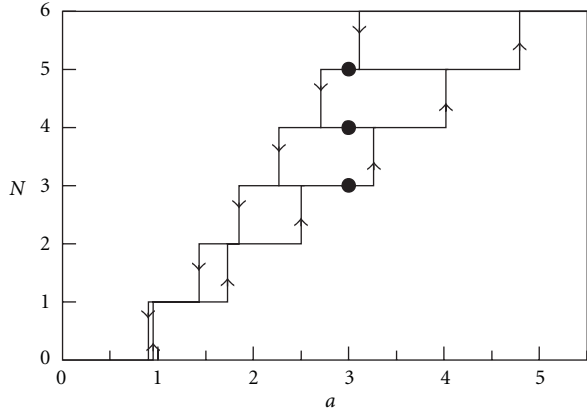


FIGURE 3: Multihysteresis dependence of the number of pulses N in established stationary operation on pumping a .

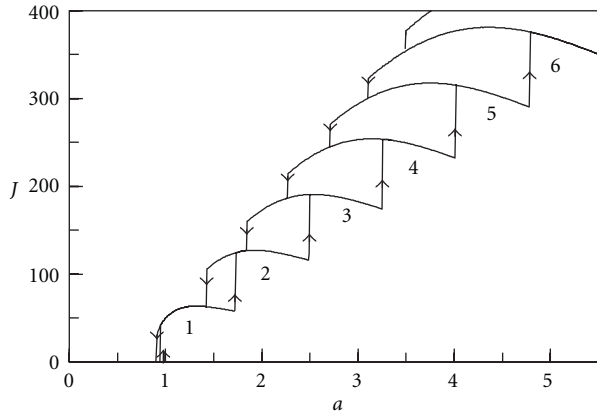


FIGURE 4: Dependence of the intracavity radiation energy J in established operation on pumping a . Digits indicate a number of pulses in a laser cavity for a corresponding branch.

the pulses disappear one by one as one can see in Figure 3 (the left step dependence $N = N(a)$). To the contrary, when, with increasing pump, the peak intensity of identical pulses reaches the value I_{cr1} , new pulses appear in the cavity one by one (the right step dependence in Figure 3). They are formed from weak seed pulses of a radiation noise. As a rule, the solitons appear and disappear by a threshold way (hard excitation and annihilation of the solitons [40]). That is, a peak intensity of each soliton is changed by a jump from 0 to I_0 and from I_0 to 0 (see Figure 5). However, the soft regime of excitation and annihilation of solitons [40] (a continuous change of the peak intensity with continuously changing pump a) is also possible. Figure 8 demonstrates the examples of the two types of changes in the second pulse (the first pulse already exists in the laser resonator). The corresponding dependences $\Lambda = \Lambda(I_0)$ are presented in Figure 9. The soft excitation and annihilation of pulses are realized if the slope of the decreasing part of the dependence $\Lambda = \Lambda(I_0)$ is greater than the slope of the increasing one.

It should be pointed out that the dependence $\Lambda = \Lambda(I_0)$ determines the phase relations of interacting solitons in bound steady states: for peak intensities in the vicinity of top

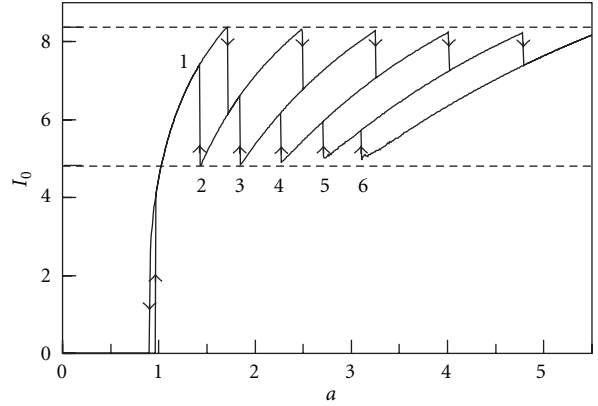


FIGURE 5: Dependence of the peak intensity I_0 of intracavity identical pulses in established operation on pumping a .

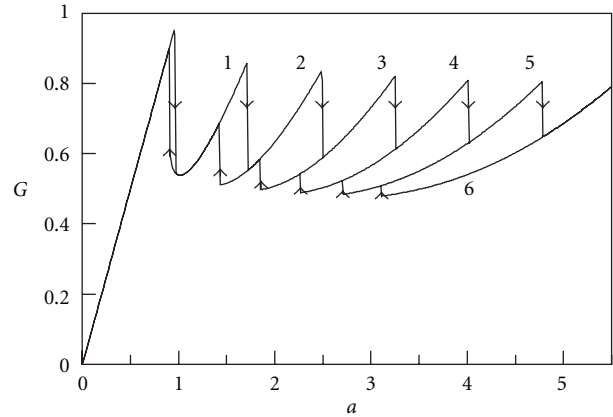


FIGURE 6: Dependence of the gain G on pumping a .

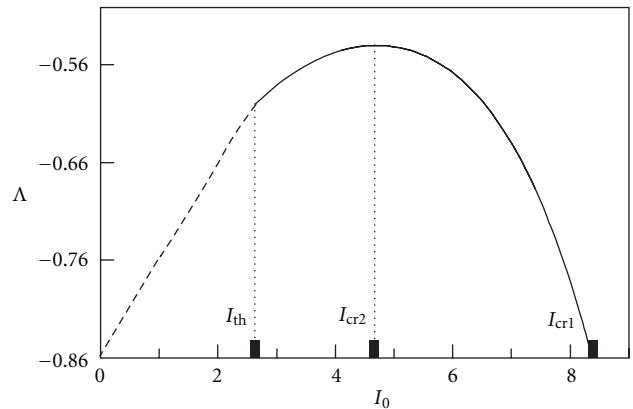


FIGURE 7: Dependence of the nonlinear-dispersion part of amplification for intracavity pulses Λ on their peak intensity I_0 . The fragment of an unstable single-pulse generation is shown as a dashed line. The value I_{cr2} corresponds maximum $\Lambda = \Lambda(I_0)$. $\Lambda(I_{cr1}) = \Lambda(0)$.

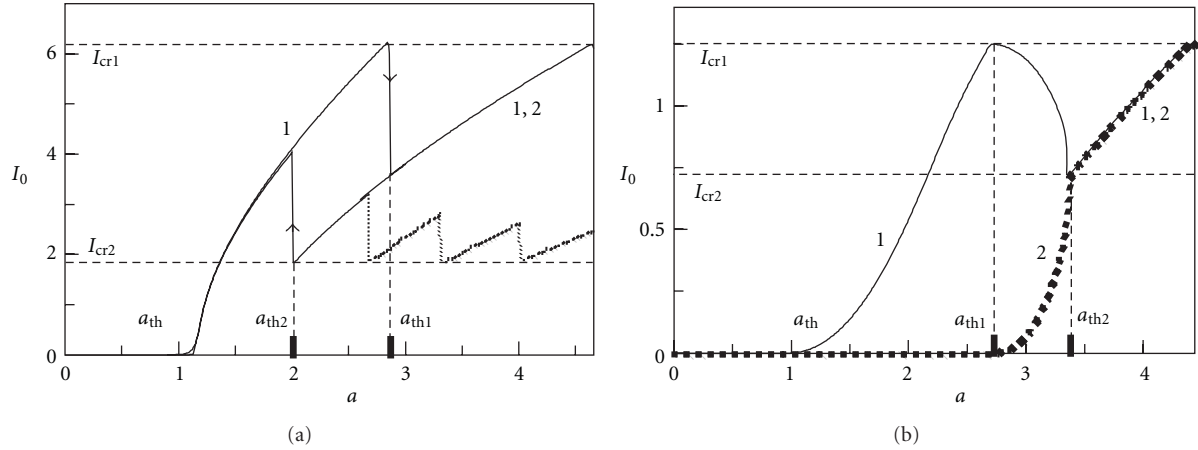


FIGURE 8: Dependences of the peak intensities I_0 for two intracavity pulses in established operation on pumping a for hard (a) and soft (b) regimes of excitation and annihilation of the second soliton. The dependences $I_0 = I_0(a)$ for first and second pulses are denoted by digits 1 and 2, respectively.

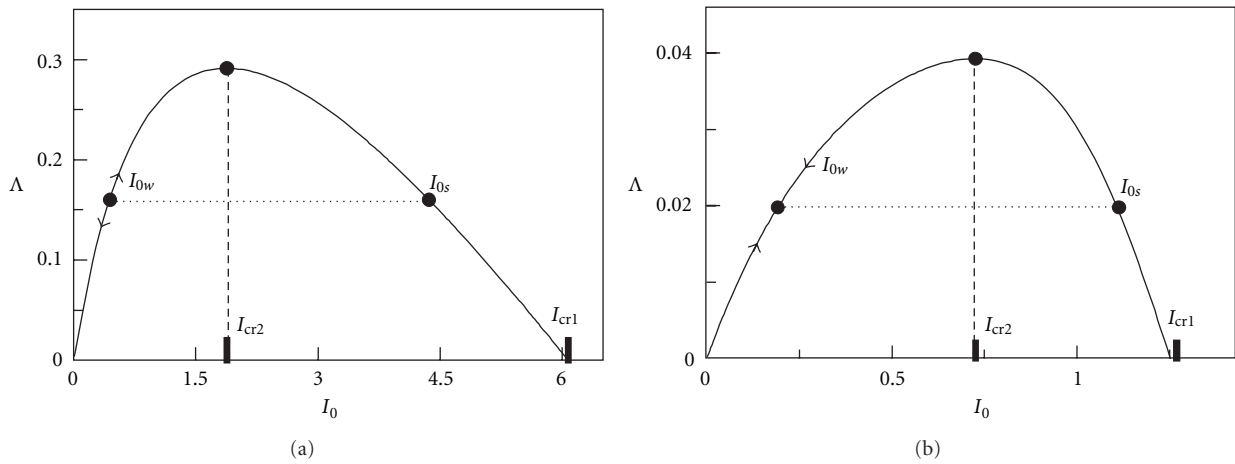


FIGURE 9: Dependences of the nonlinear-dispersion part of amplification Δ for intracavity pulses on their peak intensity I_0 for hard (a) and soft (b) regimes of excitation and annihilation of the second soliton.

of this dependence, as a rule, the phase difference is close to $\pi/2$, whereas far from the top (the decreasing part of the dependence), as a rule, the phase difference is close to 0 or π (see Section 3).

3. Bound Steady States of Interacting Solitons

In the previous section, we have studied phenomena which are related with the interaction of solitons through the gain medium in a condition of fast nonlinear losses and Kerr nonlinearity of refractive index. For these phenomena, the interaction of solitons due to an interference of their wings is insignificant (if the distances between pulses is sufficiently large, then the interference effects are weak). In this section, we study the soliton interaction which is due to an interference of their wings in conditions of the fast complex nonlinearity of intracavity elements.

3.1. Steady States of Pair Bound Solitons. In this section, for our numerical simulation, we have used typical parameters

of Er-doped fiber laser with anomalous net dispersion of group velocity. Figure 10 demonstrates the temporal and spectral profiles of a single soliton. Figure 10(a) shows also the change in a phase along the pulse. The soliton has powerful wings which result in large energy bounding pair interacting solitons.

Because of the interaction between solitons, the pair of such solitons is united in the stability formation with a large binding energy—highly-stable “two soliton molecule.” The radiation energy of such molecule is less than the energy of two solitons placed from each other on a long distance. The binding energy for two solitons in this molecule takes the discrete set of values shown on Figure 11. Large binding energies for the low-energy steady states are due to powerful wings of solitons. These steady states are stable.

For the ground steady-state (the first energy level) and for the all odd levels, the field functions are antisymmetric $E_k(\tau) = -E_k(-\tau)$ if the origin of the coordinate $\tau = 0$ corresponds to the point equally spaced from the peaks of the solitons. In this case, the peaks amplitudes of two

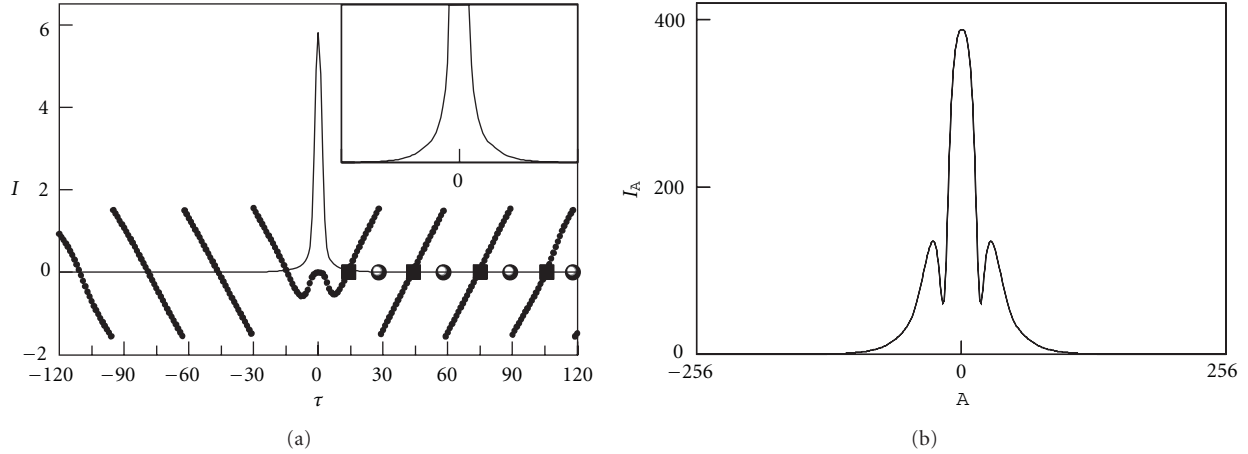


FIGURE 10: Temporal (a) and spectral (b) distributions of radiation for the single-soliton passive mode-locking. The upper right inset in (a) shows the multiplied soliton pedestal. The change of the phase along the pulse is presented in (a). All phase magnitudes are reduced to the interval $(-\pi, +\pi)$. In the point of the pulse with a maximum amplitude, the phase is equal to zero. The black squares and circles correspond to the points of the pulse where its phase is equal to π and 0, correspondingly.

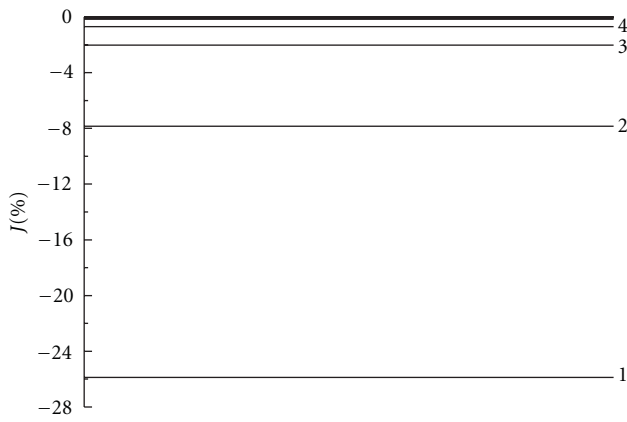


FIGURE 11: Binding energy of two solitons in stable steady states J expressed in relative units (the binding energy divided by the energy of a single soliton). The laser parameters are the same as in the case of Figure 10.

solitons are in opposite phase ($\delta\varphi \approx \pi$). For all even steady states, the field functions are symmetric $E_k(\tau) = E_k(-\tau)$ and the peak amplitudes of two solitons have the same phase ($\delta\varphi \approx 0$). Figures 12(a), 12(b), and 12(c) show the temporal distributions of intensities in the two-soliton molecule for the cases of the ground steady state (the minimal distance d_1 between solitons) and for the first and second excited steady-states (the distances between solitons approximately equals the double and triple minimal one d_1 , resp.). In the cases of the ground ($k = 1$) and second excited ($k = 3$) states, the intensity is equal to zero in the center point between solitons. For the first excited state $k = 2$, the intensity in this point is distinct from zero. Figures 12(d), 12(e), and 12(f) show the spectral profiles of the two-soliton molecule. They are symmetric. For odd states, the center spectral component is equal to zero. For even states, it is maximum. For used laser parameters, as indicated above, all steady states of the

pair interacting solitons are stable. That is, the two soliton molecule is multistable.

In the bound steady states, the second soliton in the two soliton molecule is arranged in the space point where the first soliton has the phase equal to 0 or π (see Figure 10(a)). Under such arrangement, the peak amplitude of one pulse and the wing amplitude of other pulse have the opposite-phase interference. For such interference, the peak intensities of the pulses are decreased and their amplification coefficients become larger (see the dependence $\Lambda = \Lambda(I_0)$ for $I_0 > I_{cr2}$ presented in Figures 7 and 9). We have also obtained the phase difference for the pair pulses equal to $\pi/2$. In this case, the peak intensity was in vicinity of the maximum of the dependence $\Lambda = \Lambda(I_0)$ (I_0 is close to I_{cr2}). As this takes place, for one pulse, the opposite-phase interference is realized, for the other, the in-phase one is done [33].

3.2. Information Sequences of Bound Solitons. One of the usual way of coding the information for its transfer through optical communication fiber lines consists in the following. In equidistant initial sequences of pulses, some pulses are removed. It arises two positions (a pulse is present, and a pulse is absent) which are required for the coding of the information in binary system (zero and unit). Displacement and merge of pulses in such information pulse sequences, that is due to various types of technical perturbations including noise radiation, results in loss of the informations. There are various ways of increase of a tolerance to these perturbations. Among them, there is an increase in distance between the neighboring pulses in initial pulse sequence. However, this way results in the decrease in the speed of a transfer of information. In this section, we consider the nonlinear regime of propagation of pulse information sequences. The interaction of neighboring pulses results in the stabilization of this sequence. Because various types of bonds between neighboring pulses can be realized, accordingly, the coding of the information in such sequences can

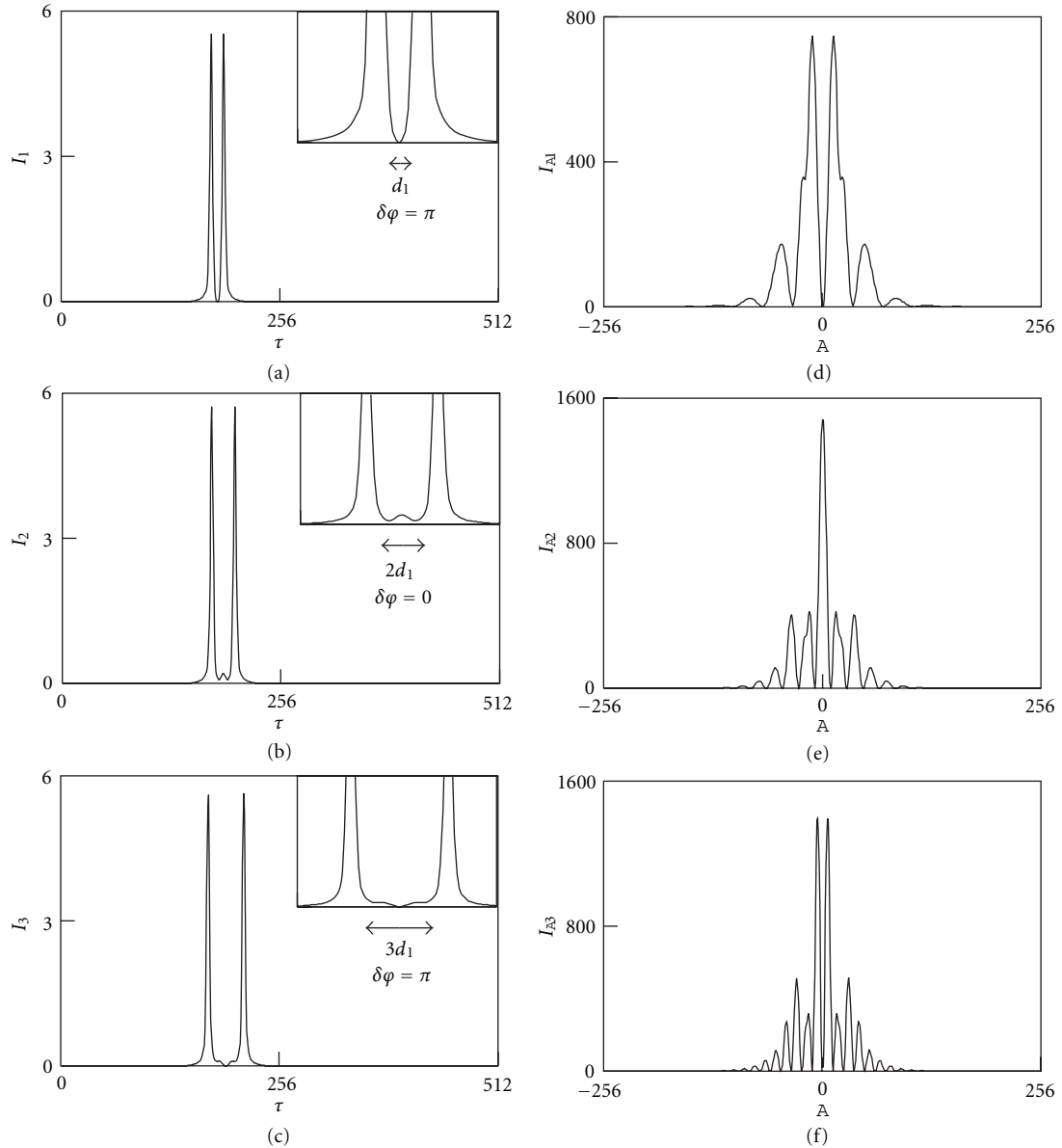


FIGURE 12: Temporal and spectral distributions of intensity of the two-soliton molecule (a), (d) for the ground steady state (minimal distance d_1 between solitons), (b), (e) for the first excited steady state, and (c), (f) for the second excited steady state. All steady states are stable. The laser parameters are the same as in the case of Figure 10.

be realized through various distributions of types of bonds between neighboring pulses along a soliton train. Thanks to powerful wings, the binding energy for such solitons appears high, that provides the high degree of tolerance against various perturbations in the case of such sequences. Dense packing of pulses in such sequence provides high speed of transfer information. Due to large binding energies, such multisoliton molecules are highly stable and noise-proof. Placing several initial pulses on certain distances from each other, after transient process, we have obtained stationary “molecular chains” with any desirable distribution of types of bonds between neighboring solitons along a pulse train. Such sequence is realized more simply with a use of the ground and first excited types of intersoliton bonds for which the

binding energies are especially great. Figure 13 shows such information soliton sequence in which the number 28062010 is coded in binary system (28.06.2010 is the data of the Second International Conference: Nonlinear Waves-Theory and Application [41]). Here, the ground type of a bond (smaller distance between pulses) corresponds to unit, and the first excited type of a bond (the greater distance between pulses) corresponds to zero. In binary system, this sequence corresponds to the number 1101011000011000100111010, that in decimal system is the number 28062010. Really, $1 \cdot 2^{24} + 1 \cdot 2^{23} + 0 \cdot 2^{22} + \dots + 1 \cdot 2^1 + 0 \cdot 2^0 = 28062010$.

Such soliton trains are highly stable formations. The high stability is primarily due to large binding energies. Furthermore, there exists a second reason of the high stability.

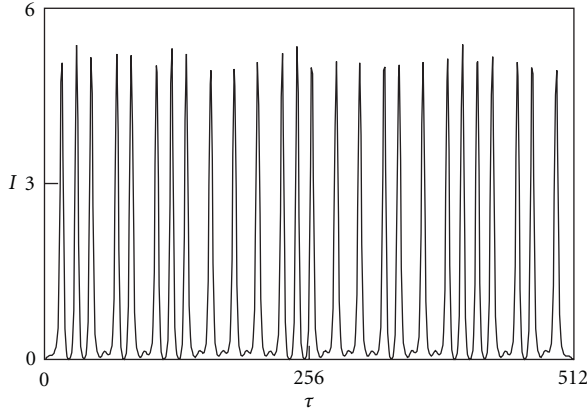


FIGURE 13: Stable molecule chain of bound solitons with the ground and first excited types of bonds in which the number 28062010 is coded in binary system 1101011000011000100111010. The greater distance between pulses corresponds to zero. The smaller distance between pulses does to unit. The laser parameters are the same as in the case of Figure 10.

It consists in the following. The perturbation energy which was initially localized in the vicinity of some pair of bound solitons is quickly collectivized among all solitons of the train. In the numerical simulation, we have used the random radiation noise to prove this stability. This noise induces up to 10% fluctuations of peak intensities of solitons but does not change the structure of soliton sequences.

4. Steady States of Interacting Solitons in Fiber Lasers with Lumped Saturable Absorber

In the previous sections, we have studied steady states of interacting solitons in passive mode-locking fiber lasers with a nonlinear polarization rotation technique. In this section, we investigate another type of nonlinear losses when passive mode-locking is realized thanks to a saturable absorber. The role of such nonlinear absorber can be played by various materials: carbon nanotubes, graphene, saturable absorbers based on quantum dots, and so on [23–25]. In this case, (2) is replaced by the following one:

$$E_{n+1}(\tau) = E_n(\tau) \exp\left(-\frac{s_{nl}}{1 + p|E_n(\tau)|^2}\right). \quad (4)$$

This equation describes the change in the field under its pass through the lumped saturating absorber, where s_{nl} is the losses for a weak field and p is the parameter of a saturation. We have studied the formation of bound states of interacting solitons and obtained analogical results as for the case of nonlinear losses due to the nonlinear polarization rotation technique. Figure 14 shows the distances between two interacting solitons in stable steady states. One can see an alternation of odd and even states as in Figures 11 and 12 in the case of nonlinear losses due to the polarization rotation technique. Here, powerful soliton wings are also realized. These powerful wings result in large bound energies of interacting pulses. For both cases of a realization of nonlinear

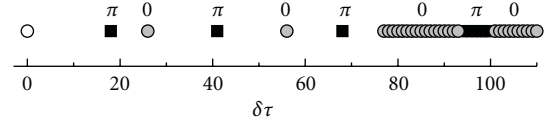


FIGURE 14: Steady-state distances between two solitons interacting through a lumped saturable absorber. The white circle corresponds to the first soliton. The black squares and grey circles do to the steady-state second soliton with the phase differences π and 0, respectively. $a = 0.5$, $D_r = 0.01$, $D_i = 0.1$, $q = 1.5$, $p = 1$, $s_{nl} = 1$.

losses, we have used sufficiently close nonlinear-dispersion parameters of the investigated laser systems.

5. About Mechanism of Formation of Powerful Soliton Wings

Large bounding energies of interacting solitons are due to their powerful wings. In this section, we analyze reasons resulting in such wings. Figure 10(b) demonstrates the additional structure on the bell-shaped spectral profile of a single soliton which has the spectrum sideband form. Sideband generation in soliton spectrum is a well-known phenomenon. The sidebands result from an interference between the soliton and dispersive waves. Such dispersive waves are emitted by a soliton when it circulates in a laser resonator and periodically experiences perturbations caused by the lumped intracavity components. The interference of such wave during several circulations forms the powerful long-distance wings of solitons. This mechanism does not work in the case of a continuously distributed intracavity nonlinear-dispersion medium. In this section, we check the hypothesis about a formation of powerful soliton wings at the expense of dispersive waves.

5.1. Model of a Continuously Distributed Intracavity Nonlinear-Dispersion Medium. In the case of a continuously distributed intracavity nonlinear-dispersion medium the evolution of radiation in a laser cavity is described by the following equation [42]:

$$\frac{\partial E}{\partial \zeta} = (D_r + iD_i) \frac{\partial^2 E}{\partial \tau^2} + \left(G - \sigma - \frac{\sigma_{nl}}{1 + p|E|^2} + iq|E|^2 \right) E, \quad (5)$$

where σ is linear losses, G is a saturable amplification (see (3)), and the term $\sigma_{nl}/(1 + p|E|^2)$ describes the continuously distributed variant of nonlinear losses (4). In the case of $D_i = 0$, $q = 0$, this equation transforms into the nonlinear diffusion equation [43] which describes passive mode-locking of lasers when any phase-modulation effects may be ignored. Equation (5) was obtained as the generalization of this nonlinear diffusion equation with a purpose of an analysis of effects of phase modulation of ultrashort pulses in passive mode-locked lasers. In the frame of (5), the multiple-pulse operation and the multihysteresis phenomena (see

Figure 3) were investigated in the papers [44, 45]. In the case $pI \ll 1$, (5) has the form

$$\frac{\partial E}{\partial \zeta} = (D_r + iD_i) \frac{\partial^2 E}{\partial \tau^2} + (G - \sigma_0 + (r + iq)|E|^2)E, \quad (6)$$

where $\sigma_0 = \sigma + \sigma_{nl}$ is the total linear losses, $r = p\sigma_{nl}$. It is the simplest equation taking into account a frequency dispersion of gain-losses and a refractive index, a nonlinearity of losses and a refractive index, and also a saturation of an amplification. Equation (6) describes the two lasing regimes: an operation with radiation filling totally laser resonator and a regime with single ultrashort pulse in laser cavity. The amplitude of this single pulse in the case of stationary generation is described by the expression

$$E = E_0 \frac{\exp(i\Omega\tau - i\delta k\zeta)}{\cosh^{1+i\alpha}\beta\tau}, \quad (7)$$

where the peak amplitude of a pulse E_0 , its reverse duration β , its frequency chirp α , parameters Ω and δk are determined from a system of algebraic equations [42]. The spectral profile of the ultrashort pulse (7) is determined by the following analytical expression [42, 46]:

$$I = \frac{\pi^2 |E_0|^2}{\beta^2} \frac{\sinh \pi\alpha}{\alpha(\cosh \pi\alpha + \cosh(\pi/\beta))}, \quad (8)$$

where ξ is a frequency detuning from the center frequency of soliton radiation. With increasing chirp α , the spectral profile is changed from a bell-shaped form to a rectangle one (see Figure 15(a)). Figure 15(b) shows the change in the frequency chirp α on the plate of the nonlinear-dispersion parameters $\xi = q/r$, $\theta = D_i/D_r$. Equation (6) has also a solution with indefinitely increasing amplitude $E \rightarrow \infty$ (that is $J \rightarrow \infty$) which is not correct because of breakdown of the condition $pI \ll 1$.

Equation (6) is close to the following equation:

$$\frac{\partial \Psi}{\partial t} = (d_r + id_i) \frac{\partial^2 \Psi}{\partial z^2} + [g + (c_1 + ic_2)|\Psi|^2]\Psi, \quad (9)$$

where d_r , d_i , g , c_1 , c_2 are constant parameters. This equation is used in a description of hydrodynamical phenomena [47, 48] (see also [49, 50]). It has also the solution in the form (7) [48, 49, 51]. However, there exists the principle distinction between these equations: equation (6) has the stable solution in the form of a single stationary soliton described by (7), but in the case of (9), such stationary solution is always unstable. In the case of (6), the stabilization of the single-pulse solution is realized through a saturation of the amplification G . If the parameter of the gain saturation is equal to zero $b = 0$ (see (3)), then (6) is transformed into (9). The stabilization of a single pulse can be achieved at the expense of nonlinear losses described by additional high-order nonlinearities [32, 52]. However, in this case, the exact elegant analytical solutions (7) and (8) for an amplitude and a spectrum of a single stationary pulse do not hold.

5.2. Model with Combination of Lumped and Continuously Distributed Nonlinear Losses. We study passive mode-locked laser with the combination of the continuously distributed saturable absorber included in (5) and the lumped saturable absorber described by (4). To follow the change of properties of soliton wings due to dispersive waves and correspondingly of properties of steady states of a pair of interacting solitons, we decrease the magnitude of the lumped saturable absorber s_{nl} up to zero. Simultaneously we increase the value of the distributed nonlinear losses σ_{nl} thus that the total losses for a weak signal for one pass of a field through the resonator remain constant. If our hypothesis is true, then dispersive waves should weaken up to zero and the amplitude of soliton wings should decrease that will result in the change of properties of bound steady states.

Figure 16 shows the spectral change in a single soliton with varying lumped part of nonlinear losses s_{nl} . One can see the decrease and disappearance of sidebands in the soliton spectrum with decreasing s_{nl} . Figure 17 shows the decrease of a bounding energy for the first excited steady state of a pair of bounding solitons with decreasing values s_{nl} . Figure 18 shows the decrease of the soliton wing with decreasing lumped part of nonlinear losses. These results demonstrate the role of dispersive waves in a formation of powerful soliton wings which determine properties of bound steady state of interacting solitons.

6. Discussion

We have developed a theoretical model to describe several behaviors which are usually observed in passively mode-locked fiber lasers. The model is based on a fiber exhibiting optical Kerr nonlinearity, gain and group velocity dispersions, and saturable gain. For our analysis, we use typical parameters for ytterbium- and erbium-doped fiber lasers operating in the normal and anomalous dispersion regimes. Two mechanisms of nonlinear losses have been analyzed. One of them is related with the nonlinear polarization rotation technique. The other is due to a saturable absorber. For both mechanisms, the analogical results have been obtained. In our study, we have chosen such laser parameters for which the researched phenomena are manifested most clearly. With other parameters, we have observed various modifications of investigated regimes. For example, we have observed the temporal oscillations of soliton amplitudes in bound states. For some parameters, the lower states were unstable. As a result of this instability, a soliton pair transits into a higher steady state. With other parameters, this instability results in a merge of solitons. With certain parameters, the investigated phenomena are masked by period-doubling effects.

The multiple-pulse passive mode-locking has been carefully investigated. It is determined by a coexistence and a competition of pulses amplified in a common gain medium. The multiple-pulse operation is realized through the effect of a quantization of intracavity radiation into identical dissipative solitons. A number of identical pulses in a laser cavity as a function of pumping are determined by multihysteresis dependence. These results are in good agreement with

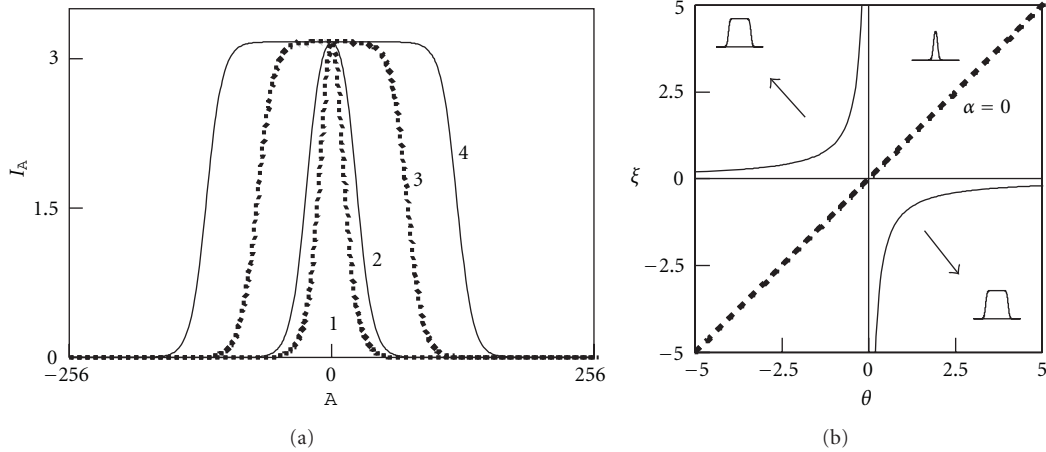


FIGURE 15: Spectra of ultrashort pulse described by (8). (a) Spectral profiles of established solitons with different chirps: (1) $\alpha = 0$, (2) $\alpha = 1$, (3) $\alpha = 3$, (4) $\alpha = 5$. (b) Variation of the chirp α on the plane of the nonlinear-dispersion parameters (ξ, θ) . For the dashed line $\alpha = 0$, for the solid curves $\alpha = \pm\sqrt{2}$, the arrows point the directions of maximal increase in the chirp α . The spectral profiles in the figure (b) demonstrate typical spectra for the three areas separated from each other by the solid curves.

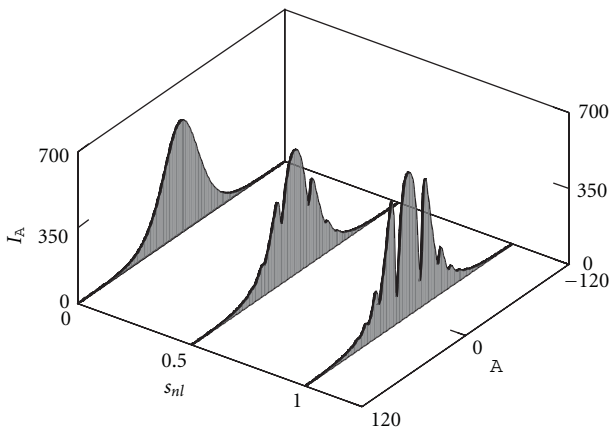


FIGURE 16: Change in spectrum of single ultrashort pulse with the change in a value of lumped part of saturable absorber s_{nl} . The total value of nonlinear losses remains the same.

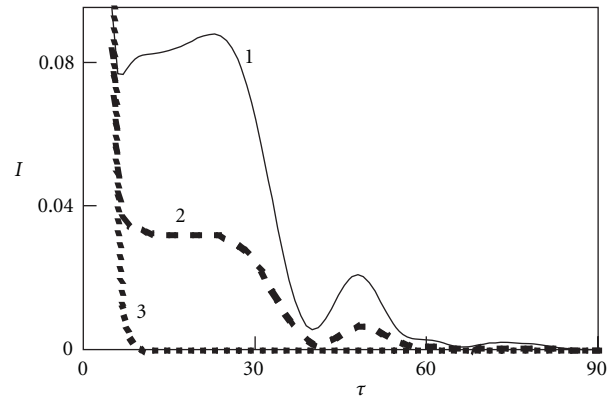


FIGURE 18: Change in the intensity of single-soliton wing with the change in a value of lumped part of saturable absorber s_{nl} : (1) $s_{nl} = 1$, (2) $s_{nl} = 0.75$, (3) $s_{nl} = 0$. The total value of nonlinear losses including lumped and distributed parts remains the same.

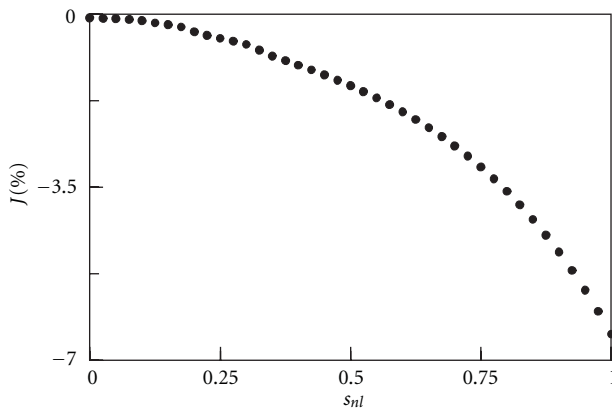


FIGURE 17: Bound energy for the first excited steady state with changing value of a lumped part of a saturable absorber s_{nl} .

experimental data reported in the literature (see e.g., [17]). It is shown that the multihysteresis dependence of a number of pulses on pumping results in analogical multihysteresis dependences for an intracavity energy and a peak intensity of intracavity solitons.

It is found that a competition and a coexistence of solitons in a laser cavity is determined by the dependence of the nonlinear-dispersion part of an amplification on a peak intensity of solitons $\Lambda = \Lambda(I_0)$ (see Figures 7 and 9). For achievement of a single-pulse generation, it is necessary to increase the parameter I_{cr2} that the condition $I_0 < I_{cr2}$ is satisfied for all intracavity pulses. In this case, the multiple-pulse generation is suppressed and, as result, the single pulse operation is realized. In such a way, it is possible to expect

a generation of pulses with extremely high energy. This problem demands detailed studying.

Usually at a multiple-pulse generation, all pulses have identical parameters. It is realized when a hard regime of an annihilation and an excitation of new pulses is realized. However, as it is shown in the given paper, the soft regime of an annihilation and an excitation is also possible. In this case, one of pulses has smaller amplitude than other pulses having identical parameters.

An interaction of pulses through an interference of their wings in fast intracavity nonlinear medium is more fine effect than the realization of a multiple-pulse generation. The dependence of the nonlinear-dispersion part of an amplification on a peak intensity of solitons $\Lambda = \Lambda(I_0)$ dictates the phase difference of interacting solitons: it is close to π , $\pi/2$, 0. However, various stationary states have distinguished degrees of stability. The degree of stability essentially depends on type of nonlinearity and from values of nonlinear-dispersion parameters. This fact is well known from the papers [32, 52]. If master equation is close to nonlinear Schrödinger equation (dissipative terms are small), then all steady states are unstable, but steady states with $\pi/2$ phase difference have extremely weak instability, that is, they are practically stable [52]. If dissipative terms are not small, then $\pi/2$ steady states are merely stable [32] (authors of both the papers used model with complex quadratic dispersion and complex cubic-quintic nonlinearity).

Thanks to powerful wings, large binding energies of interacting solitons can be obtained. In our numerical experiment, we have realized high-stable noise-proof multisoliton molecules. We have shown that sets of various types of bonds between neighboring pulses in such molecule can be obtained. Accordingly, the coding of the information in these soliton sequences can be realized through various distributions of types of bonds between neighboring pulses along a soliton chain. Dense packing of pulses in the bound soliton sequence provides high speed of transfer of an information in fiber communications line working in nonlinear bound-soliton-based regime. Such systems can be also useful for storage and processing of an information. The problem of such coding of a data stream into a bound soliton chain (and also of decoding) demands a detailed study.

In the case of a realization of the same type of a bond between all neighboring solitons in a structure with a very large number of pulses, we obtain an analog of a crystal of finite extent. This fully ordered state was named a soliton crystal by analogy with the results of Mitschke and his coauthors on pulse reshaping in a passive synchronously pumped fiber-ring resonator [53, 54]. If such soliton crystal with a single type of a bond fills completely the total ring laser cavity, then harmonic passive mode-locking is realized. This regime is interesting for a creation of generators of ultrashort pulses with superhigh rate of a repetition of pulses in output radiation. Generators of pair of ultrashort pulses with the certain fixed distance between pulses also can find numerous applications.

We have investigated a mechanism of a formation of powerful soliton wings connected with a lumped saturable absorber. In case of the nonlinear polarization rotation

technique, the nonlinear losses are realized in the polarizer and they are lumped. In the case of a saturable absorber, the nonlinear losses can be lumped and continuously distributed. We have analyzed a laser model with a combination of lumped and continuously distributed parts of the total saturable absorber. Keeping the total nonlinear losses constant, we have varied their lumped part and studied properties of bound steady states of interacting solitons. We have found that the dispersive waves emitted by solitons because of lumped intracavity elements form powerful soliton wings resulting in great bounding energy of interacting solitons in steady states. The role of dispersive waves in a realization of a mechanism of a repulse between solitons and, as a result, realization of harmonic passive mode-locking calls for further investigation.

7. Conclusion

On basis of numerical simulation, we have studied the basic features in a realization of multiple-pulse operation of passive mode-locked fiber lasers. It is found that in the case of the hard regime of an annihilation and an excitation of new solitons with changing pump, all intracavity solitons have identical parameters (a peak intensity, a duration, a chirp, and so on). However, in the case of the soft regime of an annihilation and an excitation, one of pulses has a peak intensity smaller than other identical intracavity solitons. It is found that the multihysteresis dependence of a number of pulses on pump results in an analogical multihysteresis dependence for the intracavity radiation energy and for the peak intensity of identical solitons. An interaction of pulses through an interference of their wings in fast intracavity nonlinear medium has been investigated. Bound steady states of a two soliton molecule are determined. We have demonstrated the possibility to form information soliton sequences with any desirable distribution of the types of bonds between neighboring pulses along soliton trains. Thanks to large values of binding energies, such sequences have a high level of stability against perturbations. It is found that dispersive waves emitted by solitons because of lumped nonlinear losses form powerful soliton wings resulting in great bounding energy of interacting solitons in steady states.

Acknowledgments

The work is supported by the Agence Nationale de la Recherche (Contract ANR-2010-BLANC-0417-01-SOLICRISTAL) and by the RF President's Grant MK-2602.2011.2.

References

- [1] P. G. Kryukov, "Ultrashort-pulse lasers," *Quantum Electronics*, vol. 31, no. 2, pp. 95–119, 2001.
- [2] A. A. Ivanov, M. V. Alfimov, and A. M. Zheltikov, "Femtosecond pulses in nanophotonics," *Physics-Uspokhi*, vol. 47, no. 7, pp. 687–704, 2004.

- [3] M. E. Fermann and I. Hartl, "Ultrafast fiber laser technology," *IEEE Journal on Selected Topics in Quantum Electronics*, vol. 15, no. 1, Article ID 4773318, pp. 191–206, 2009.
- [4] T. Brabec and F. Krausz, "Intense few-cycle laser fields: frontiers of nonlinear optics," *Reviews of Modern Physics*, vol. 72, no. 2, pp. 545–591, 2000.
- [5] E. V. Baklanov and P. V. Pokasov, "Optical frequency standards and femtosecond lasers," *Quantum Electronics*, vol. 33, no. 5, pp. 383–400, 2003.
- [6] G. P. Agrawal, *Nonlinear Fiber Optics*, Elsevier Science and Technology Books, Academ Press, Burlington, Mass, USA, 2006.
- [7] N. Akhmediev and A. Ankiewicz, *Dissipative Solitons*, Lecture Notes in Physics, Springer, Berlin, Germany, 2005.
- [8] F. W. Wise, A. Chong, and W. H. Renninger, "High-energy femtosecond fiber lasers based on pulse propagation at normal dispersion," *Laser & Photonics Reviews*, vol. 2, no. 1-2, pp. 58–73, 2008.
- [9] S. Chouli and P. Grelu, "Rains of solitons in a fiber laser," *Optics Express*, vol. 17, no. 14, pp. 11776–11781, 2009.
- [10] D. Y. Tang, L. M. Zhao, X. Wu, and H. Zhang, "Soliton modulation instability in fiber lasers," *Physical Review A*, vol. 80, pp. 023806–023813, 2009.
- [11] F. Amrani, A. Haboucha, M. Salhi, H. Leblond, A. Komarov, and F. Sanchez, "Dissipative solitons compounds in a fiber laser. Analogy with the states of the matter," *Applied Physics B*, vol. 99, no. 1-2, pp. 107–114, 2010.
- [12] S. Kobtsev, S. Kukarin, S. Smirnov, S. Turitsyn, and A. Latkin, "Generation of double-scale femto/pico-second optical lumps in mode-locked fiber lasers," *Optics Express*, vol. 17, no. 23, pp. 20707–20713, 2009.
- [13] P. Grelu, F. Belhache, F. Gutty, and J. M. Soto-Crespo, "Relative phase locking of pulses in a passively mode-locked fiber laser," *Journal of the Optical Society of America B*, vol. 20, no. 5, pp. 863–870, 2003.
- [14] H. A. Haus, "Mode-locking of lasers," *IEEE Journal on Selected Topics in Quantum Electronics*, vol. 6, no. 6, pp. 1173–1185, 2000.
- [15] V. I. Denisov, B. N. Nyushkov, and V. S. Pivtsov, "Self-mode-locked all-fibre erbium laser with a low repetition rate and high pulse energy," *Quantum Electronics*, vol. 40, no. 1, pp. 25–27, 2010.
- [16] A. Komarov, A. Haboucha, K. Komarov, H. Leblond, M. Salhi, and F. Sanchez, "Soliton interaction in fiber laser," in *Recent Research Developments in Optics*, S. G. Pandalai, Ed., vol. 7, pp. 63–112, 2009.
- [17] D. Y. Tang, W. S. Man, and H. Y. Tam, "Stimulated soliton pulse formation and its mechanism in a passively mode-locked fibre soliton laser," *Optics Communications*, vol. 165, no. 4, pp. 189–194, 1999.
- [18] A. Hideur, T. Chartier, M. Sahli, C. Ozkul, C. M. Brunel, and F. Sanchez, "Mode-lock, Q-switch and CW operation of an Yb-doped double-clad fiber ring laser," *Optics Communications*, vol. 198, no. 1, pp. 141–146, 2001.
- [19] A. B. Grudinin, D. J. Richardson, and D. N. Payne, "Energy quantisation in figure eight fibre laser," *Electronics Letters*, vol. 28, no. 1, pp. 67–68, 1992.
- [20] A. Komarov, H. Leblond, and F. Sanchez, "Multistability and hysteresis phenomena in passively mode-locked fiber lasers," *Physical Review A*, vol. 71, no. 5, Article ID 053809, pp. 1–9, 2005.
- [21] D. Y. Tang, L. M. Zhao, B. Zhao, and A. Q. Liu, "Mechanism of multisoliton formation and soliton energy quantization in passively mode-locked fiber lasers," *Physical Review A*, vol. 72, no. 4, pp. 1–9, 2005.
- [22] A. Komarov, H. Leblond, and F. Sanchez, "Theoretical analysis of the operating regime of a passively-mode-locked fiber laser through nonlinear polarization rotation," *Physical Review A*, vol. 72, no. 6, pp. 063811–063818, 2005.
- [23] J.-C. Chiu, Y.-F. Lan, and J.-J. Kang, "Passively mode-locked lasers using saturable absorber incorporating dispersed single wall carbon nanotubes," in *Proceedings of the IEEE Electronic Component and Technology Conference*, pp. 827–830, San Diego, Calif, USA, 2009.
- [24] H. Zhang, D. Tang, R. J. Knize, L. Zhao, Q. Bao, and K. P. Loh, "Graphene mode locked, wavelength-tunable, dissipative soliton fiber laser," *Applied Physics Letters*, vol. 96, no. 11, Article ID 111112, 2010.
- [25] Z. Sun, T. Hasan, D. Popa et al., "Ultrafast fiber laser mode-locked by graphene based saturable absorber," in *Proceedings of the Lasers and Electro-Optics/Quantum Electronics and Laser Science Conference: 2010 Laser Science and Photonics Applications (CLEO/QELS 2010)*, San Jose, Calif, USA, May 2010.
- [26] P. Grelu, F. Belhache, F. Gutty, and J. M. Soto-Crespo, "Phase-locked soliton pairs in a stretched-pulse fiber laser," *Optics Letters*, vol. 27, no. 11, pp. 966–968, 2002.
- [27] M. Olivier, V. Roy, M. Piché, and F. Babin, "Pulse collisions in the stretched-pulse fiber laser," *Optics Letters*, vol. 29, no. 13, pp. 1461–1463, 2004.
- [28] D. Y. Tang, W. S. Man, H. Y. Tam, and P. D. Drummond, "Observation of bound states of solitons in a passively mode-locked fiber laser," *Physical Review A*, vol. 64, no. 3, Article ID 033814, 2001.
- [29] A. K. Komarov, K. P. Komarov, H. Leblond, and F. Sanchez, "Spectral control over the interaction of ultrashort pulses in fiber lasers," *Optics and Spectroscopy*, vol. 103, no. 5, pp. 825–830, 2007.
- [30] N. Akhmediev, J. M. Soto-Crespo, M. Grapinet, and P. Grelu, "Dissipative soliton interactions inside a fiber laser cavity," *Optical Fiber Technology*, vol. 11, no. 3, pp. 209–228, 2005.
- [31] B. A. Malomed, "Bound solitons in the nonlinear Schrödinger-Ginzburg-Landau equation," *Physical Review A*, vol. 44, no. 10, pp. 6954–6957, 1991.
- [32] N. Akhmediev, A. Ankiewicz, and J. M. Soto-Crespo, "Multi-soliton solutions of the complex ginzburg-landau equation," *Physical Review Letters*, vol. 79, no. 21, pp. 4047–4051, 1997.
- [33] A. Komarov, K. Komarov, and F. Sanchez, "Quantization of binding energy of structural solitons in passive mode-locked fiber lasers," *Physical Review A*, vol. 79, no. 3, Article ID 033807, 2009.
- [34] K. S. Abedin, J. T. Gopinath, L. A. Jiang, M. E. Grein, H. A. Haus, and E. P. Ippen, "Self-stabilized passive, harmonically mode-locked stretched-pulse erbium fiber ring laser," *Optics Letters*, vol. 27, no. 20, pp. 1758–1760, 2002.
- [35] C. X. Yu, H. A. Haus, E. P. Ippen, W. S. Wong, and A. Sysoliatin, "Gigahertz-repetition-rate mode-locked fiber laser for continuum generation," *Optics Letters*, vol. 25, no. 19, pp. 1418–1420, 2000.
- [36] B. Ortaç, A. Hideur, G. Martel, and M. Brunel, "2-GHz passive harmonically mode-locked Yb-doped double-clad fiber laser," *Applied Physics B*, vol. 81, no. 4, pp. 507–509, 2005.
- [37] A. Komarov, H. Leblond, and F. Sanchez, "Passive harmonic mode-locking in a fiber laser with nonlinear polarization rotation," *Optics Communications*, vol. 267, no. 1, pp. 162–169, 2006.

- [38] A. Komarov, A. Haboucha, and F. Sanchez, "Ultra-high-repetition-rate bound-soliton harmonic passive mode-locked fiber lasers," *Optics Letters*, vol. 33, no. 19, pp. 2254–2256, 2008.
- [39] A. Haboucha, H. Leblond, M. Salhi, A. Komarov, and F. Sanchez, "Coherent soliton pattern formation in a fiber laser," *Optics Letters*, vol. 33, no. 5, pp. 524–526, 2008.
- [40] Y. I. Khanin, *Principles of Laser Dynamics*, Elsevier, Amsterdam, The Netherlands, 1995.
- [41] A. Komarov, K. Komarov, D. Meshcheriakov, F. Amrani, and F. Sanchez, "Dissipative solitons in passive mode-locked fiber lasers with nonlinear polarization rotation technique," in *Proceedings of the Second International Conference: Nonlinear Waves—Theory and Applications*, Technical Digest, p. 207, Beijing, China, June 2010.
- [42] K. P. Komarov, "Theory of stationary ultrashort pulses in solid-state lasers with passive mode-locking," *Optics and Spectroscopy*, vol. 60, no. 2, pp. 231–234, 1986.
- [43] K. P. Komarov and V. D. Ugozhaev, "Steady-state pulses in solid-state lasers with passive mode locking," *Optics and Spectroscopy*, vol. 55, no. 5, pp. 564–568, 1983.
- [44] A. K. Komarov, K. P. Komarov, and A. S. Kuch'yanov, "On phase-modulational bifurcation during passive mode locking in lasers," *JETP Letters*, vol. 67, no. 4, pp. 280–283, 1998.
- [45] A. K. Komarov and K. P. Komarov, "Multistability and hysteresis phenomena in passive mode-locked lasers," *Physical Review E*, vol. 62, no. 6 B, pp. R7607–R7610, 2000.
- [46] K. P. Komarov, A. S. Kuch'yanov, and V. D. Ugozhayev, "Generation of stationary ultra-short pulses by a passive mode-locking solid-state laser," *Optics Communications*, vol. 57, no. 4, pp. 279–284, 1986.
- [47] L. M. Hocking, K. Stewartson, J. T. Stuart, and S. N. Brown, "A nonlinear instability burst in plane parallel flow," *Journal of Fluid Mechanics*, vol. 51, no. 4, pp. 705–735, 1972.
- [48] L. M. Hocking and K. Stewartson, "On the nonlinear response of a marginally unstable plane parallel flow to a two-dimensional disturbance," *Proceedings of the Royal Society A*, vol. 326, pp. 289–313, 1972.
- [49] A. C. Newell, "Envelope equations," *Lectures in Applied Mathematics*, vol. 15, pp. 157–163, 1974.
- [50] A. C. Newell and J. A. Whitehead, "Finite bandwidth, finite amplitude convection," *Journal of Fluid Mechanics*, vol. 38, no. 2, pp. 279–303, 1969.
- [51] N. R. Pereira and L. Stenflo, "Nonlinear Schrödinger equation including growth and damping," *Physics of Fluids*, vol. 20, no. 10, pp. 1733–1734, 1977.
- [52] V. V. Afanasjev, B. A. Malomed, and P. L. Chu, "Stability of Bound States of pulses in the Ginzburg-Landau equations," *Physical Review E*, vol. 56, no. 5, pp. 6020–6023, 1997.
- [53] B. A. Malomed, A. Schwache, and F. Mitschke, "Soliton lattice and gas in passive fiber-ring resonators," *Fiber and Integrated Optics*, vol. 17, no. 4, pp. 267–277, 1998.
- [54] S. Rutz and F. Mitschke, "Towards thermodynamics of solitons: cooling," *Journal of Optics B*, vol. 2, no. 3, pp. 364–366, 2000.

Research Article

The Proper Orthogonal Decomposition for Dimensionality Reduction in Mode-Locked Lasers and Optical Systems

Eli Shlizerman,¹ Edwin Ding,² Matthew O. Williams,¹ and J. Nathan Kutz¹

¹Department of Applied Mathematics, University of Washington, Seattle, WA 98195-2420, USA

²Department of Mathematics and Physics, Azusa Pacific University, P.O. Box 7000, Azusa, CA 91702-7000, USA

Correspondence should be addressed to J. Nathan Kutz, kutz@amath.washington.edu

Received 6 May 2011; Accepted 24 June 2011

Academic Editor: Sonia Boscolo

Copyright © 2012 Eli Shlizerman et al. This is an open access article distributed under the Creative Commons Attribution License, which permits unrestricted use, distribution, and reproduction in any medium, provided the original work is properly cited.

The onset of multipulsing, a ubiquitous phenomenon in laser cavities, imposes a fundamental limit on the maximum energy delivered per pulse. Managing the nonlinear penalties in the cavity becomes crucial for increasing the energy and suppressing the multipulsing instability. A proper orthogonal decomposition (POD) allows for the reduction of governing equations of a mode-locked laser onto a low-dimensional space. The resulting reduced system is able to capture correctly the experimentally observed pulse transitions. Analysis of these models is used to explain the sequence of bifurcations that are responsible for the multipulsing instability in the master mode-locking and the waveguide array mode-locking models. As a result, the POD reduction allows for a simple and efficient way to characterize and optimize the cavity parameters for achieving maximal energy output.

1. Introduction

Ultrashort lasers have a large variety of applications, ranging from small scale problems such as ocular surgeries and biological imaging to large-scale problems such as optical communication systems and nuclear fusion. In the context of telecommunications and broadband sources, the laser is required to robustly produce pulses in the range of 200 femtoseconds to 50 picoseconds. The generation of such short pulses is often referred to as mode-locking [1, 2]. One of the most widely used mode-locked lasers developed to date is a ring cavity laser with a combination of waveplates and a passive polarizer. The combination of such components acts as an effective saturable absorber, providing an intensity discriminating mechanism to shape the pulse [3–7]. It was first demonstrated experimentally in the early 90s that ultrashort pulse generation and robust laser operation could be achieved in such a laser cavity [3, 4]. Since then, a number of theoretical models have been proposed to characterize the mode-locked pulse evolution and its stability, including the present work which demonstrates that the key phenomenon of multipulsing can be completely characterized by a low-dimensional model with modes created by a proper orthogonal decomposition (POD).

Mode-locking can be achieved through a variety of mechanisms, for example, *nonlinear polarization rotation* [1] or *waveguide arrays* [2]. In the context of mode-locking with nonlinear polarization rotation, the master mode-locking equation proposed by Haus [3, 8–11], which is the complex Ginzburg-Landau equation with a bandwidth-limited gain, was the first model used to describe the pulse formation and mode-locking dynamics in the ring cavity laser. The Ginzburg-Landau equation was originally developed in the context of particle physics as a model of superconductivity and has since been widely used as a prototypical model for nonlinear wave propagation and pattern-forming systems. In the context of mode-locking with waveguide arrays, the nonlinear mode coupling inherent in semiconductor waveguide arrays is exploited to produce the saturable absorber needed for mode-locking [12–14]. The governing equation in this context is the waveguide array mode-locking model (WGAML).

In both of these systems, a large number of stationary solutions are supported by this equation [14–16]. These stationary solutions can be categorized as single-pulse, double-pulse, and in general n -pulse solution depending on the strength of the cavity gain. The phenomenon for which a single mode-locked pulse solution splits into two or more pulses

is known as multipulsing [1, 2, 17] and has been observed in a wide variety of experimental and theoretical configurations [12, 18–24]. Specifically, when the pulse energy is increased, the spectrum of the pulse experiences a broadening effect. Once the spectrum exceeds the bandwidth limit of the gain, the pulse becomes energetically unfavorable, and a double-pulse solution is generated which has a smaller bandwidth. The transition from a single-pulse to a double-pulse solution can be via various mechanisms: abrupt jump from single pulse to double pulse, creation of periodic structures and chaotic/translational behavior. *It is the aim of this manuscript to characterize the translational behavior in the nonlinear polarization rotation and WGAML systems and provide a framework for the study of the multipulsing phenomena when parameters are varied.*

A number of analytical and numerical tools have been utilized over the past fifteen years to study the mode-locking stability and multipulsing transition. One of the earliest theoretical approaches was to consider the energy rate equations derived by Namiki et al. that describe the averaged energy evolution in the laser cavity [25]. Other theoretical approaches involved the linear stability analysis of stationary pulses [12, 26–28]. These analytical methods were effective in characterizing the stability of stationary pulses but were unable to describe the complete pulse transition that occurs during multipulsing.

Computationally, there is no efficient (algorithmic) way to find bifurcations by direct simulations, since solutions that possess a small basin of attraction are difficult to find. Alternative, local approach is to follow the single-pulse solution using continuation methods; however, to the limitation of the analytic tools, the transition region is difficult to characterize computationally even with the fastest and the most accurate algorithms available [29]. Such difficulties has led to the consideration of reduction techniques that simplify the full governing equation and allow for a deeper insight of the multipulsing instability. One obvious method for a low-dimensional reconstruction of the dynamics is to use an appropriate eigenfunction expansion basis for characterizing the system. Such eigenfunction expansions represent a natural basis for the dynamics as have been demonstrated in various photonic applications [30–32]. For nonlinear systems; however, it is not always clear what eigenfunction basis should be used nor is it clear that the optimal basis set can be found by such a technique. Nevertheless, it provides a powerful and effective method for recasting the dynamics in a lower-dimensional framework. Among other reduction techniques, the variational method was first used by Anderson et al. in the context of nonlinear evolution equations with nonhamiltonian dissipative perturbations [33, 34]. Since then, it has been widely used to study various aspects in nonlinear optics such as soliton resonance and pulse interactions [35–37]. In the context of mode-locking, the method (or the associated method of moments) was successful in characterizing the single-pulse dynamics of the governing systems [37–39].

The limitation of the variational method is that the accuracy of the results depends largely on the approach used to describe the true dynamics. When multipulsing occurs, the

form of the solution in the laser system changes significantly, and the prediction by the variational reduction is ambiguous. Unlike the variational approach [38, 39], the low-dimensional model considered here is constructed using the method of POD [40]. The proper orthogonal decomposition (POD), also known as principal component analysis (PCA) or the Karhunen-Loève (KL) expansion, is a singular-value decomposition- (SVD-) based technique often used to generate a low-rank, orthogonal basis that optimally (in an L^2 -sense [41]) represents a set of data. Although the POD technique can be applied to generic data sets, it is often used on data obtained from systems with a physical, biological, and/or engineering application [40, 42, 43]. The resulting set of the POD modes is often paired with the standard Galerkin projection technique in order to generate a set of ODEs for the mode amplitudes [40]. This combination has proven to be very powerful and is used in a number of fields including nonlinear optics [44, 45], turbulence [40], fluid flow [46–49], convective heating [50], and even neuroscience [51]. As a result, the POD method provides a generic, analytic tool that can be used efficiently, unlike the direct methods. The resulting POD system is able to capture the whole bifurcation sequence from the single mode-locked pulse to the double-pulse solution observed in numerical simulations of both systems of mode-locking. The key idea behind the method is that there exists an “ideal” (optimal) basis in which a given system can be written (diagonalized) so that in this basis, all redundancies have been removed, and the largest variances of particular measurements are ordered. In the language being developed here, this means that the system has been written in terms of its principle components or in a proper orthogonal decomposition. As already mentioned, such techniques are commonly used as a tool in exploratory data analysis and for making predictive models.

This paper is outlined as follows: Section 2 describes the procedure for obtaining the POD modes from a given set of data. A simple example of the POD technique is applied to N -soliton dynamics. This illustrates the key features of the method. The application of the POD reduction to the cubic-quintic Ginzburg-Landau equation and the waveguide array mode-locking model are then explored in Sections 4 and 5, respectively. Section 6 summarizes the results of the paper.

2. Proper Orthogonal Decomposition

Here we provide a short review of the POD method and describe its application to the derivation of reduced models for nonlinear evolution equations (see [40]). Abstractly, the POD method developed here can be represented by considering the following partial differential equation (PDE) system:

$$\mathbf{U}_t = N(\mathbf{U}, \mathbf{U}_x, \mathbf{U}_{xx}, \dots, x, t), \quad (1)$$

where \mathbf{U} is a vector of physically relevant quantities, and the subscripts t and x denote partial differentiation. The function $N(\cdot)$ captures the space-time dynamics that is specific to the system being considered. Along with this PDE are some prescribed boundary conditions and initial conditions.

As a specific solution method for (1), we consider the separation of variable and basis expansion technique.

In particular, standard eigenfunction expansion techniques assume a solution of the form

$$u(x, t) = \sum_{n=1}^{\infty} a_n(t) \phi_n(x), \quad (2)$$

where the $\phi_n(x)$ is an orthogonal set of eigenfunctions, and we have assumed that the PDE is now described by a scalar quantity $u(x, t)$. The $\phi_n(x)$ can be any orthogonal set of functions such that

$$(\phi_j(x), \phi_k(x)) = \delta_{jk} = \begin{cases} 1, & j = k, \\ 0, & j \neq k, \end{cases} \quad (3)$$

where δ_{jk} is the Dirac function, and the notation $(\phi_j, \phi_k) = \int \phi_j \phi_k^* dx$ gives the inner product. For a given physical problem, one may be motivated to use a specified set of eigenfunctions such as those special functions that arise for specific geometries or symmetries. More generally, for computational purposes, it is desired to use a set of eigenfunctions that produce accurate and rapid evaluation of the solutions of (1), that is, a Fourier mode basis and the associated fast Fourier transform. In the method developed here, optimal POD basis functions are generated from a singular value decomposition of the representative dynamics of the governing equations, thus, recasting the dynamics of the system into the best low-dimensional framework.

The POD method is related to the singular value decomposition (SVD). Computationally, the SVD is implemented as a built-in routine in many scientific software packages, such as MATLAB or NumPy. To generate a complete set of POD modes, a data set is compiled and represented as the matrix \mathbf{X} . Each row of the matrix consists of a sample solution taken at a specific value of time, and the number of rows in the matrix is the number of samples taken at evenly spaced values in time. Therefore, if the data consists of m samples with n points per sample, then $\mathbf{X} \in \mathbb{C}^{m \times n}$. The SVD factorizes the matrix \mathbf{X} into three matrices

$$\mathbf{X} = \mathbf{U} \mathbf{\Sigma} \mathbf{V}^*, \quad (4)$$

where $\mathbf{U} \in \mathbb{C}^{m \times m}$, $\mathbf{V} \in \mathbb{C}^{n \times n}$, and $\mathbf{\Sigma} \in \mathbb{R}^{m \times n}$, and the asterisk denotes the conjugate transpose. In a matrix form, the factorization in (4) is expressed as

$$\mathbf{X} = \begin{bmatrix} \vec{u}_1 \\ \vdots \\ \vec{u}_i \\ \vdots \\ \vec{u}_m \end{bmatrix} \begin{bmatrix} \sigma_1 & & & & \\ & \ddots & & & \\ & & \sigma_j & & \\ & & & \ddots & \\ & & & & \sigma_n \\ 0 & \dots & \dots & \dots & 0 \end{bmatrix} \begin{bmatrix} \vec{\phi}_1 \\ \vdots \\ \vec{\phi}_j \\ \vdots \\ \vec{\phi}_n \end{bmatrix}. \quad (5)$$

The matrix $\mathbf{\Sigma}$ is a diagonal matrix with nonnegative elements σ_j . For $m > n$, j is an index that takes the values $j = 1, \dots, n$; otherwise, it takes the values $j = 1, \dots, m$. The σ_j are referred to as the singular values of \mathbf{X} and are ordered such that

$\sigma_1 \geq \sigma_2 \geq \dots \geq 0$. The matrices \mathbf{U} and \mathbf{V} are composed of the eigenvectors \vec{u}_i (rows of \mathbf{U}) and $\vec{\phi}_j$ (rows of \mathbf{V}^*) of the covariance matrices $\mathbf{X}\mathbf{X}^*$ and $\mathbf{X}^*\mathbf{X}$, respectively. As a result, the singular value decomposition allows the decomposition of the k th row of \mathbf{X} into

$$\vec{\chi}^k = \sum_{j=1}^n \sigma_j u_{kj} \vec{\phi}_j, \quad (6)$$

assuming that $m > n$. Hence, the SVD returns a complete orthonormal set of basis functions for the rows of the data matrix \mathbf{X} . The elements of this basis are the vectors $\vec{\phi}_j$ and are referred to as the POD modes. *The key idea of this paper is embodied in (6). Specifically, the POD-Galerkin method attempts to provide an accurate approximation of the $\sigma_j u_{kj}$ with a system of ordinary differential equations.*

One way to reduce the dimensionality of the matrix \mathbf{X} is to use a subset of the POD basis. The relative importance of the j th POD mode $\vec{\phi}_j$ in the approximation of the matrix \mathbf{X} is determined by the relative energy E_j of that mode, defined as [40, 52]

$$E_j = \frac{\sigma_j^2}{\sum_{i=1}^n \sigma_i^2}, \quad (7)$$

where the total energy is normalized such that $\sum_{j=1}^n E_j = 1$. If the sum of the energies of the retained modes is unity, then these modes can be used to completely reconstruct \mathbf{X} . Typically, the number of modes required to capture all of the energy is very large and does not result in a significant dimensionality reduction. In practice; however, it has been found that the matrix can be accurately approximated by using POD modes whose corresponding energies sum to almost all of the total energy. Then the POD basis that is used in the approximation is a truncated basis, where the POD modes with negligible energy are neglected. In practice, the truncated basis with energies that sum to 99% of the total energy is a plausible truncation. The advantage of using a truncated set of POD modes rather than any other set of modes is that the representation of the data generated by the POD modes is guaranteed to have a smaller least squares error than the representation of the data generated by any other orthonormal set of the same size [40].

3. Soliton Dynamics: A Simple Example Application

To give a specific demonstration of this technique, consider the nonlinear Schrödinger (NLS) equation

$$iu_t + \frac{1}{2} u_{xx} + |u|^2 u = 0 \quad (8)$$

with the boundary conditions $u \rightarrow 0$ as $x \rightarrow \pm\infty$. Note that, for this example, time t and space x are represented in a standard way versus the traditional moving frame reference of optics. If not for the nonlinear term, this equation could be solved easily in closed form. However, the nonlinearity mixes the eigenfunction components in the expansion (2) making a simple analytic solution not possible.

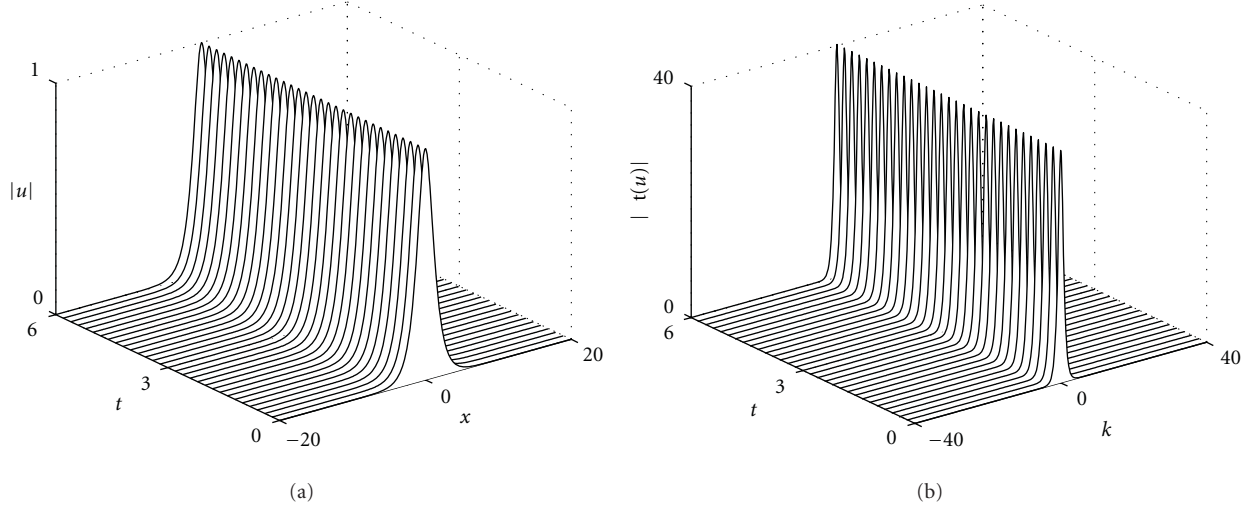


FIGURE 1: Evolution of the $N = 1$ soliton. Although it appears to be a very simple evolution, the phase is evolving in a nonlinear fashion, and approximately 50 Fourier modes are required to model accurately this behavior.

It now remains to consider a specific spatial configuration for the initial condition. For the NLS, there are the set of special initial conditions corresponding to the soliton solutions

$$u(x, 0) = N \operatorname{sech}(x), \quad (9)$$

where N is an integer. We will consider the soliton dynamics with $N = 1$ and $N = 2$, respectively. In order to do so, the initial condition is projected onto the Fourier modes with the fast Fourier transform (denoted by a hat). Rewriting (8) in the Fourier domain, that is, Fourier transforming, gives the set of differential equations

$$\hat{u}_t = -\frac{i}{2}k^2\hat{u} + i|\hat{u}|^2\hat{u}, \quad (10)$$

where the spatial Fourier mode (k is the wavenumber) mixing occurs due to the nonlinear mixing in the cubic term. This gives the system of differential equations to be solved for in order to evaluate the NLS behavior.

The dynamics of the $N = 1$ and $N = 2$ solitons are demonstrated in Figures 1 and 2, respectively. During evolution, the $N = 1$ soliton only undergoes phase changes while its amplitude remains stationary. In contrast, the $N = 2$ soliton undergoes periodic oscillations. In both cases, a large number of Fourier modes, about 50 and 200, respectively, are required to model the simple behaviors illustrated.

The potentially obvious question to ask in light of our dimensionality reduction thinking is this: is the soliton dynamics really a 50 or 200 degree-of-freedom system as implied by the Fourier mode numerical solution technique? The answer is no. Indeed, the inverse scattering transform ensures that there is an orthogonal, low-dimensional basis in terms of *nonlinear, soliton modes*. Such a technique is analytically difficult to handle and requires in-depth knowledge of the technique. On the other hand, with the appropriate basis, that is, the POD modes generated from the SVD, it can be shown that the dynamics is a simple reduction to 1 or 2 modes, respectively. Indeed, it can easily be shown that the $N = 1$ and $N = 2$ are truly low dimensional by computing

the singular value decomposition of the evolutions shown in Figures 1 and 2, respectively.

Figures 3 and 4 demonstrate the low-dimensional nature explicitly by computing the singular values of the numerical simulations along with the modes to be used in our new eigenfunction expansion. What is clear is that for both of these cases, the dynamics is truly low dimensional with the $N = 1$ soliton being modeled exceptionally well by a single POD mode while the $N = 2$ dynamics is modeled quite well with two POD modes. Thus, in performing the expansion (2), the modes chosen should be the POD modes generated from the simulations themselves. In the following subsections, the dynamics of the modal interaction for these two cases are derived, showing that quite a bit of analytic progress can then be made within the POD framework.

3.1. $N = 1$ Soliton Reduction. To take advantage of the low-dimensional structure, we first consider the $N = 1$ soliton dynamics. Figure 1 shows that a single mode in the SVD dominates the dynamics. Thus, the dynamics is recast in a single mode so that

$$u(x, t) = a(t)\phi(x), \quad (11)$$

where now there is no sum in (2) since there is only a single-mode $\phi(x)$. Plugging this expansion into the NLS equation (8) yields the following:

$$ia_t\phi + \frac{1}{2}a\phi_{xx} + |a|^2a|\phi|^2\phi = 0. \quad (12)$$

The inner product is now taken with respect to ϕ which gives

$$ia_t + \frac{\alpha}{2}a + \beta|a|^2a = 0, \quad (13)$$

where

$$\alpha = \frac{(\phi_{xx}, \phi)}{(\phi, \phi)}, \quad (14)$$

$$\beta = \frac{(|\phi|^2\phi, \phi)}{(\phi, \phi)},$$

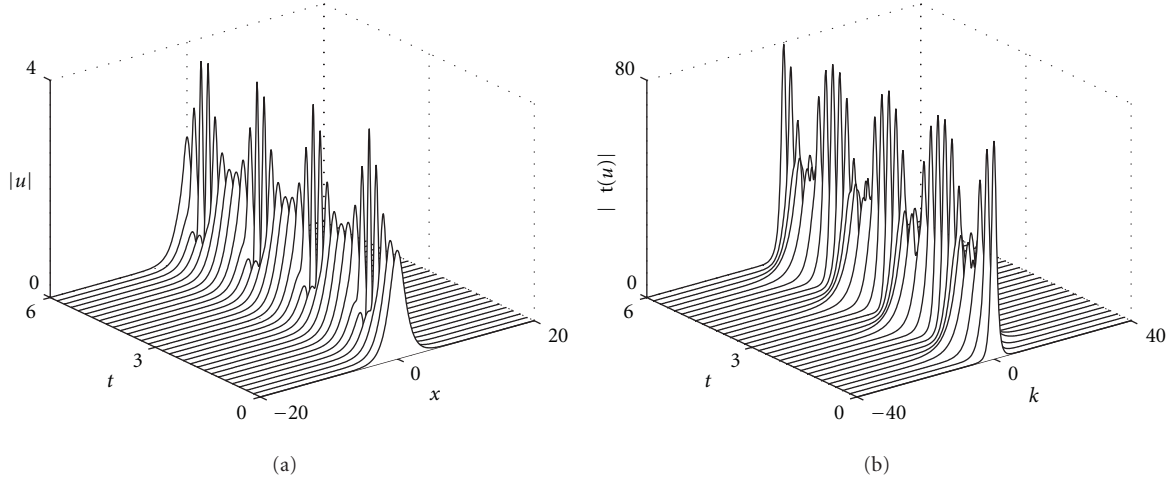


FIGURE 2: Evolution of the $N = 2$ soliton. Here a periodic dynamics is observed, and approximately 200 Fourier modes are required to model accurately the behavior.

and the inner product is defined as integration over the computational interval so that $(\phi, \psi) = \int \phi \psi^* dx$. Note that the integration is over the computational domain and the $*$ denotes the complex conjugate and where $(\phi, \phi) = 1$.

The differential equation for $a(t)$ given by (13) can be solved explicitly to yield

$$a(t) = a(0) \exp \left[i \frac{\alpha}{2} t + i \beta |a(0)|^2 t \right], \quad (15)$$

where $a(0)$ is the initial value condition for $a(t)$. To find the initial condition, recall that

$$u(x, 0) = \text{sech}(x) = a(0)\phi(x). \quad (16)$$

Taking the inner product with respect to $\phi(x)$ gives

$$a(0) = \frac{(\text{sech}(x), \phi)}{(\phi, \phi)}. \quad (17)$$

Thus, the one-mode expansion gives the approximate PDE solution

$$u(x, t) = a(0) \exp \left[i \frac{\alpha}{2} t + i \beta |a(0)|^2 t \right] \phi(x). \quad (18)$$

This solution is the low-dimensional POD approximation of the PDE expanded in the best basis possible, that is, the SVD determined basis.

For the $N = 1$ soliton, the spatial profile remains constant while its phase undergoes a nonlinear rotation. The POD solution (18) can be solved exactly to give a characterization of this phase rotation. Figure 5 shows both the full PDE dynamics along with its one-mode approximation.

3.2. $N = 2$ Soliton Reduction. The case of the $N = 2$ soliton is a bit more complicated and interesting. In this case, two modes clearly dominate the behavior of the system. These two modes are now used to approximate the dynamics

observed in Figure 2. In this case, the two-mode expansion takes the form

$$u(x, t) = a_1(t)\phi_1(x) + a_2(t)\phi_2(x), \quad (19)$$

where the ϕ_1 and ϕ_2 are simply taken from the first two columns of the \mathbf{U} matrix in the SVD. Inserting this approximation into the governing equation (8) gives

$$\begin{aligned} i(a_{1t}\phi_1 + a_{2t}\phi_2) + \frac{1}{2}(a_1\phi_{1xx} + a_2\phi_{2xx}) \\ + (a_1\phi_1 + a_2\phi_2)^2 (a_1^*\phi_1^* + a_2^*\phi_2^*) = 0. \end{aligned} \quad (20)$$

Multiplying out the cubic term gives the equation

$$\begin{aligned} i(a_{1t}\phi_1 + a_{2t}\phi_2) + \frac{1}{2}(a_1\phi_{1xx} + a_2\phi_{2xx}) \\ + (|a_1|^2 a_1 |\phi_1|^2 \phi_1 + |a_2|^2 a_2 |\phi_2|^2 \phi_2 + 2|a_1|^2 a_2 |\phi_1|^2 \phi_2 \\ + 2|a_2|^2 a_1 |\phi_2|^2 \phi_1 + a_1^2 a_2^* \phi_1^2 \phi_2^* + a_2^2 a_1^* \phi_2^2 \phi_1^*). \end{aligned} \quad (21)$$

All that remains is to take the inner product of this equation with respect to both $\phi_1(x)$ and $\phi_2(x)$. Recall that these two modes are orthogonal, thus, the resulting 2×2 system of nonlinear equations results in

$$\begin{aligned} ia_{1t} + \alpha_{11}a_1 + \alpha_{12}a_2 + (\beta_{111}|a_1|^2 + 2\beta_{211}|a_2|^2)a_1 \\ + (\beta_{121}|a_1|^2 + 2\beta_{221}|a_2|^2)a_2 + \sigma_{121}a_1^2 a_2^* + \sigma_{211}a_2^2 a_1^* = 0, \end{aligned}$$

$$\begin{aligned} ia_{2t} + \alpha_{21}a_1 + \alpha_{22}a_2 + (\beta_{112}|a_1|^2 + 2\beta_{212}|a_2|^2)a_1 \\ + (\beta_{122}|a_1|^2 + 2\beta_{222}|a_2|^2)a_2 + \sigma_{122}a_1^2 a_2^* + \sigma_{212}a_2^2 a_1^* = 0, \end{aligned} \quad (22)$$

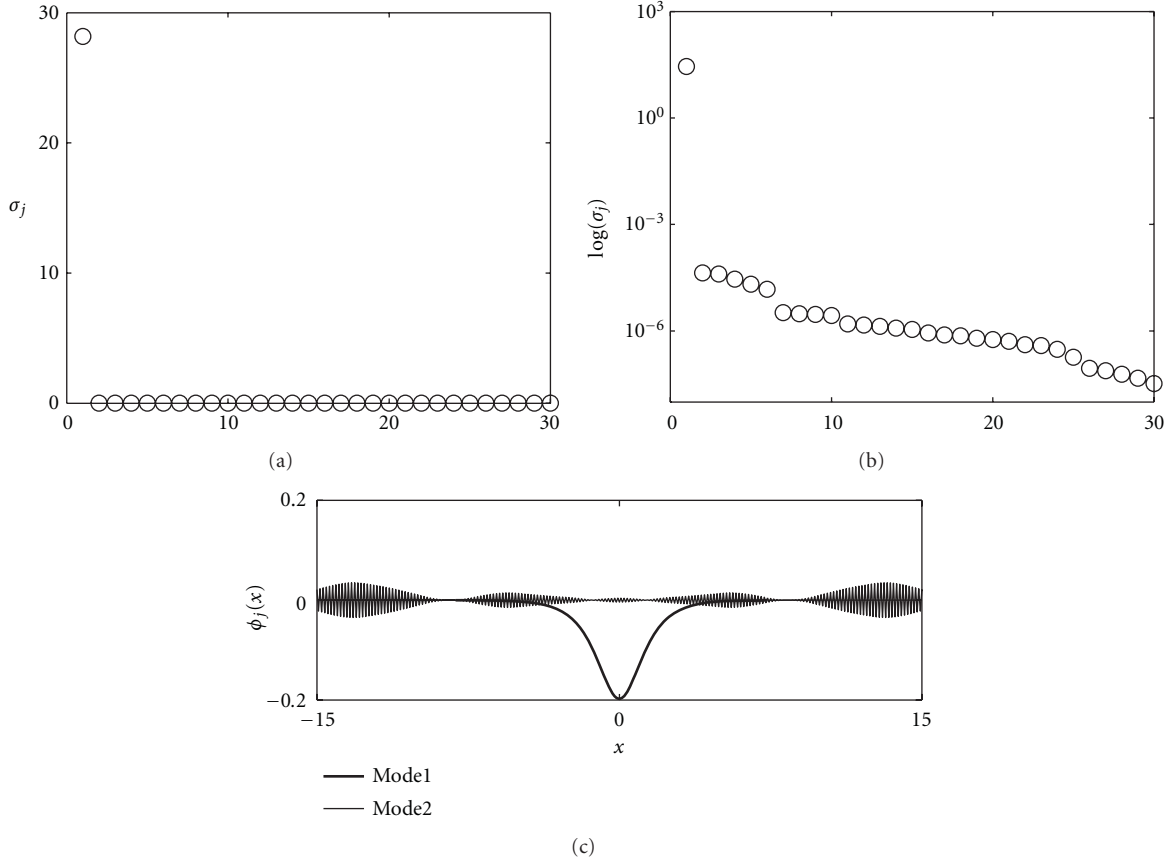


FIGURE 3: Projection of the $N = 1$ evolution to POD modes. The top two figures are the singular values σ_j of the evolution demonstrated in (1) on both a regular scale and log scale. This demonstrates that the $N = 1$ soliton dynamics is primarily a single-mode dynamics. The first two modes are shown in the bottom panel. Indeed, the second mode is meaningless and is generated from noise and numerical roundoff.

where

$$\begin{aligned}\alpha_{jk} &= \frac{(\phi_{j_{xx}}, \phi_k)}{2}, \\ \beta_{jkl} &= \left(|\phi_j|^2 \phi_k, \phi_l \right), \\ \sigma_{jkl} &= \left(\phi_j^2 \phi_k^*, \phi_l \right),\end{aligned}\quad (23)$$

and the initial values of the two components are given by

$$\begin{aligned}a_1(0) &= \frac{(2\text{sech}(x), \phi_1)}{(\phi_1, \phi_1)}, \\ a_2(0) &= \frac{(2\text{sech}(x), \phi_2)}{(\phi_2, \phi_2)}.\end{aligned}\quad (24)$$

This gives a complete description of the two-mode dynamics predicted from the SVD analysis.

The 2×2 system (22) can be easily simulated with any standard numerical integration algorithm (e.g., fourth-order Runge-Kutta). Before computing the dynamics, the inner products given by α_{jk} , β_{jkl} and σ_{jkl} must be calculated along with the initial conditions $a_1(0)$ and $a_2(0)$.

Note that the two-mode dynamics does a good job in approximating the solution as demonstrated in Figure 6.

However, there is a phase drift that occurs in the dynamics that would require higher precision in both taking time slices of the full PDE and more accurate integration of the inner products for the coefficients. Indeed, the most simple trapezoidal rule has been used to compute the inner products, and its accuracy is somewhat suspected. Higher-order schemes could certainly help improve the accuracy. Additionally, incorporation of the third mode could also help. In either case, this demonstrates sufficiently how one would in practice use the low-dimensional structures for approximating PDE dynamics.

4. Cubic-Quintic Ginzburg-Landau's Equation

As a more complicated example, we consider the master mode-locking model that describes the evolution of the nonlinear polarization rotation mode-locking system. The master mode-locking model is known as the cubic-quintic Ginzburg-Landau equation (CQGLE). The model describes the averaged pulse evolution in a ring cavity laser subjected to the combined effect of chromatic dispersion, fiber birefringence, self- and cross-phase modulations for the two orthogonal components of the polarization vector in the fast- and slow-fields, bandwidth-limited gain saturation, cavity attenuation, and the intensity-discriminating element

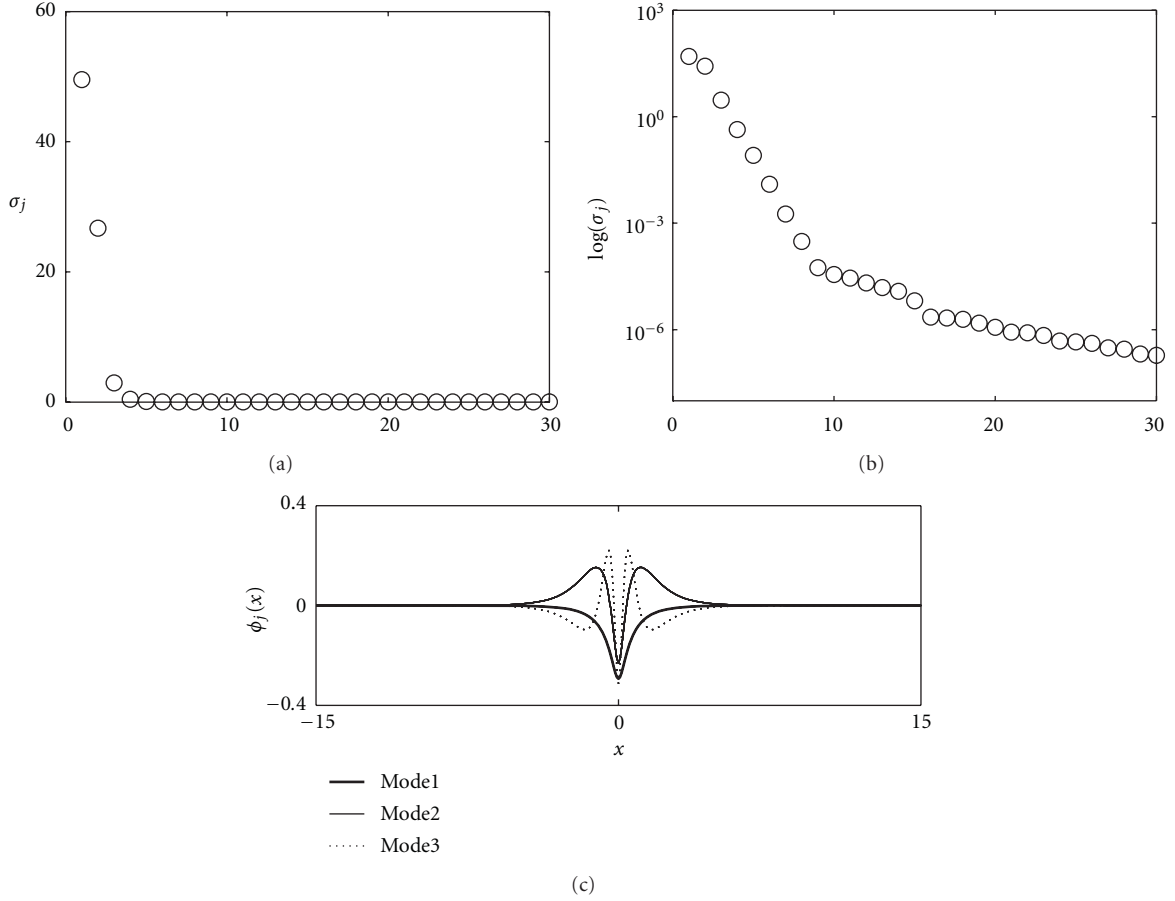


FIGURE 4: Projection of the $N = 2$ evolution to POD modes. The top two figures are the singular values σ_j of the evolution demonstrated in (2) on both a regular scale and a log scale. This demonstrates that the $N = 2$ soliton dynamics is primarily a two-mode dynamics as these two modes contain approximately 95% of the evolution energy. The first three modes are shown in the bottom panel.

(saturable absorber) of the cavity. In particular, the equation takes the form

$$\begin{aligned} i \frac{\partial u}{\partial Z} + \frac{D}{2} \frac{\partial^2 u}{\partial T^2} + \gamma |u|^2 u - \nu |u|^4 u \\ = ig(Z) \left(1 + \tau \frac{\partial^2}{\partial T^2} \right) u - i\delta u + i\beta |u|^2 u - i\mu |u|^4 u, \end{aligned} \quad (25)$$

where

$$g(Z) = \frac{2g_0}{1 + \|u\|^2/e_0} = \frac{2g_0}{1 + (1/e_0) \int_{-\infty}^{\infty} |u|^2 dT}. \quad (26)$$

Here u represents the complex envelope of the electric field propagating in the fiber. The independent variables Z and T denote the propagating distance (number of cavity round-trips) and the time in the rest frame of the pulse, respectively. D characterizes the dispersion in the cavity and is positive for anomalous dispersion and negative for normal dispersion. We will restrict ourselves to the case of anomalous dispersion ($D > 0$) which is consistent with experiments presented in [3, 4]. The rest of the parameters are also assumed to be positive throughout this paper, which is usually the case for physically realizable laser systems [11]. The parameter γ represents the self-phase modulation of the field which results primarily

from the nonlinearity (Kerr) of the refractive index, while ν (quintic modification of the self-phase modulation), β (cubic nonlinear gain), and μ (quintic nonlinear loss) arise directly from the averaging process in the derivation of the CQGLE [10, 11].

For the linear dissipative terms (the first three terms on the right-hand side of the CQGLE), δ is the distributed total cavity attenuation. The gain $g(Z)$, which is saturated by the total cavity energy (L^2 -norm) $\|u\|^2$, has two control parameters g_0 (pumping strength) and e_0 (saturated pulse energy). In what follows, we will assume without loss of generality that $e_0 = 1$ so that the cavity gain is totally controlled by g_0 . The parameter τ characterizes the parabolic bandwidth of the saturable gain. Unless specified otherwise, the parameters are assumed to be $D = 0.4$, $\gamma = 1$, $\nu = 0.01$, $\tau = 0.1$, $\delta = 1$, $\beta = 0.3$, and $\mu = 0.02$. These parameters are physically achievable in typical ring cavity lasers [11].

To obtain a low-dimensional model that is able to describe the multipulsing transition of the CQGLE as a function of the gain parameter g_0 , we consider a combination of POD modes $\vec{\phi}_j$ from different regions. The underlying idea is to use the dominating POD modes from different attractors of the CQGLE so that the resulting low-dimensional system

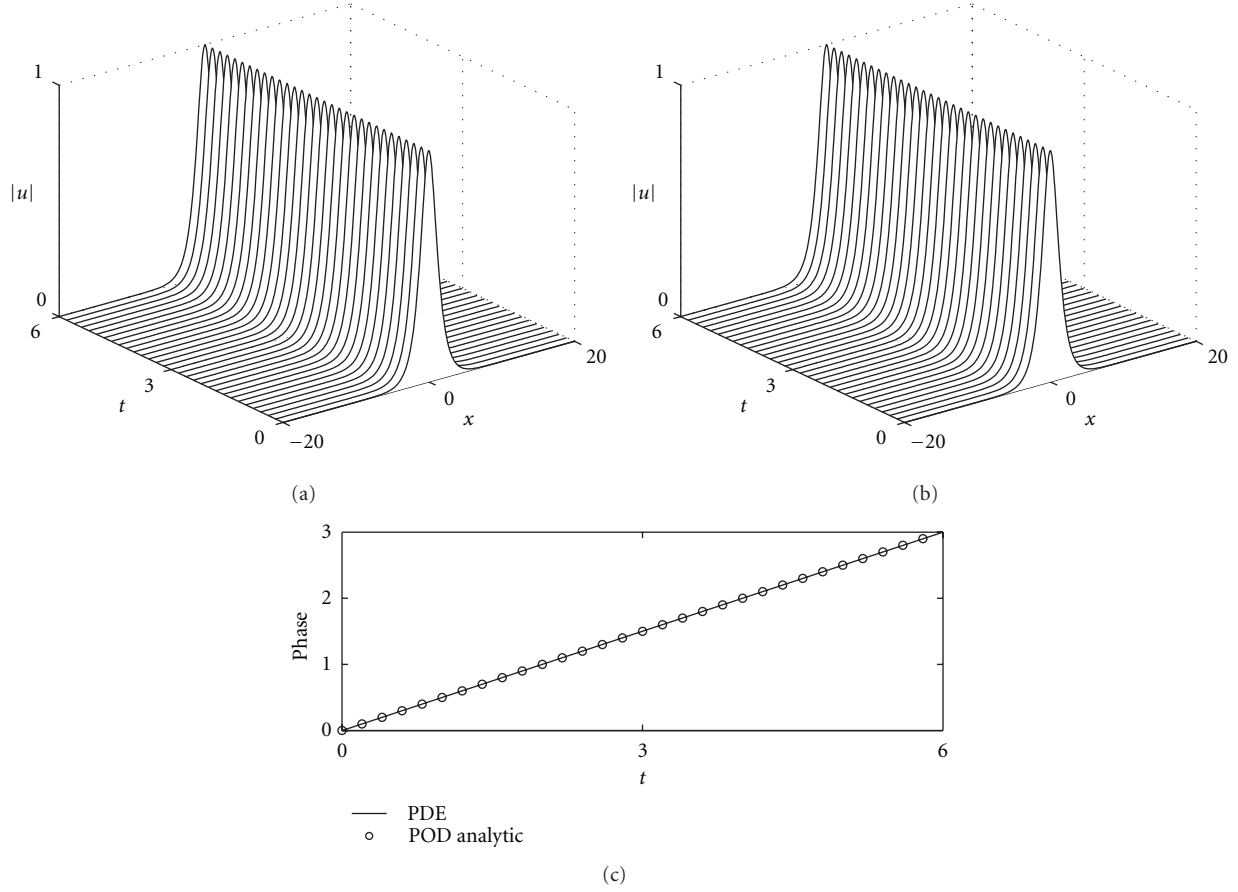


FIGURE 5: Comparison of (a) full PDE dynamics and (b) one-mode POD dynamics. In the bottom figure, the phase of the pulse evolution at $x = 0$ is plotted for the full PDE simulations and the one-mode analytic formula (circles) given in (18).

carries as much information as possible and thus approximates the mode-locking dynamics better [40]. We illustrate this by combining the first m modes from the single-pulse region with the first n modes from the double-pulse region.

Denote S as the union of the two sets of orthonormal basis mentioned above, that is,

$$S = \{\vec{\phi}_1^{(1)}, \dots, \vec{\phi}_m^{(1)}, \vec{\phi}_1^{(2)}, \dots, \vec{\phi}_n^{(2)}\}. \quad (27)$$

Here $\vec{\phi}_j^{(1)}$ and $\vec{\phi}_j^{(2)}$ are the POD modes computed from the single-pulse and double-pulse region, respectively. The original field u can be projected onto the elements of S as

$$u = e^{i\theta_1} \left(a_1 S_1 + \sum_{j=2}^{m+n} a_j e^{i\psi_j} S_j \right), \quad (28)$$

where S_j represent the elements of the combined basis S , a_j are the modal amplitudes, θ_1 is the phase of the first mode, and ψ_j denote the phase differences with respect to θ_1 . One can obtain a low-dimensional system governing the evolutions of the modal amplitudes a_k and the phase differences ψ_k by substituting (28) into the CQGLE, multiplying the resulting equation by the complex conjugate of S_k ($k = 1, \dots, m+n$), integrating over all T and then separating the result into real and imaginary parts. The reduced

system has, however, a complicated form due to the fact the elements in the combined basis S are not all orthonormal to each other. To address this issue, one can orthogonalize the combined basis S prior to the projection to obtain a new basis $\{\Phi_j\}_{j=1}^{m+n}$, which can be achieved by the Gram-Schmidt algorithm. The reduced model derived from the new basis Φ_j has a simpler form than the one derived directly from S , since it does not have terms that are due to nonorthogonality of the basis functions. This reduced model will be called the $(m+n)$ model, which indicates the number of modes taken from the single-pulse (m) and double-pulse (n) region.

We specifically consider the $(1+3)$ model in this work [44]. The orthonormal basis $\{\Phi_j\}_{j=1}^4$ obtained using the Gram-Schmidt algorithm is shown in Figure 7. By construction, the first mode Φ_1 in the new basis is identical to $\vec{\phi}_1^{(1)}$. The second mode Φ_2 contains a tall pulse which is identical to the first mode at $T = -6$ and a small bump in the origin. In general, this tall pulse can be located on either the left or the right of the origin, depending on the data set \mathbf{X} for which the POD modes are computed from. The other two modes have complicated temporal structures, and their oscillatory nature is mainly due to the orthogonalization.

4.1. Classification of Solutions of the $(1+3)$ Model. In this section, we study the dynamics governed by the $(1+3)$ model,

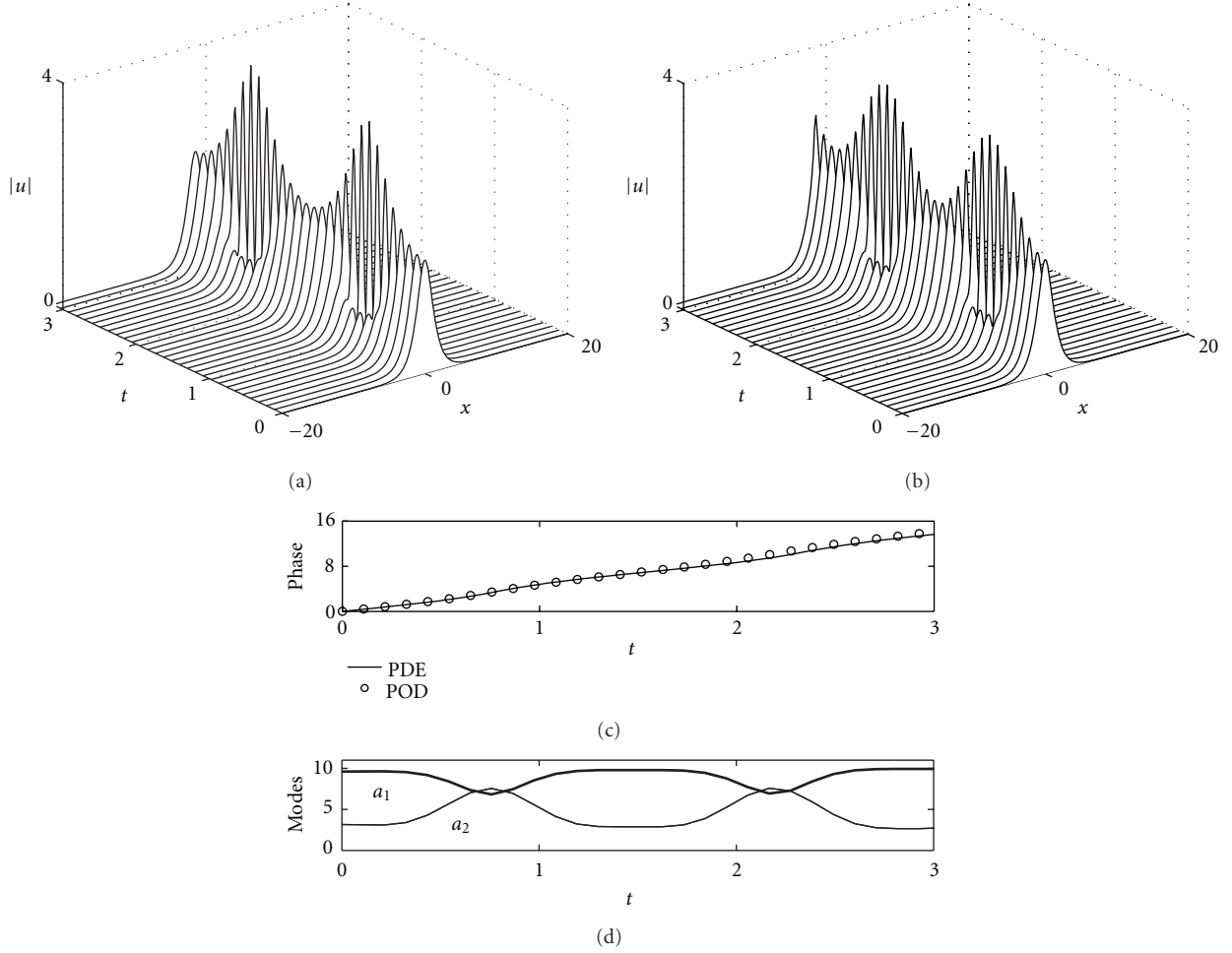


FIGURE 6: Comparison of (a) full PDE dynamics and (b) two-mode POD dynamics. In the bottom two figures, the phase of the pulse evolution at $x = 0$ (middle panel) is plotted for the full PDE simulations and the two-mode dynamics along with the nonlinear oscillation dynamics of $a_1(t)$ and $a_2(t)$ (bottom panel).

whose basis functions are shown in Figure 7. This four-mode model is 7 dimensional in the sense that the dynamic variables are the four modal amplitudes a_1, a_2, a_3, a_4 and the three phase differences ψ_2, ψ_3, ψ_4 . To effectively characterize any periodic behavior in the system, it is customary to use the new set of variables

$$\begin{aligned} x_1 &= a_1, \\ x_j &= a_j \cos \psi_j, \quad y_j = a_j \sin \psi_j \end{aligned} \quad (29)$$

for $j = 2, 3, 4$, so that the formal projection of the field is given by

$$u = e^{i\theta_1} \left(x_1 \Phi_1 + \sum_{j \geq 2} (x_j + iy_j) \Phi_j \right). \quad (30)$$

Figure 8 shows the solution of the (1+3) model expressed in terms of the above variables and the reconstructed field u at different cavity gain g_0 . At $g_0 = 3$ (top panel), the (1+3) model supports a stable fixed point with $x_1 = 2.2868$ while the other variables are nearly zero; that is, the steady state content of u mainly comes from Φ_1 , and; thus, a

single mode-locked pulse centered at the origin is expected. Increasing g_0 eventually destabilizes the fixed point, and a periodic solution is formed (middle panel) which corresponds to a limit cycle in the 7-dimensional phase space. The reconstructed field has a tall pulse centered at the origin due to the significant contribution of x_1 (and hence Φ_1). The small-amplitude side pulses are resulted from the linear combination of the higher-order modes present in the system, and their locations are completely determined by the data matrix \mathbf{X} representing the double-pulse evolution of the CQGLE. Further increasing g_0 causes the limit cycle to lose its stability and bifurcate to another type of stable fixed point. Unlike the first fixed point, this new fixed point has significant contributions from both x_1 and y_2 which are associated to Φ_1 and Φ_2 . Since the other variables in the system become negligible when $Z \rightarrow \infty$, a double-pulse solution is formed. The (1+3) model is able to describe both the single-pulse and double-pulse evolution of the CQGLE. The two key features of the periodic solution of the CQGLE are explicitly revealed: (i) the existence of side pulses and (ii) the small-amplitude oscillations of the entire structure. In fact, these two features are also observed in the full

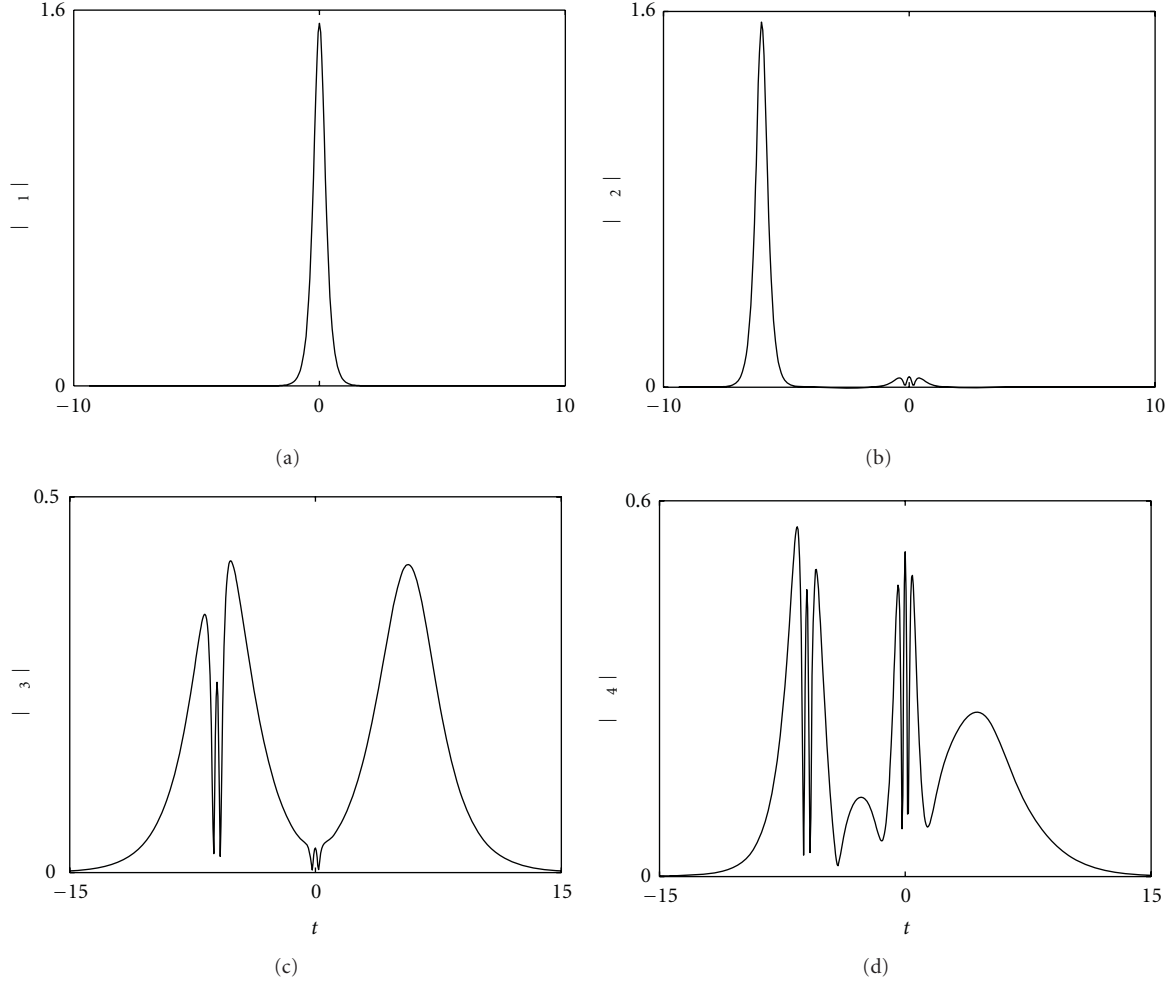


FIGURE 7: Basis functions used in the (1 + 3) model. These functions are obtained by applying the Gram-Schmidt algorithm to the set $S = \{\phi_1^{(1)}, \phi_1^{(2)}, \phi_2^{(2)}, \phi_3^{(2)}\}$.

simulations of the CQGLE. The (1 + 3) model also captures the amplification and suppression of the side pulses in the formation of the double-pulse solution in the CQGLE.

We construct a global bifurcation diagram in Figure 9 to characterize the transition between the single-pulse and double-pulse solutions of the (1 + 3) model. The diagram shows the total cavity energy of the reconstructed field u as a function of the cavity gain g_0 , which is obtained using MATCONT [53]. In terms of the dynamic variables, the energy of the field is given by

$$\|u\|^2 = x_1^2 + \sum_{j \geq 2} (x_j^2 + y_j^2). \quad (31)$$

In the diagram, the branch with the lowest energy corresponds to the single-mode-locked pulses of the (1 + 3) model. With increasing g_0 , the reconstructed mode-locked pulse readjusts its amplitude and width accordingly to accommodate the increase in the cavity energy. The branch of the single-pulse solutions is stable until $g_0 = 3.181$ where a Hopf bifurcation occurs. The fluctuation in the cavity energy as a result of the periodic solution is small at first but increases gradually with g_0 . At $g_0 = 3.764$, the periodic solution becomes unstable by a fold bifurcation of the limit cycle.

In this case, a discrete jump is observed in the bifurcation diagram, and a new branch of solutions is reached. This new branch represents the double-pulse solution of the system and has higher energy than the single-pulse branch and the periodic branch.

The bifurcation diagram also illustrates that, in the region $1.681 \leq g_0 \leq 3.181$, the single-pulse and the double-pulse solutions are stable simultaneously. This bistability is not restricted to the (1 + 3) model as it also happens in the CQGLE as well [10, 17]. Given a set of parameters, the final form of the solution is determined by the basin of attraction of the single-pulse and double-pulse branches rather than the initial energy content. When the initial condition is selected such that it is “close” to the double-pulse branch (characterized by the Euclidean distance between them), the result of linear analysis holds, and a double-pulse mode-locked state can be achieved. For random initial data that is far away from both branches, the system tends to settle into the single-pulse branch as it is more energetically favorable [12].

4.2. Comparison of Different (m + n) Models. To demonstrate that the (1 + 3) model is the optimal (m + n) model to

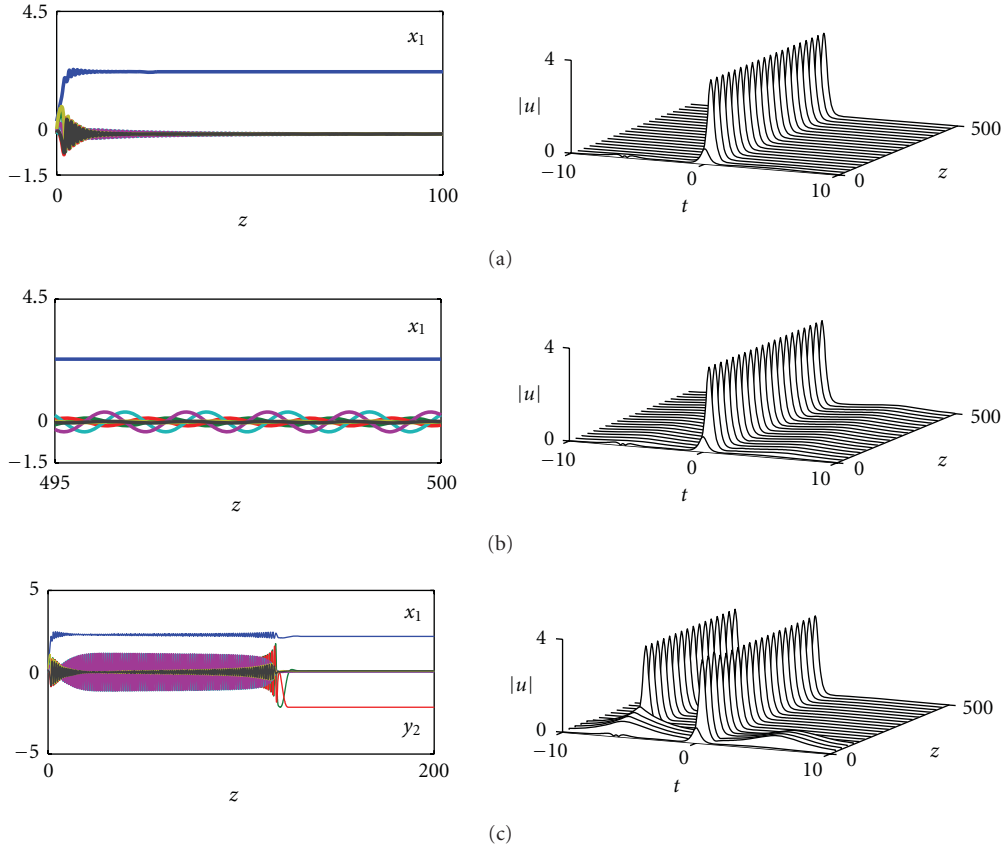


FIGURE 8: Left: the solution of the (1+3) model at $g_0 = 3$ (top), $g_0 = 3.24$ (middle), and $g_0 = 3.8$ (bottom). Here, only the significant variables (in absolute value) are labeled. Right: the corresponding reconstructed field u from the variables of the (1+3) model.

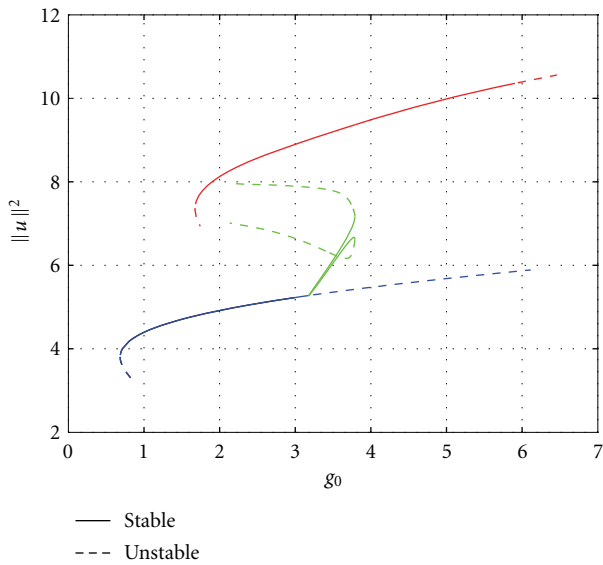


FIGURE 9: Bifurcation diagram of the total cavity energy of the reconstructed field u as a function of g_0 . Here the bottom branch (blue) represents the single-pulse solution, and the top branch (red) represents the double-pulse solution. The middle branch (green) denotes the extrema of the energy of the periodic solution.

characterize the transition from a single-mode-locked pulse into two pulses that occurs in the CQGLE, we consider the (1+2) model whose results are shown in the top row of Figure 10. This model can be derived by setting the variables x_4 and y_4 in the (1+3) model to zero. At $g_0 = 3$ a tall stable pulse is formed at $T = -6$ together with a small residual at the origin. The entire structure has close resemblance to Φ_2 from the Gram-Schmidt procedure (see Figure 7). The tall pulse agrees with the single-pulse solution of the CQGLE quantitatively. When the structure loses its stability, a periodic solution is formed which persists even at unrealistically large values of cavity gain such as $g_0 = 7$.

The middle row of the same figure shows the numerical simulations of the (1+4) model, which is derived from the combination of the first POD mode from the single-pulse region with the first four modes from the double-pulse region. This model is able to reproduce all the key dynamics observed during the multipulsing phenomenon shown in Figure 8. The difference between the (1+4) model and the (1+3) model is the locations at which the bifurcations occur. In the previous section we showed that the single-pulse solution described by the (1+3) model loses stability at $g_0 = 3.181$ (Hopf bifurcation), and the subsequent periodic solution bifurcates into the double-pulse solution at $g_0 = 3.764$. For the (1+4) model, these two bifurcations occur

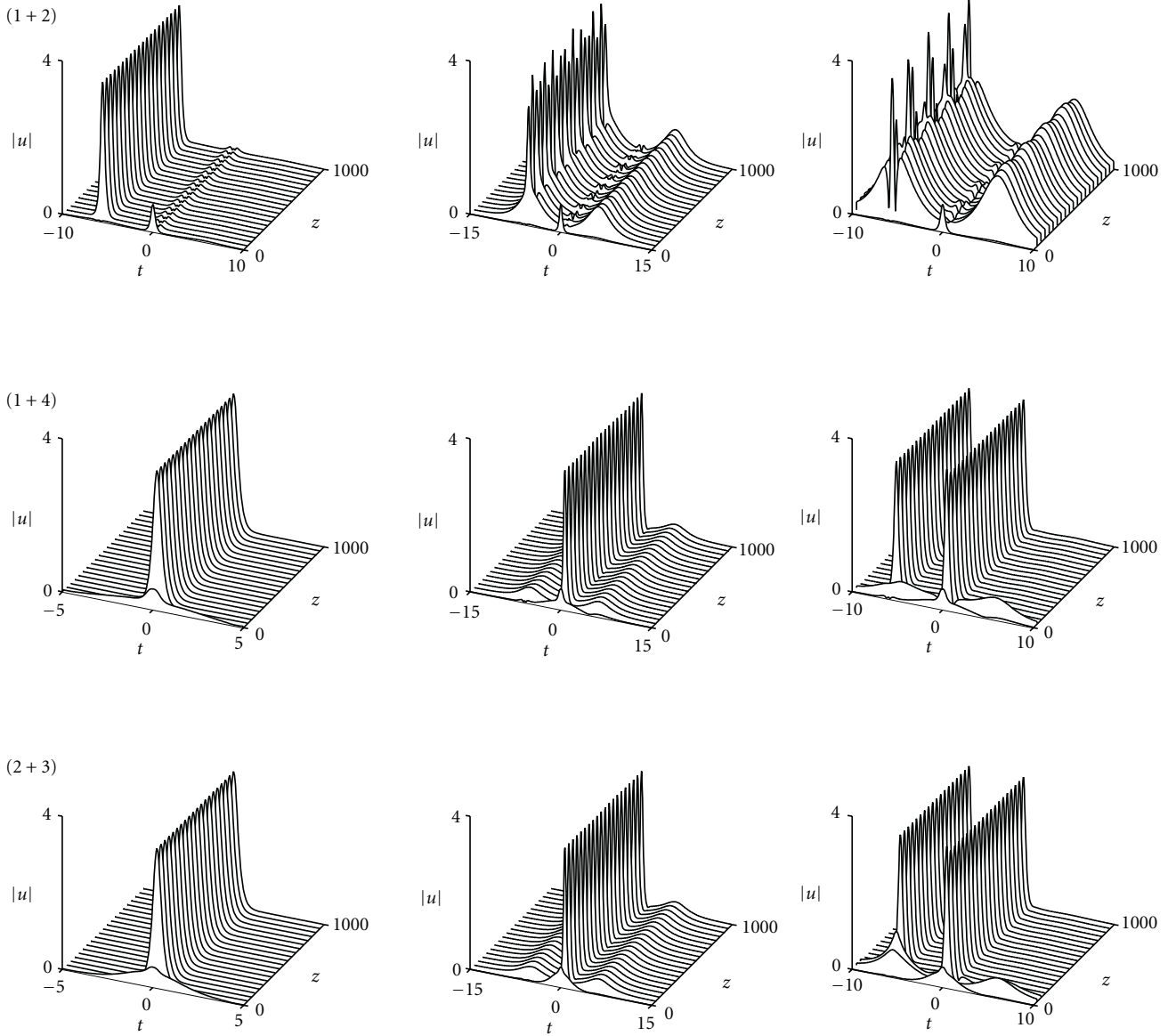


FIGURE 10: Top: the reconstructed field of the (1 + 2) model at $g_0 = 3$ (left), $g_0 = 4.3$ (middle), and $g_0 = 7$ (right). Middle: the reconstructed field of the (1 + 4) model at $g_0 = 3$ (left), $g_0 = 3.4$ (middle), and $g_0 = 3.8$ (right). Bottom: the reconstructed field of the (2 + 3) model at $g_0 = 3$ (left), $g_0 = 3.4$ (middle), and $g_0 = 3.7$ (right).

at $g_0 = 3.173$ and $g_0 = 3.722$, respectively, which are closer to the values predicted using the full simulations of the CQGLE ($g_0 \approx 3.15$ and $g_0 \approx 3.24$). The (2 + 3) model (bottom row of Figure 10) produces similar results as the (1 + 3) and the (1 + 4) models, with pulse transitions occurring at $g_0 = 3.177$ and 3.678 . The comparison here shows that the third POD mode $\tilde{\phi}_3^{(2)}$ from the double-pulse region is essential for getting the right pulse transition. Once this mode is included, further addition of the POD modes has only a minor effect on the accuracy of the low-dimensional model.

5. Waveguide Array Mode-Locking Model

The waveguide array mode-locking model (WGAML) describes the mode-locking process in a fiber waveguide

system that combines the saturable absorption of the waveguide with the saturating and the bandwidth-limited gain of erbium-doped fiber [12, 14]. The governing equations for such a system are given by

$$\begin{aligned}
 i \frac{\partial A_0}{\partial Z} + \frac{D}{2} \frac{\partial^2 A_0}{\partial T^2} + \beta |A_0|^2 A_0 \\
 - ig(Z) \left(1 + \tau \frac{\partial^2}{\partial T^2} \right) A_0 + iy_0 A_0 + CA_1 = 0,
 \end{aligned} \tag{32}$$

$$i \frac{\partial A_1}{\partial Z} + C(A_0 + A_2) + iy_1 A_1 = 0,$$

$$i \frac{\partial A_2}{\partial Z} + CA_1 + iy_2 A_2 = 0,$$

with

$$g(z) = \frac{2g_0}{1 + \|A_0\|^2/e_0}, \quad (33)$$

where A_0 , A_1 , and A_2 are the envelopes of the electric field in waveguides 0, 1, and 2, respectively. The normalized parameters used in the following sections are

$$(D, \beta, C, \gamma_0, \gamma_1, \gamma_2, \tau, e_0) = (1, 8, 5, 0, 0, 10, 0.1, 1), \quad (34)$$

where D controls the strength and the type (normal or anomalous) of the chromatic dispersion, β is the strength of the Kerr nonlinearity, g is the saturating gain, τ is the bandwidth of the gain, γ_j is a linear loss in the j th waveguide, and C controls the strength of the evanescent coupling between adjacent waveguides. For a derivation and description of the governing equations, see the work of Proctor and Kutz [14] as well as Kutz and Sandstede [12]. As shown by Kutz and Sandstede [12], the WGAML undergoes a region of chaotic translating behaviors for sufficiently large values of g_0 . This creates major difficulties in applying reduced dimensional models based on the POD [45]. Therefore, in this paper we restrict ourselves to the set of solutions that are even up to a translation in T .

In order to develop a low-dimensional model, we assume that

$$\begin{aligned} A_0(T, z) &= \sum_{j=1}^N a_j(z) \phi_j^{(0)}(T), \\ A_1(T, z) &= \sum_{j=1}^N b_j(z) \phi_j^{(1)}(T), \\ A_2(T, z) &= \sum_{j=1}^N c_j(z) \phi_j^{(2)}(T), \end{aligned} \quad (35)$$

where $\phi_j^{(i)}$ is the j th POD mode from the i th waveguide, and N is the total number of retained POD modes. Substituting (35) into the WGAML in (32) and taking an inner product with each of $\phi_j^{(i)}$ gives the following system of ordinary differential equations

$$\begin{aligned} \frac{\partial a_n}{\partial Z} &= \left(i\frac{D}{2} + g\tau \right) \sum_{j=1}^N \langle \phi_n^{(0)}, \partial_T^2 \phi_j^{(0)} \rangle a_j + (g - \gamma_0) a_n \\ &+ iC \sum_{j=1}^N \langle \phi_n^{(0)}, \phi_j^{(1)} \rangle b_j \\ &+ i\beta \sum_{j=1}^N \sum_{k=1}^N \sum_{m=1}^N \langle \phi_n^{(0)}, \phi_k^{(0)} \phi_j^{(0)} \phi_m^{(0)*} \rangle a_j a_k a_m^*, \end{aligned} \quad (36)$$

$$\frac{\partial b_n}{\partial Z} = iC \sum_{j=1}^N \left(\langle \phi_n^{(1)}, \phi_j^{(0)} \rangle a_j + \langle \phi_n^{(1)}, \phi_j^{(2)} \rangle c_j \right) - \gamma_1 b_n,$$

$$\frac{\partial c_n}{\partial Z} = iC \sum_{j=1}^N \langle \phi_n^{(2)}, \phi_j^{(1)} \rangle b_j - \gamma_2 c_n,$$

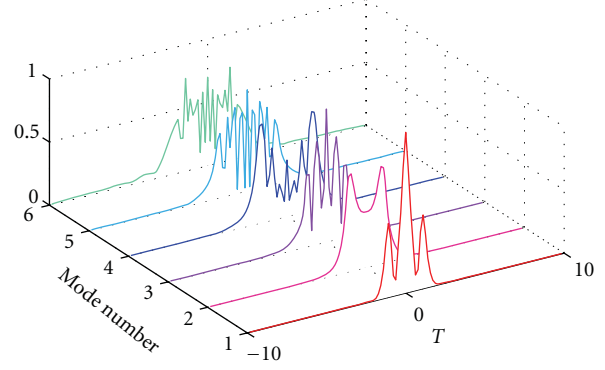


FIGURE 11: POD modes taken from the combined data set for the 0th waveguide that are capable of qualitatively reproducing the dynamics observed in the full WGAML model.

where $\langle u, v \rangle = \int_{-\infty}^{\infty} u^* v dT$ and

$$g = \frac{2g_0}{1 + \sum_{j=1}^N |a_j|^2/e_0}. \quad (37)$$

The resulting system is a set of $3N$ nonlinear evolution equations for the coefficient of the POD modes. This reduced set of equations is quite generic and is valid for any set of orthonormal functions, whether obtained through the POD or some other means. In order for this reduced model to be an accurate approximation of the full evolution equations over a range of g_0 , the $\phi_j^{(i)}$ must be chosen carefully. The process through which the $\phi_j^{(i)}$ were obtained is described in Section 5.1. In Section 5.2, we use these modes to determine the bifurcations of the reduced model.

5.1. POD Mode Selection. In order to accurately capture the dynamics of the WGAML, the POD modes must be drawn from a particular set of data. Unlike with the CQGLE case, we do not combine POD modes drawn from different regimes through an orthonormalization process. Instead, we combine individual runs obtained at different values of g_0 into one combined dataset. Each individual run consists of a short-time but high-resolution solution for $Z \in [0, 10]$ with a sampling period of $\Delta Z = 5 \times 10^{-3}$. The initial conditions used were a small perturbation away from the attractor for the fixed value of g_0 . By combining these individual runs into a single data set, the SVD provides the set of POD modes that best captures the energy of the global dynamics through the transition from one to two pulses.

Figure 11 shows the first six POD modes generated using the methodology described in the preceding paragraph for solutions of the even WGAML model. Only the modes of the 0th waveguide are shown. However, there are two additional sets of modes, one for each of the other two waveguides. The data set includes information from the single-pulse, the breather, the chaotic, and the double-pulse solutions. These six modes capture over 99% of the modal energy, and 99.9% may be captured by including an additional four modes. The resulting modes do not resemble the modes that would be

acquired from any run with a fixed value of g_0 . Indeed, the POD modes appear to be a nontrivial combination of the modes from all the runs at different gain values. These modes would be impossible to predict *a priori* even with knowledge about the solutions of the system.

5.2. Low-Dimensional Dynamics. In this section, the reduced model is used to study the multipulsing transition of the WGAML. The reduced model is obtained by the Galerkin projection of WGAML model in (32) onto the global POD modes in Figure 11. This produces a system of differential equations of the form shown in (36). To determine the validity of the reduced model, we compare the full version of the evolution equations and the POD model dynamics for fixed values of g_0 in the relevant ranges for single-pulse, breather, chaotic, and double-pulse solutions using low-amplitude noise as the initial condition in both the full and reduced dynamics. The evolution considered is for a long period of time so that the attractor is reached for each value g_0 considered. In this manner, the full and reduced dynamics of the WGAML starting from a cold-cavity configuration can be compared. In addition to comparing the solutions at a single value of g_0 , we also compare the branches of single-pulse and breather solutions in both models. This allows the multipulsing transition to be studied in both systems.

The first row of Figure 12 shows the single-pulse, breather, chaotic, and double-pulse solutions reconstructed using a six-mode POD model, ordered from left to right. To obtain these solutions, the reduced model was evolved forward for 1000 units in Z starting with a low-amplitude white-noise initial condition. These results compare favorably with the same four regimes of the even WGAML dynamics shown in the second row of Figure 12, whose solutions were obtained by evolving for 200 units in Z starting from low amplitude even white noise. The reduced model qualitatively captures the dynamics and the profile of the solution. The primary difference is the value of g_0 at which these solutions are obtained. The stationary solutions of the POD model lose stability at lower values of g_0 than the stationary solutions of the WGAML. Further, the breather solutions in the POD model remain stable for larger values of g_0 than those in the WGAML. Due to the vastly smaller dimension of the reduced model and the range of g_0 for which the POD generated differential equations are valid, some disparity between the models is inevitable.

The advantage of the reduced model over the full dynamics is that the bifurcation diagram, including the stability and bifurcations of periodic solutions, can be explicitly calculated and categorized in the reduced model. The bifurcation software, MATCONT [53], was used to track and compute the stability of the single-pulse and breather solutions of the WGAML. The chaotic and the double-pulse solutions were obtained using direct numerical simulations. While other solution branches may exist, they do not appear as attractors for white-noise initial conditions and are not discussed here.

The first row of Figure 13 shows the bifurcation diagram of the reduced model including solution branches for the stationary, breather, chaotic, and double-pulse solutions. The branches marked in solid (blue) curves are linearly stable

stationary solutions, and the branches marked in dashed (red) curves are linearly unstable stationary solutions. For the periodic solutions, the branches marked by black x symbols and denote the extrema of

$$\|\vec{A}\|^2 = \|A_0\|^2 + \|A_1\|^2 + \|A_2\|^2, \quad (38)$$

where $\|A_n\|^2 = \int_{-\infty}^{\infty} |A_n(T)|^2 dT$. If no extrema exist, the mean value $\|\vec{A}\|$ is denoted with a black dot. This bifurcation diagram reveals the sequence of bifurcations responsible for the multi-pulse transition. At the lowest values of g_0 , the only stable solution is the quiescent (trivial) solution because the gain is insufficient to overcome the cavity losses. The first nontrivial solution is the single-pulse solution, which first appears from the saddle-node bifurcation that is labeled (a) in Figure 13 at $g_0 = 0.7229$. The value of g_0 represents the minimum gain needed for a single-pulse solution to exist in the WGAML. Although only the modes of the 0th waveguide are shown, these single-pulse solutions distribute energy in all three of the waveguides, and the presence of energy in the other two waveguides is critical for the stabilization of these solutions. For larger values of g_0 , there are two branches of single-pulse solutions that emanate from (a). The first branch is a high-amplitude stable branch of solutions, and the other is a low-amplitude unstable branch. Following the low-amplitude unstable branch of solutions, another saddle-node bifurcation, which is labeled (b) in Figure 13, occurs. This bifurcation creates a stable branch of low-amplitude stationary solutions. Because their basin of attraction is small, these solutions are unlikely to appear for white-noise initial conditions. They are, however, known to exist in the full WGAML dynamics [29]. This extra branch of stationary solutions loses stability through a Hopf bifurcation at the point labeled (c) in Figure 13. Therefore, the branch of low-amplitude stationary solutions does not play a role in the multi-pulse transition process.

On the other hand, the branch of larger-amplitude solutions participates in the multi-pulse transition. This branch of single-pulse solutions can be shown to be stable. Because we have assumed even solutions, the zero eigenvalue associated with translational invariance does not exist in the low-dimensional system. On the other hand, the zero eigenvalue associated with phase invariance persists. Although the values of the eigenvalues differ, the stability results agree qualitatively with the full results obtained with the Floquet-Fourier-Hill method [29]. For a range of g_0 , all other eigenvalues have negative real parts with the exception of the zero eigenvalue. As g_0 increases, this branch becomes unstable through a supercritical Hopf bifurcation, which is shown in Figure 13 at (d). The Hopf bifurcation occurs when the eigenvalues of the linearized operator include a complex-conjugate pair of eigenvalues with zero real part. As a result, the single-pulse solution becomes unstable, but a stable limit-cycle is generated. These limit cycles are the breather solutions of the WGAML.

As g_0 is increased, the breather solutions themselves will lose stability through two bifurcations in rapid succession. The first of these bifurcations is a period-doubling bifurcation. After the period-doubling bifurcation, the solution is

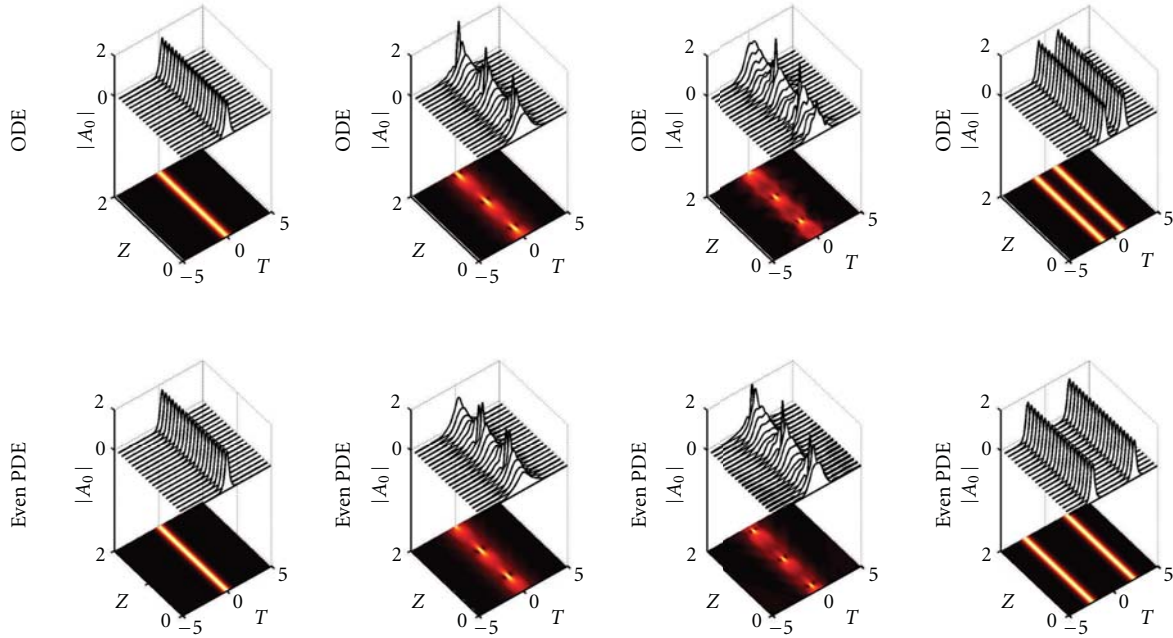


FIGURE 12: Top: surface and pseudocolor plots of the single-pulse, breather, chaotic, and double-pulse solutions computed for the finite-dimensional model at $g_0 = 1.5, 2.5, 3.495,$ and $3.5,$ respectively. Bottom: the same plots for the even WGAML model taken at $g_0 = 2.3, 2.5, 3.1,$ and $3.2,$ respectively. The reduced model accurately reproduces the four behaviors observed.

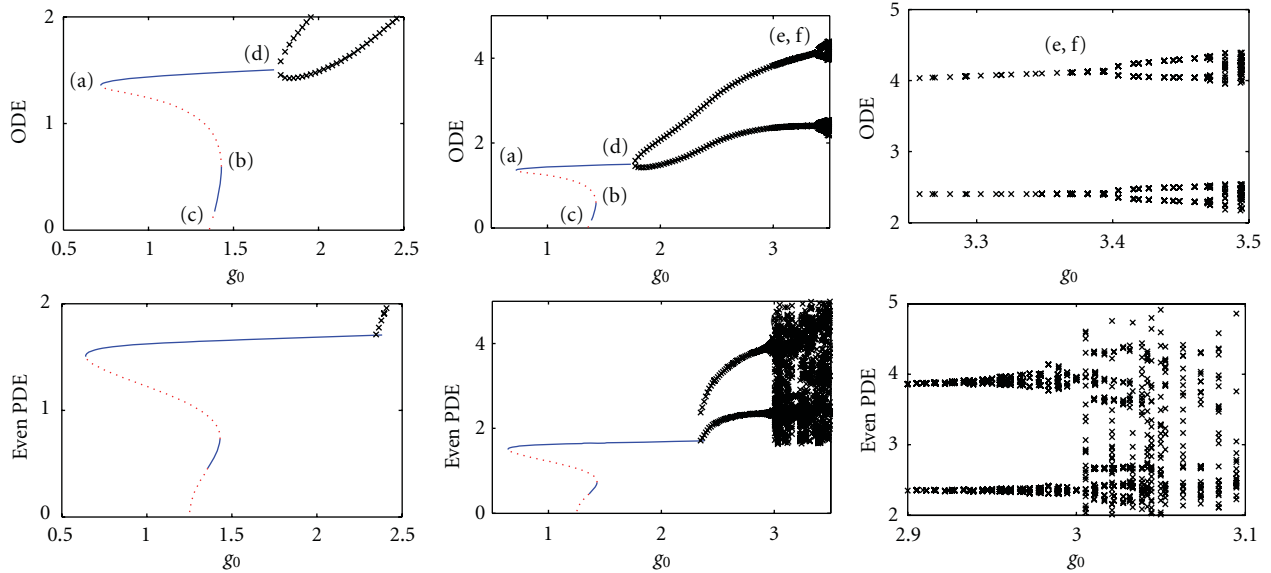


FIGURE 13: Top: the bifurcation diagram of energy (L^2 norm) versus g_0 for the multi-pulse transition in the POD model. Bottom: the bifurcation diagram of the multi-pulse transition of the WGAML model. The different plots show the same diagram with emphasis on different regions of the transition. For the stationary solutions, emphasized on the left, linearly unstable regions are dashed (red) lines while linearly stable regions are solid (blue) lines. Stationary solutions that were not computed explicitly are denoted with dots. For the periodic solutions, the x s are the local extrema of the energy (L^2 norm).

still periodic in Z but with a larger period. In the reduced model, the Floquet multipliers can be computed explicitly. One of the multipliers was found to be -1 , so the bifurcation that occurs is indeed a period-doubling bifurcation. The new stable period-doubled limit cycles almost immediately lose stability through supercritical Neimark-Sacker bifurcation. The Neimark-Sacker bifurcation, also called a Torus

bifurcation or secondary Hopf-bifurcation, occurs when a complex-conjugate pair of the Floquet multipliers leave the unit circle. In this case, the limit cycle loses stability, but a torus that encloses the original limit cycle becomes stable. The Neimark-Sacker bifurcation indicates the presence of quasi-periodic solutions in the POD model. The period doubling and the Neimark-Sacker bifurcations can be seen

TABLE 1: The values of g_0 associated with each bifurcation in the ODE and PDE. The labels correspond to the bifurcations of the ODE in Figure 13. Values in parenthesis are estimated from the same figure.

Label	Bifurcation type	ODE	Even PDE
(a)	Saddle node	0.7229	0.6522
(b)	Saddle node	1.424	1.429
(c)	Hopf	1.398	1.369
(d)	Hopf	1.753	2.404
(e)	Period doubling	3.3872	(3.0 \pm 0.1)
(f)	Neimark-Sacker	3.3873	(3.0 \pm 0.1)

in the top right panel of Figure 13 when the pair of extrema splits at the points labeled (e) and (f). MATCONT is unable to track branches of quasiperiodic solutions, but as shown in Figure 13, further bifurcations occur, and the ODE exhibits chaos. At the same time, the double-pulse solutions are gaining stability, and the system completes the transition from single- to double-pulse solutions.

The bifurcation diagram of the ODE shows remarkable qualitative agreement with the bifurcation diagram of the full WGAML dynamics illustrated in the second row of Figure 13. For the full system, linear stability has only been determined for the stationary solutions [29]. For the stationary solutions, the types of bifurcations agree completely between the reduced and full models. Additionally, the value of g_0 agrees relatively well for all of the bifurcations as shown in Table 1. Although explicit stability results do not exist for the breather solutions, the same qualitative sequence occurs. The breather solutions lose stability around $g_0 = 2.9$ and serves as a route to chaos in Z .

6. Conclusion

The POD method, used here to construct the low-dimensional models for two different mode-locking systems, results as a robust tool for the study of the dynamics of nonlinear evolution equations describing various optical systems. In many cases where the observed dynamics are coherent but not trivial and exhibit various phenomena, the POD is the natural choice to construct a reduced and tractable model. If the model correctly reproduces the observed dynamics, it can then be studied using simpler computational methods and in special cases analytically in order to identify the bifurcations responsible for observed phenomena. The POD methodology can be easily modified for changes in the model. Such robustness of the method, allows one to study the operating regimes of mode-locked lasers as a function of the parameters in the system, specifically the change in gain that occurs during the multi-pulse transition.

For the mode-locking dynamics governed by the CQGLE model, the reduced system obtained via the POD method is able to capture the pulse transition that occurs in the laser when the cavity gain g_0 is increased. It is shown that a four-mode reduction (also known as the (1+3) model) is adequate to capture the transition from a single-mode-locked pulse to two pulses through an intermediate periodic state observed

in the CQGLE. It is found that the form of the single-pulse, double-pulse, and the periodic solutions observed in the full numerics of the CQGLE can be accurately represented by the fixed points and limit cycles of the (1 + 3) model. When g_0 is increased, the fixed point representing the single-mode-locked pulse bifurcates into a stable limit cycle (periodic solution) through a Hopf bifurcation and then into a new type of fixed point (double-pulse solution). The pulse profiles predicted by the (1 + 3) model agree well with those generated by the full system. The model also demonstrates a bistability between the single-pulse solution and the double-pulse solution which also occurs in the CQGLE. The bifurcation diagram can be used as a guideline for achieving different types of solutions by choosing the initial condition appropriately.

For the mode-locking dynamics governed by the WGAML, the reduced model obtained by projecting the even WGAML model onto six global POD modes qualitatively reproduces the dynamics over the relevant range of gain values for which the transition from a single pulse to a double pulse occurs. In particular, for low values of g_0 , the model completely reproduces the dynamics of the single-pulse solution, including its bifurcations in a region of low amplitude solutions discovered earlier [29]. With increasing gain g_0 , the single-pulse solution bifurcates to a limit cycle via a Hopf bifurcation, matching the study of WGAML model [12]. Our analysis indicates that as the limit cycle grows when g_0 is further increased, it will eventually become chaotic through a series of bifurcations, initiated by a period-doubling bifurcation and then almost immediately followed by a Neimark-Sacker (Torus) bifurcation. The chaos in the Z direction is terminated by the double-pulse solution gaining stability and becoming the attractor for low-amplitude solutions. Here, the WGAML was modeled as a three-waveguide array. However, using the same methodology, a system of N -waveguide arrays could be studied. Only minor modifications to (36) are required to model a system with a different number of waveguides.

The parameters in the two reduced models constructed here indicate the physical setup of the mode-locking system, and their values were considered as fixed. By allowing variation of some of the parameters, the reduced models can serve as a framework for investigating optimal mode-locking and studying the nontrivial behavior observed in the multipulsing transition [21, 24]. Specifically, by using the described methodology, the application of standard continuation methods (such as MATCONT) and stability analysis to the reduced model allows for the constructing of a bifurcation diagram for the reduced model. Such a diagram indicates the impact of the parameters on the multi-pulse transition. It can reveal operating regimes for which multi-pulse transition is abrupt or results with a more complex behavior. Furthermore, it can be used to determine the optimal working regime for the mode-locking laser (maximal suppression of the multi-pulse instability), by searching for a set of parameters for which there is a maximal range of input cavity gain that supports stable single-pulse solutions.

In addition, models based on the POD are sometimes able to predict dynamics in regions outside of the data set,

where the POD modes were computed, the low-dimensional model can be used to find interesting regions within the system without having to develop an appropriate approach. Once these regions have been identified, by altering the used data set, a more accurate representation of the region can be developed. In summary, the POD reduction gives a completely new and insightful way to explore the dynamics and bifurcations of a given system.

Acknowledgments

J. N. Kutz acknowledges support from the National Science Foundation (NSF) (DMS-0604700) and the US Air Force Office of Scientific Research (AFOSR) (FA9550-09-0174).

References

- [1] H. A. Haus, "Mode-locking of lasers," *IEEE Journal on Selected Topics in Quantum Electronics*, vol. 6, no. 6, pp. 1173–1185, 2000.
- [2] J. N. Kutz, "Mode-locked soliton lasers," *SIAM Review*, vol. 48, no. 4, pp. 629–678, 2006.
- [3] K. Tamura, H. A. Haus, and E. P. Ippen, "Self-starting additive pulse mode-locked erbium fibre ring laser," *Electronics Letters*, vol. 28, no. 24, pp. 2226–2228, 1992.
- [4] H. A. Haus, E. P. Ippen, and K. Tamura, "Additive-pulse mode-locking in fiber lasers," *IEEE Journal of Quantum Electronics*, vol. 30, pp. 200–208, 1994.
- [5] A. Chong, J. Buckley, W. Renninger, and F. Wise, "All-normal-dispersion femtosecond fiber laser," *Optics Express*, vol. 14, no. 21, pp. 10095–10100, 2006.
- [6] A. Chong, W. H. Renninger, and F. W. Wise, "Properties of normal-dispersion femtosecond fiber lasers," *Journal of the Optical Society of America B*, vol. 25, no. 2, pp. 140–148, 2008.
- [7] T. Brabec, C. Spielmann, P. F. Curley, and F. Krausz, "Kerr lens mode locking," *Optics Letters*, vol. 17, pp. 1292–1294, 1992.
- [8] H. A. Haus, J. G. Fujimoto, and E. P. Ippen, "Structures for additive pulse mode-locking," *Journal of the Optical Society of America B*, vol. 8, p. 2068, 1991.
- [9] W. H. Renninger, A. Chong, and F. W. Wise, "Dissipative solitons in normal-dispersion fiber lasers," *Physical Review A*, vol. 77, no. 2, Article ID 023814, 2008.
- [10] A. Komarov, H. Leblond, and F. Sanchez, "Quintic complex Ginzburg-Landau model for ring fiber lasers," *Physical Review E*, vol. 72, no. 2, Article ID 025604, pp. 1–4, 2005.
- [11] E. Ding and J. N. Kutz, "Operating regimes, split-step modeling, and the Haus master mode-locking model," *Journal of the Optical Society of America B*, vol. 26, no. 12, pp. 2290–2300, 2009.
- [12] J. N. Kutz and B. Sandstede, "Theory of passive harmonic mode-locking using waveguide arrays," *Optics Express*, vol. 16, no. 2, pp. 636–650, 2008.
- [13] D. D. Hudson, K. Shish, T. R. Schibli et al., "Nonlinear femtosecond pulse reshaping in waveguide arrays," *Optics Letters*, vol. 33, no. 13, pp. 1440–1442, 2008.
- [14] J. L. Proctor and J. N. Kutz, "Theory and simulation of passive mode-locking by use of waveguide arrays," *Optics Letters*, vol. 30, no. 15, pp. 2013–2015, 2005.
- [15] N. N. Akhmediev, A. Ankiewicz, and J. M. Soto-Crespo, "Multisoliton solutions of the complex ginzburg-landau equation," *Physical Review Letters*, vol. 79, no. 21, pp. 4047–4051, 1997.
- [16] J. M. Soto-Crespo, N. N. Akhmediev, V. V. Afanasjev, and S. Wabnitz, "Pulse solutions of the cubic-quintic complex Ginzburg-Landau equation in the case of normal dispersion," *Physical Review E*, vol. 55, no. 4, pp. 4783–4796, 1997.
- [17] A. Komarov, H. Leblond, and F. Sanchez, "Multistability and hysteresis phenomena in passively mode-locked fiber lasers," *Physical Review A*, vol. 71, no. 5, Article ID 053809, pp. 1–9, 2005.
- [18] C. Y. Wang, W. Zhang, K. F. Lee, and K. M. Yoo, "Pulse splitting in a self-mode-locked Ti:sapphire laser," *Optics Communications*, vol. 137, no. 1–3, pp. 89–92, 1997.
- [19] M. Lai, J. Nicholson, and W. Rudolph, "Multiple pulse operation of a femtosecond Ti:sapphire laser," *Optics Communications*, vol. 142, no. 1–3, pp. 45–49, 1997.
- [20] M. Horowitz, C. R. Menyuk, T. F. Carruthers, and I. N. Duling, "Theoretical and experimental study of harmonically mode-locked fiber lasers for optical communication systems," *Journal of Lightwave Technology*, vol. 18, no. 11, pp. 1565–1574, 2000.
- [21] B. G. Bale, K. Kieu, J. N. Kutz, and F. Wise, "Transition dynamics for multi-pulsing in mode-locked lasers," *Optics Express*, vol. 17, no. 25, pp. 23137–23146, 2009.
- [22] Q. Xing, L. Chai, W. Zhang, and C. Y. Wang, "Regular, period-doubling, quasi-periodic, and chaotic behavior in a self-mode-locked Ti:sapphire laser," *Optics Communications*, vol. 162, no. 1, pp. 71–74, 1999.
- [23] J. M. Soto-Crespo, M. Grapinet, P. Grelu, and N. Akhmediev, "Bifurcations and multiple-period soliton pulsations in a passively mode-locked fiber laser," *Physical Review E*, vol. 70, no. 6, Article ID 066612, pp. 1–11, 2004.
- [24] P. Grelu, F. Belhache, F. Guty, and J. M. Soto-Crespo, "Phase-locked soliton pairs in a stretched-pulse fiber laser," *Optics Letters*, vol. 27, no. 11, pp. 966–968, 2002.
- [25] S. Namiki, E. P. Ippen, H. A. Haus, and C. X. Yu, "Energy rate equations for mode-locked lasers," *Journal of the Optical Society of America B*, vol. 14, no. 8, pp. 2099–2111, 1997.
- [26] T. Kapitula, J. N. Kutz, and B. Sandstede, "Stability of pulses in the master mode-locking equation," *Journal of the Optical Society of America B*, vol. 19, no. 4, pp. 740–746, 2002.
- [27] T. Kapitula, N. Kutz, and B. Sandstede, "The Evans function for nonlocal equations," *Indiana University Mathematics Journal*, vol. 53, no. 4, pp. 1095–1126, 2004.
- [28] J. M. Soto-Crespo, N. N. Akhmediev, and V. V. Afanasjev, "Stability of the pulselike solutions of the quintic complex Ginzburg-Landau equation," *Journal of the Optical Society of America B*, vol. 13, no. 7, pp. 1439–1449, 1996.
- [29] C. R. Jones and J. N. Kutz, "Stability of mode-locked pulse solutions subject to saturable gain: computing linear stability with the Floquet-Fourier-Hill method," *Journal of the Optical Society of America B*, vol. 27, no. 6, pp. 1184–1194, 2010.
- [30] S. K. Turitsyn and V. K. Mezentsev, "Dynamics of self-similar dispersion-managed soliton presented in the basis of chirped Gauss-Hermite functions," *JETP Letters*, vol. 67, no. 9, pp. 640–646, 1998.
- [31] S. K. Turitsyn, T. Schäfer, and V. K. Mezentsev, "Self-similar core and oscillatory tails of a path-averaged chirped dispersion-managed optical pulse," *Optics Letters*, vol. 23, no. 17, pp. 1351–1353, 1998.
- [32] Y. S. Kivshar, T. J. Alexander, and S. K. Turitsyn, "Nonlinear modes of a macroscopic quantum oscillator," *Physics Letters, Section A*, vol. 278, no. 4, pp. 225–230, 2001.
- [33] A. Bondeson, M. Lisak, and D. Anderson, "Soliton perturbations: a variation principle for the soliton parameters," *Physica Scripta*, vol. 20, no. 3–4, pp. 479–485, 1979.

- [34] D. Anderson, M. Lisak, and A. Berntson, "A variational approach to nonlinear evolution equations in optics," *Pramana*, vol. 57, no. 5-6, pp. 917–936, 2001.
- [35] B. A. Malomed, "Resonant transmission of a chirped soliton in a long optical fiber with periodic amplification," *Journal of the Optical Society of America B*, vol. 13, no. 4, pp. 677–686, 1996.
- [36] D. Anderson and M. Lisak, "Bandwidth limits due to mutual pulse interaction in optical soliton communications systems," *Optics Letters*, vol. 11, p. 174, 1986.
- [37] W. Chang, A. Ankiewicz, J. M. Soto-Crespo, and N. Akhmediev, "Dissipative soliton resonances," *Physical Review A*, vol. 78, no. 2, Article ID 023830, 2008.
- [38] E. Ding and J. N. Kutz, "Stability analysis of the mode-locking dynamics in a laser cavity with a passive polarizer," *Journal of the Optical Society of America B*, vol. 26, no. 7, pp. 1400–1411, 2009.
- [39] B. G. Bale and J. N. Kutz, "Variational method for mode-locked lasers," *Journal of the Optical Society of America B*, vol. 25, no. 7, pp. 1193–1202, 2008.
- [40] P. Holmes, J. Lumley, and G. Berkooz, Eds., *Turbulence, Coherent Structures, Dynamical Systems and Symmetry*, Cambridge University Press, Cambridge, UK, 1996.
- [41] L. N. Trefethen and D. Bau, *Numerical Linear Algebra*, SIAM, 1997.
- [42] D. S. Broomhead and G. P. King, "Extracting qualitative dynamics from experimental data," *Physica D*, vol. 20, no. 2-3, pp. 217–236, 1986.
- [43] L. Sirovich, "Turbulence and the dynamics of coherent structures part i: coherent structures," *Quarterly of Applied Mathematics*, vol. 45, p. 561, 1987.
- [44] E. Ding, E. Shlizerman, and J. N. Kutz, "Modeling multipulsing transition in ring cavity lasers with proper orthogonal decomposition," *Physical Review A*, vol. 82, Article ID 023823, 2010.
- [45] M. O. Williams, E. Shlizerman, and J. N. Kutz, "The multipulsing transition in mode-locked lasers: a low-dimensional approach using waveguide arrays," *Journal of the Optical Society of America B*, vol. 27, no. 12, pp. 2471–2481, 2010.
- [46] M. Ilak and C. W. Rowley, "Reduced-order modeling of channel flow using traveling POD and balanced POD," in *Proceedings of the 3rd AIAA Flow Control Conference*, pp. 864–874, June 2006.
- [47] M. Ilak and C. W. Rowley, "Modeling of transitional channel flow using balanced proper orthogonal decomposition," *Physics of Fluids*, vol. 20, no. 3, Article ID 034103, 2008.
- [48] E. A. Christensen, M. Brøns, and J. N. Sørensen, "Evaluation of proper orthogonal decomposition-based decomposition techniques applied to parameter-dependent nonturbulent flows," *SIAM Journal on Scientific Computing*, vol. 21, no. 4, pp. 1419–1434, 1999.
- [49] P. del Sastre and R. Bermejo, *Numerical Mathematics and Advanced Applications*, Springer, 2006.
- [50] A. Liakopoulos, P. A. Blythe, and H. Gunes, "A reduced dynamical model of convective flows in tall laterally heated cavities," *Proceedings of the Royal Society of London*, vol. 453, no. 1958, pp. 663–672, 1997.
- [51] L. Sirovich, R. Everson, E. Kaplan, B. W. Knight, E. O'Brien, and D. Orbach, "Modeling the functional organization of the visual cortex," *Physica D*, vol. 96, no. 1–4, pp. 355–366, 1996.
- [52] A. Chatterjee, "An introduction to the proper orthogonal decomposition," *Current Science*, vol. 78, no. 7, pp. 808–817, 2000.
- [53] A. Dhooge, W. Govaerts, and Y. A. Kuznetsov, "MATCONT: a MATLAB package for numerical bifurcation analysis of ODEs," *ACM Transactions on Mathematical Software*, vol. 29, no. 2, pp. 141–164, 2003.

Review Article

Nonlinear Optical Signal Processing for Tbit/s Ethernet Applications

L. K. Oxenløwe, M. Galili, H. C. Hansen Mulvad, H. Hu, J. L. Areal, E. Palushani, H. Ji, A. T. Clausen, and P. Jeppesen

DTU Fotonik, Department of Photonics Engineering, Technical University of Denmark, Building 343, 2800 Kongens Lyngby, Denmark

Correspondence should be addressed to L. K. Oxenløwe, lkox@fotonik.dtu.dk

Received 31 May 2011; Accepted 12 July 2011

Academic Editor: Christophe Finot

Copyright © 2012 L. K. Oxenløwe et al. This is an open access article distributed under the Creative Commons Attribution License, which permits unrestricted use, distribution, and reproduction in any medium, provided the original work is properly cited.

We review recent experimental demonstrations of Tbaud optical signal processing. In particular, we describe a successful 1.28 Tbit/s serial data generation based on single polarization 1.28 Tbaud symbol rate pulses with binary data modulation (OOK) and subsequent all-optical demultiplexing. We also describe the first error-free 5.1 Tbit/s data generation and demodulation based on a single laser, where a 1.28 Tbaud symbol rate is used together with quaternary phase modulation (DQPSK) and polarization multiplexing. The 5.1 Tbit/s data signal is all-optically demultiplexed and demodulated by direct detection in a delay-interferometer-balanced detector-based receiver, yielding a BER less than 10^{-9} . We also present subsystems making serial optical Tbit/s systems compatible with standard Ethernet data for data centre applications and present Tbit/s results using, for instance silicon nanowires.

1. Introduction

Historically, quadrupling the serial line rate has resulted in reducing the cost per bit by 40%, mostly due to a reduction of terminal equipment and related power consumption [1]. For any given line rate, there will be trade-offs between the complexity of the line cards, the modulation format, the transmission reach, and the available technology at a given point in time. However, considering the historical facts, it is clear that there must be a potential for cost and power reductions when using higher serial line rates. It is merely a question of uncovering the right technological solutions. Today, electronic signal processing seems limited to about 120 Gbit/s [2], as stated by the high-speed electronics community itself, so it becomes relevant to explore optical signal processing and in particular in the context of high serial bit rates. Optical signal processing is well suited for serial data signals, since a single ultrafast optical switch can process the entire data content in one go. This may lead to a potential reduction in power consumption, as concluded in [3], where they state the following “photonic technologies may be well suited for processes such as the all-optical

wavelength conversion and signal regeneration, where the number of signal processing devices is small.” This is exactly the case for high serial line rates where a single device may perform the signal processing of the full data signal. Therefore, we believe it is relevant and interesting to conduct more research in the field of ultra-high-speed serial optical communications.

In the year 2000, the first demonstration of reaching Tbit/s data rates on a single wavelength channel was achieved [4] using 640 Gbaud polarization-multiplexing (pol-MUX) and simple OOK. Recently, it has become apparent that Tbit/s bit rates for Ethernet applications will be needed very soon [5] and that the overall necessary capacity per fiber will reach several tens of Tbit/s [6], while the need for power reductions is getting more and more evident, where the Internet today emits more than 2% of the global man-made CO₂ emission. This has spurred on a regained focus on increasing the bit rates, both with a single-channel perspective and with a spectral efficiency perspective using advanced modulation formats and latest advances in coherent receiver technology. A high single-channel bit rate has generally had the effect of cutting the overall systems

cost, due to reduced network complexity, fewer components, and hence lower power consumption per bit. A high spectral efficiency may also help in power per bit savings, since the bandwidth is more efficiently used. Using OFDM has a high component count in the terminals but, on the other hand, is very resilient to transmission impairments and hence needs less inline equipment for, for example, regeneration. So the optimum path to energy-efficient high-bandwidth communication systems is still open, and all routes must be explored to ensure future sustainability.

Recent highlights of the endeavors to boost the bit rates to the Tbit/s regime include the record breaking 2.56 Tbit/s using DQPSK and pol-MUX on a 640 Gbaud RZ pulse rate [7] and a recent upgrade to 8 PSK on 640 Gbaud with pol-MUX resulted in below FEC-limit 3.56 Tbit/s using coherent reception and 2.38 Tbit/s using 16 QAM on 640 Gbaud without pol-MUX [8]. Including pol-MUX was also attempted but was not below the FEC limit, but could have resulted in 4.76 Tbit/s. The combination of time division multiplexing and coherent receiver techniques has also been successfully studied by the Kikuchi group and recently led to a 1.28 Tbit/s based on 16 QAM on a 160 Gbaud pol-MUX OTDM pulse train [9]. Using coherent OFDM has also recently been demonstrated to reach 1 Tbit/s [10] and even 1.2 Tbit/s [11]. The simple OOK purely serial format has the advantage of having a low component count with simple line cards, *as well as being the simplest format with several well-established suggestions for all-optical regeneration, which may also aid in driving the power consumption down. Successful demonstrations of regenerating the phase have also been obtained recently [12], and this may also be applied to OTDM phase-modulated data.* Drawbacks of binary OTDM are the relatively low spectral efficiency and the severe challenges with respect to long-haul transmission. Until very recently, the baud rate had been limited to 640 Gbaud, but a new record of 1.28 Tbit/s was recently demonstrated [13] using only optical time division multiplexing (OTDM) from 10 Gbit/s and remaining in one single polarization, that is, a purely serial 1.28 Tbaud symbol rate.

In this paper, we describe recent progress on 1.28 Tbit/s data generation and demultiplexing and discuss opportunities and limitations of this technology. Using 300 fs wide (FWHM) 1.28 Tbaud symbols for more advanced modulation formats has also been demonstrated with a world-first error-free 5.1 Tbit/s data generation and demodulation [14]. DQPSK and polarization multiplexing were used, and the details of this will also be presented here.

2. Experimental Demonstrations: Background

A schematic of the experimental setup used for the demonstrations described here is shown in Figure 1. An erbium glass oscillator pulse generating laser (ERGO) supplies a 10 GHz optical pulse train at 1557 nm having a pulse width of 1.3 ps. A Mach-Zender modulator (MOD) is used to encode a data sequence (2^7-1 PRBS) on the pulse train. The 10 Gbit/s modulated pulse train is compressed down to 350 fs in a highly nonlinear fiber (HNLF) SPM-based chirp unit followed by linear dispersion and subsequently multiplexed

to 160-320-640-1280 Gbit/s in a passive fiber delay PRBS and polarization-maintaining multiplexer (MUX). The multiplexed data is then subjected to various experiments.

Several interesting functionalities have already been demonstrated at 640 Gbit/s and show promise for higher bit rates. This goes for transmission and clock recovery, wavelength conversion, and add/drop multiplexing, all of which have been demonstrated at 640 Gbit/s in our testbed [15–20]. These functionalities are likely to be possible to perform at 1.28 Tbit/s, as the physical properties involved in the signal processing are fast enough. For the clock recovery scheme described in [15, 16], a periodically poled Lithium Niobate (PPLN) device was used as an all-optical mixer, and it was fast enough to resolve the 640 Gbit/s data signal. In [21] is described how a similar PPLN device is used to compress an optical pulse to less than 100 fs, revealing the great speed potential of the $\chi^{(2)}$ process, which takes place on an fs timescale. So these devices have great potential for Tbit/s applications. The HNLF used for wavelength conversion and add/drop multiplexing in [17–20] are the same types as used for the 1.28 Tbit/s experiment, so they have already proven themselves able to operate at Tbit/s speeds. An alternative to HNLF is the very nonlinear chalcogenide waveguides. In [22], we showed that such a device could be used to demultiplex a 640 Gbit/s data signal, and as with the HNLF and the PPLN, the active effect used for the optical signal processing is ultrafast, and the only speed limitation lies in the design of the dispersion (this goes for all the devices). Recently, in [23], it was shown that these waveguides indeed have a THz response with a modulation bandwidth on the order of 2.5 THz. This means that this technology would also lend itself favorably to Tbit/s serial communication systems. Very recently, it was thus demonstrated that 1.28 Tbit/s demultiplexing is indeed possible with such a chalcogenide device [24].

3. 1.28 Tbit/s OOK Serial Data Generation

A detailed set-up drawing of the 1.28 Tbit/s experiment is shown in Figure 2. In this back-to-back set-up, only a single pulse source is used. This feeds both the data generation part and the control pulse part in the demultiplexer. The pulses are split in two parts after an SPM-based wavelength conversion unit. A supercontinuum is generated in 400 m of dispersion-flattened HNLF (DF-HNLF1). DF-HNLF1 has dispersion $D = -0.45$ ps/nm km and slope $S = 0.006$ ps/nm² km at 1550 nm, nonlinear coefficient $\gamma = 10.5$ W⁻¹ km⁻¹). It is very important that the HNLF is slightly negative in dispersion and has a very flat dispersion profile, as this gives the best supercontinuum—in this case a 70 nm wide spectrum, see Figure 3. The top branch is filtered through a 9 nm wide filter, which is offset by 15 nm from the original pulse source wavelength. This has two effects: firstly, a *Mamyshev regeneration* takes place suppressing the inevitable pulse pedestals from the external cavity mode-locked laser, and secondly, a linear chirp is obtained across the pulse, and by carefully measuring out the path to the demultiplexer, the resulting dispersion is such that a transform-limited short pulse of width 400 fs

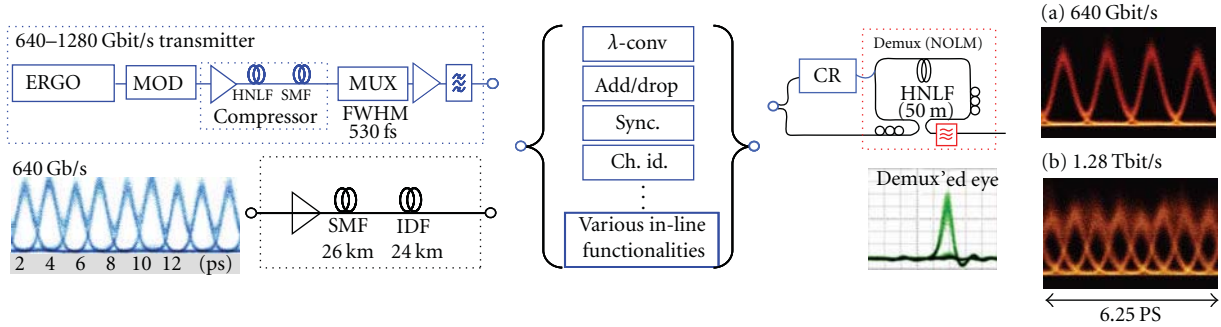


FIGURE 1: Schematic of the DTU OTDM test bed for generating 640–1280 Gbit/s data. Insets: (a) 640 Gbit/s eye diagram, (b) 1.28 Tbit/s eye diagram.

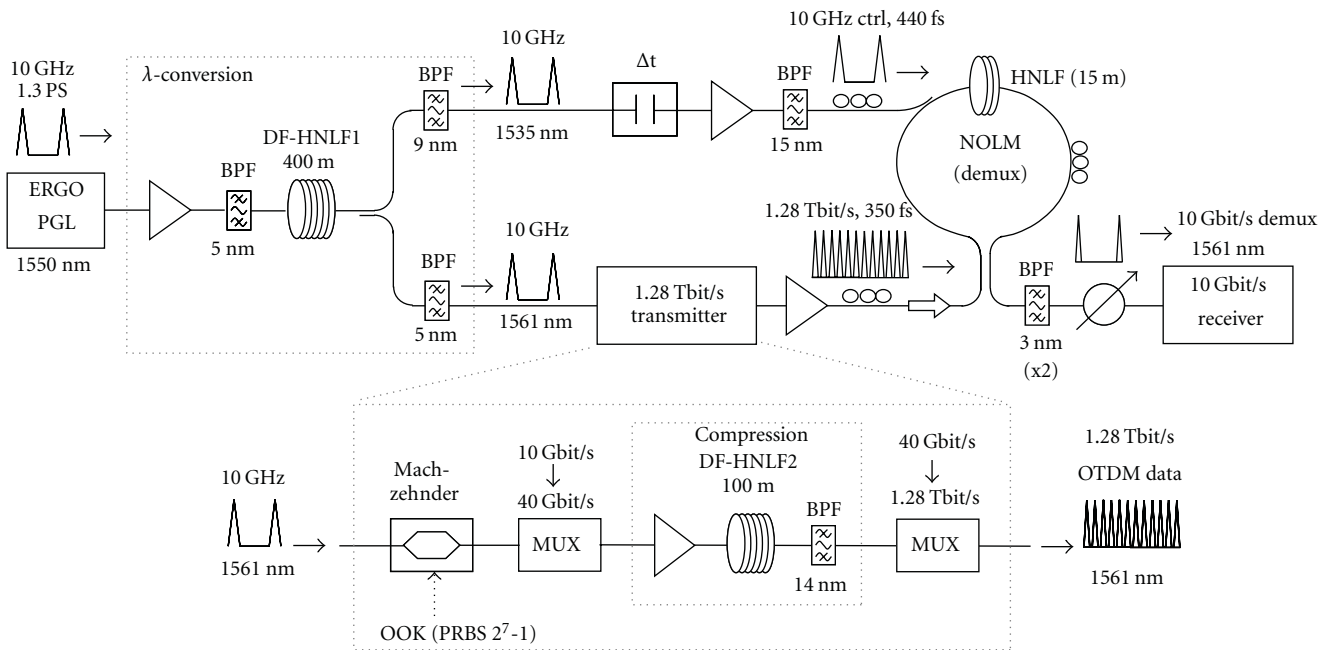


FIGURE 2: Experimental set-up for a back-to-back demonstration of 1.28 Tbit/s serial data generation and demultiplexing.

FWHM is obtained at the input to the HNLF in the nonlinear optical loop mirror (NOLM). The lower branch is also offset filtered by 11 nm in a 5 nm wide filter to separate it effectively from the original wavelength. These pulses, now at 1561 nm, are data modulated at 10 Gbit/s with a 2^7-1 PRBS OOK data signal. The PRBS length is merely chosen for convenience, as the multiplexer is designed to preserve this PRBS word. Longer word lengths become impractical for this type of lab-solution MUX. For all experiments mentioned here, the PRBS length does not matter, since only truly ultrafast optical switching effects are used, which effectively alleviates any potential patterning effects. Changing the PRBS length would thus only serve to characterize the 10 Gbit/s photodetector and receiver. This has of course been done, with no difference between a 2^7-1 and a $2^{31}-1$ PRBS word. Following the data modulation, the data is multiplexed to 40 Gbit/s, and then it is further compressed in a second SPM-based compression stage (DF-HNLF2: $D =$

-1.7 ps/(nm km), $S = 0.004$ ps/(nm² km) 1560 nm) with a 14 nm bandpass filter. The data pulses are then sent through the remainder of the multiplexer, reaching 1.28 Tbit/s and being compressed down to about 350 fs.

The 1.28 Tbit/s data is subsequently demultiplexed in the NOLM, which contains a 15 m short HNLF with a zero dispersion at 1545 nm and a slope of 0.015 ps/nm² km. With a short HNLF and a zero dispersion wavelength in between the control and data, walk-off is reduced to a negligible level (less than 50 fs). Furthermore, the short HNLF helps to enhance overall stability by reducing the amount of second-order PMD. The demultiplexed data channels are characterized in terms of bit error rate (BER) performance.

The heart of an ultra-high-speed serial data system is the short-pulse generation. Figure 3 shows details of the pulse compression. The optimally compressed pulses are as short as 196 fs FWHM, which is adequate for 1.28 Tbit/s signals. *Please note that there is a small background offset in the*

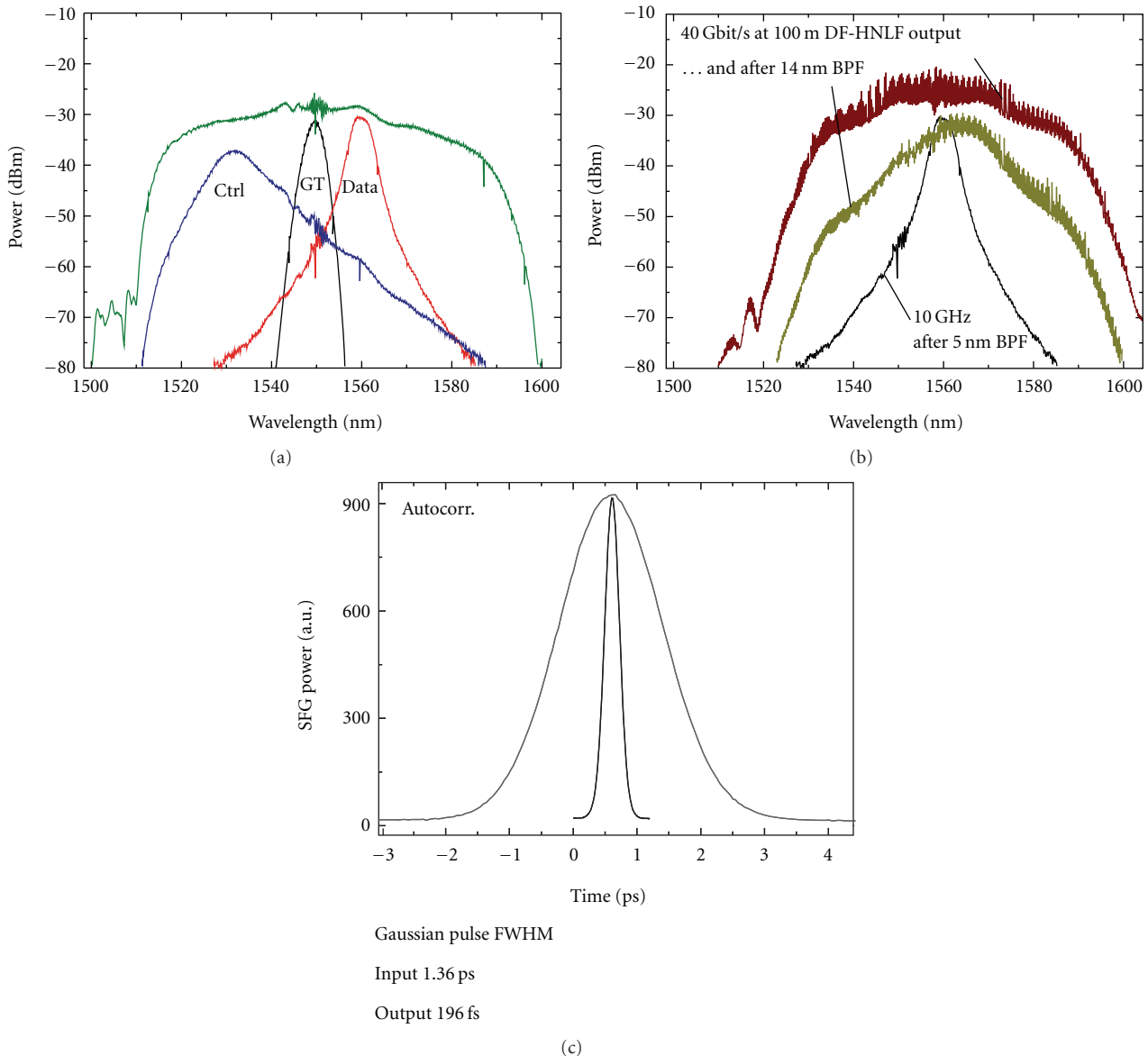


FIGURE 3: Pulse compression for 1.28 Tbit/s pulses. (a) Spectra at the input and output of DF-HNL1. The “GT” trace is the input to the DF-HNL1 creating the 70 nm wide supercontinuum trace. From this supercontinuum, a control and data spectrum is carved out. (b) The data spectra at DF-HNL2 showing the input (data output from DF-HNL2), the resulting generated supercontinuum in DF-HNL2 and the final filtered (14 nm) compressed output. (c) Autocorrelation traces of the input data pulse and the optimally compressed pulse revealing a 196 fs FWHM pulse.

autocorrelation traces, caused partly by ASE noise. In practice, the multiplexer stages and other parts of the full system result in a small broadening of this, so the data pulses end up being around 350 fs wide FWHM. This is still adequate for 1.28 Tbit/s, as will be seen below.

The compressed pulses are multiplexed, and the resultant eye diagrams, as measured on an optical sampling oscilloscope (OSO) with a 1 ps timing resolution, are shown in Figure 4. The resolution of the OSO is obviously not sufficient to resolve the 350 fs pulses, but the OTDM time slot for a 1.28 Tbit/s data signal is about 750 fs, which can just be discerned by the OSO. Therefore, the OSO can show

open-eye diagrams at 1.28 Tbit/s. But the real pulse widths are much shorter than it seems here. Figure 4 also shows a 640 Gbit/s eye diagram, and as can be seen on that there is ample room between the data pulses for an extra time slot.

The generated 1.28 Tbit/s data signal is subsequently sent to the NOLM demultiplexer. It is very important that there is as low a spectral overlap as possible between the control and data in the NOLM, which is challenging if the system is constrained to remain in the C-band and the spectra are about 15 nm wide each. However, as seen in Figure 5, there is a small overlap, but the effect of this can be minimized by keeping the detrimental SPM broadening at a minimum

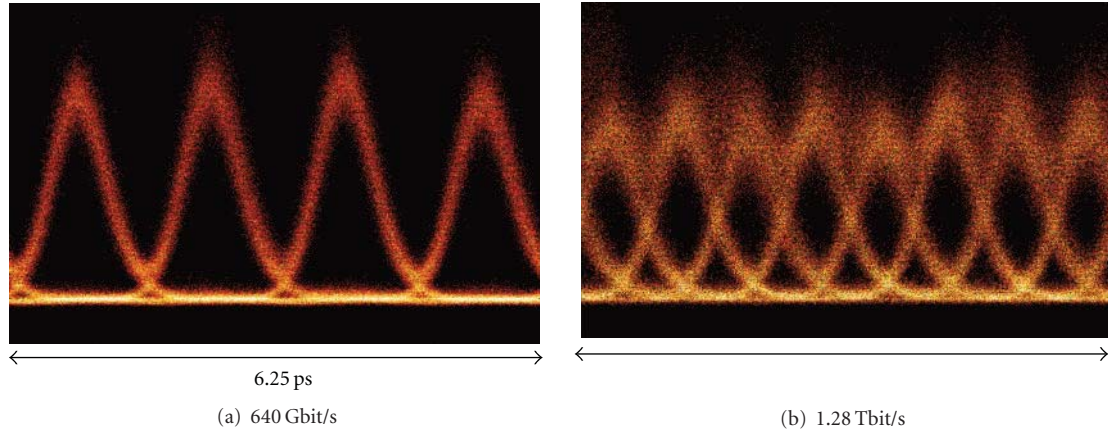


FIGURE 4: 1.28 Tbit/s data generation. Eye diagrams measured by an optical sampling oscilloscope with limited timing resolution to 1 ps. (a) 640 Gbit/s eye diagram. (b) 1.28 Tbit/s eye diagram. Note that the real pulses are only about 350 fs wide.

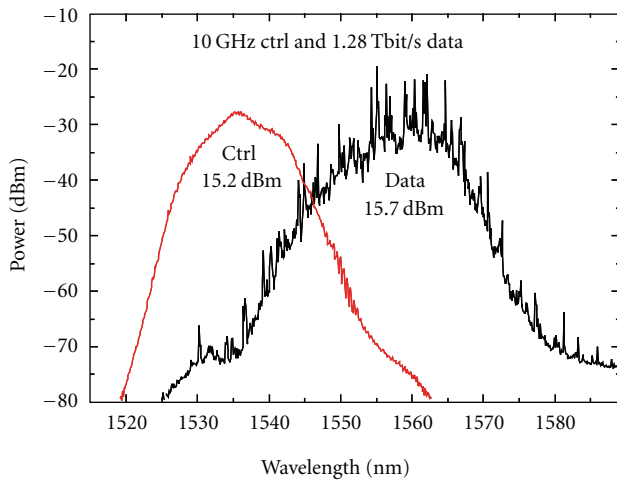


FIGURE 5: Spectral overlap of control and data pulses in the NOLM.

by careful adjustment of the polarization. This is enabled because a short HNLf is used in the NOLM, and by using a moderate control power to get a good SPM/XPM balance (in this case $\sim 0.7\pi$ XPM). The control power used is 15.2 dBm, and the data signal input power is 15.7 dBm.

The demultiplexing results are shown in Figure 6. 1.28 Tbit/s demultiplexing is seen to be error-free. For comparison with the performance at 640 Gbit/s, the last multiplexer stage is shut, yielding a 640 Gbit/s signal. Tracking the very same channel (channel 0) while turning the final multiplexer stage on again ensures that it is the same channel that is measured on. This channel is shown with a triangular symbol in Figure 6 and reveals a modest power penalty of about 2.4 dB. To ensure that the final multiplexing is properly adjusted, the BER curves for the neighboring channels (ch.0-1) and (ch.0+1) are also shown, and they have almost identical BER performances with the same sensitivity of -33.3 dBm. There is however an indication of an error-floor below BER 10^{-10} for the 1.28 Tbit/s data. The demultiplexed eye diagrams in Figure 6 are all clear and

open, with a tendency of more noise appearing for higher bit rates. This is not surprising, as the pulse tail overlap will increase for higher bit rates. The 10 Gbit/s back-to-back (b2b) baseline is measured straight out of the data modulator, that is, before the pulse compression and without being sent through the NOLM demultiplexer. This means that the pulse shape is different from the multiplexed cases, which results in different BER slopes.

In order to validate the integrity of the full 1.28 Tbit/s data signal, all 128 channels are characterized. Figure 7 shows the BER results for all 128 demultiplexed OTDM tributaries of the 1.28 Tbit/s data signal.

The integrity of the 1.28 Tbit/s data signal is tested by verifying that error-free performance can be obtained for all channels after demultiplexing. This test is performed by lowering the attenuation before the receiver sufficiently to obtain a BER $< 10^{-9}$ for each individual channel. Note that the error detector decision level is not adjusted for minimum BER, but only until a BER $< 10^{-9}$ is detected. For all 128 channels, a BER $< 10^{-9}$ can be obtained, confirming the integrity of the 1.28 Tbit/s data signal. The variation in BER performance is attributed to the MUX, in which the channels propagate through different lengths of SMF and therefore acquire slightly different pulse widths at the MUX output. Furthermore, small misalignments of the temporal delays in the MUX stages are also expected to contribute to the aforementioned variations.

3.1. Transmission Performance. It is well known that transmission of narrow pulses is a challenge, due to dispersion and PMD. It is also clear that a 1.28 Tbit/s data signal is more interesting if it can be transmitted over fiber. In order to characterize this, we investigated the transmission performance over an 80 km standard single mode (SMF) fiber span only compensated by 11 km dispersion compensating fiber (DCF) and a 1 km dispersion-shifted fiber (DSF) for additional slope compensation. The fibers are kindly provided by OFS Fitel Denmark Aps. The PMD is mitigated by launching the data signal into a principal state of polarization, and monitoring the polarization state at the output of the fiber.

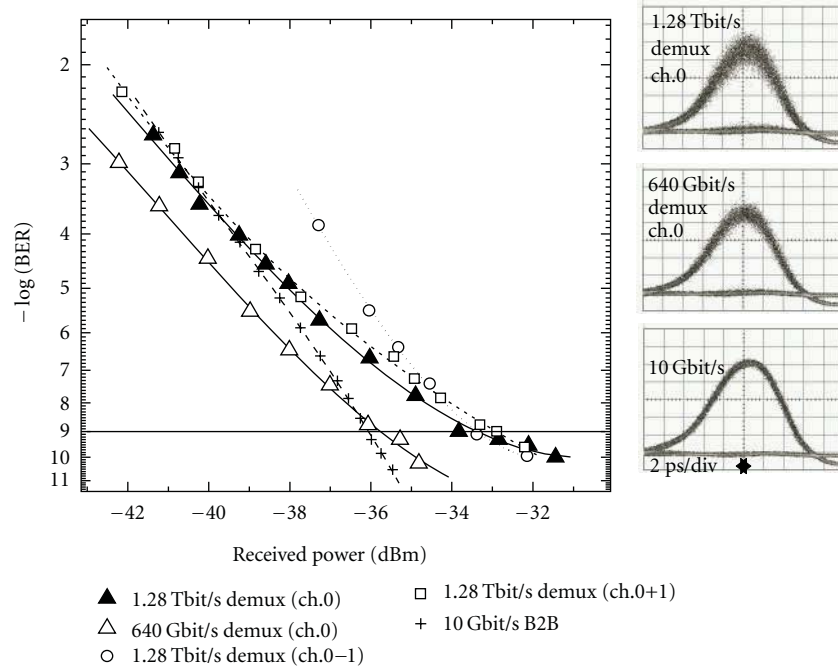


FIGURE 6: BER results for 1.28 Tbit/s demultiplexing. Left: BER performance showing error-free ($\text{BER} < 10^{-9}$) performance. Right: demultiplexed eye diagrams for 1.28 Tbit/s (top), 640 Gbit/s (middle), and the 10 Gbit/s back to back (bottom).

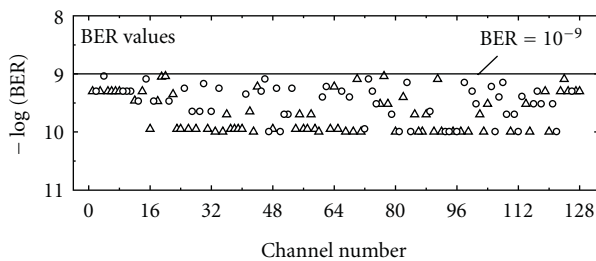


FIGURE 7: BER values for all 128 tributaries. All channels are error-free ($\text{BER} < 10^{-9}$) corroborating the open eyes from Figure 1, taken from [13].

Figure 8 shows a schematic of the transmission set-up. A 10 GHz clock signal is transmitted along with the data signal to synchronize the receiver. The 1.28 Tbit/s transmitter and receiver are the same as described above, except for the control pulse for the NOLM, which is derived from a second ERGO laser driven by the o/e -converted transmitted clock signal and compressed in a separate pulse compressor similar to the one described above.

Figure 9 shows the residual dispersion of the fiber span with a residual disp. within ± 50 fs/nm over nearly 20 nm (as specified by manufacturer). The data pulses for 1.28 Tbit/s (at ~ 1556 nm) can then be transmitted with negligible broadening, see Figure 9(b).

The preliminary experiments show promising results for transmission over this fiber span. The pulse broadening is kept at a minimum, with a broadening from 375 fs to

400 fs FWHM. In terms of BER performance, a BER of 10^{-6} is obtained. Interestingly enough, it is not the dispersion that causes the biggest problems in this set-up, but rather the available OSNR. The spectrum of the data is so wide that it has energy distributed all over the C-band, and the competition in the EDFAs with the transmitted clock signal made it difficult to find a good balance—either the clock OSNR was good with low resulting phase noise and timing jitter, or the data signal OSNR was good. But a perfect balance between the two was not achieved in this preliminary experiment.

Very recently, it was demonstrated that it is really possible to transmit the Tbaud pulses over significant fibre lengths [25]. Figure 10 shows the principle and results for transmitting a 1.28 Tbit/s differential phase-shift-keying (DPSK) data signal over 50 km superlarge area transmission fibre with inverse dispersion fibre for dispersion compensation (SLA-IDF) using a transmitted clock. The result is error-free, and there is thus no fundamental dispersion issues limiting the transmission of these sub-ps pulses, as long as the dispersion is carefully compensated. Here, only standard IDF was used with small pieces of DCF and DSF to fine-tune the dispersion. *The 50 km transmission link is composed of a 25 km SLA ($D = 20$ ps/nm/km, $S = 0.06$ ps/nm²/km and $\text{PMD} = 0.04$ ps/km^{1/2}) and a 25 km IDF ($D = -20$ ps/nm/km, $S = -0.06$ ps/nm²/km, and $\text{PMD} = 0.02$ ps/km^{1/2}).*

In a real system, dispersion will vary as a function of temperature, and therefore adaptive dispersion compensation techniques will be necessary. There are good suggestions available today such as, for example, the optical fourier transform (OFT) technique [26], or a spectral pulse shaper (SPS) with

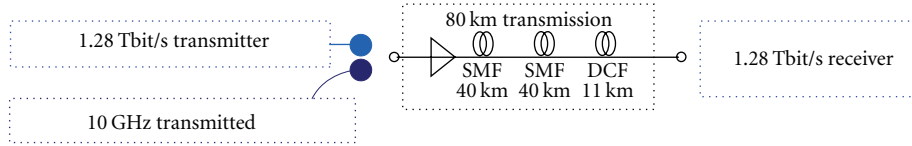


FIGURE 8: Transmission set-up. A transmitted 10 GHz clock signal are used for synchronizing the receiver. 80 km SMF and 11 km DCF is used.

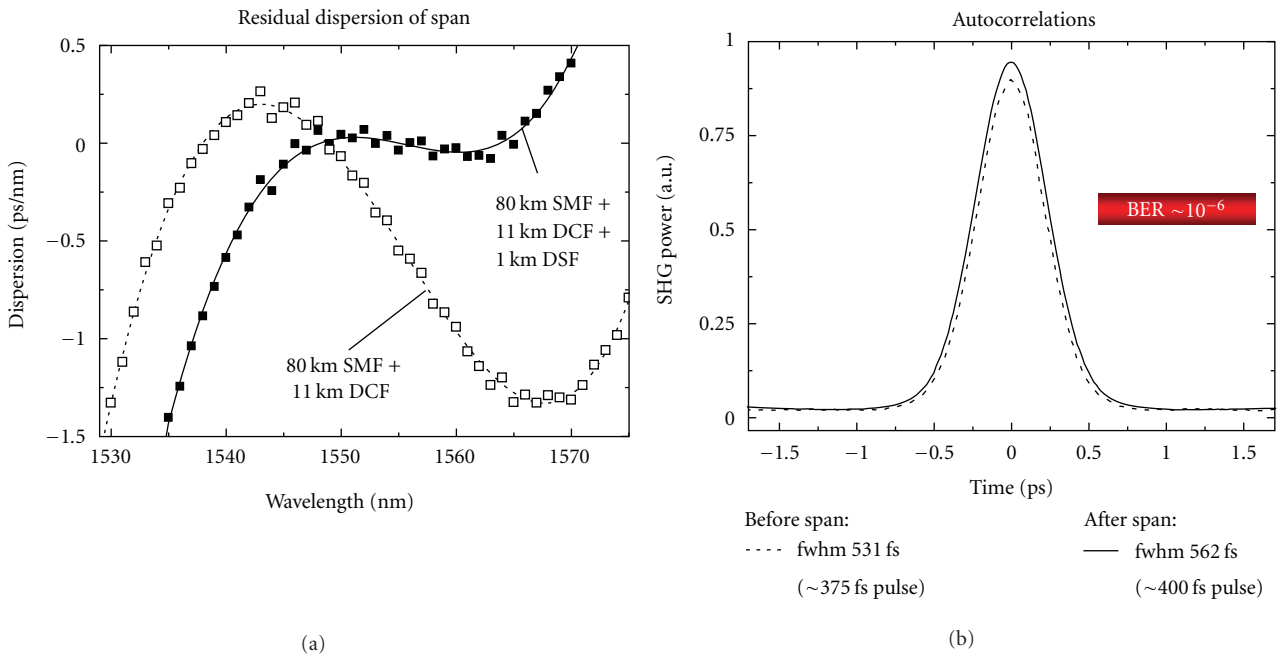


FIGURE 9: Preliminary transmission results. The stated “fwhm” pulse widths are autocorrelation measurements. The deconvoluted FWHM pulse widths are in brackets (375/400 fs).

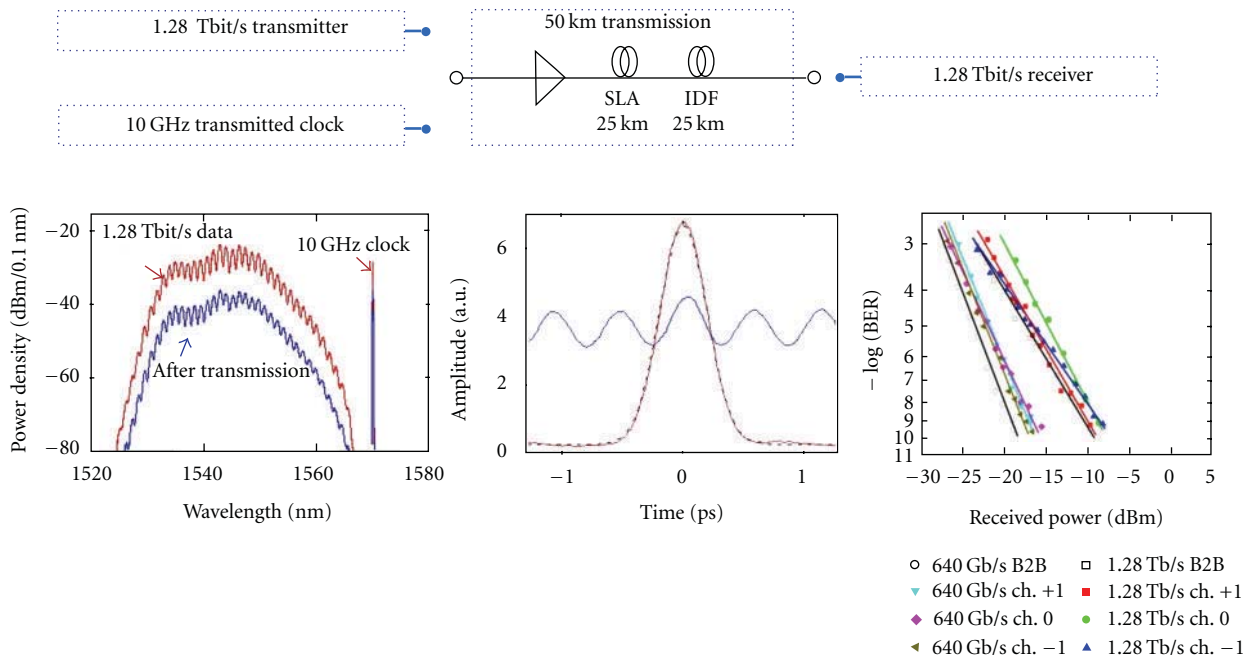


FIGURE 10: 1.28 Tbit/s DPSK transmission over 50 km SLA-IDF using an L-band 10 GHz transmitted clock [25].

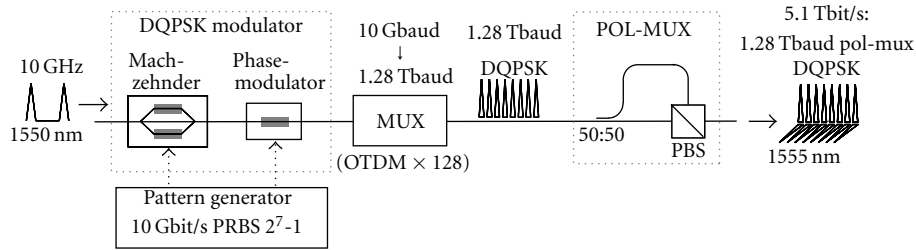


FIGURE 11: 5.1 Tbit/s data generation set-up.

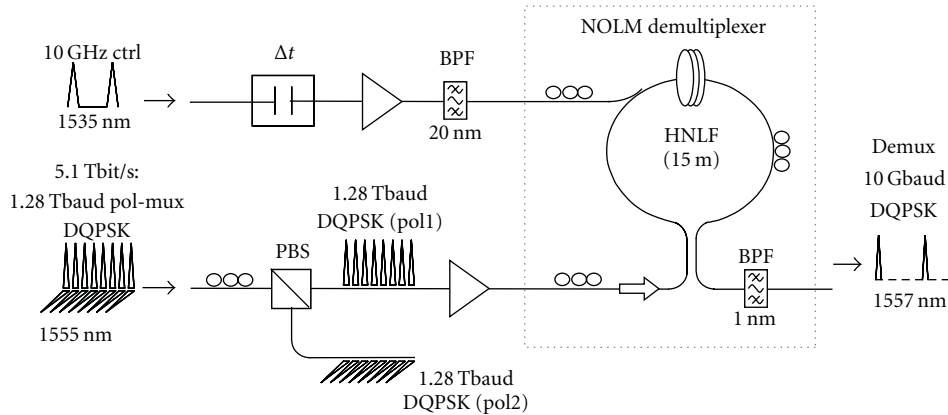


FIGURE 12: 5.1 Tbit/s demultiplexer receiver with a pol-DEMUX (PBS) and an NOLM DEMUX, yielding 10 Gbaud symbols.

adjustable phase [27]. For PMD, a liquid crystal modulator scheme has been demonstrated to compensate for all-order PMD on subpicosecond pulses in a potentially adaptive setup [28]. To conclude on this section, it is possible to generate an error-free 1.28 Tbit/s purely serial data signal, and even transmission is demonstrated, when careful compensation of the dispersion is applied.

4. 5.1 Tbit/s Dqpsk Pol-MUX Data Generation

In this section, we describe the upgrade from 1.28 Tbit/s to 5.1 Tbit/s. The main idea behind this experiment is to use the generated record high symbol rate of 1.28 Tbaud, as described above. Each pulse is now compressed to about 400 fs first, and subsequently phase modulated rather than intensity modulated. A differential quaternary phase-shift-keying (DQPSK) data signal is encoded onto the pulses in two steps. First, a push-pull Mach-Zehnder modulator is used to add a 2^7-1 PRBS DPSK data signal to the 10 GHz compressed pulses.

The data generation is schematically represented in Figure 11. The second level of data to generate the DQPSK signal is added by a LiNbO₃ phase modulator. This modulator is also adding a decorrelated 2^7-1 PRBS data signal with a $\pi/2$ offset compared to the DPSK signal, thus assuring an even distribution of the quaternary phase levels. Note that the aggregated DQPSK data signal is not a preserved PRBS sequence. However, as mentioned above, the specific data sequence is not important here, as a pattern-dependent-free receiver is used. The 20 Gbit/s (10 Gbaud) DQPSK data signal is then multiplexed in the same split-and-delay

multiplexer as described above up to 1.28 Tbaud, that is, 2.56 Tbit/s. Then an additional polarization multiplexing is imposed on the data signal, by splitting the signal in two in a 3-dB coupler, and then aligning the polarization to match the inputs to a polarization beam splitter (PBS). The PBS combines the two orthogonally polarized 1.28 Tbaud data copies in a 5.1 Tbit/s DQPSK pol-multiplexed data signal.

The 5.1 Tbit/s data signal is then sent to the same NOLM demultiplexer as described above, see Figure 12.

Before entering the NOLM, the 5.1 Tbit/s data signal is split in its two polarization states by a second PBS. Each polarization state is characterized separately, one after the other. The control pulse for the NOLM is derived the same way as above.

The demultiplexed 10 Gbaud DQPSK data signal is further demodulated in a standard 10 Gbaud DQPSK receiver, see Figure 13. A delay interferometer (DLI) with a phase tuner is used to choose the I or the Q component, and the DLI outputs are detected in a balanced photodetector and evaluated in a BER counter.

Figure 14 shows an autocorrelation trace of the 1.28 Tbaud data signal together with the 10 GHz control pulse. The data pulses are about 410 fs wide (FWHM) in this case, and the control pulse is around 440 fs wide. The data signal is well equalized and correctly separated. The BER results are shown in Figure 15 for a 640 Gbaud 2.56 Tbit/s signal and a 1.28 Tbaud 5.1 Tbit/s signal. In both cases, error-free performance is achieved.

At 1.28 Tbit/s (640 Gbaud, no pol-MUX), the 10 Gbit/s I/Q components have sensitivities of -35.3 dBm and -34.8 dBm. There is a penalty of less than 3 dB compared

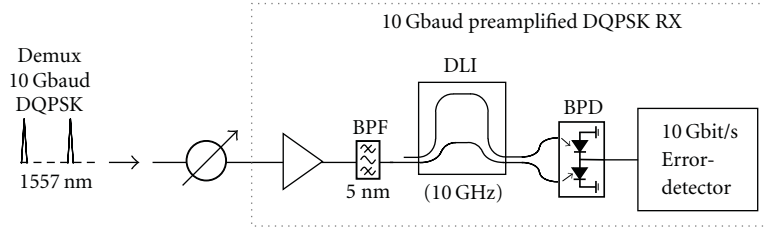


FIGURE 13: 5.1 Tbit/s demodulator receiver with a preamplifier, a delay interferometer, and a balanced detector.

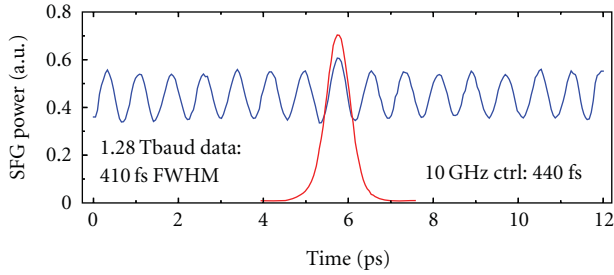


FIGURE 14: 1.28 Tbaud data pulses with DQPSK modulation.

to the 10 Gbaud reference I/Q sensitivity of -37.5 dBm (obtained by injecting the DQPSK modulator output directly into the DQPSK receiver). When adding pol-MUX to reach 2.56 Tbit/s, the penalty is only increased by 0.5 dB. The symbol rate is subsequently doubled to 1.28 Tbaud, yielding a total bit rate of 5.1 Tbit/s. Figure 14 (bottom) shows the BER results for the case, when using pol-MUX, showing the I/Q components of a demultiplexed 10 Gbaud channel, and the inset (top right) shows the demodulated eye diagram for this case. The eye is clearly open, and the BER confirms error-free performance of both polarizations and both the I and Q components. BER values $< 10^{-9}$ are detected for all measured curves, hence demonstrating that error-free performance can be obtained for the 5.1 Tbit/s data signal. There is however an error floor below 10^{-9} and a penalty of $\sim 7-10$ dB relative to the 10 Gbaud DQPSK reference sensitivity. This is primarily attributed to a slightly too large data pulse FWHM of ~ 410 fs compared to the 1.28 Tbaud bit slot of ~ 785 fs, resulting in some pulse tail overlap. Finally, note that the BPFs in the receiver differ between the measurements on 640 and 1280 Gbaud, causing the difference in reference sensitivity. At 640 Gbaud, narrow 0.3 nm and 0.9 nm BPFs are used to achieve the best reference sensitivity, but at the cost of a limit in the amount of received power. At 1.28 Tbaud, a higher received power is required to reach a BER $< 10^{-9}$, and 1 nm and 5 nm BPFs are therefore selected.

To conclude on this section, we have shown that it is indeed possible to achieve several Tbit/s on a single laser source and that Tbaud symbol rates are appropriate for this usage.

5. Network Applications

At 640 Gbit/s, several essential network functionalities have already been demonstrated. This goes for add/drop multiplexing [19, 20, 29], wavelength conversion [17, 18, 30, 31],

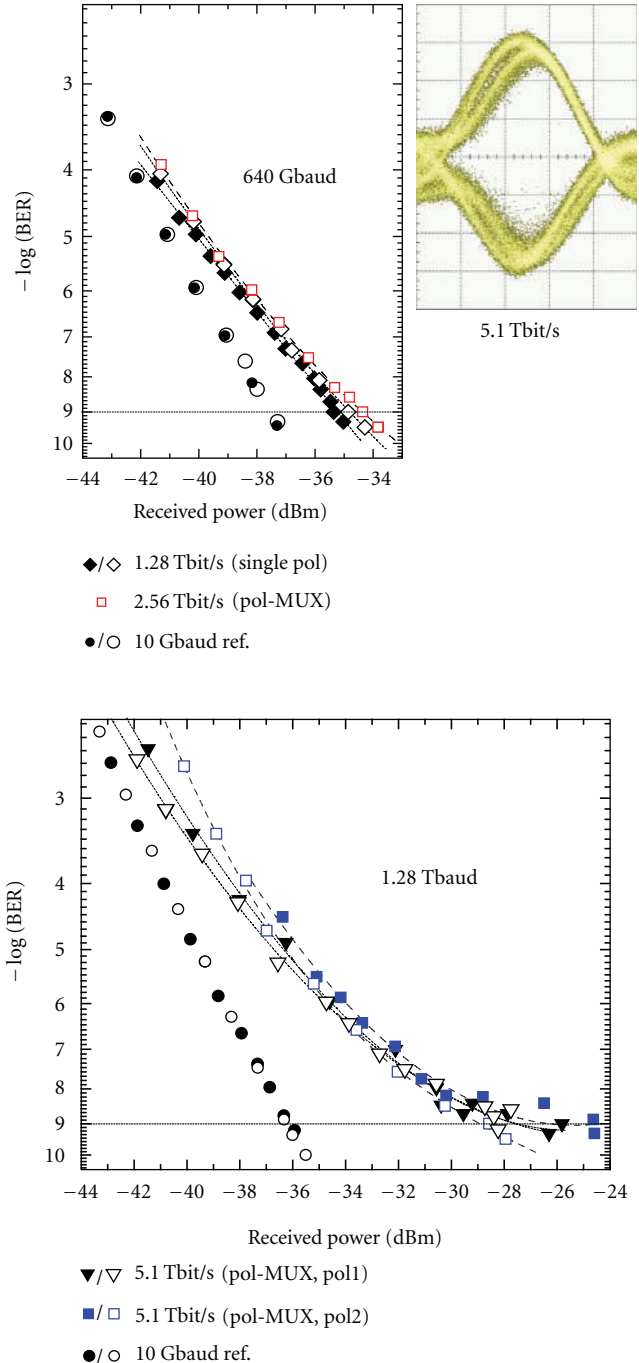


FIGURE 15: 5.1 Tbit/s demultiplexing and demodulation.

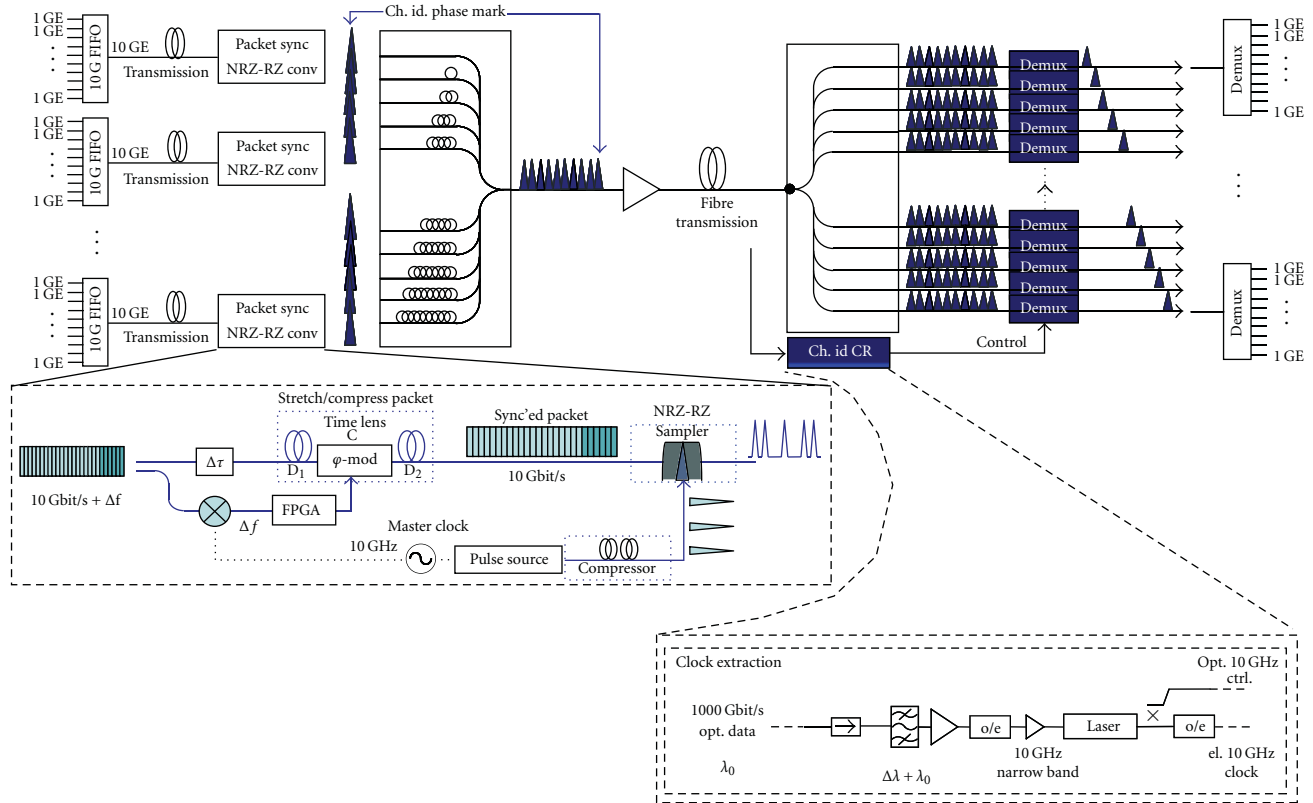


FIGURE 16: Suggested Ethernet compatible optical TDM system. Each 10 GE packet is synchronised to the local master clock via a time-lens-based sync unit, essentially stretching or compressing the data packet to fit the individual bits to the local rep rate. The synchronised bits in the packet are then individually converted to RZ pulses, for example, by optical sampling, allowing for subsequent time domain multiplexing, by interleaving the bits with those from other synchronised packets. Thus, each packet is ascribed its own time slot. Time slot N may also be marked with a channel ID, for example, by a slight phase modulation, allowing for easy channel identification and sub rate clock recovery at the receiver. The demultiplexing may take place in several ways and is here only conceptually shown as parallel demux-units for simplicity.

clock recovery using an SOA [32] and a PPLN [33], and full transmission including clock recovery and error-free demultiplexing [32, 33]. To get full advantage of these high-speed functionalities, one would need to design new network scenarios or rethink the network. For instance, as suggested in Figure 16, it may be beneficial to create a high-speed bus to carry Ethernet data packets (frames) in optical TDM time slots, that is, multiplex Ethernet packets into timeslots by bit interleaving.

Ethernet is basically a TDM-based technology, and when considering the need for future Tbit/s Ethernet [5] and the Tbit/s capacity encountered in massive data centres, it makes sense to explore the potential of optical TDM in conjunction with Ethernet. Figure 16 shows an Ethernet compatible optical TDM scenario. The heart of this scheme is to use the optical time lens effect [34] derived from the space-time duality [35] to slightly stretch or compress the asynchronous Ethernet data packets to synchronize them to a local master clock. When synchronised they may be NRZ-RZ converted, for example, through optical sampling or pulse compression, and subsequently multiplexed together with other Ethernet packets or optical TDM channels.

In this scheme, each Ethernet packet would be assigned an OTDM time slot. The scheme has already been demonstrated in a proof-of-principle experiment reaching an aggregate bit rate of 50 Gbit/s [36] and recently 320 Gbit/s [37]. The results are error-free as shown in Figure 17. This scheme is scalable to Tbit/s.

As Ethernet packets are asynchronous, and optical TDM systems are very synchronous, it becomes important to synchronize the data packets to a local master clock. This can be carried out using the concept of a time lens [34, 35] by which the packet may be stretched or compressed to fit with the local clock frequency. Results on this are shown in Figure 17 where a 10 Gbit/s data packet is synchronised to four 10 Gbit/s optical TDM channels and then multiplexed together with these [36]. To prove the principle, subsequent demultiplexing was done and error-free performance confirmed. This principle is scalable to terabits per second.

Figure 18 shows results on another network building block, namely, that of channel identification combined with clock recovery. In this scheme, a small spectral feature is added to one optical TDM channel in the transmitter, and this is then simply filtered out in the receiver, allowing for

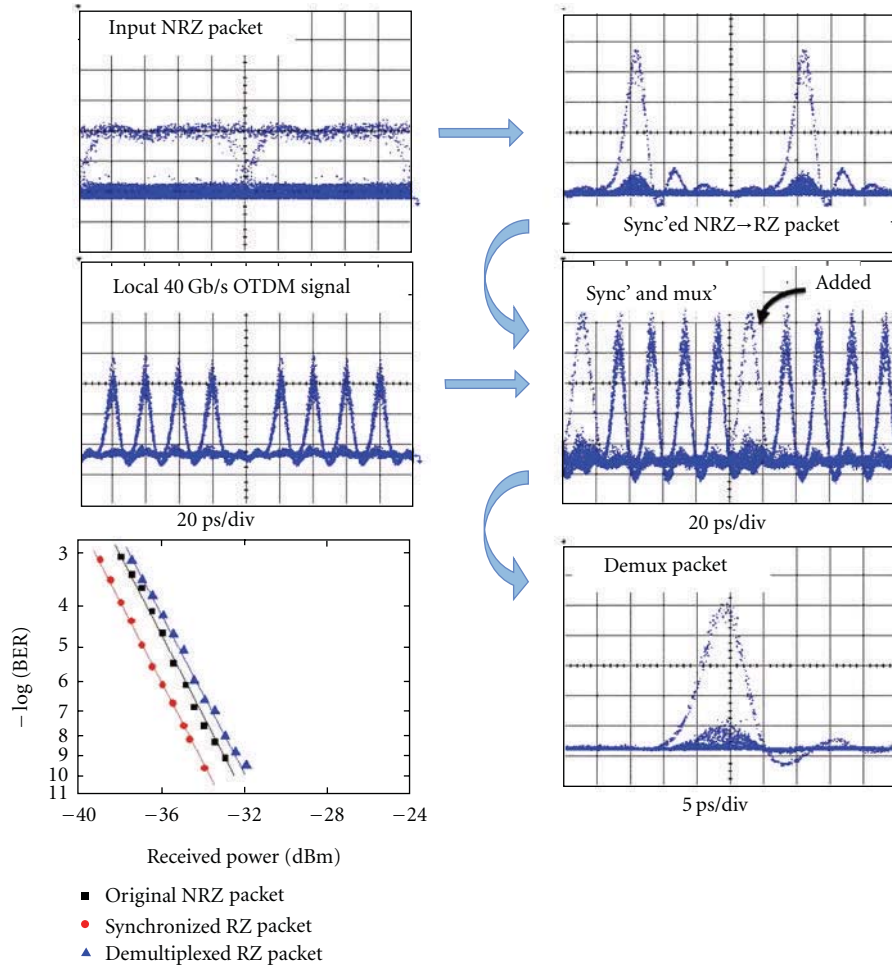


FIGURE 17: Time-lens-based data packet synchronisation and RZ conversion. A 12,000 bits long NRZ packet offset with 200 kHz to the local clock is synchronised, RZ-converted, and multiplexed with a 40 Gbit/s OTDM signal. To prove the principle, demultiplexing with error-free BER performance is performed [19].

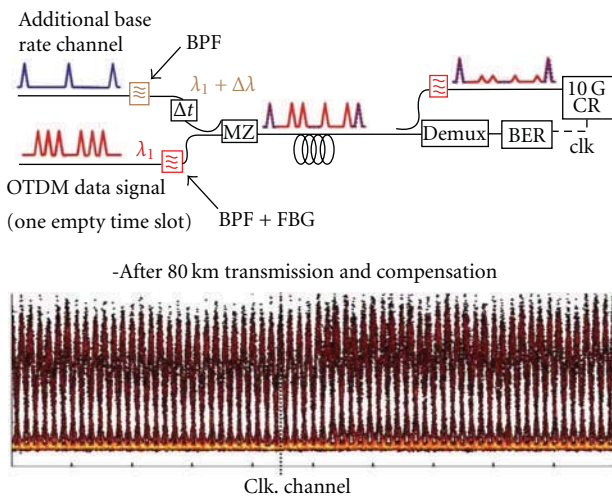


FIGURE 18: 650 Gbit/s channel identification and simultaneous clock recovery by adding a small spectral feature to one TDM channel [38].

easy identification of that particular channel. This scheme was demonstrated at 650 Gbit/s, that is, where a marked channel was added to a 640 Gbit/s optical TDM signal [38]. Again, this scheme should be scalable to Tbit/s speeds. The added channel could stem from an Ethernet packet, and several spectral marks could be envisaged to allow for individual labeling of the TDM data packets.

Ultrafast data signals like Tbaud data require equally ultra-fast switches and are sensitive to temporal issues such as pulse widths and timing jitter. Therefore, timing jitter tolerant switching techniques are interesting. To this end, the OFT/time lens concept has again turned out to be very useful to create flat-top pulses [40] and compensate for dispersion [26], retiming [34], packet compression [41], and packet synchronisation [36]. Several pulse shaping schemes have been demonstrated for sub-ps flat-top pulse generation, such as the optical differentiation technique [42], and the Mach-Zehnder delay technique [43], and used for timing-tolerant as well as polarization-independent switching [44].

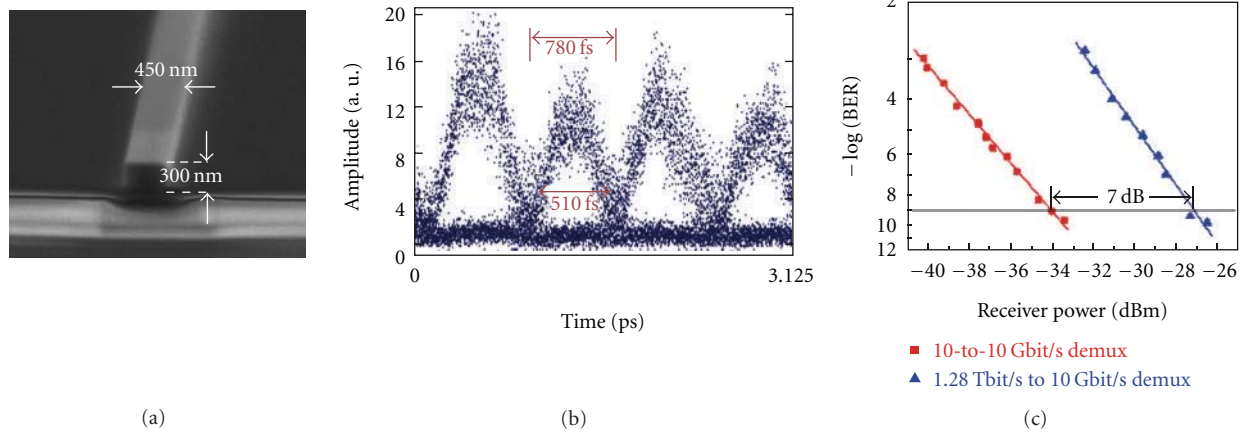


FIGURE 19: Ultra-fast silicon photonics. Using four-wave mixing in a silicon nanowire (a) is demonstrated to perform Tbit/s optical signal processing by sampling a 1.28 Tbit/s serial data signal (b) and error-free demultiplexing [39].

6. Switching Materials

Most Tbaud experiments have been carried out using a highly non-linear-fibre-(HNLF) based switch, for example, a non-linear optical loop mirror (NOLM). HNLF has superior efficiency and is convenient to use but is not compact and cannot be integrated onto a chip. Very recently, it was demonstrated that compact devices can be used for Tbit/s switching, for example, chalcogenide (ChG) waveguides and silicon nanowires [24, 39]. These results, together with 640 Gbit/s semiconductor-optical-amplifier-(SOA-) based demultiplexers [45, 46], show great promise for making compact multifunctional optical chips with ultra-high-speed potential. Figure 19 shows recent results on the use of a silicon nanowire for optical signal processing of a 1.28 Tbit/s serial data signal. The Si-nanowire is used as a nonlinear waveguide for four wave mixing (FWM) between a control and a data pulse in order to perform all-optical sampling (Figure 19(b)). These measured eye diagrams constitute the shortest sampled data pulses reported so far. The sampled data pulse width is 510 fs, and the distance between data pulses is 785 fs. The Si-nanowire is also used for demultiplexing the 1.28 Tbit/s data signal, and as seen in Figure 19(c), error-free performance is achieved. This is the highest signal processing speed reported to date using silicon—and indeed pure silicon.

7. Conclusion

We have described the generation and use of 1.28 Tbaud serial symbol rates for a 1.28 Tbit/s OOK data experimental demonstration and a 5.1 Tbit/s DQPSK pol-MUX data experimental demonstration. We have also described that there are several technology platforms that can potentially deal with such high symbol rates, with a number of these, including compact alternatives, already demonstrated at 640 Gbit/s (640 Gbaud). We have shown that Tbit/s optical TDM is feasible even for transmission. We have described efforts to embrace network scenarios and demonstrated data packet synchronisation for future Tbit/s Ethernet systems,

for example, in Data Centres. Finally we have touched upon some emerging techniques which could enable more resilient and efficient switching, such as the time lens concept and silicon nanowires. This means that Tbit/s serial optical data may be a feasible path to accommodate for the future need for high-capacity communication systems.

Acknowledgments

This work is partly funded by the European-Research-Council-(ERC-) independent researcher starter grant project SOCRATES and the Danish Research Council projects NANO-COM and NOSFERATU, and the European Network of Excellence, Euro-Fos. OFS Fitel Denmark Aps is acknowledged for providing HNLF.

References

- [1] B. Mikkelsen, C. Rasmussen, F. Liu, P. Mamyshev, and S. Dey, "40 Gbit/s based ULH transmission," in *Proceedings of the 9th OptoElectronics and Communications Conference (OECC '04)*, July 2004, Paper 14C3-1.
- [2] R. Driad, R. E. Makon, V. Hurm et al., "INP DHBT-based ICs for 100 Gbit/s data transmission," in *the International Conference on Indium Phosphide and Related Materials (IPRM '08)*, May 2008.
- [3] K. Hinton, G. Raskutti, P. M. Farrell, and R. S. Tucker, "Switching energy and device size limits on digital photonic signal processing technologies," *IEEE Journal on Selected Topics in Quantum Electronics*, vol. 14, no. 3, pp. 938–945, 2008.
- [4] M. Nakazawa, T. Yamamoto, and K. R. Tamura, "1.28Tbit/s-70km OTDM transmission using third- and fourth-order simultaneous dispersion compensation with a phase modulator," *Electronics Letters*, vol. 36, no. 24, pp. 2027–2029, 2000.
- [5] B. Metcalfe, <http://www.ofcnfoec.org/Home/Program/Plenary-Session.aspx>.
- [6] E. B. Desurvire, "Capacity demand and technology challenges for lightwave systems in the next two decades," *Journal of Lightwave Technology*, vol. 24, no. 12, pp. 4697–4710, 2006.
- [7] H. G. Weber, S. Ferber, M. Kroh et al., "Single channel 1.28 Tbit/s and 2.56 Tbit/s DQPSK transmission," *Electronics Letters*, vol. 42, no. 3, pp. 67–68, 2006.

- [8] C. Schmidt-Langhorst et al., "Generation and coherent time-division demultiplexing of up to 5.1 Tb/s single-channel 8-PSK and 16-QAM signals," in *Proceedings of the Conference on Optical Fiber Communication (OFC '09)*, 2009, paper PDPC6.
- [9] C. Zhang et al., "Demodulation of 1.28 Tbit/s polarization-multiplexed 16-QAM signals on a single carrier with digital coherent receiver," in *Proceedings of the Conference on Optical Fiber Communication (OFC '09)*, 2009, paper OTuG3.
- [10] Y. Ma et al., "1 Tb/s per channel coherent optical OFDM transmission with subwavelength bandwidth access," in *Proceedings of the Conference on Optical Fiber Communication (OFC '09)*, 2009, PD paper PDPC1.
- [11] R. Dischler et al., "Transmission of 1.2 Tbit/s continuous waveband PDM-OFDM-FDM signal with spectral efficiency of 3.3 bit/s/Hz over 400 km of SSMF," in *Proceedings of the Conference on Optical Fiber Communication (OFC '09)*, 2009, paper PDPC2.
- [12] R. Slavik, F. Parmigiani, J. Kakande et al., "All-optical phase and amplitude regenerator for next-generation telecommunications systems," *Nature Photonics*, vol. 4, no. 10, pp. 690–695, 2010.
- [13] H. C. Hansen Mulvad, L. K. Oxenløwe, M. Galili, A. T. Clausen, L. Grüner-Nielsen, and P. Jeppesen, "1.28Tbit/s single-polarisation serial OOK optical data generation and demultiplexing," *Electronics Letters*, vol. 45, no. 5, pp. 280–281, 2009.
- [14] H. C. Hansen Mulvad, M. Galili, L. K. Oxenløwe et al., "Error-free 5.1 Tbit/s data on a single-wavelength channel using a 1.28 Tbaud symbol rate," in *Proceedings of the 22nd Annual Meeting of the IEEE Photonics Society, Belek-Antalya, Turkey, October 2009*.
- [15] L. K. Oxenløwe, F. Gómez-Agis, C. Ware et al., "640-Gbit/s data transmission and clock recovery using an ultrafast periodically poled lithium niobate device," *Journal of Lightwave Technology*, vol. 27, no. 3, pp. 205–213, 2009.
- [16] L. K. Oxenløwe, F. Gomez Agis, C. Ware et al., "640Gbit/s clock recovery using periodically poled lithium niobate," *Electronics Letters*, vol. 44, no. 5, pp. 370–372, 2008.
- [17] M. Galili, L. K. Oxenløwe, H. C. H. Mulvad, A. T. Clausen, and P. Jeppesen, "Optical wavelength conversion by cross-phase modulation of data signals up to 640 Gb/s," *IEEE Journal on Selected Topics in Quantum Electronics*, vol. 14, no. 3, pp. 573–579, 2008.
- [18] M. Galili, H. C. H. Mulvad, L. Grüner-Nielsen et al., "640 Gbit/s optical wavelength conversion using FWM in a polarisation maintaining HNLF," in *the 34th European Conference on Optical Communication (ECOC '08)*, September 2008.
- [19] H. C. Hansen Mulvad et al., "640 Gbit/s optical time-division add-drop multiplexing in a non-linear optical loop mirror," in *IEEE Lasers and Electro-Optics Society Winter Topical Meeting*, Innsbruck, Austria, January 2009, Paper MC4.4.
- [20] H. C. H. Mulvad, M. Galili, L. Grüner-Nielsen, L. K. Oxenløwe, A. T. Clausen, and P. Jeppesen, "640 Gbit/s time-division add-drop multiplexing using a non-linear polarisation-rotating fibre loop," in *the 34th European Conference on Optical Communication (ECOC '08)*, September 2008.
- [21] S. Ashihara, T. Shimura, K. Kuroda et al., "Optical pulse compression using cascaded quadratic nonlinearities in periodically poled lithium niobate," *Applied Physics Letters*, vol. 84, no. 7, pp. 1055–1057, 2004.
- [22] M. Galili, J. Xu, H. C. H. Mulvad et al., "Breakthrough switching speed with an all-optical chalcogenide glass chip: 640 Gbit/s demultiplexing," *Optics Express*, vol. 17, no. 4, pp. 2182–2187, 2009.
- [23] M. Pelusi, F. Luan, T. D. Vo et al., "Photonic-chip-based radio-frequency spectrum analyser with terahertz bandwidth," *Nature Photonics*, vol. 3, no. 3, pp. 139–143, 2009.
- [24] T. D. Vo, H. Hu, M. Galili et al., "Photonic chip based 1.28 Tbaud transmitter optimization and receiver OTDM demultiplexing," in *Proceedings of the Conference on Optical Fiber Communication (OFC '10)*, 2010, paper PDPC5.
- [25] H. Hu, M. Galili, L. K. Oxenløwe et al., "Error-free transmission of serial 1.28 Tbaud RZ-DPSK signal," in *the European Conference on Optical Communication (ECOC '10)*, Turin, Italy, September 2010, Paper P4.18.
- [26] M. Nakazawa, T. Hirooka, F. Futami, and S. Watanabe, "Ideal distortion-free transmission using optical Fourier transformation and Fourier transform-limited optical pulses," *IEEE Photonics Technology Letters*, vol. 16, no. 4, pp. 1059–1061, 2004.
- [27] Y. Paquot et al., "Automatic higher-order dispersion measurement and compensation of a 1.28 Tbaud signal," in *Proceedings of the Conference on Lasers and Electro-Optics (CLEO '11)*, 2011, paper CFP3.
- [28] M. Akbulut, A. M. Weiner, and P. J. Miller, "Wideband all-order polarization mode dispersion compensation via pulse shaping," *Optics Letters*, vol. 30, no. 20, pp. 2691–2693, 2005.
- [29] H. C. Hansen Mulvad, L. K. Oxenløwe, A. T. Clausen, M. Galili, L. Grüner-Nielsen, and P. Jeppesen, "Error-free 320 Gb/s simultaneous add-drop multiplexing," in *Proceedings of the Conference on Optical Fiber Communication (OFC '07)*, Anaheim, Calif, USA, March 2007, Paper OTuI.
- [30] H. Sotobayashi, W. Chujo, and T. Ozeki, "Inter-wavelength-band conversions and demultiplexings of 640 Gbit/s OTDM signals," in *Proceedings of the Conference on Optical Fiber Communication (OFC '02)*, pp. 261–262, 2002.
- [31] H. Hu, E. Palushani, M. Galili et al., "1.28 Tb/s wavelength conversion for polarisation multiplexed RZ-DPSK signals," in *Proceedings of the Conference on Optical Fiber Communication (OFC '10)*, San Diego, Calif, USA, March 2010, Paper OWP1.
- [32] E. Tangdiongga et al., "SOA-based clock recovery and demultiplexing in a lab trial of 640- Gb/s OTDM transmission over 50-km Fibre Link," in *the 33rd European Conference and Exhibition of Optical Communication (ECOC '07)*, 2007, PD 1.2.
- [33] L. K. Oxenløwe, F. Gomez Agis, C. Ware et al., "640 Gbit/s data transmission and clock recovery using an ultra-fast periodically poled lithium niobate device," in *Proceedings of the Conference on Optical Fiber Communication (OFC '08)*, San Diego, Calif, USA, February 2008, PDP22.
- [34] L. F. Mollenauer and C. Xu, "Time-lens timing-jitter compensator in ultra-long haul DWDM dispersion managed soliton transmissions," in *the Conference on Lasers and Electro-Optics (CLEO '02)*, pp. CPDB11–CPDB13, May 2002.
- [35] Brian H. Kolner, "Space-time duality and the theory of temporal imaging," *IEEE Journal of Quantum Electronics*, vol. 30, no. 8, pp. 1951–1963, 1994.
- [36] H. Hu, E. Palushani, J. L. Areal et al., "Optical frame synchronizer for 10 G Ethernet packets aiming at 1 Tb/s OTDM Ethernet," in *Proceedings of the Conference on Optical Fiber Communication, Collocated National Fiber Optic Engineers Conference (OFC/NFOEC '10)*, 2010.
- [37] J. L. Areal, H. Hu, and E. Palushani, "Synchronization and NRZ-to-RZ conversion of 10 Gbit/s Ethernet-like data packets and subsequent optical TDM multiplexing to 330 Gbit/s," in *Proceedings of the Conference on Optical Fiber Communication (OFC '11)*, 2011.
- [38] M. Galili, H. C. Hansen Mulvad, H. Hu et al., "650 Gbit/s OTDM transmission over 80 km SSMF incorporating clock

- recovery, channel identification and demultiplexing in a Polarisation insensitive receiver,” in *Proceedings of the Conference on Optical Fiber Communication, Collocated National Fiber Optic Engineers Conference (OFC/NFOEC '10)*, 2010, OWO3.
- [39] H. Ji, H. Hu, M. Galili et al., “Optical waveform sampling and error-free demultiplexing of 1.28 Tbit/s serial data in a silicon nanowire,” in *the Conference on Optical Fiber Communication, Collocated National Fiber Optic Engineers Conference (OFC/NFOEC '10)*, 2010, PDPC7.
- [40] E. Palushani, L. K. Oxenløwe, M. Galili, H. C. H. Mulvad, A. T. Clausen, and P. Jeppesen, “Flat-top pulse generation by the optical fourier transform technique for ultrahigh speed signal processing,” *IEEE Journal of Quantum Electronics*, vol. 45, no. 11, pp. 1317–1324, 2009.
- [41] M. A. Foster et al., “Generation of 270 Gb/s NRZ data packets from a 10-Gb/s signal using a temporal telescopic system,” in *Proceedings of the Conference on Optical Fiber Communication (OFC '09)*, 2009, OWS4.
- [42] L. K. Oxenløwe, R. Slavík, M. Galili et al., “640 Gb/s timing jitter-tolerant data processing using a long-period fiber-grating-based flat-top pulse shaper,” *IEEE Journal on Selected Topics in Quantum Electronics*, vol. 14, no. 3, pp. 566–572, 2008.
- [43] E. Palushani, H. Hu, L. K. Oxenløwe et al., “640 Gb/s timing tolerant demultiplexing using a cascaded long-period fiber grating pulse shaper,” in *the 35th European Conference on Optical Communication (ECOC '09)*, 2009.
- [44] H. C. H. Mulvad, M. Galili, L. K. Oxenløwe, A. T. Clausen, L. Grüner-Nielsen, and P. Jeppesen, “Polarization-independent high-speed switching in a standard non-linear optical loop mirror,” in *Proceedings of the Conference on Optical Fiber Communication/National Fiber Optic Engineers Conference (OFC/NFOEC '08)*, 2008.
- [45] E. Tangdiongga et al., “SOA-based clock recovery and demultiplexing in a lab trial of 640- Gb/s OTDM transmission over 50-km fibre link,” in *the 33rd European Conference and Exhibition of Optical Communication (ECOC '07)*, 2007, PD 1.2.
- [46] T. Hirooka, M. Okazaki, T. Hirano, P. Guan, M. Nakazawa, and S. Nakamura, “All-optical demultiplexing of 640 Gbit/s OTDM-DPSK signal using a semiconductor SMZ switch,” in *the 35th European Conference on Optical Communication (ECOC 09)*, 2009, paper 4.3.2.

Research Article

Amplification of Frequency-Modulated Similariton Pulses in Length-Inhomogeneous Active Fibers

I. O. Zolotovskii,¹ D. I. Sementsov,¹ A. A. Sysolyatin,² A. S. Belanov,³ and M. S. Yavtushenko¹

¹Ul'yanovsk State University, 42 L. Tolstogo Street, Ul'yanovsk 432700, Russia

²Fiber Optics Research Center, 38 Vavilov Street, Moscow 119333, Russia

³Moscow State University of Instrument Engineering and Computer Sciences, 20 Stromynka Street, Moscow 107996, Russia

Correspondence should be addressed to D. I. Sementsov, sementsovdi@ulsu.ru

Received 4 May 2011; Accepted 21 June 2011

Academic Editor: Christophe Finot

Copyright © 2012 I. O. Zolotovskii et al. This is an open access article distributed under the Creative Commons Attribution License, which permits unrestricted use, distribution, and reproduction in any medium, provided the original work is properly cited.

The possibility of an effective gain of the self-similar frequency-modulated (FM) wave packets is studied in the length-inhomogeneous active fibers. The dynamics of parabolic pulses with the constant chirp has been considered. The optimal profile for the change of the group-velocity dispersion corresponding to the optimal similariton pulse amplification has been obtained. It is shown that the use of FM pulses in the active (gain) and length-inhomogeneous optical fibers with the normal group-velocity dispersion can provide subpicosecond optical pulse amplification up to the energies higher than 1 nJ.

1. Introduction

Generation of stable self-similar FM optical pulses, referred to as similaritons, in an active (gain) medium with the normal group-velocity dispersion (GVD) opens up extensive advantages over the classical ways of an optical pulse amplification [1–16]. In the case of the optical pulse amplification in an anomalously dispersive medium, it is difficult to avoid various instabilities as well as Raman laser effect that could considerably distort the wave packet profile. However, in the normal GVD medium, there also arise some definite problems. Some known methods of the pulse amplification in homogeneous optical fibers are sensitive to the stochastic diameter variation of the mentioned fibers [17–19]. Therefore, the use of “long” amplifiers (the length >100 m) with a low gain increment $\gamma > 1 \text{ M}^{-1}$ proves inefficient.

To overcome this problem, it is reasonable to use the compact inhomogeneous amplifiers with the normal GVD increasing over the length and gain increment of the fiber material $\gamma \ll 1 \text{ M}^{-1}$. In this case, the following parameters can be efficiently controlled over the optical fiber length (due to a relatively short amplifier length): the fiber core diameter, dispersion, and nonlinearity. The present work

analyses the dynamics of the parabolic FM wave packet in the length-inhomogeneous amplifier and describes the conditions for their stable (self-similar) propagation in a form of the similariton wave packet.

2. Basic Equations

We will consider the optical pulse dynamics in the inhomogeneous amplifying medium. In this case, the field of the wave packet which evolves in an optical fiber can be expressed as

$$\vec{E}(t, r, z) = \frac{1}{2} \vec{e} U(r, z) \times \left\{ A(t, z) \exp \left[i \left(\omega_0 t - \int_0^z \beta'(\xi) d\xi \right) \right] + \text{C.C.} \right\}, \quad (1)$$

where \vec{e} is the unit vector of the light field polarization; $U(r, z)$ function describes the radial field propagation in an optical fiber; ω_0 represents the carrier frequency of a wave packet; $\beta'(z)$ is the real component of the propagation constant. The nonlinear Schrödinger equation with coefficients

inhomogeneous over the optical fiber length is valid for the time pulse envelope $A(t, z)$

$$\frac{\partial A}{\partial z} - i \frac{D(z)}{2} \frac{\partial^2 A}{\partial \tau^2} + iR(z)|A|^2 A = g(z)A, \quad (2)$$

where the following parameters are introduced: $\tau = t - \int_0^z d\xi/u(\xi)$ is the time of the traveling coordinate system; $u(z) = (\partial\beta(z)/\partial\omega)_0^{-1}$ and $D(z) = (\partial^2\beta(z)/\partial\omega^2)_0$ are the group velocity and the fiber GVD; $R(z)$ is Kerr nonlinearity coefficient. The dependence of the fiber parameters on the longitudinal coordinate z is associated, first of all, with their dependence on the effective mode area $S_m(z)$. Thus, the parameter of the mode amplification is related not only to the material gain $\gamma(z)$ but also to the mode area as well in the following correlation:

$$g(z) = \gamma(z) - \frac{1}{2S_m(z)} \frac{dS_m(z)}{dz}, \quad (3)$$

where,

$$S_m(z) = 2\pi \int_0^\infty |U_m(r, z)|^2 r dr \quad (4)$$

is the mode area. Let us assume the dispersion and nonlinearity parameters to be the functions of z coordinate which are defined as $D(z) = D_0 d(z)$ and $R(z) = R_0 r(z)$, where D_0, R_0 are the values of these parameters at the fiber input. Introduction of a new variable $\xi(z) = \int_0^z d(z') dz'$ and the pulse envelope $C(\tau, z) = \sqrt{r(z)/d(z)} A(\tau, z)$ to (2) yields the equation with the constant dispersion and nonlinearity but length-inhomogeneous gain

$$\frac{\partial C}{\partial \xi} - i \frac{D_0}{2} \frac{\partial^2 C}{\partial \tau^2} + iR_0 |C|^2 C = g_{\text{ef}}(\xi)C. \quad (5)$$

The effective and inhomogeneous (with the respect to a new coordinate ξ) gain increment is defined as

$$g_{\text{ef}}(\xi) = \frac{\gamma(\xi)}{d(\xi)} - \frac{1}{2} \frac{\partial}{\partial \xi} \ln \frac{S_m(\xi)}{S_m(0)} \frac{d(\xi)}{r(\xi)}. \quad (6)$$

Having performed all substitutions, the problem to describe the nonlinear pulse propagation in the optical fiber with such parameters inhomogeneous over the length as GVD, nonlinearity, gain and effective mode area is reduced to the description of the optical pulse propagation in the fiber with the homogeneous dispersion D_0 and nonlinearity R_0 and inhomogeneous effective gain g_{ef} , which strongly depends on the mode profile $S_m(z)$.

3. Conditions of Similariton Existence in the Amplifying Fiber

As known, the singularity of a similariton pulse propagation consists of the fact that the pulse envelope, irrespective of its original profile, asymptotically approaches to a parabolic shape scaled along the pulse coordinate [4–9]. In this case, the pulse can be expressed as:

$$A(\tau, z) = A(z)G_{\text{par}}(z, \tau) \exp[i(\phi(z) + \alpha(z)\tau^2)], \quad (7)$$

where $\phi(z)$ is the pulse phase; $\alpha(z)$ is the FM rate (chirp) which is constant for a similariton. Here, function $G_{\text{par}}(\tau, z)$ assigns the profile of the parabolic pulse envelope and is determined by

$$G_{\text{par}} = \begin{cases} \sqrt{\frac{1 - \tau^2}{\tau_s^2(z)}}, & \tau \leq \tau_s(z), \\ 0, & \tau > \tau_s(z), \end{cases} \quad (8)$$

where $\tau_s(z)$ is the pulse duration.

It is known that the condition under which (5) has an exact solution in a form of FM parabolic pulse can be expressed as [6–9]

$$g_{\text{ef}} - 3\alpha_0 D_0 = 0. \quad (9)$$

In the case of an active optical fiber, the condition for producing a stable similariton, that is, condition (7), can be given as

$$\gamma_0 - 3\alpha_0 D_0 = 0. \quad (10)$$

It is noteworthy that the available sources of picosecond pulses used to generate similariton FM pulses, as a rule, can produce (after passing through the complementary dispersive components) chirp of some $10^{23} - 10^{24} \text{ c}^{-2}$. Moreover, the GVD values of the amplifying fibers being used do not exceed $3 \cdot 10^{-26} \text{ c}^2/\text{M}$ (in practice, for instance, the GVD of Er^{3+} -doped fibers, in rare cases, exceed this value [6–8, 19, 20]). As a consequence, the gain increment of the homogeneous fiber which is responsible for the FM similariton production must be appreciably lower than 0.1 m^{-1} (a more precise analyses yields γ value not more than 0.01 m^{-1}). In this case, to increase the pulse energy more than by an order of magnitude is required that the fiber length exceed 10 meters (and even 100 meters). As it follows from the experiments on Er-, Yb-, and Bi-doped fibers [7, 8], as well as from the numerical simulation [18, 19], self-similar FM pulses are very sensitive to the fluctuation of the gain increment and variation of the fiber amplifier diameter. By virtue of this fact, it proves difficult to use long (longer than 100 meters) active fibers to reach considerable (more than by an order of magnitude) pulse energy increase. The way out could be a short fiber (<10 meters) with a high gain ($\gamma > 1 \text{ M}^{-1}$) and GVD sharply increasing over its length. Further, the possibility of an efficient “rapid” parabolic FM pulse amplification will be studied in the length-inhomogeneous fiber with W-profile of the refractive index distribution over the fiber cross-section. Taking into account expression (6), condition (9) acquires the following form for the effective gain increment:

$$6\alpha_0 D(z) = 2\gamma(z) - \frac{1}{S_m} \frac{\partial S_m}{\partial z} + \frac{1}{R} \frac{\partial R}{\partial z} - \frac{1}{D} \frac{\partial D}{\partial z}. \quad (11)$$

Here, the nonlinearity-dependent term can be rewritten as

$$\frac{1}{R} \frac{\partial R}{\partial z} = \frac{1}{n_2} \frac{\partial n_2}{\partial z} - \frac{1}{S_{\text{ef}}} \frac{\partial S_{\text{ef}}}{\partial z}, \quad (12)$$

where n_2 is the cubic nonlinearity parameter, and effective mode area is introduced as

$$S_{\text{ef}}(z) = \frac{2\pi \left(\int_0^\infty |U_m(r, z)|^2 r dr \right)^2}{\int_0^\infty |U_m(r, z)|^4 r dr}. \quad (13)$$

Using the derived relations, we will arrive to the following equation describing the GVD profile over the fiber length:

$$\frac{\partial D}{\partial z} - f(z)D(z) + 6\alpha_0 D^2(z) = 0, \quad (14)$$

where the function $f(z) = 2\gamma(z) - (1/S_m)(\partial S_m/\partial z) + (1/R)(\partial R/\partial z)$ is introduced.

Solution of (14) allows to obtain a required profile of the GVD variation which provides a self-similar propagating regime of the parabolic FM pulses. This equation represents a well-known Bernoulli equation, and its solution can be written in the following way:

$$D(z) = D_0 F(z) \times \frac{\exp\left[2 \int_0^z \gamma(z') dz'\right]}{1 + 6\alpha_0 D_0 \int_0^z F(z') \exp\left[2 \int_0^{z'} \gamma(z'') dz''\right] dz'}, \quad (15)$$

where D_0 is the input GVD, and the following notion is introduced:

$$F(z) = \frac{S_{\text{ef}}(0) S_{m0} n_2(z)}{S_{\text{ef}}(z) S_m(z) n_{20}}. \quad (16)$$

If the material gain is kept constant over the whole fiber length and relation $F(z) \approx 1$ is fulfilled (that is, valid, with a high precision, for most practically important cases, and, first of all, for W-profile fibers [18–20]), the required GVD profile will have the following view:

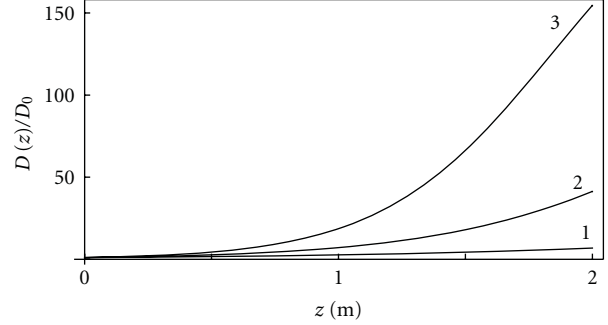
$$D(z) = \frac{\gamma D_0 e^{2\gamma z}}{\gamma + 3\alpha_0 D_0 (e^{2\gamma z} - 1)}. \quad (17)$$

Taking into account (17), the efficient amplification of frequency-modulated pulses could be carried out when $\gamma/3\alpha_0 > D(0)$ and the normal dispersion is increasing along the active fiber length. If $\gamma/3\alpha_0 < D(0)$, then the dispersion should decrease along the length, and if $\gamma/3\alpha_0 \approx D(0)$, the dispersion should be constant along amplifier length. It could be noted that the first case is fast scenario (the amplifier length is less than 10 m) and the second is slow.

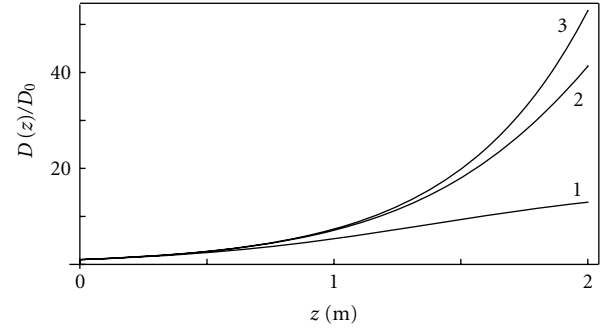
Figures 1(a) and 1(b) show the relative dispersion function along the amplifier length to reach optimal similariton amplification. The grow of similariton pulse energy is possible if the GVD is increasing essentially. The relation between the final and initial similariton energy is close to the $D(z)/D(0)$.

For a passive fiber with the negligibly low optical loss (i.e., fiber with $\gamma \rightarrow 0$), the GVD satisfying the condition for the similariton existence in W-profile fiber will have a hyperbolic shape (что полностью соответствует результатам полученным в работах [11, 13])

$$D(z) = \frac{D_0}{1 + 6\alpha_0 D_0 z}. \quad (18)$$



(a)



(b)

FIGURE 1: The GVD profiles providing self-similar propagation of FM parabolic pulses in the optical fiber with the following fixed parameters: $\tau_0 = 10^{-12}$ s, $D_0 = 2 \cdot 10^{-27}$ s²/m and fitting parameters: $\alpha_0 = 10^{24}$ s⁻², $\gamma = (0.5; 1.0; 1.5)$ m⁻¹ (a) and $\gamma = 1$ m⁻¹, $\alpha_0 = (10^{23}, 10^{24}, 10^{25})$ s⁻² (b). One can see that exponential character of GVD at $\gamma \approx 1$ m⁻¹ is kept for the fibers shorter than 2 m.

Besides, in the general case, the following relation can be written for the similariton pulse duration [9]:

$$\tau_s(z) = \tau_0 \exp\left(2\alpha_0 \int_0^z D(z') dz'\right), \quad (19)$$

taking into account relation (15), we can express it as

$$\tau_s(z) = \tau_0 \left[1 + 6\alpha_0 D_0 \int_0^z F(z') \exp\left(2 \int_0^{z'} \gamma(z'') dz''\right) dz' \right]^{1/3}. \quad (20)$$

If $F(z) = 1$ and $\gamma = 0$, we obtain the following known relation for the pulse duration [3, 4]:

$$\tau_s(z) = \tau_0 [1 + 6\alpha_0 D_0 z]^{1/3}. \quad (21)$$

In the general case, the formation energy for the parabolic similariton can be defined as follows [9]:

$$W_s = \frac{8cD(0)\alpha_0^2\tau_0^3}{3\omega_0 n_2(0)} S_{\text{ef}}(0). \quad (22)$$

Equations (22) and (11) describe the condition under which the stable self-similar pulses similaritons are generated. The energy change of the wave packet during its propagation through the fiber is defined

$$W_s(z) = W(0) \exp\left(2 \int_0^z \gamma(z') dz'\right). \quad (23)$$

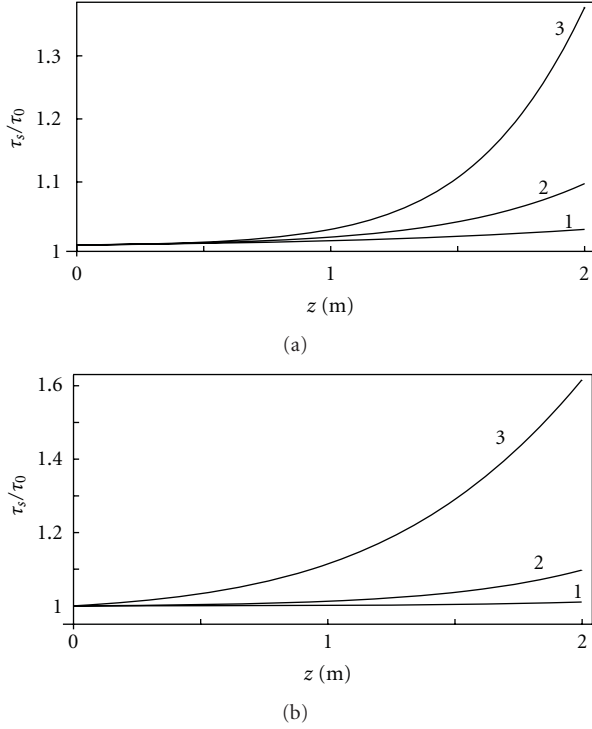


FIGURE 2: The normalized duration of similariton pulse versus output gain with the following fixed parameters: $\tau_0 = 10^{-12}$ s, $D_0 = 2 \cdot 10^{-27}$ s²/m and fitting parameters: $\alpha_0 = 10^{24}$ s⁻², $\gamma = (0.5; 1.0; 1.5)$ m⁻¹ (a) and $\gamma = 1$ m⁻¹, $\alpha_0 = (10^{23}, 10^{24}, 10^{25})$ s⁻² (b). One can see the pulse duration increase with the increasing output gain and fiber length.

The similariton pulse width as a function of active fiber length is shown on Figures 2(a) and 2(b) for different values of γ and frequency modulation. For indicated fiber lengths and essential similariton energy increase, there is only a weak width change. As a result, there is a tiny spectrum modification if the chirp parameter is constant. Definitely, this condition is important for stable similariton amplification.

The stability of $g_{ef}(\xi)$ should be taken into account in relation to external perturbations. It has been shown earlier [15] that the frequency-modulated parabolic pulses are stable to $g_{ef}(\xi)$ variations. One could believe that the dispersion parameter would be stable too (in accordance with (6)). It is essential for efficient amplification. In addition, the influence of high-order dispersion effects is small for proposed technique of frequency-modulated pulses amplification. Indeed, if the fiber amplifier does not exceed 10 m, the significance of the 3 rd order dispersion would be not essential. For instance, in the case of picosecond pulse with initial chirp of $\alpha_0 < 10^{24}$ c⁻² the characteristic length $L^{(3)} \gg 10^3$ M.

4. Compression of FM Pulses

As follows from the performed analysis, the regime of the parabolic pulse amplification in a medium with normal dispersion is accompanied by the increase of its duration

while preserving the chirp. A further increase in the peak power of the pulse due to its temporal compression should be performed in a passive dispersive medium providing a minimal nonlinear effects (it is required to avoid, as far as possible, the corresponding noises and aberration as well as the development of different kinds of instabilities [9, 10]). This procedure can be performed already outside the amplifying fiber: either in a passive anomalous dispersion fiber with a low nonlinearity (hollow fibers can be used for this purpose), or on a couple of diffraction gratings acting as an effective dispersion element. At present, this technology for producing high-energy laser pulses is the most developed [21–23]. The technology providing compression in an all-fiber regime is supposed to be the method of using hollow crystal fibers with a low cubic nonlinearity [24, 25].

The duration of a bandwidth-limited pulse with the parameters $\tau_s(L)$ and α_0 at the compressor input (after propagating through the fiber amplifier of the length L) after passing through the compressor is as follows [9, 23]:

$$\tau_{\text{com}} = \frac{\tau_s(L)}{\sqrt{1 + (\alpha_0 \tau_s^2(L))^2}}. \quad (24)$$

When the inequality $\alpha_0 \tau_s^2(L) \gg 1$ is fulfilled, we have $\tau_{\text{com}} \sim 1/\alpha_0 \tau_s(L)$. The peak power of the compressed bandwidth-limited pulse can be determined by

$$P_{\text{max}} \cong P_0 \alpha_0 \tau_0 \tau_s(L) \exp\left(2 \int_0^L \gamma(z) dz\right). \quad (25)$$

It follows from the obtained relations that the more we “stretch” the pulse with a constant nonzero chirp in time, the more compressed the pulse will be and the higher the peak power can be obtained after pulse propagation through the compressor. Thus, if the input chirp is $\alpha_0 = 10^{24}$ c⁻², the original pulse duration is $\tau_0 = 10^{-12}$ c, the amplifier length is $L = 1$ M, and the gain increment is $\gamma = 2$ M⁻¹, the peak power can be increased in 100 times after chirp vanish (here, according to (20), we accept that after propagating through the amplifying fiber the pulse duration becomes twice as high). The offered scheme of pulse amplification and subsequent FM pulse compression is actively used nowadays in solid-state laser systems for generating high-power pulses.

The offered scheme of pulse amplification and subsequent FM pulse compression is actively used nowadays in solid-state laser systems for generating high-power pulses.

It seems that this technique based on similariton amplification and grating compressor would allow to move forward to generation of a few cycles pulses. Taking into consideration that the similariton energy may be at the level of 10 nJ and above, the output peak power could be at megawatt level. Definitely, this technique may be especially fruitful in 1550 nm spectral region (Er-doped fiber as amplifier) [24, 25]. Provided that increment gain $\gamma > 0.5$ m, the amplifier length should be enough small (e.g., 5 m) to amplify the input ps similariton more than in order. It seems the novel waveguide structure like a Bragg fiber would be useful to improve the parameters of such a all-fiber similariton amplifier. For instance, if the waveguide structure

allows to control the GVD by 2 orders, it will result to the corresponding energy increase of FM wave packet.

At present, there is a practical way to design and produce single mode fibers with chromatic dispersion varying along the length in accordance with some prearranged law [17]. This method performs a precise control of the fiber core diameter during the drawing. This technology became possible owing to digital signal processing used for the control of the drawing process. At present, fibers with various dispersion functions can be produced, for example, dispersion decreasing or dispersion increasing. The length of fiber with varying dispersion may be in the range from several meters to several kilometers. The dispersion deviation from the prearranged value is less than 0.1 ps/nm/km. To design the fiber with varying dispersion, the preform with dispersion shifted waveguide structure could be used. One can obtain the relation between the chromatic dispersion and outer fiber diameter solving the scalar wave equation for the preform profile and fixed drawing coefficient. The approach to produce fibers with chromatic dispersion varying along the length in accordance with a prearranged law became possible owing to digital signal processing used for the control of the drawing process. A real-time software designed enabled measuring and remembering the process parameters during the drawing and closing a feedback loop. The software and hardware tools enabled us to control the fiber diameter during drawing. After that, the current diameter is compared with the prearranged value, and then, a control parameter (the drawing speed) was calculated in accordance with the algorithm used. Working in such a manner, the feedback system could control well of the fiber diameter. Reliable operation of the digital control system in a wide drawing speed range has allowed to fabricate single mode fibers with chromatic dispersion varying along length. The necessary length dependence of the fiber diameter was written in the memory of the control computer. During the drawing, the current fiber length is registered along with the other parameters, the current diameter was compared with the prearranged value for the given length, and the necessary change of the drawing speed is worked out by the control algorithm to produce the desirable diameter.

5. Conclusion

Thus, in the present paper, we have obtained the conditions for appearance of stable parabolic pulses in the optical fibers with W-profile of radial propagation of the refractive index in the normal group velocity dispersion region. The relation for the GVD profile describing an optimally fast FM parabolic pulse amplification was offered. It was shown that the use of length-inhomogeneous FM similaritons (resistant to the wave instability) with the slightly increasing normal group-velocity dispersion allows to produce fiber laser systems with a high peak power $P > 1\text{MW}$.

Acknowledgment

This work was supported by the Federal Agency on Science and Innovations within the framework the Federal Task

Program "Academic and Teaching Staff of Innovative Russia in 2009-2013".

References

- [1] M. E. Fermann, V. I. Kruglov, B. C. Thomsen, J. M. Dudley, and J. D. Harvey, "Self-similar propagation and amplification of parabolic pulses in optical fibers," *Physical Review Letters*, vol. 84, no. 26, pp. 6010–6013, 2000.
- [2] G. Chang, H. G. Winful, A. Galvanauskas, and T. B. Norris, "Self-similar parabolic beam generation and propagation," *Physical Review E*, vol. 72, no. 1, Article ID 016609, pp. 1–4, 2005.
- [3] J. M. Dudley, C. Finot, D. J. Richardson, and G. Millot, "Self-similarity in ultrafast nonlinear optics," *Nature Physics*, vol. 3, no. 9, pp. 597–603, 2007.
- [4] T. Hirooka and M. Nakazawa, "Parabolic pulse generation by use of a dispersion-decreasing fiber with normal group-velocity dispersion," *Optics Letters*, vol. 29, no. 5, pp. 498–500, 2004.
- [5] A. I. Latkin, S. K. Turitsyn, and A. A. Sysoliatin, "Theory of parabolic pulse generation in tapered fiber," *Optics Letters*, vol. 32, no. 4, pp. 331–333, 2007.
- [6] A. Y. Plotskii, A. A. Sysoliatin, A. I. Latkin et al., "Experiments on the generation of parabolic pulses in fibers with length-varying normal chromatic dispersion," *Zhurnal Eksperimental'noi i Teoreticheskoi Fiziki*, vol. 85, no. 7, pp. 397–401, 2007.
- [7] A. V. Andrianov, S. V. Muraviov, A. V. Kim, and A. A. Sysoliatin, "Generation of optical soliton pulses smoothly tunable in a wide frequency range in silica fibers with variable dispersion," *JETP Letters*, vol. 85, no. 8, pp. 364–368, 2007.
- [8] I. O. Zolotovskii, D. I. Sementsov, A. K. Senatorov, A. A. Sysolyatin, and M. S. Yavtushenko, "Dynamics of similariton pulses in length-inhomogeneous active fibres," *Quantum Electronics*, vol. 40, no. 3, pp. 229–233, 2010.
- [9] A. S. Zeytunyan, K. A. Palandjan, G. L. Esayan, and L. K. Muradyan, "Nonlinear dispersive similariton: spectral interferometric study," *Quantum Electronics*, vol. 40, no. 4, pp. 327–328, 2010.
- [10] J. Laegsgaard and P. J. Roberts, "Influence of air pressure on soliton formation in hollow-core photonic bandgap fibers," *Journal of the Optical Society of America B*, vol. 26, no. 9, pp. 1795–1800, 2009.
- [11] S. Wabnitz and C. Finot, "Theory of parabolic pulse propagation in nonlinear dispersion-decreasing optical fiber amplifiers," *Journal of the Optical Society of America B*, vol. 25, no. 4, pp. 614–621, 2008.
- [12] C. Dai, Y. Wang, and J. Zhang, "Analytical spatiotemporal localizations for the generalized (3+1)-dimensional nonlinear Schrödinger equation," *Optics Letters*, vol. 35, no. 9, pp. 1437–1439, 2010.
- [13] C. Finot, B. Barviau, G. Millot, A. Guryanov, A. Sysoliatin, and S. Wabnitz, "Parabolic pulse generation with active or passive dispersion decreasing optical fibers," *Optics Express*, vol. 15, no. 24, pp. 15824–15835, 2007.
- [14] D. Ghosh, M. Basu, and S. Sarkar, "Generation of self-similar parabolic pulses by designing normal dispersion decreasing fiber amplifier as well as its staircase substitutes," *Journal of Lightwave Technology*, vol. 27, no. 17, pp. 3880–3887, 2009.
- [15] V. I. Kruglov, A. C. Peacock, J. M. Dudley, and J. D. Harvey, "Self-similar propagation of high-power parabolic pulses in optical fiber amplifiers," *Optics Letters*, vol. 25, no. 5-24, pp. 1753–1755, 2000.

- [16] C. Finot, J. M. Dudley, B. Kibler, D. J. Richardson, and G. Millot, "Optical parabolic pulse generation and applications," *IEEE Journal of Quantum Electronics*, vol. 45, no. 11, Article ID 5308680, pp. 1482–1489, 2009.
- [17] V. A. Bogatyryov, M. M. Bubnov, E. M. Dianov, and A. A. Sysolyatin, "Advanced fibres for soliton systems," *Pure and Applied Optics*, vol. 4, no. 4, article 009, pp. 345–347, 1995.
- [18] U. G. Akhmetshin, V. A. Bogatyrev, A. K. Senatorov, A. A. Sysolyatin, and M. G. Shalygin, "New single-mode fibres with the flat spectral dependence of the chromatic dispersion varying over the fibre length," *Quantum Electronics*, vol. 33, no. 3, pp. 265–267, 2003.
- [19] M. E. Likhachev, M. M. Bubnov, K. V. Zotov et al., "Erbium-doped aluminophosphosilicate optical fibres," *Quantum Electronics*, vol. 40, no. 7, pp. 633–638, 2010.
- [20] D. A. Gruk, V. A. Bogatyrev, A. A. Sysolyatin, V. M. Paramonov, A. S. Kurkov, and E. M. Dianov, "Broadband radiation source based on an ytterbium-doped fibre with fibre-length-distributed pumping," *Quantum Electronics*, vol. 34, no. 3, pp. 247–248, 2004.
- [21] G. A. Mourou, T. Tajima, and S. V. Bulanov, "Optics in the relativistic regime," *Reviews of Modern Physics*, vol. 78, no. 2, pp. 309–371, 2006.
- [22] V. V. Lozhkarev, S. G. Garanin, R. R. Gerke et al., "100-TW femtosecond laser based on parametric amplification," *Zhurnal Eksperimental'noi i Teoreticheskoi Fiziki*, vol. 82, no. 4, pp. 196–199, 2005.
- [23] S. A. Akhmanov, V. A. Vysloukh, and A. S. Chirkin, *Optics of Femtosecond Laser Pulses*, AIP, New York, NY, USA, 1992.
- [24] D. N. Papadopoulos, Y. Zaouter, M. Hanna et al., "Generation of 63 fs 4.1 MW peak power pulses from a parabolic fiber amplifier operated beyond the gain bandwidth limit," *Optics Letters*, vol. 32, no. 17, pp. 2520–2522, 2007.
- [25] D. J. Richardson, J. Nilsson, and W. A. Clarkson, "High power fiber lasers: current status and future perspectives," *Journal of the Optical Society of America B*, vol. 27, no. 11, pp. B63–B92, 2010.

Review Article

Manipulating the Propagation of Solitons with Solid-Core Photonic Bandgap Fibers

O. Vanvincq, A. Kudlinski, A. Bétourné, A. Mussot, Y. Quiquempois, and G. Bouwmans

Laboratoire PhLAM, UMR CNRS 8523, IRCICA, Université Lille 1, 59655 Villeneuve d'Ascq Cedex, France

Correspondence should be addressed to A. Kudlinski, alexandre.kudlinski@univ-lille1.fr

Received 7 April 2011; Accepted 20 June 2011

Academic Editor: Miguel González Herráez

Copyright © 2012 O. Vanvincq et al. This is an open access article distributed under the Creative Commons Attribution License, which permits unrestricted use, distribution, and reproduction in any medium, provided the original work is properly cited.

We review the dynamics of soliton self-frequency shift induced by Raman gain in special solid-core photonic bandgap fibers and its consequences in terms of supercontinuum generation. These photonic bandgap fibers have been designed to allow nonlinear experiments in the first bandgap without suffering from significant loss even when working close to the photonic bandgap edge. We studied experimentally, numerically, and analytically the extreme deceleration of the soliton self-frequency shift at the long-wavelength edge of the first transmission window. This phenomenon is interpreted as being due to a large variation of the group-velocity dispersion in this spectral range and has been obtained with no significant power loss. Then, we investigated experimentally and numerically the generation of supercontinuum in this kind of fibers, in both spectral and temporal domains. In particular, we demonstrated an efficient tailoring of the supercontinuum spectral extension as well as a strong noise reduction at its long-wavelength edge.

1. Introduction

Solid-core photonic bandgap (PBG) fibers are one class of microstructured optical fibers in which light is confined in a low-index solid core by the PBGs of the cladding [1]. In the case of two-dimensional PBGs, the periodic microstructured cladding is usually composed of periodic high-index inclusions embedded in a low-index background [1]. The core region then corresponds to a defect (lack of inclusion) in the center of the periodic structure. Because of the intrinsic nature of the PBG waveguidance, the fiber transmission properties are characterized by discrete spectral bands [1, 2] in which the group-velocity dispersion (GVD), attenuation, and effective mode area of the fundamental core mode are strongly wavelength dependent [3], especially near the PBG edges [1, 4]. These singular characteristics are thus of particular interest in the field of nonlinear (NL) fiber optics. The potential of solid-core PBG fibers for NL propagation experiments has already been pointed out by the report of soliton propagation and phase-matched dispersive wave generation [5, 6], even across different PBG [7]. Degenerate four-wave mixing [8], frequency doubling and tripling [9], and supercontinuum (SC) generation across adjacent PBGs have also been investigated numerically [10].

In this paper, we present an overview of our recent work showing how the particular properties of solid-core PBG fibers can influence soliton propagation and SC generation. First, we detail the linear properties of the fabricated solid-core PBG fibers under investigation through experiments and numerical modelling. Then, we demonstrate experimentally that the soliton self-frequency shift (SSFS) effect can be strongly mitigated [11]. A simple analytical model indicates that this is caused by the strong third-order dispersion experienced by solitons as they approach the PBG edge. Finally, we show that this SSFS quasicancellation allows to control the spectral extent of infrared SC in the long-pulse regime [12] and, simultaneously, leads to a significant reduction of spectral power fluctuations at the SC long-wavelength edge [13].

2. Linear Properties of the Solid-Core Photonic Bandgap Fibers

The solid-core PBG fibers used in various experiments reported in this paper are all based on the same double periodicity structure [11, 12], although their optogeometrical characteristics (summarized in Table 1) slightly vary from one fiber to another. The scanning electron microscope

TABLE 1: Table summarizing the optogeometrical properties of the three fabricated solid-core PBG fibers under investigation.

	d_{Ge} (μm)	d_{air} (μm)	Λ (μm)	ZDW (nm)	NL coefficient ($\text{W}^{-1} \cdot \text{km}^{-1}$)	PBG edge (nm)
Fiber 1	2.19	2.33	3.09	905	6 (at 1200 nm)	1535
Fiber 2	2.20	2.25	3.25	915	6.9 (at 1064 nm)	1580
Fiber 3	2.22	2.27	3.28	921	6.8 (at 1064 nm)	1590

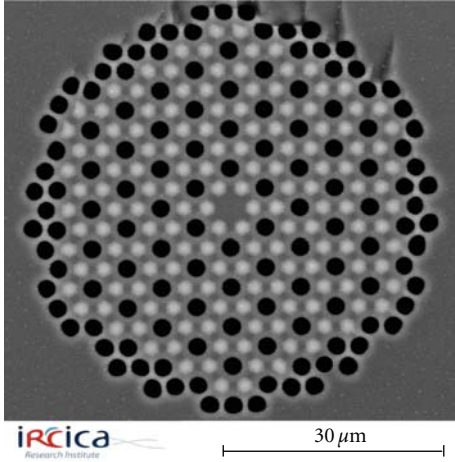


FIGURE 1: SEM image of the solid-core PBG fiber 1. Black regions are air holes, light gray regions are GeO_2 -doped inclusions, and the dark gray background is pure silica.

(SEM) image shown in Figure 1 illustrates such a double periodicity solid-core PBG fiber. The periodical high-index resonators (light gray regions in Figure 1) present in the cladding are responsible for the PBG guidance and are made of germanium-doped silica with a parabolic refractive index profile and a maximal index difference Δn of 32×10^{-3} (as compared to pure silica). They are embedded in a pure silica background (dark gray). Because we decided to work in the first PBG (mainly to minimize the effective area in order to maximize the NL coefficient), air holes of diameter d_{air} (depicted in black in Figure 1) were periodically added into the cladding structure for reducing the otherwise relatively high confinement losses in this PBG [14, 15]. The core region corresponds to a defect (lack of air hole) in the center of the periodic structure. The geometrical parameters of the three solid-core PBG fibers investigated here are summarized in Table 1, where the pitch Λ corresponds to the distance between two neighboring germanium-doped inclusions.

Although all fibers were characterized the same way, we only present here the linear properties of fiber 1, whose SEM image is depicted in Figure 1. Other fibers present similar characteristics, with a slight red-shift of the PBG transmission windows due to a slightly greater pitch Λ . Figure 2 shows the experimental transmission spectrum of a white light SC source through a 2 m long sample of the solid-core PBG fiber. The first PBG is very broad and extends from 740 to 1535 nm, whereas the second one is much sharper and extends from 510 to 650 nm. As for usual solid-core PBG fibers, typical resonances can be observed in the first ring of

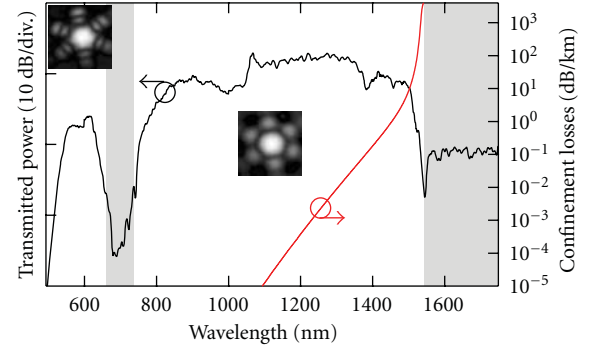


FIGURE 2: Transmission spectrum of the solid-core PBG fiber 1 (black line, left axis) measured with a SC source, and computed confinement losses across the first PBG (red line, right axis). Insets show the near-field mode profile in the first (right) and second (left) PBG. Gray areas depict spectral regions in which the PBG guidance in the core is not allowed.

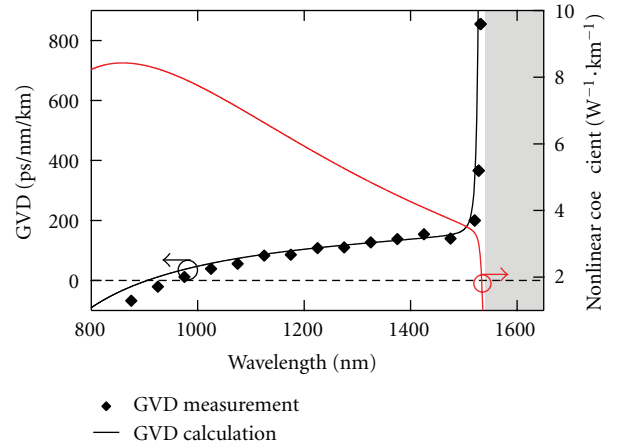


FIGURE 3: Calculated GVD curve of the solid-core PBG fiber 1 (solid black line, left axis), and corresponding measurements with a white-light interferometry setup (markers). Spectral evolution of the computed NL coefficient (red line, right axis). The gray area depicts the region outside the first PBG transmission window.

high-index resonators [4], with the number of intensity maxima indicating the PBG order (insets of Figure 2). The red curve (right axis) shows confinement losses across the first PBG calculated with a finite element mode solver. They are less than 1 dB/km across most of the PBG, and as expected they drastically increase to the dB/m range near the PBG edge. Figure 3 shows the calculated GVD curve of the solid-core PBG fiber 1 (solid black line), as well as measurements

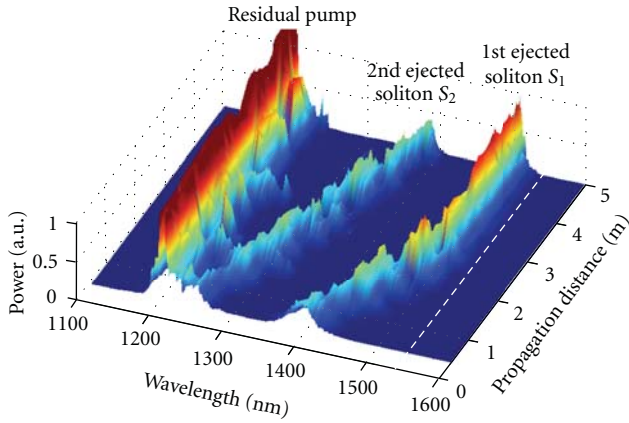


FIGURE 4: Evolution of the experimental output spectrum (linear scale) with fiber length (from 0.4 to 5 m) for 270 fs pump pulses at 1200 nm. The white dashed line represents the PBG edge.

(markers) performed with a low coherence interferometric method [16]. The GVD slightly increases from the zero-dispersion wavelength (ZDW), located around 900 nm, to about 200 ps/nm/km at 1510 nm. For higher wavelengths, the GVD increase suddenly becomes much more important because of an anticrossing point between the fundamental core mode and cladding modes at 1535 nm, delimiting the practical PBG transmission window [12]. In this region near the PBG edge, the GVD reaches extreme values well higher than 1000 ps/nm/km: measurements (not displayed in Figure 3 for the sake of clarity) indicates a GVD value 4760 ps/nm/km at 1535 nm, in excellent agreement with the calculated curve. This leads the third-order dispersion β_3 to reach extremely high values in the order of 10^{-37} s³/m in this spectral region. Finally, we also studied numerically the spectral dependance of the NL coefficient γ defined as $\gamma = n_2\omega/cA_{\text{eff}}$ [17], with n_2 the NL refractive index of pure silica and A_{eff} the mode effective area. Because the effective area also increases strongly near the PBG edge (due to the anticrossing phenomenon), the NL coefficient γ decreases rapidly near the PBG edge (see red curve in Figure 3) from about $6 \text{ W}^{-1} \cdot \text{km}^{-1}$ at 1200 nm to less than $1.3 \text{ W}^{-1} \cdot \text{km}^{-1}$ at 1535 nm.

In the following, we will see that the strong and unusual spectral dependencies of GVD and NL coefficient near the PBG edge can be used to tailor and manipulate the propagation of solitons approaching this spectral region through SSFS, included in the context of long-pulse SC generation.

3. Quasicancellation of the Soliton Self-Frequency Shift

3.1. Experimental Evidence. To illustrate this possible manipulation of the SSFS, NL propagation experiments were first performed by launching 270 fs pulses with a repetition rate of 1 kHz at 1200 nm into a 5 m long sample of the solid-core PBG fiber 1. This pump wavelength has been chosen from a compromise between a wavelength not too close to the long-wavelength edge of the first PBG (in order to

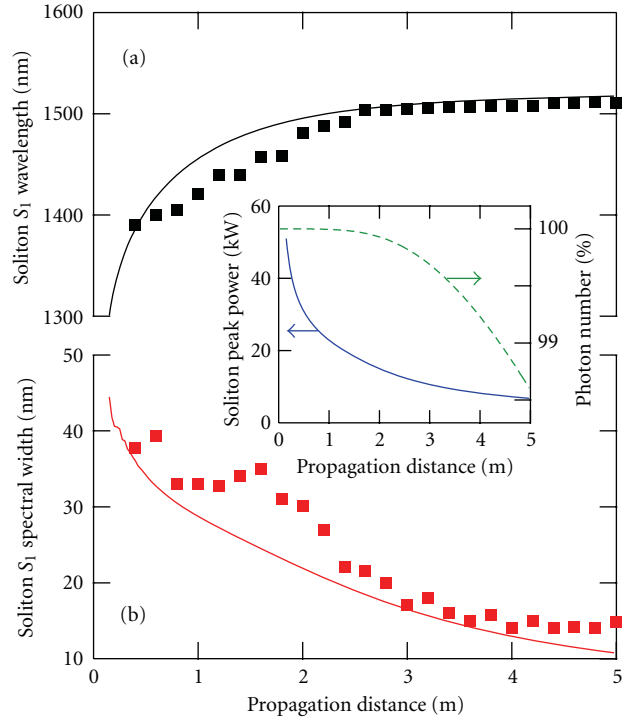


FIGURE 5: (a) Central wavelength of the first ejected soliton S_1 as a function of propagation distance. (b) Evolution of the soliton S_1 spectral width as a function of propagation distance. Solid lines and markers, respectively, correspond to numerical simulations and experimental measurements. Inset: numerical simulation of soliton S_1 peak power (blue solid line, left axis) and of the total photon number (green dashed line, right axis) versus propagation distance.

observe a significant SSFS) and not too close to the ZDW (in order to avoid SC generation). Similarly, the input peak power was adjusted so that it was high enough to observe SSFS for several solitons while being low enough to avoid SC generation. The pump peak power effectively launched into the fiber core was estimated to about 10–20 kW. Figure 4 shows a representation of the output spectrum (in linear scale) as a function of fiber length from 0.4 to 5 m. It was obtained from a cut-back measurement in which the output spectrum was recorded every 20 cm while keeping the launch conditions unchanged. The input Gaussian pulse breaks up into two fundamental solitons (labeled S_1 and S_2) through a fission mechanism [18, 19] caused by Raman scattering and higher-order dispersion effects [19, 20]. As expected, both solitons then red-shift through Raman-induced SSFS [21, 22]. The most striking feature in the soliton dynamics is that, after 2.5 m, the first ejected soliton, S_1 , becomes frequency locked at a central wavelength of about 1510 nm, that is, when its spectrum starts to overlap with the PBG located at 1535 nm (depicted in white dotted line in Figure 4). This is even more clearly illustrated in Figure 5(a) which shows a plot of the S_1 soliton central wavelength (black squares) as a function of the propagation distance. A clear slope change in the SSFS rate is observed at the fiber length of 2.5 m. Red squares in Figure 5(b) represent the evolution of soliton S_1 full width at half maximum (FWHM) spectral width versus

propagation length. It is shown that, as soliton S_1 red-shifts, it initially experiences a spectral compression from about 40 nm to 15 nm within the first 3 m. For longer propagation distances, that is, when the soliton is frequency locked, its spectral width stabilizes to about 15 nm, without any significant change in its spectral power density, as observed in Figure 4. Note that the same phenomenon was observed for the soliton S_2 (at a longer fiber length) and even for more than five ejected solitons by increasing the pump power. These experiments clearly show that the SSFS is extremely decelerated (and even quasicancelled) when the solitons approach the PBG edge, this effect being accompanied by a spectral compression.

3.2. Confirmation with Numerical Simulations. In order to get further insight into this phenomenon, we performed numerical simulations by integrating the generalized NL Schrödinger equation (GNLSE) taking into account the mode profile dispersion [23]. In this case, it writes [23, 24]:

$$\begin{aligned} & \frac{\partial \tilde{C}(z, \omega)}{\partial z} \\ &= i(\beta(\omega) - \beta_0 - \beta_1(\omega - \omega_0))\tilde{C}(z, \omega) - \frac{\alpha(\omega)}{2}\tilde{C}(z, \omega) \quad (1) \\ &+ i\bar{\gamma}(\omega)\mathcal{F}\left(C(z, t)\int_{-\infty}^{\infty}R(t-t')|C(z, t')|^2 dt'\right), \end{aligned}$$

where the NL coefficient takes the following form [24]:

$$\bar{\gamma}(\omega) = \frac{n_2\omega n_0}{cn_{\text{eff}}(\omega)\sqrt{A_{\text{eff}}(\omega)A_{\text{eff}}(\omega_0)}} \quad (2)$$

and $\tilde{C}(z, \omega) = \tilde{A}(z, \omega)(A_{\text{eff}}(\omega_0)/A_{\text{eff}}(\omega))^{1/4}$, $\tilde{A}(z, \omega)$ being the complex spectral envelope. The coefficient β_0 corresponds to the mode propagation constant $\beta(\omega)$ at the center frequency of the input pulse spectrum ω_0 , and β_1 is the first derivative of $\beta(\omega)$ (i.e., $d\beta(\omega)/d\omega$). The symbol \mathcal{F} denotes the Fourier transform of the function in argument, and $\alpha(\omega)$ is the fiber linear power attenuation at ω . The silica response function is defined by $R(t) = (1 - f_R)\delta(t) + f_R h_R(t)$ where $f_R = 0.18$ and $h_R(t)$ is the Raman response function which is approximated by the analytical expression given in [25].

Figure 6 shows a propagation simulation over 5 m of a 270 fs Gaussian pulse with 15 kW peak power centered at 1200 nm, corresponding to the input experimental pulses. The frequency dependence of all parameters, that is, $\alpha(\omega)$, $\beta(\omega)$, and $A_{\text{eff}}(\omega)$, associated with the experimental fiber was taken into account. This simulation shows excellent qualitative agreement with the experimental results of Figure 4. The input pulse experiences fission leading to the ejection of two fundamental solitons, labeled S_1 to S_2 , and the SSSF associated to soliton S_1 is strongly decelerated near the PBG edge. This effect is accompanied by a spectral compression and an increase of its spectral power density. Black and red solid lines in Figure 5, respectively, correspond to the simulated soliton S_1 central wavelength and FWHM spectral width. They show good quantitative agreement with experiments, especially when the solitons approach the PBG

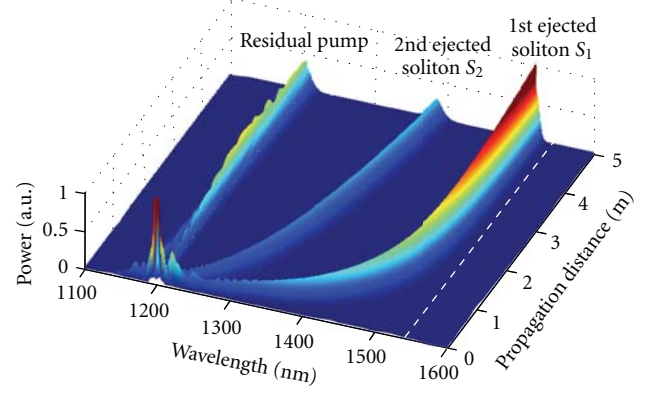


FIGURE 6: Numerical simulation of the propagation of a 270 fs Gaussian pulse with 15 kW peak power centered at 1200 nm, showing fission and ejection of two fundamental solitons S_1 and S_2 . All frequency-dependant parameters of the fiber were taken into account. The white dashed line represents the PBG edge.

edge (for propagation distances greater than 2.5 m). The blue solid curve in the inset of Figure 5 represents the soliton S_1 peak power as a function of propagation distance. Although its spectral power density increases (as shown in Figure 6), its peak power (in the temporal domain) decreases along propagation, because the soliton temporally broadens. The variation of total photon number as a function of fiber length is displayed in the green dashed curve in the inset of Figure 5. It decreases (due to linear attenuation) by only less than 1.5% within the first 5 m, which indicates that the soliton S_1 does not significantly suffer from the high attenuation at the PBG edge. This suggests that the quasicancellation of the SSFS does not occur at the expense of significant attenuation. At this point, however, the physics at the origin of this phenomenon has not been elucidated yet.

3.3. Discussion. First, let us recall that, as a soliton reaches the PBG edge, the values of the GVD evaluated at its central frequency strongly increase while its NL coefficient is largely reduced (see Figure 3). All these spectral evolutions are expected to be detrimental to the efficiency of the SSFS as they lead, directly or indirectly, to a significant increase of the pulse duration which is known to strongly affect the SSFS efficiency [17, 22]. In the following, we will present an analytical approach that allows to quantify the relative weight of the spectral dependence of the GVD ($d\beta_2/d\omega$) and NL coefficient ($d\bar{\gamma}/d\omega$) on the SSFS rate. For the sake of clarity, we only consider hereafter fundamental solitons as input pulses. This is justified by the fact that experimental input pulses experience fission which leads to pulse breakup and ejection of actual fundamental solitons [18–20]. The characteristics of these input pulses (hyperbolic secant pulses of 21 fs duration FWHM and 100 kW peak power) were estimated from the measurement of the soliton S_1 spectral width in Figure 5(b), assuming a soliton order $N^2 = 1$.

The starting point of our analysis is the well-known Gordon formula allowing to predict the SSFS rate, $d\langle\omega\rangle/dz$, of a fundamental soliton of mean frequency $\langle\omega\rangle$ and

duration T as a function of propagation distance z [22]. It writes

$$\frac{d\langle\omega\rangle}{dz} = -\frac{f_R|\beta_2(z)|T(z)\pi}{4}I(z), \quad (3)$$

where

$$I(z) = \int \Im(\tilde{h}_R(\Omega')) \frac{\Omega'^3}{\sinh^2(T(z)\pi\Omega'/2)} d\Omega' \quad (4)$$

and $\Im(\tilde{h}_R)$ is the imaginary part of the Fourier transform of the Raman response, which is related to the Raman gain spectrum [22]. Then, assuming that (i) the soliton remains fundamental, (ii) confinement losses are negligible, and (iii) the photon number is conserved, it is possible to find the following evolution of the soliton duration T as a function of propagation distance z [11]:

$$T(z) = \frac{\bar{\gamma}(0)^2|\beta_2(z)|}{\bar{\gamma}(z)^2|\beta_2(0)|} T_0, \quad (5)$$

where $T_0 = T(z=0)$ is the initial soliton temporal width. Figure 7 shows the evolution of the soliton central wavelength along propagation calculated by integrating (3) with help of (5) (red line) and by the numerical resolution of the GNLSE given by (1) (black line). A reasonable agreement is obtained between both curves, especially for the longest propagation distances (i.e., when the soliton appears to be frequency locked), the relative discrepancy on the frequency shift being less than 3% for values of z larger than 1 m. Thus, this Figure 7 shows that (i) the SSFS deceleration near the PBG edge is directly linked to the fiber properties, as claimed above and that (ii) the soliton central frequency can be predicted easily and very accurately for the longest propagation distances, without requiring the resolution of the GNLSE.

Then, in order to distinguish the effect of the spectral dependence of $\bar{\gamma}$ and the one of the spectral dependence of β_2 , we now calculate the *variation* of the SSFS rate with propagation distance z . Assuming that $\beta_2 < 0$, that is, $|\beta_2| = -\beta_2$, this writes [11]

$$\begin{aligned} \frac{d^2\langle\omega\rangle}{dz^2} &= \frac{f_R T(z)\pi I(z)}{4} \\ &\times \left[\frac{2\beta_2(z)}{\bar{\gamma}(z)} (4 - K(z)) \frac{d\bar{\gamma}}{dz} - (3 - K(z)) \frac{d\beta_2}{dz} \right], \end{aligned} \quad (6)$$

where

$$\begin{aligned} K(z) &= \frac{1}{I(z)} \int \left[\Im(\tilde{h}_R(\Omega')) - \left(\frac{d\Im(\tilde{h}_R)}{d\Omega} \right)_{\Omega'} \right] \\ &\times \frac{\Omega'^3}{\sinh^2(T(z)\pi\Omega'/2)} d\Omega'. \end{aligned} \quad (7)$$

From (6), it can be seen that the variation of SSFS rate during the propagation depends on the variation of β_2 and

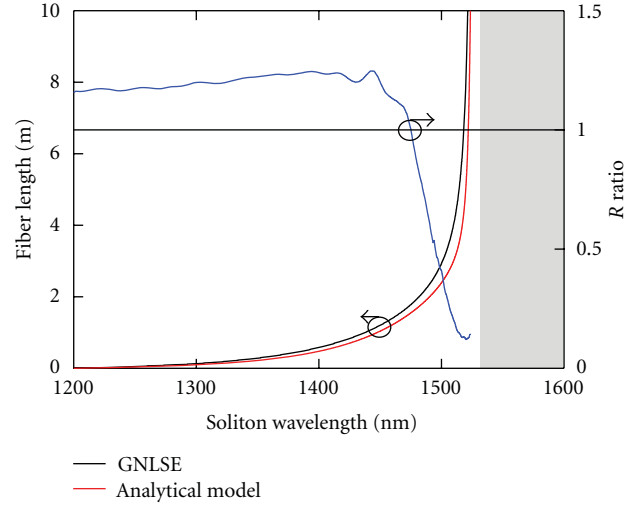


FIGURE 7: Left axis: evolution of the soliton central wavelength with fiber length calculated by integration of the GNLSE (black line) and with (5) in the case of the Gordon model (red line). Right axis: evolution of the R ratio defined by (8) with soliton wavelength.

$\bar{\gamma}$ with z . Since the fiber is assumed to be invariant along its length, the variations of β_2 and $\bar{\gamma}$ with z are in fact only due to their spectral evolution as the soliton red-shifts, that is, $\beta_2(\omega(z))$ and $\bar{\gamma}(\omega(z))$. Consequently, the derivative of β_2 and $\bar{\gamma}$ with respect to z in (6) can mathematically be expressed in terms of their derivative with respect to ω . We then introduce the R ratio defined as

$$R = -\left(\frac{4 - K(z)}{3 - K(z)} \right) \frac{2\beta_2}{\bar{\gamma}} \frac{d\bar{\gamma}/d\omega}{d\beta_2/d\omega} \quad (8)$$

so that values of R higher than 1 indicate that the NL coefficient variation $d\bar{\gamma}/d\omega$ dominates the evolution of SSFS rate while values of R smaller than 1 mean that the dynamics of the SSFS is mainly driven by the GVD variation $d\beta_2/d\omega$, that is, by the third-order dispersion term β_3 .

The blue curve of Figure 7 (right axis) shows a plot of the R ratio as a function of soliton wavelength calculated with (8). From this plot, it can be seen that the spectral variation of $\bar{\gamma}$ dominates the beginning of the SSFS dynamics, whereas for wavelengths higher than 1475 nm the effect induced by the spectral variation of β_2 becomes predominant. More importantly, the R value just below the PBG edge (located at 1535 nm) is about 0.1, which clearly means that the extreme deceleration of the SSFS is due to the large GVD slope $|\beta_3|$ near the PBG edge rather than the large NL coefficient diminution.

Finally, let us mention that, in the absence of loss, a real cancellation of the SSFS, that is, $d\langle\omega\rangle/dz = 0$, implies that β_2 and/or A_{eff} are infinite in order to get T also equal to infinite. Thus, the strong decrease of the SSFS efficiency near the PBG edge does not lead, strictly speaking, to a true suppression of the SSFS for a finite propagation distance. However, the extreme deceleration observed all along this paper is enough to consider that the soliton frequency can be considered, at least from a practical point of view, as frequency locked.

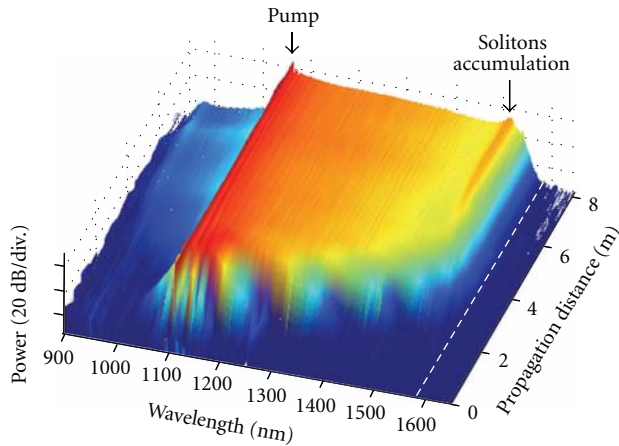


FIGURE 8: Experimental dynamics of the SC formation as a function of fiber length in the solid-core PBG fiber 2 for a pump power of 2.3 kW. The white dashed line represents the PBG edge.

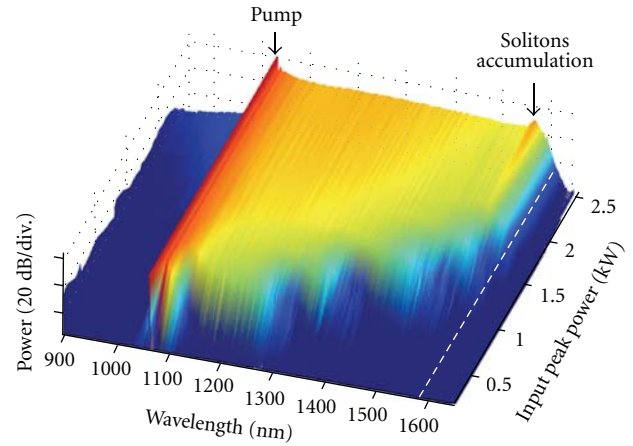


FIGURE 9: Experimental dynamics of the SC formation as a function of launched pump peak power. The white dashed line represents the PBG edge.

4. Tailoring the SC Extension

The SSFS is one of the main mechanisms involved in the generation of octave-spanning SC [26]. Indeed, in both the short- and long-pulse pumping regimes [27], the long-wavelength part of the SC spectrum is composed of red-shifting fundamental solitons initially created, respectively, by pulse fission and modulation instability (MI) [26]. Given that the spectral extent in the visible is intimately linked to the infrared one through a group index matching between solitons and trapped dispersive waves [28, 29], the SSFS dynamics lies at the heart of the SC generation process. There have been many attempts to optimize the spectral extension of SC sources, but, in most applications, only a small part of the SC spectrum is useful. There is thus an increasing interest in tailoring the spectral extent so that SC generation only occurs over the required spectral region. Fibers with two ZDWs have been employed in this way [30, 31]. Because the region of anomalous GVD can be suitably adjusted through a control of the microstructured cladding parameters, the SSFS can be cancelled near the long-wavelength ZDW, which results in a stop of the infrared spectral broadening. However, the SSFS cancellation is accompanied by the emission of a dispersive wave at higher wavelengths, so that the energy of frequency locked solitons exponentially decreases. In this section, we show that the cancellation of the SSFS observed in solid-core PBG fibers described above allows to control the SC spectral extent without any significant loss of energy.

4.1. Dynamics of the SC Formation. SC experiments were performed using the solid-core PBG fiber 2 of Table 1, in which long-wavelength PBG edge is located at 1580 nm. The pump laser used to generate the SC was a linearly polarized microchip laser emitting 0.6 ns pulses at 1064 nm with a repetition rate of 7 kHz. The coupling efficiency in the fibre core is estimated to be 50%. In the following, input power always refers to the power effectively launched into the fibre core.

At first, we investigated the dynamics of the SC formation with propagation distance by cutting the fiber back from 8 to 0.1 m and recording the output spectrum every 0.5 m, for a fixed pump power of 2.3 kW. Figure 8 shows the evolution of the output spectrum as a function of propagation distance. The spectrum initially presents two symmetric side lobes characteristic of MI classically observed when pumping in the anomalous GVD regime. In the temporal domain, this corresponds to the generation of a solitonic train, in which pulses strongly differ from each other in terms of peak power and duration. The spectrum then mainly broadens towards the infrared (because we pump relatively far away from the ZDW in the anomalous dispersion regime) until a fiber length of about 4 m is reached. At this propagation distance, the SC ranges from 1050 to 1580 nm. The infrared spectral broadening is due to the SSFS of each individual soliton generated from MI. Since they are characterized by very different properties, their SSFS efficiency can be very different, which leads to the SC. For further increasing fiber lengths to 8 m, the long-wavelength spectral broadening completely stops, due to the SSFS cancellation of each soliton approaching the PBG edge, following the mechanism described in Section 3. This leads to an accumulation of solitons just below the PBG edge (located at 1580 nm), which can be seen as a spectral power peak centered around 1550 nm. Consequently, the SC long-wavelength spectral extent can be tailored over a given spectral range through a suitable design of the fiber linear properties and, in particular, of the long-wavelength PBG edge.

To further illustrate this, we performed an additional experiment in which the dynamics of the SC formation was investigated as a function of pump peak power, for a fixed fiber length of 10 m. To do that, the output spectrum was recorded with 0.2 kW increments for pump peak powers ranging from 0.2 to 2.6 kW. The result of these measurements is displayed in Figure 9. Similar to previous experiments of Figure 8, the spectrum mainly broadens towards the infrared when the pump peak power is increased from 0 up to about

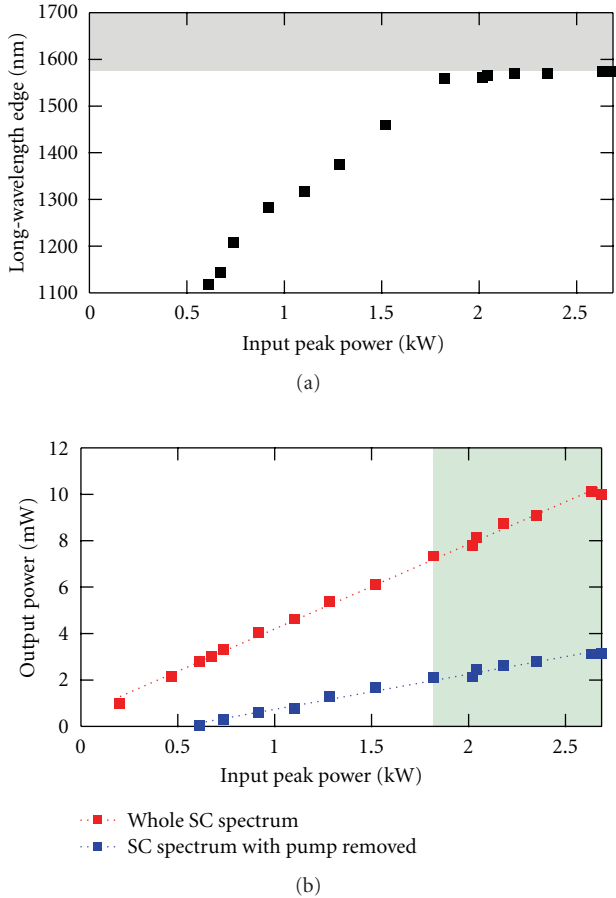


FIGURE 10: (a) Measurement of the long-wavelength edge of the SC spectrum as a function of input peak power in a 10 m-long solid-core PBG fiber sample. The gray area depicts the region outside the first PBG transmission window. (b) Measured output average power over the whole SC spectrum (red squares) and by removing the output pump peak with a 1064 nm notch filter (blue squares), as a function of input peak power. Dotted lines are linear fits. The green area corresponds to input peak powers for which the SC spectral extent stops (i.e., for input peak powers greater than 1.8 kW).

1.7 kW. For higher pump powers, the spectral broadening suddenly stops at the long-wavelength PBG edge. This is even more clearly illustrated in Figure 10(a) which represents the long-wavelength SC edge (measured for a 10 dB drop with respect to the spectral power at 1100 nm) as a function of input peak power. A clear cancellation of the spectral broadening at the PBG edge (depicted in gray) is observed for peak powers higher than 1.7 kW. As discussed above, this effect is accompanied by an accumulation of solitons which can be seen as a spectral power peak at 1550 nm, that is, just below the PBG edge located at 1580 nm.

4.2. Discussion. As shown by Figure 4 and discussed in Section 3, the SSFS cancellation occurs without any reduction of the spectral power density. This thus suggests, in the frame of SC generation, that the SC spectrum width can be limited by the PBG effect without any significant

power loss. In order to check this experimentally, we plotted in Figure 10(b) the output average power measured over the whole SC spectrum (red squares) as a function of the input peak power. These measurements can be linearly fitted (red line), and the slope does not change once the SSFS cancellation has occurred and the SC spectral broadening has stopped (corresponding to the green region). In order to check that this was not due to the residual pump peak in the SC, we performed the same kind of measurements after filtering it with a notch filter at 1064 nm at the fiber output. The results are displayed with blue markers in Figure 10 and show that the output SC power (without the contribution of the 1064 nm pump) still increases with the input peak power. This confirms that the tailoring of the SC extent is not done through a simple long-wavelength filtering due to the PBG effect, which would lead to a significant output power reduction. In our case, the fact that solitons are frequency locked rather than attenuated near the PBG edge allows to keep most of the launched power into the SC and thus to optimize the pump power budget.

5. Reduction of Pulse-to-Pulse Power Fluctuations at the SC Long-Wavelength Edge

In this section, we focus our attention on pulse-to-pulse fluctuations of the SC spectral power near the long-wavelength edge of the spectrum. Indeed, in the long-pulse regime, the spectral broadening originates from the MI process which is seeded by noise and the long-wavelength SC edge is characterized by statistically rare optical rogue waves [32], originating from soliton dynamics [32–35]. Consequently, the SC is characterized by a low coherence, and pulse-to-pulse fluctuations of the spectral power at the long-wavelength SC edge are very important [32, 36]. Here, we investigate the impact of the SSFS cancellation observed in solid-core PBG fibers on pulse-to-pulse fluctuations of the long-wavelength SC edge.

5.1. Experiments. Experiments were performed using the solid-core PBG fiber 3 of Table 1, in which long-wavelength PBG edge is located at 1590 nm. Following the results of Section 4, a SC was generated using a 7 m long fiber sample and a pump power of 3 kW. Figure 11(a) shows a measurement of the spectral broadening as a function of propagation distance (made using a cutback technique). As expected, the infrared spectral broadening stops near the PBG edge, depicted with the dashed white line. Figures 11(b1) and 11(b2) shows the spectra obtained at 7 m and 2.5 m, respectively. Although the spectral extent is comparable in both cases, the shape of the spectrum is different. Indeed, while the long-wavelength edge is relatively smooth for a fiber length of 2.5 m, it becomes much sharper at 7 m, where the cancellation of the SSFS imposes a saturation of the spectral broadening. This phenomenon causes a soliton accumulation whose spectral signature is the peak located around 1560 nm, as discussed in the previous section.

Pulse-to-pulse power fluctuations of the corresponding SC obtained at 2.5 and 7 m were then studied experimentally.

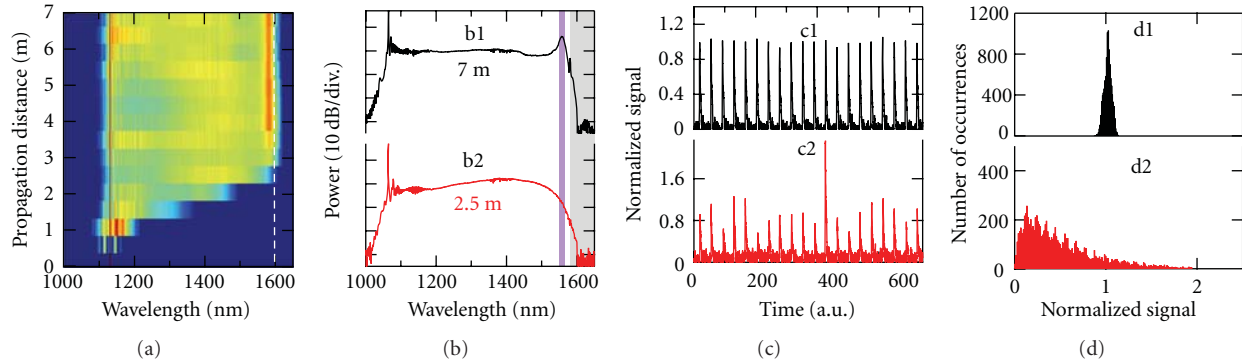


FIGURE 11: (a) Measurement of the spectral broadening as a function of propagation distance in the solid-core PBG fiber 3. The white dashed line represents the PBG edge. (b) Measured spectra for a fiber length of 7 m (b1) and 2.5 m (b2). (c1 and c2) Samples of corresponding pulse train recorded after a 10 nm bandpass spectral filtering at 1550 nm (depicted by the purple region in (b)). (d1 and d2) Corresponding statistical distribution of the signal amplitude over 10,000 records. The signal amplitude is normalized to the average over the 10,000 pulses.

To do this, the SC output was collimated and spectrally filtered with a 10 nm bandpass filter centered at 1550 nm, that is, on the soliton accumulation peak. Pulse-to-pulse fluctuations in this 10 nm wide spectral regions were measured using the method firstly proposed in [37]. The energy of spectrally filtered pulses is proportional to their peak power, so that rogue events and their associated characteristics can be captured through a simplified measurement of shot-to-shot pulse energy [37]. This was done in our experiments using a photodiode and an analog oscilloscope, with the same photodiode maximum signal amplitude and trigger level for both fiber lengths. Note that, in our experiments, this setup provides a measurement of the average energy of each pulse, but it does not allow to quantify noise-sensitive instabilities related to the actual temporal coherence of the SC, as explained in [38] for instance. The percentage of shot-to-shot variations, σ , was evaluated using $\sigma = 100 \times (V_{\max} - V_{\min}) / (V_{\max} + V_{\min})$ where V_{\max} and V_{\min} are, respectively, the maximum and minimum photodiode signal amplitude measured at least for 10 of the 10,000 recorded pulses.

Figures 11(c1) and 11(c2) show samples of pulse trains measured for each investigated fiber length after the 10 nm bandpass filter at 1550 nm, from which pulse-to-pulse fluctuations σ can be evaluated. The pulse amplitude has been normalized to its average value over the 10,000 measurements for this plot. Pulse-to-pulse fluctuations calculated at 1550 nm are as high as 80% after 2.5 m while they drop down to 10% after 7 m. Besides, the corresponding statistical distributions at 1550 nm have very different shapes, as attested by Figures 11(d1) and 11(d2) which represent histograms calculated over 10,000 measurements for fiber lengths of 2.5 m and 7 m, respectively. The distribution is highly asymmetric after 2.5 m but becomes Gaussian-like at 7 m, that is, once solitons have reached the PBG edge. These observations thus suggest that there is a correlation between the cancellation of the SSFS occurring near the PBG edge (leading to a saturation of the SC spectrum for propagation distances longer than about 3 m), and the enhanced pulse-to-pulse stability and statistical distributions in the same spectral region.

5.2. Confirmation with Simulations. In order to get insight into these results, we performed numerical simulations using the GNLSE given by (1). At first, we simply attempted to reproduce experimental results of Figure 11. To do this, all available fiber characteristics and experimental conditions have been taken into account with no free parameter, with the exception of the pulse duration that has been reduced to 50 ps (against 600 ps in experiments). Indeed, shortening the pulse duration in simulations (while staying in the long-pulse regime though) allows to significantly reduce the computation time without significantly affecting the SC dynamics. The input pump peak power was 3 kW, and quantum noise was modeled by adding one photon per mode with random phase on each spectral discretization bin of the input field [26]. In order to study the statistical behavior of the pulse train, we performed 200 simulations with random initial noise conditions.

Simulations results are displayed in Figure 12, with the same organization as Figure 11 for easy comparison. Figures 12(a), 12(b1), and 12(b2), which show the dynamics of the SC formation, correspond to the averaged spectra over 200 simulation shots. The agreement with experiments is excellent, and the typical spectral features discussed above about the spectrum shape at its long-wavelength edge are accurately reproduced. The simulated temporal properties shown in Figures 12(c1), 12(c2), 12(d1), and 12(d2) have been calculated using a numerical gaussian filter of 10 nm (FWHM) centered at 1562 nm, which corresponds to the maximum of the spectral power peak observed near the PBG edge (see plot 12(b1)). Taking the inverse Fourier transform gives the temporal profile of the SC filtered at the corresponding wavelength, whose average power has been calculated. Samples of the modeled pulse trains corresponding to 20 simulation shots are displayed in Figures 12(c1) and 12(c2), for, respectively, fiber lengths of 7 and 2.5 m. Corresponding statistical distributions calculated from all the 200 simulations are shown in Figures 12(d1) and 12(d2) and also show excellent agreement with experiments.

All these simulation results therefore allow to reproduce not only the main spectral features observed in the

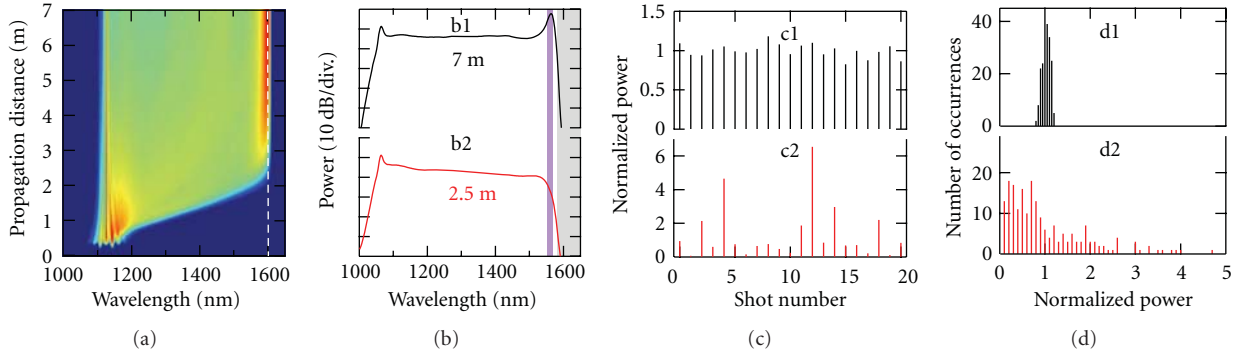


FIGURE 12: (a) Simulation of the spectral broadening as a function of propagation distance in the solid-core PBG fiber 3 (averaged over 200 simulation shots). The white dashed line represents the PBG edge. (b) Simulated averaged spectra for fiber lengths of 7 m (b1) and 2.5 m (b2). (c1 and c2) Samples of corresponding pulse train after spectral filtering at 1562 nm (depicted by the purple region in (b)). (d1 and d2) Corresponding histograms over 200 pulses at 1562 nm, where the power is normalized to its average over the 200 shots.

experiments (dynamics of the SC formation, typical spectral shape at the long-wavelength edge), but also the measured statistical features of the pulse train (pulse-to-pulse fluctuations as a function of wavelength and propagation distance, shape of the distribution). At this point, however, numerical simulations do not allow to discuss on the physical mechanisms responsible for the enhanced pulse-to-pulse stability near the PBG edge.

5.3. Discussion. Numerical simulations using the GNLSE accurately reproduce our experiments and can consequently be used to discuss the physical mechanisms causing the enhanced stability of the SC long-wavelength edge. To this end, the spectrotemporal representation has proved to be a powerful tool in studying the dynamics of SC generation [26]. Figures 13(a)–13(d) show the evolution of a simulated spectrogram for fiber lengths of 1, 2.5, 4, and 7 m.

Figure 13(a) shows how MI initially generates solitons that subsequently red-shifts through Raman-induced SSFS as can be seen from Figure 13(b). In such a long-pulse pumping regime, the presence of statistically rare temporal events in SC experiments can find two complementary physical origins. Firstly, it can be due to a single high peak power soliton generated from MI for particular initial noise conditions [32, 33]. Because of its higher peak power, it experiences a more efficient SSFS than other solitons and, consequently, becomes statistically rare at highest wavelengths due to the low probability for these particular noise conditions to happen [32]. Note that, in this case, the requirements for a soliton to be statistically rare at the long-wavelength SC edge, are only to experience a slightly more efficient SSFS than the other ones [39]. Secondly, following these early interpretations, it has been suggested that rare and brief events can arise from the collision of two or more solitons travelling with different group velocities [34, 35, 39, 40] because of the convective nature of the system [41]. Note that these two explanations are complementary for explaining long-tail statistical distributions usually observed at the SC long-wavelength edge [41].

In the case of the present experiments, however, this dynamics is strongly affected by the SSFS cancellation occurring near the PBG edge, as can be seen from Figures 13(c) and 13(d). Firstly, these figures show that, as long as solitons are frequency locked around 1562 nm, they all have very close group velocities at this location in the spectrum. Consequently, once they have reached the PBG edge, they cannot collide anymore, which prevents the formation of brief spikes [34] and leads to an enhanced pulse-to-pulse stability at the SC edge. Secondly, since all solitons whose SSFS has been cancelled near the PBG edge have very close characteristics, power fluctuations are reduced in this spectral region as compared to the usual case in which only a few solitons with slightly higher peak power are rare at the long-wavelength edge [32, 33].

As a consequence, the reduction of pulse-to-pulse fluctuations at the long-wavelength edge as a function of propagation distance is intimately linked to the cancellation of the SSFS discussed in Section 3. It is thus in fact due to the specific linear properties inherent to solid-core PBG fibers and, in particular, to the strong third-order dispersion near the PBG edge, as shown in Figure 3.

6. Conclusion

In conclusion, we showed that the SSFS and its dynamics can be strongly and easily manipulated thanks to the specific properties of the solid-core PBG fibers used in our various experimental and numerical studies. Indeed, we demonstrated that a quasicancellation of the SSFS could be obtained in this kind of fibers thanks to the large increase of β_2 observed on the long-wavelength edge of the first PBG. We established, through experimental and numerical studies, that this phenomenon could be achieved without significant power loss. Thanks to these results, we demonstrated and clearly interpreted that these fibers could be used to tailor efficiently the spectral extension of SC at no power cost. Moreover, we revealed and explained that the long-wavelength edge of SC generated in this kind of fibers can present strong quantitative and qualitative differences

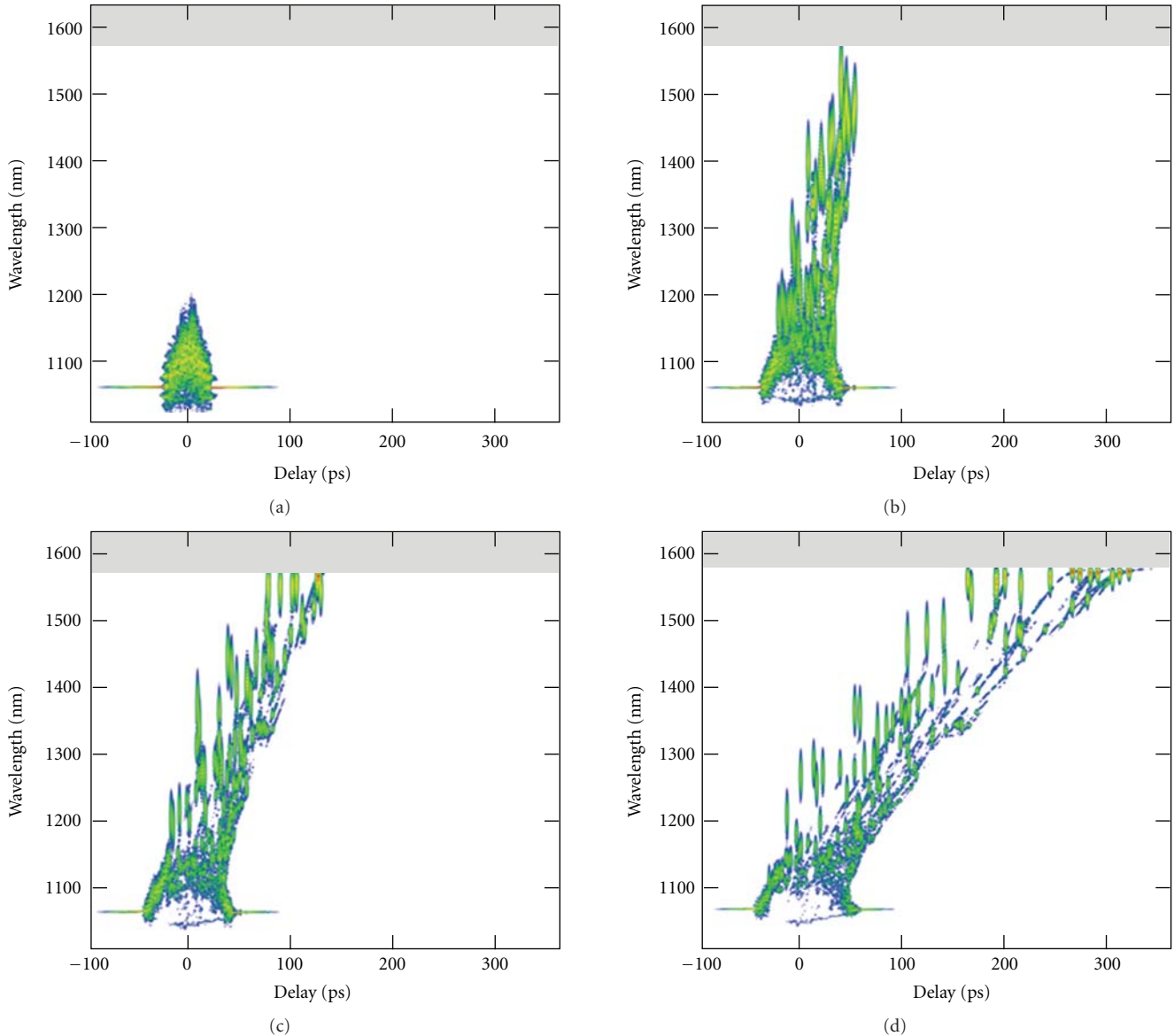


FIGURE 13: Simulated spectrograms representing the spectrotemporal dynamics of the SC generation for four propagation distances z of 1, 2.5, 4, and 7 m, respectively, from (a) to (d).

in terms of temporal stability compared to SC generated in more conventional fibres: the power fluctuations in this spectral domain are indeed strongly reduced and have a Gaussian-like statistical distribution and not the more usual L -shaped statistics associated with the presence of optical rogue waves generally observed at the long-wavelength edge of more conventional SC. We believe these results to be helpful for building SC sources for the next generation of time-resolved coherent antistokes Raman scattering (CARS) microscopes for instance [42].

Acknowledgments

The authors acknowledge Rémi Habert for experimental assistance and Karen Delplace for assistance in fiber fabrication. This work was partly supported by the French

Ministry of Higher Education and Research, the Nord-Pas de Calais Regional Council, and FEDER through the “Contrat de Projets Etat Région (CPER) 2007-2013” and the “Campus Intelligence Ambiante” (CIA).

References

- [1] F. Luan, A. K. George, T. D. Hedley et al., “All-solid photonic bandgap fiber,” *Optics Letters*, vol. 29, no. 20, pp. 2369–2371, 2004.
- [2] A. Argyros, T. A. Birks, S. G. Leon-Saval, C. M. B. Cordeiro, and P. S. J. Russell, “Guidance properties of low-contrast photonic bandgap fibres,” *Optics Express*, vol. 13, no. 7, pp. 2503–2511, 2005.
- [3] V. Pureur, A. Betourne, G. Bouwmans et al., “Overview on solid core photonic bandgap fibers,” *Fiber and Integrated Optics*, vol. 28, no. 1, pp. 27–50, 2009.

- [4] G. Bouwmans, L. Bigot, Y. Quiquempois, F. Lopez, L. Provino, and M. Douay, "Fabrication and characterization of an all-solid 2D photonic bandgap fiber with a low-loss region (< 20 dB/km) around 1550 nm," *Optics Express*, vol. 13, pp. 8452–8459, 2005.
- [5] A. Fuerbach, P. Steinvurzel, J. A. Bolger, A. Nulsen, and B. J. Eggleton, "Nonlinear propagation effects in antiresonant high-index inclusion photonic crystal fibers," *Optics Letters*, vol. 30, no. 8, pp. 830–832, 2005.
- [6] B. Kibler, T. Martynkien, M. Szpulak et al., "Nonlinear femtosecond pulse propagation in an all-solid photonic bandgap fiber," *Optics Express*, vol. 17, no. 12, pp. 10393–10398, 2009.
- [7] A. S. Cerqueira Jr., C. M. B. Cordeiro, F. Biancalana et al., "Nonlinear interaction between two different photonic bandgaps of a hybrid photonic crystal fiber," *Optics Letters*, vol. 33, no. 18, pp. 2080–2082, 2008.
- [8] P. D. Rasmussen, J. Laegsgaard, and O. Bang, "Degenerate four wave mixing in solid core photonic bandgap fibers," *Optics Express*, vol. 16, no. 6, pp. 4059–4068, 2008.
- [9] A. Bétourné, Y. Quiquempois, G. Bouwmans, and M. Douay, "Design of a photonic crystal fiber for phase-matched frequency doubling or tripling," *Optics Express*, vol. 16, no. 18, pp. 14255–14262, 2008.
- [10] V. Paturel and J. M. Dudley, "Nonlinear spectral broadening of femtosecond pulses in solid-core photonic bandgap fibers," *Optics Letters*, vol. 35, no. 16, pp. 2813–2815, 2010.
- [11] O. Vanvincq, A. Kudlinski, A. Bétourné, Y. Quiquempois, and G. Bouwmans, "Extreme deceleration of the soliton self-frequency shift by the third-order dispersion in solid-core photonic bandgap fibers," *Journal of the Optical Society of America B*, vol. 27, no. 11, pp. 2328–2335, 2010.
- [12] A. Bétourné, A. Kudlinski, G. Bouwmans, O. Vanvincq, A. Mussot, and Y. Quiquempois, "Control of supercontinuum generation and soliton self-frequency shift in solid-core photonic bandgap fibers," *Optics Letters*, vol. 34, no. 20, pp. 3083–3085, 2009.
- [13] O. Vanvincq, B. Barviau, A. Mussot, G. Bouwmans, Y. Quiquempois, and A. Kudlinski, "Significant reduction of power fluctuations at the long-wavelength edge of a supercontinuum generated in solid-core photonic bandgap fibers," *Optics Express*, vol. 18, no. 23, pp. 24352–24360, 2010.
- [14] A. Bétourné, G. Bouwmans, Y. Quiquempois, M. Perrin, and M. Douay, "Improvements of solid-core photonic bandgap fibers by means of interstitial air holes," *Optics Letters*, vol. 32, no. 12, pp. 1719–1721, 2007.
- [15] M. Perrin, Y. Quiquempois, G. Bouwmans, and M. Douay, "Coexistence of total internal reflexion and bandgap modes in solid core photonic bandgap fibre with interstitial air holes," *Optics Express*, vol. 15, no. 21, pp. 13783–13795, 2007.
- [16] M. Tateda, N. Shibata, and S. Seikai, "Interferometric method for chromatic dispersion measurement in a single-mode optical fiber," *IEEE Journal of Quantum Electronics*, vol. 17, no. 3, pp. 404–407, 1981.
- [17] G. P. Agrawal, *Nonlinear Fiber Optics*, Academic Press, New York, NY, USA, 4th edition, 2007.
- [18] E. M. Dianov, A. Y. Karasik, P. V. Mamyshv et al., "Stimulated-Raman conversion of multisoliton pulses in quartz optical fibers," *JETP Letters*, vol. 41, pp. 294–297, 1985.
- [19] Y. Kodama and A. Hasegawa, "Nonlinear pulse propagation in a monomode dielectric guide," *IEEE Journal of Quantum Electronics*, vol. 23, no. 5, pp. 510–524, 1987.
- [20] P. Beaud, W. Hodel, B. Zysset, and H. P. Weber, "Ultrashort pulse propagation, pulse breakup and fundamental soliton formation in a single-mode optical fiber," *IEEE Journal of Quantum Electronics*, vol. 23, no. 11, pp. 1938–1946, 1987.
- [21] F. M. Mitschke and L. F. Mollenauer, "Discovery of the soliton self-frequency shift," *Optics Letters*, vol. 11, no. 10, pp. 659–661, 1986.
- [22] J. P. Gordon, "Theory of the soliton self-frequency shift," *Optics Letters*, vol. 11, no. 10, pp. 662–664, 1986.
- [23] J. Laegsgaard, "Mode profile dispersion in the generalized nonlinear Schrödinger equation," *Optics Express*, vol. 15, no. 24, pp. 16110–16123, 2007.
- [24] J. C. Travers, M. H. Frosz, and J. M. Dudley, "Nonlinear fibre optics overview," in *Supercontinuum Generation in Optical Fibers*, J. M. Dudley and J. R. Taylor, Eds., chapter 3, Cambridge University Press, Cambridge, UK, 2010.
- [25] D. Hollenbeck and C. D. Cantrell, "Multiple-vibrational-mode model for fiber-optic Raman gain spectrum and response function," *Journal of the Optical Society of America B*, vol. 19, no. 12, pp. 2886–2892, 2002.
- [26] J. M. Dudley, G. Genty, and S. Coen, "Supercontinuum generation in photonic crystal fiber," *Reviews of Modern Physics*, vol. 78, no. 4, pp. 1135–1184, 2006.
- [27] The long-pulse pumping regime refers to cases in which the pump pulse duration ΔT is much longer than the MI oscillation period ΔT_{MI} , given by $\Delta T_{MI} = 2\pi\sqrt{|\beta_2|/(2\gamma P)}$, with β_2 the second-order dispersion coefficient, γ the NL coefficient and P the pump peak power. Cases in which ΔT is in the order or less than ΔT_{MI} correspond to the short-pulse pumping regime.
- [28] A. V. Gorbach and D. V. Skryabin, "Light trapping in gravity-like potentials and expansion of supercontinuum spectra in photonic-crystal fibres," *Nature Photonics*, vol. 1, no. 11, pp. 653–657, 2007.
- [29] J. M. Stone and J. C. Knight, "Visibly "white" light generation in uniform photonic crystal fiber using a microchip laser," *Optics Express*, vol. 16, no. 4, pp. 2670–2675, 2008.
- [30] A. Kudlinski, G. Bouwmans, Y. Quiquempois, and A. Mussot, "Experimental demonstration of multiwatt continuous-wave supercontinuum tailoring in photonic crystal fibers," *Applied Physics Letters*, vol. 92, no. 14, Article ID 141103, 2008.
- [31] A. Kudlinski, G. Bouwmans, M. Douay, M. Taki, and A. Mussot, "Dispersion-engineered photonic crystal fibers for CW-pumped supercontinuum sources," *Journal of Lightwave Technology*, vol. 27, no. 11, pp. 1556–1564, 2009.
- [32] D. R. Solli, C. Ropers, P. Koonath, and B. Jalali, "Optical rogue waves," *Nature*, vol. 450, no. 7172, pp. 1054–1057, 2007.
- [33] J. M. Dudley, G. Genty, and B. J. Eggleton, "Harnessing and control of optical rogue waves in supercontinuum generation," *Optics Express*, vol. 16, no. 6, pp. 3644–3651, 2008.
- [34] A. Mussot, A. Kudlinski, M. Kolobov, E. Louvergneaux, M. Douay, and M. Taki, "Observation of extreme temporal events in CW-pumped supercontinuum," *Optics Express*, vol. 17, no. 19, pp. 17010–17015, 2009.
- [35] G. Genty, C. M. de Sterke, O. Bang, F. Dias, N. Akhmediev, and J. M. Dudley, "Collisions and turbulence in optical rogue wave formation," *Physics Letters, Section A*, vol. 374, no. 7, pp. 989–996, 2010.
- [36] F. Vanholsbeeck, S. Martin-Lopez, M. González-Herráez, and S. Coen, "The role of pump incoherence in continuous-wave supercontinuum generation," *Optics Express*, vol. 13, no. 17, pp. 6615–6625, 2005.
- [37] C. Lafargue, J. Bolger, G. Genty, F. Dias, J. M. Dudley, and B. J. Eggleton, "Direct detection of optical rogue wave energy

- statistics in supercontinuum generation,” *Electronics Letters*, vol. 45, no. 4, pp. 217–219, 2009.
- [38] H. Kubota, K. R. Tamura, and M. Nakazawa, “Analyses of coherence-maintained ultrashort optical pulse trains and supercontinuum generation in the presence of soliton-amplified spontaneous-emission interaction,” *Journal of the Optical Society of America B*, vol. 16, no. 12, pp. 2223–2232, 1999.
- [39] M. Erkintalo, G. Genty, and J. M. Dudley, “On the statistical interpretation of optical rogue waves,” *European Physical Journal*, vol. 185, no. 1, pp. 135–144, 2010.
- [40] K. Hammani, B. Kibler, C. Finot, and A. Picozzi, “Emergence of rogue waves from optical turbulence,” *Physics Letters, Section A*, vol. 374, no. 34, pp. 3585–3589, 2010.
- [41] M. Taki, A. Mussot, A. Kudlinski, E. Louvergneaux, M. Kolobov, and M. Douay, “Third-order dispersion for generating optical rogue solitons,” *Physics Letters, Section A*, vol. 374, no. 4, pp. 691–695, 2010.
- [42] D. A. Sidorov-Biryukov, E. E. Serebryannikov, and A. M. Zheltikov, “Time-resolved coherent anti-Stokes Raman scattering with a femtosecond soliton output of a photonic-crystal fiber,” *Optics Letters*, vol. 31, no. 15, pp. 2323–2325, 2006.